COMPREHENSIVE CHARACTERIZATION OF NICKEL-BASED METALLIC FOAMS AND THEIR APPLICATIONS AS ELECTROCATALYST MATERIALS

by

Julia van Drunen

A thesis submitted to the Department of Chemistry
in conformity with the requirements for
the degree of Doctor of Philosophy

Queen’s University
Kingston, Ontario, Canada
December, 2013

Abstract

This contribution explores the applicability of nickel-based metallic foams as active electrodes and as electrocatalyst support materials. A comprehensive characterization of Ni and multi-component Ni-based foams is presented and includes the analysis of their structural, chemical, and electrochemical properties. Several materials and surface science techniques as well as electrochemical methods are used to examine the structural characteristics, surface morphology, and surface-chemical composition of these materials. X-ray photoelectron spectroscopy is employed to analyze the surface and near-surface chemical composition. The specific and electrochemically active surface areas (A_s, A_{ecsa}) are determined using cyclic voltammetry (CV). The foams exhibit structural robustness typical of bulk materials and they have large A_s, in the 200 – 600 $cm^2\ g^{-1}$ range. In addition, they are dual-porosity materials and possess both macro and meso pores.

Nickel foam electrodes are applied as electrocatalysts for the oxidation of isopropanol. The process is studied under well-defined experimental conditions using cyclic voltammetry. The outcome of these experiments demonstrates that isopropanol oxidation requires the presence of β-NiOOH on the Ni foam electrode. This surface oxide is generated at potentials near the potential of the isopropanol oxidation; however, the two processes do not occur exactly at the same potentials. The Ni foam anodes sustain a current density of ca. 2.6 mA cm^{-2} throughout an electrolysis time of up to 600 minutes without significant loss of electrocatalytic activity. Isopropanol is converted to acetone at a rate of ca. 5.6 mM per hour.

The applicability of Ni foams as support materials for Pt is investigated. Platinum particles are deposited on Ni foam in low loading amounts via the chemical reduction of Pt^{2+} and Pt^{4+} originating from aqueous Pt salt solutions. The resulting Pt / Ni foams are characterized using electrochemical, analytical, and materials analysis techniques, including SEM to examine the morphology of the deposited material, CV to evaluate the A_{ecsa} of the deposited Pt, and inductively coupled plasma optical emission spectrometry (ICP-OES) to determine the mass of deposited Pt. The Pt / Ni foams are applied as electrocatalysts for hydrogen evolution, hydrogen reduction, oxygen evolution, and oxygen reduction reactions in alkaline electrolyte.

Co-Authorship

Work done in this thesis was carried out by the author under the supervision of Professor Gregory Jerkiewicz at the Department of Chemistry at Queen's University, Kingston, Canada. Portions of this thesis contain experimental work that was carried out in collaboration with the group of Professor Diane Beauchemin at Queen's University, the group of Professor Byron D. Gates at Simon Fraser University, Burnaby, Canada, and the group of Doctor J.–M. Lèger at Université de Poitiers, Poitiers France. Portions of this thesis are published, in press, and submitted as manuscripts in peer-reviewed scientific journals. The specific contributions of co-authors are outlined below.

1. J. van Drunen, B. Kinkead, M. C. P. Wang, E. Sourty, B. D. Gates, and G. Jerkiewicz, "Comprehensive Structural, Surface-Chemical and Electrocehmical Characterization of Nickel-Based Metallic Foams", *ACS. Applied Materials and Interfaces*, 5 (2013) 6712 – 6722.

This manuscript is presented in Chapter 4. The contributions of co-authors are as follows. The XPS analysis of Inconel foam was carried out by Dr. M. C. P. Wang, with interpretation of the data by J. van Drunen, Dr. M. C. P. Wang, and Prof. B. D. Gates. The XPS analysis of Ni foam was carried out by J van Drunen. The SEM and EDS analysis was carried out by J van Drunen and B. Kinkead. The TEM and ET analysis were carried out by Dr. E. Sourty. All electrochemical analysis, FIB analysis, and chemical etching studies were carried out by J van Drunen. Interpretation and discussion of the results was carried out by J. van Drunen under the guidance of Prof. G. Jerkiewicz.

2. J. van Drunen, T. W. Napporn, B. Kokoh, G. Jerkiewicz, “Electrochemical Oxidation of Isopropanol Using a Nickel Foam Electrode”, *Journal of Electroanalytical Chemistry,* In Press (2013) http://dx.doi.org/10.1016/j.elechem.2013.-8.003.

This manuscript is presented in Chapter 5. All experimental work was carried out by J. van Drunen at the Institut de Chimie des Milieux et des Matériaux de Poitiers, Université de Poitiers under the supervision of Dr. T. W. Napporn. The HPLC analysis was carried out with the guidance of Prof. B. Kokoh. Interpretation of the results was carried out by J. van Drunen under the guidance of Prof. G. Jerkiewicz and Dr. T. W. Napporn.

3. J van Drunen, B. Kinkead, Y. Makonnen, B. D. Gates, D. Beauchemin, G. Jerkiewicz, “Nickel-Based Metallic Foams as Electrochemically Active Supports for Platinum Electrocatalysts”, submitted to *ACS. Applied Materials and Interfaces,* (2013)

This manuscript is presented in Chapter 6. The method applied for the preparation of Pt / Ni foams was developed by J. van Drunen. The SEM imaging and EDS analysis of Pt / Ni foam was performed by B. Kinkead under the supervision of Prof. B. D. Gates and interpreted by J. van Drunen. All FIB and electrochemical analysis of Pt / Ni foams was carried out by J. van Drunen. The ICP-OES experimental work was carried out by Y. Makonnen under the supervision of Prof. B. Beauchemin. Interpretation of the ICP-OES data was performed by Y. Makonnen and J. van Drunen. All analysis of the electrocatalytic activity of Pt / Ni foams was carried out by J. van Drunen under the guidance of Prof. G. Jerkiewicz.

Acknowledgements

I would like to express my sincere gratitude towards my supervisor, Prof. Jerkiewicz, for sharing his passion for electrochemistry. His guidance and support over the course of my graduate studies is greatly appreciated. I would also like to express my appreciation to Dr. Teko Napporn, Prof. Byron Gates, and Prof. Brad Diak for all of their valuable help and advice over the course of this research. I would like to thank my committee members, Prof. Richard Oleschuk and Prof. Nick Mosey, for helpful feedback and discussions.

I would like to thank my lab mates, past and present, for so many good memories and great discussions. I would like to extend my gratitude to my colleagues at the Université de Poitiers for making me feel welcome during my time in France. I would also like to thank my colleagues at Simon Fraser University, especially Brandy Kinkead, for a very productive collaboration. I could not imagine a better group of people to work and learn with.

I would like to thank my friends and colleagues at Queen's University for the great times that I have had here. I am especially grateful to Yoseif Makonnen and Liz Murray for their immense support during the preparation of this thesis. Most importantly, I would like to thank my family their support, love, and encouragement over the years.

Statement of Originality

This work presents the first comprehensive structural, chemical, and electrochemical characterization of nickel-based metallic foams. Furthermore, an extensive electrochemical study of the oxidation of isopropanol using a nickel foam anode was carried out that reveals new details regarding the mechanism of this reaction. Pt / Ni foam materials were prepared using an original method, fully characterized, and applied as electrocatalyst materials for the hydrogen and oxygen electrode reactions.

Julia van Drunen

December, 2013

Table of Contents

List of Figures

between the CV cycle number, the A_{ecsa} of Pt (black squares), and I_{DL} from the CV profile (red triangles) (B). The total anodic and cathodic charges (Q_{anodic}, Q_{cathodic}) from $0.05 < E < 1.30$ V as a function of CV cycle number (C). (p. 180)

Figure 6.10. FIB ion images of Pt / Ni foam (type BB 10) before (A) and after (B) four hundred CV cycles in 0.50 M KOH at $T = 298$ K and $s = 100$ mV s^{-1}. (p. 182)

Figure 6.11. LSV profiles for the HER in 0.50 M KOH using the following electrodes: Ni foam (purple); Pt$_{\text{poly}}$ (blue); and Pt / Ni foams with different fractions of Pt A_{ecsa}: 0.25 (black), 0.31 (red), 0.46 (green) (A). Enlarged version for the low E region of the graph above (B); $s = 0.1$ mV s^{-1}, $T = 293$ K, E is corrected for IR drop. Current density values are normalized to the total A_{ecsa} of the electrode (Ni foam + Pt). (p. 186)

Figure 6.12. j_{HER} values at $E = -0.150$ V for Pt$_{\text{poly}}$, Ni foam, and Pt / Ni foam electrodes with various fractions of Pt A_{ecsa} plotted as a function of the A_{ecsa} Pt / A_{ecsa} total. These values are obtained from LSV profiles carried out in 0.50 M KOH at $T = 293$ K with $s = 0.1$ mV s^{-1}. Black circles correspond to j_{HER} values normalized to the total A_{ecsa} of the electrode; red triangles correspond to j_{HER} values normalized to the A_{ecsa} of Pt. (p. 188)

Figure 6.13. HER Tafel polarization plots for Pt$_{\text{poly}}$, and Pt / Ni foam electrodes with various fractions of Pt A_{ecsa} plotted as a function of the A_{ecsa} Pt / A_{ecsa} total. The data was obtained from staircase-type polarization experiments carried out in 0.50 M KOH at $T = 293$ K (A). Illustration for the determination of the Tafel slope (b) and exchange current density ($j_{0,\text{ HER}}$) (B). (p. 191)

Figure 6.14. LSV profiles for the HOR in 0.50 M KOH using the following electrodes: Ni foam (black); Pt$_{\text{poly}}$ (red); and Pt / Ni foams with different fractions of Pt A_{ecsa}: 0.30 (green), 0.40 (purple), 0.46 (blue) (A). Enlarged version for the low potential region of the graph above (B); $s = 0.1$ mV s^{-1}, $T = 293$ K, E is corrected for IR drop. Current density values are normalized to the A_{ecsa} of Pt only. (p. 195)

List of Tables

List of Abbreviations

A_{ecsa}	electrochemical surface area
AFC	alkaline fuel cell
a_{H+}	activity of proton
a_{H2}	activity of hydrogen gas
A_s	specific surface area
b	Tafel slope
BE	XPS binding energy value
BSE	back-scattered electron
C^{∞}	bulk concentration of a species
CA	chronoamperometry
CC	chronocoulometry
C_{dl}	double layer capacitance
CE	counter electrode
CV	cyclic voltammetry
CVD	chemical vapor deposition
D	diffusion coefficient
DAAFC	direct alcohol alkaline fuel cell
DAFC	direct alcohol fuel cell
DBFC	direct borohydride fuel cell
E	potential
E^0	standard potential
E_B	binding energy
EDS	energy-dispersive X-ray spectroscopy
E_K	kinetic energy
E_{peak}	peak potential
ET	electron tomography
F	faraday’s constant
FC	fuel cell
FGI	functional group interconversion
FIB	focused ion beam
HER	hydrogen evolution reaction
HOR	hydrogen oxidation reaction

HPLC	high performance liquid chromatography
HRXPS	high-resolution X-ray photoelectron spectroscopy
$\mathrm{H}_{\mathrm{UPD}}$	underpotential deposition of hydrogen
I	current
ICP-OES	inductively coupled plasma optical emission spectroscopy
I_{DL}	double-layer current
IPA	isopropyl alcohol
I_{peak}	maximum peak current
I_{s}	specific current
j	current density
j^0	exchange current density
LSV	linear sweep voltammetry
ML	monolayer
n	number of electrons transferred
$\mathrm{Ni}_{\mathrm{poly}}$	polycrystalline nickel
OER	oxygen evolution reaction
ORR	oxygen reduction reaction
OTE	optically transparent electrode
PEMFC	proton exchange membrane fuel cell
$\mathrm{Pt}_{\mathrm{poly}}$	polycrystalline platinum
PVD	physical vapor deposition
Q	charge
q	charge density
Q_{s}	specific charge
R	ideal gas constant
RE	reference electrode
RHE	reversible hydrogen electrode
s	scan rate
SE	secondary electron
SEM	scanning electron microscopy
SI	secondary ion
T	temperature
t	time
$t_{\mathrm{Ar\text{-}etch}}$	Ar ion etch time

$t_{\mathrm{electrolysis}}$	electrolysis time
TEM	transmission electron microscope
t_{etch}	chemical etch time
UHP	ultra-high purity
UPD	underpotential deposition
WDS	wavelength-dispersive X-ray spectroscopy
WE	working electrode
XPS	X-ray photoelectron spectroscopy
α_{a}	anodic charge transfer coefficient
α_{c}	cathodic charge transfer coefficient
η	overpotential
ρ	bulk density
Φ_{S}	work function

Chapter 1

Introduction

1.1 Introduction

Electrochemistry is the branch of chemistry that studies chemical reactions involving the transfer of electrons at the interface of an electrode and an electrolyte. Aqueous electrochemistry is a subset of this field that focuses on reactions taking place in a liquid solution made up of water and an electrolyte. A typical experimental set-up generally consists of electrodes, electrolyte, an electrochemical cell, and an external circuit with a mechanism that allows the experimentalist to control and monitor parameters such as potential or current. The term electrocatalysis refers to the optimization of an electrode processes through careful design of the electrode material and the conditions of the electrolyte [1].

In the field of heterogeneous catalysis, the role of the catalyst is to increase the rate of a chemical reaction by providing a low-energy pathway for the reaction to follow. The catalyst does not participate as a reactant and it is not consumed in the process. The use of a catalyst also does not affect the position of the equilibrium [2]. The role of an electrocatalyst can be described in a similar manner. The electrocatalyst is a substance, generally a solid electrode, which accelerates an electrochemical reaction without being consumed in the process [3]. Therefore, an electrocatalyst can be thought of as a heterogeneous catalyst for an electrochemical process. The activity of an electrocatalyst towards a particular reaction is marked by its ability to increase the standard rate constant of the reaction. This increase in the rate constant is generally observed as an increase in the faradic current of the reaction [4]. An electrode is said to have good electrocatalytic activity for a reaction when the exchange current density is high and the Tafel slope is small [3]. Figure 1.1 demonstrates the electrochemical behavior of good and poor electrocatalysts [5]. The following processes take place during an electrocatalyzed reaction.

(i) The reactants are adsorbed at the surface of the electrocatalyst such that a high concentration of reactants is available in this vicinity for the reaction to occur.

(ii) Charge transfer takes place. This is facilitated by the potential at the electrode.

(iii) Products are desorbed from the electrode.

In order for the rate of the overall reaction to remain high, it is important that the desorption processes occur rapidly. If products are adsorbed strongly on the electrocatalyst, the activity decreases; this process is called electrode blocking.

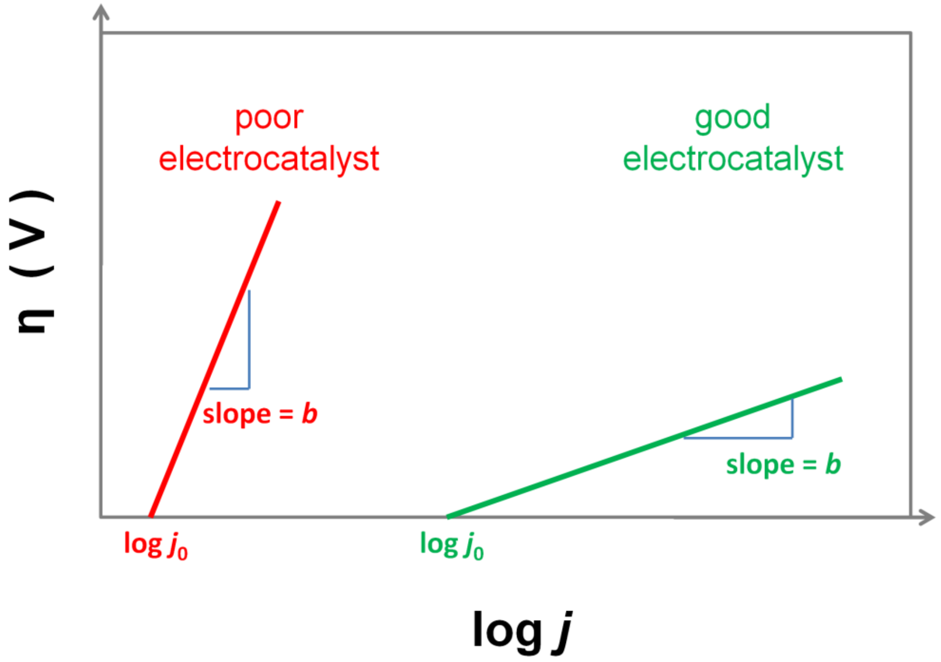

Figure 1.1. Tafel polarization plot (overpotential (η) vs. current density (*j*) for an anodic electrochemical process. The red line corresponds to a poor electrocatalyst; the green line corresponds to a good electrocatalyst.

Noble metals offer the best electrocatalytic performance for many industrially relevant electrochemical processes. Platinum, palladium, rhodium, and gold are among the most studied electrocatalysts. Platinum has the highest activity for both the hydrogen-electrode reaction and the oxygen-electrode reaction [3]. However, these high-performing metals are some of the most expensive electrode materials because they are precious metals and are in low abundance in nature [6]. There are a few different approaches that are used to decrease the cost of electrocatalytic materials while maintaining the necessary level of performance: (i) decreasing the amount of precious metal used; (ii) combining precious metals with other electrocatalytic materials; (iii) designing high-performance non-precious metal electrocatalysts. Since precious metals have such good performance as electrocatalysts, many researchers focus on strategies to minimize the amount used by developing high surface area materials. This strategy is taken to the molecular level through the design of Pt and Au nanoparticles that are fabricated to have a particular shape or even to maximize the surface area proportion of a preferred crystal facet [7, 8]. Another way to reduce the amount of precious metal needed for an electrocatalytic process is to develop electrocatalysts that utilize precious metals in combination with less expensive materials. In this respect, strategies include the development of alloys [9 – 13], bimetallic materials [11, 14], and materials that have precious metals dispersed upon a support [15 – 17]. There are also a large number of researchers focusing on the development of electrocatalysts that do not utilize precious metals [6, 18, 19]. The development of effective non-precious metal electrocatalysts often entails the synthesis of new materials that are specially designed to perform all of the tasks necessary in electrocatalysis (adsorption of reactants, electron transfer, and desorption of products). Besides material design, a major challenge in the field of non-precious metal electrocatalysis is achieving the required electrode stability for commercial applications. The design and development of highly effective non-precious metal electrocatalysts is a huge challenge in the field of electrochemistry.

In the category of non-precious metal electrocatalysts, nickel electrodes stand out as being very successful. Nickel and nickel-based electrodes are applied in several industrial electrochemical processes including water electrolysis and hydrogenation reactions. Platinum has a higher electrocatalytic activity than Ni for the hydrogen evolution reaction, but Ni cathodes are used in industrial water electrolyzers due to their low cost. Figure 1.2 displays a volcano plot for the hydrogen evolution reaction that compares several metals in terms of their activity [20, 21].

The current density values for each metal are plotted as a function of their metal-to-hydrogen bond strength. The precious metals are located near the apex of the volcano plot. Nickel, copper, and iron are all considered relatively good electrocatalysts for this reaction.

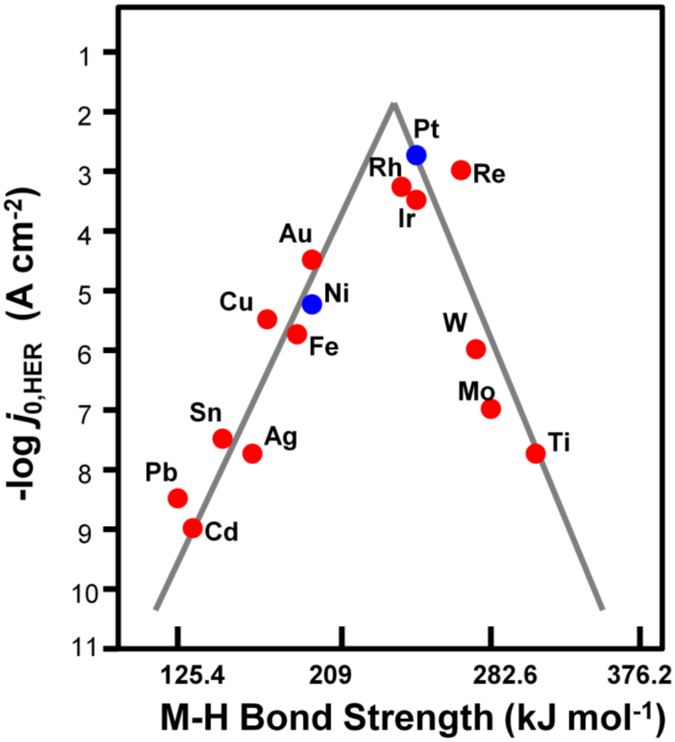

Figure 1.2. Volcano plot for the hydrogen evolution reaction; log j_0 values are plotted as a function of M – H bond energy [20, 21].

Nickel-based electrocatalysts are only applied in electrochemical reactions that are carried out in alkaline electrolyte because Ni is unstable in acidic media. The potential versus pH plot (Pourbaix diagram) for Ni in water at 25˚C demonstrates that Ni dissolves into Ni^{2+} in the $-0.20 < E < 0.6$ V range at pH < 0.65 [22]. The instability of Ni in acidic media limits the applications of Ni electrocatalysts to reactions that can be carried out in alkaline or neutral environments. Commercial water electrolyzers operate primarily using strongly alkaline electrolytes. There are also alkaline hydrogen and alcohol fuel cells that utilize Ni electrocatalysts.

The primary goal of this research is to examine nickel-based metallic foam materials for applications in electrochemistry and electrocatalysis. Nickel-based metallic foams are open-cell, three-dimensional materials that were originally manufactured as electrode supports and charge carriers for rechargeable alkaline batteries. These materials possess several properties that make them interesting candidates for applications in electrocatalysis: (i) tunable pore size and density; (ii) an open-pore structure that allows electrolyte to flow through the electrode; (iii) large specific and electrochemical surface areas; and (iv) electrochemical stability in aqueous alkaline electrolytes. In addition to these properties, Ni foams are manufactured on a large scale and can be cut to virtually any size and shape.

At the beginning of this research, it was our goal to fully characterize Ni-based metallic foams in terms of their physical, chemical, and electrochemical properties. A material can be successfully applied as an electrocatalyst only once it is fully understood on the structural and chemical level. A comprehensive characterization of Ni foams is presented in Chapter 4. The applicability of Ni foam as an electocatalyst for the oxidation of isopropyl alcohol is explored in Chapter 5. Chapter 6 examines the application of Ni foams as a support material for Pt particles. These Pt / Ni foams are utilized as electrocatalysts towards hydrogen and oxygen reactions in alkaline media. In the same chapter, unmodified Ni foams are also applied towards hydrogen evolution, hydrogen oxidation, oxygen reduction, and oxygen evolution reactions in order to evaluate their electrocatalytic activity towards these reactions.

1.2 References

(1) S. Trasatti, *Electrochim. Acta*, **2000**, 45, 2377-2385 .

(2) C. Housecroft and A. G. Sharpe, *Inorganic Chemistry*, Prentice Hall, New York, **2012**.

(3) J. O'.M. Bockris and S. Srinivasan, *Fuel Cells: Their Electrochemistry*, McGraw-Hill, New York, **1969**.

(4) A. J. Bard, G. Inzelt and F. Scholz, *Electrochemical Dictionary*, Springer-Verlag, Berlin, Germany, **2008**.

(5) G. Jerkiewicz, Electrocatalytic Parameters, Chem 415. Queen's University, **2013**.

(6) R. Bashyam and P. Zelenay, *Nature*, **2006**, 443, 63-66.

(7) C. Coutanceau, P. Urchaga, S. Brimaud and S. Baranton, *Electrocatalysis*, **2012**, 3, 75-87.

(8) C. Wang, H. Daimon, T. Onodera, T. Koda and S. Sun, *Angewandte Chemie International Edition*, **2008**, 47, 3588-3591.

(9) T. Toda, H. Igarashi and M. Watanabe, *J Electroanal Chem*, **1999**, 460, 258-262.

(10) K. Sasaki, J. Wang, M. Balasubramanian, J. McBreen, F. Uribe and R. Adzic, *Electrochim. Acta*, **2004**, 49, 3873-3877.

(11) F. H. Lima, C. D. Sanches and E. A. Ticianelli, *J. Electrochem. Soc.*, **2005**, 152, A1466-A1473.

(12) S. Mukerjee and S. Srinivasan, *J Electroanal Chem*, **1993**, 357, 201-224.

(13) Stamenkovic, V., Mun, B. S., K. J. J. Mayrhofer, P. N. Ross and N. M. Markovic, *Journal of the American Chemical Society*, **2006**, 128, 8813-8819.

(14) J. Luo, M. M. Maye, V. Petkov, N. N. Kariuki, L. Wang, P. Njoki, D. Mott, Y. Lin and C. Zhong, *Chemistry of materials*, **2005**, 17, 3086-3091.

(15) V. Radmilovic, H. Gasteiger and P. Ross, *Journal of Catalysis*, **1995**, 154, 98-106.

(16) E. Auer, A. Freund, J. Pietsch and T. Tacke, *Applied Catalysis A: General*, **1998**, 173, 259-271.

(17) E. Verlato, S. Cattarin, N. Comisso, A. Gambirasi, M. Musiani and L. Vazquez-Gomez, *Electrocatal.*, **2012**, 3, 48-58.

(18) A. Ishihara, Y. Ohgi, K. Matsuzawa, S. Mitsushima and K. Ota, *Electrochim. Acta*, **2010**, 55, 8005-8012.

(19) Y. Gorlin and T. F. Jaramillo, *J. Am. Chem. Soc.*, **2010**, 132, 13612-13614.

(20) B. Conway and G. Jerkiewicz, *Electrochim. Acta*, **2000**, 45, 4075-4083.

(21) S. Trasatti, *Electroanal. Chem. Intertacial Electrochem.*, **1972**, 39, 163-184.

(22) R. Cowan and R. Staehle, *J. Electrochem. Soc.*, **1971**, 118, 557-568.

Chapter 2

Background Information and Literature Review

2.1 The Significance of Nickel in Electrochemistry and Electrocatalysis

2.1.1 The Importance of Nickel as an Industrial Material

Nickel is a valuable commodity that is used in a variety of industries. The fabrication of stainless steels and metallic alloy materials accounts for a large portion of the Ni used worldwide. Canada is a major Ni producing country; in 2011, it ranked fourth in terms of Ni production (after Russia, the Philippines, and Indonesia), and Canadian Ni production had increased by 27% from 2010 to 2011 [1]. Countries that are recently emerging as significant Ni producers include Brazil, Madagascar, and Botswana [1, 2]. In the United States of America, the consumption of Ni in 2011 was broken down into the following uses: stainless and alloy steels (46%), nonferrous alloys and superalloys (34%), electroplating (14%), and other (6%). Applications of these materials include electrical equipment, applications in the petroleum and chemical industries, construction materials, household appliances, and industrial machinery [1]. In terms of electrochemical technologies, the most well-known use of Ni is in batteries; some of the batteries that utilize Ni electrodes are outlined in Table 2.1 [3 – 6]. Nickel is an important electrocatalyst that is often used in combination with other metals in order to improve its electrocatalytic performance. Electrocatalysis using Ni and combined Ni and Pt materials is a main theme within this thesis, thus this Literature Review Chapter is included to provide detailed background information and relevant examples of Ni and Pt materials as they are applied in electrochemistry and electrocatalysis.

Table 2.1. Examples of battery systems utilizing nickel electrodes

Name	**Anode**	**Cathode**	**Cell Voltage**	**Applications**	**Reference**
NiCd	Cd / $Cd(OH)_2$	NiOOH / $Ni(OH)_2$	1.25 V	Portable devices (small electronics, toys, emergency lighting, cordless tools)	[6 – 8]
NiZn	Zn / $Zn(OH)_2$	NiOOH / $Ni(OH)_2$	1.50 V	Portable devices (digital cameras, cordless tools), light electric vehicles and bicycles,	[8]
NiFe	Fe / $Fe(OH)_2$	NiOOH / $Ni(OH)_2$	1.25 V	Stationary applications where durability is important (mining and railway industries, off-grid residential uses)	[8]
NiMH	M / MH	NiOOH / $Ni(OH)_2$	1.2 V	Electric vehicles, telecommunication satellites, robotics	[2, 5, 8]
$NaNiCl_2$ or Zebra	Na / NaCl	$NiCl_2$ / Ni	2.58 V	Electric vehicles	[9]

2.1.2 The Electrochemical Behavior of Nickel in Aqueous Alkaline Media

When discussing the electrochemical behavior of Ni, it is convenient to consider the three oxide phases formed when a positive potential is applied to the metallic Ni electrode. A cyclic voltametry (CV) profile of Ni in aqueous alkaline solution reveals features corresponding to the formation of three oxide species as the potential is increased from –0.20 to 1.60 V vs. RHE [10]. The anodic peak corresponding to the formation of the first surface oxide, α-$Ni(OH)_2$, is present in the E range of –0.20 to 0.50 V [11 – 13]. If the CV scan is reversed at a potential lower than 0.50 V, the full reduction of α-$Ni(OH)_2$ to metallic Ni will occur, giving rise to a cathodic peak in the CV profile at $-0.12 \leq E \leq 0.12$ V [14, 15]. When the potential is brought to values lower than 0.00 V, appreciable current density as a result of the hydrogen evolution reaction (HER) is observed along with the formation of H_2 (gas) bubbles at the electrode [14, 15]. The HER overlaps in potential with the reduction of α-$Ni(OH)_2$. If the forward CV scan is continued to potentials higher than 0.50 V, the α-$Ni(OH)_2$ already present on the electrode converts to β-$Ni(OH)_2$, and additional β-$Ni(OH)_2$ is formed [10, 16]. This species is formed in the E region between 0.50 V and 1.30 V, which is known as the passive potential region for Ni [17]. Of these two $Ni(OH)_2$ structures, the β phase is more stable. Formation of this phase is irreversible, meaning that β-$Ni(OH)_2$ cannot be removed from the surface of the electrode by simply reversing the potential and reducing the oxide electrochemically. Once formed, β-$Ni(OH)_2$ can be removed through chemical etching, mechanical polishing, and thermal reduction in a hydrogen environment [18, 19]. The α and β $Ni(OH)_2$ species have different crystallographic structures; the α phase incorporates either water or alkali cations from the electrolyte and has a lattice constant that is larger than that of β-$Ni(OH)_2$ [16, 17]. The final oxidation species to be formed is NiOOH at $E > 1.30$ V; the β-$Ni(OH)_2$ species is oxidized reversibly to β-NiOOH which has a similar crystallographic structure and lattice constant [10, 13]. If an increasing positive potential is continuously applied, a γ-NiOOH phase is formed. This species adopts a crystallographic structure similar to that of α-$Ni(OH)_2$ and can be electrochemically reduced back to β-$Ni(OH)_2$ [20, 21]. Past the potential of 1.55 V, the oxygen evolution reaction (OER) takes place, occurring concurrently with the growth of NiOOH [10]. Further discussion of the electrochemical behavior of Ni in alkaline media is included in Chapters 4, 5, and 6, as it relates to the results presented in therein.

2.2 Select Applications of Nickel in Electrocatalysis

2.2.1 Alkaline Water Electrolysis

The availability of high-purity hydrogen gas is an important challenge for the implementation of fuel cells as viable energy delivering technologies. The global demand for hydrogen gas grows at a rate of approximately 10% per year and is driven by the use of hydrogen in fertilizer production, food processing, metallurgical applications, and many other industries [22, 23]. Hydrogen may be generated through steam reforming of biomass-derived fuels or fossil fuels; however, the H_2 gas formed using this process is of low purity [24]. In addition, the use of carbon based fuels to generate H_2 gas perpetuates the global dependence on hydrocarbons instead of offering a true alternative fuel source. In contrast, H_2 gas of high purity can be generated through the electrochemical conversion of water to H_2 and O_2 gasses, as shown in equation 2.1 [23, 24]. It is generally accepted that the mechanism for this reaction in alkaline media proceeds through the steps outlined in equations 2.2 – 2.4 [25 – 31]. In order for this process to take place, 237.2 kJ mol^{-1} of electrical energy and 48.6 kJ mol^{-1} of thermal energy are required [24]. The high electricity requirement for this process has been a deterrent for the development of water electrolysis technologies. The growing availability of renewable electricity from sources such as wind and solar energy has recently improved the outlook for water electrolysis technology [22]. These electricity sources are intermittent in nature; their electricity output is inconsistent and fluctuates depending on the weather. The coupling of a wind or solar electricity source with an alkaline electrolyser allows surplus electricity to be used in the production of H_2 gas via water electrolysis. This H_2 gas can then be used in a fuel cell to supplement electricity when production from the renewable source is insufficient.

$$H_2O_{\text{liquid}} \longrightarrow H_{2\,\text{gas}} + \tfrac{1}{2}\,O_{2\,\text{gas}} \tag{2.1}$$

$$M + H_2O + e^- \rightleftharpoons MH + OH^- \tag{2.2}$$

$$MH + H_2O + e^- \rightleftharpoons M + H_2 + OH^- \tag{2.3}$$

$$2\,MH \rightleftharpoons 2\,M + H_2 \tag{2.4}$$

Alkaline water electrolysis is a mature technology for hydrogen generation that is already used in commercial applications. The system consists of two electrodes, separated by a diaphragm, submerged in aqueous KOH solution (20 – 30% KOH). The hydrogen evolution reaction (HER) takes place at the cathode; the oxygen evolution reaction (OER) takes place at the anode. The role of the diaphragm is to allow mobility of H_2O and OH^- between the two electrodes while preventing the gasses generated at each electrode from intermixing. A schematic representation of an alkaline electrolysis system is shown in Figure 2.1 [24]. There are four important parameters to be considered when evaluating a viable electrode material for alkaline electrolysis: (i) electrocatalytic activity; (ii) stability; (iii) scalability; and (iv) cost [32]. Commercial alkaline electrolyzers use Ni-based electrodes, which are a logical choice due to the stability of Ni in alkaline media [32, 33], the activity of Ni as a water electrolysis catalyst [32, 34], and the relatively low cost of Ni-based materials.

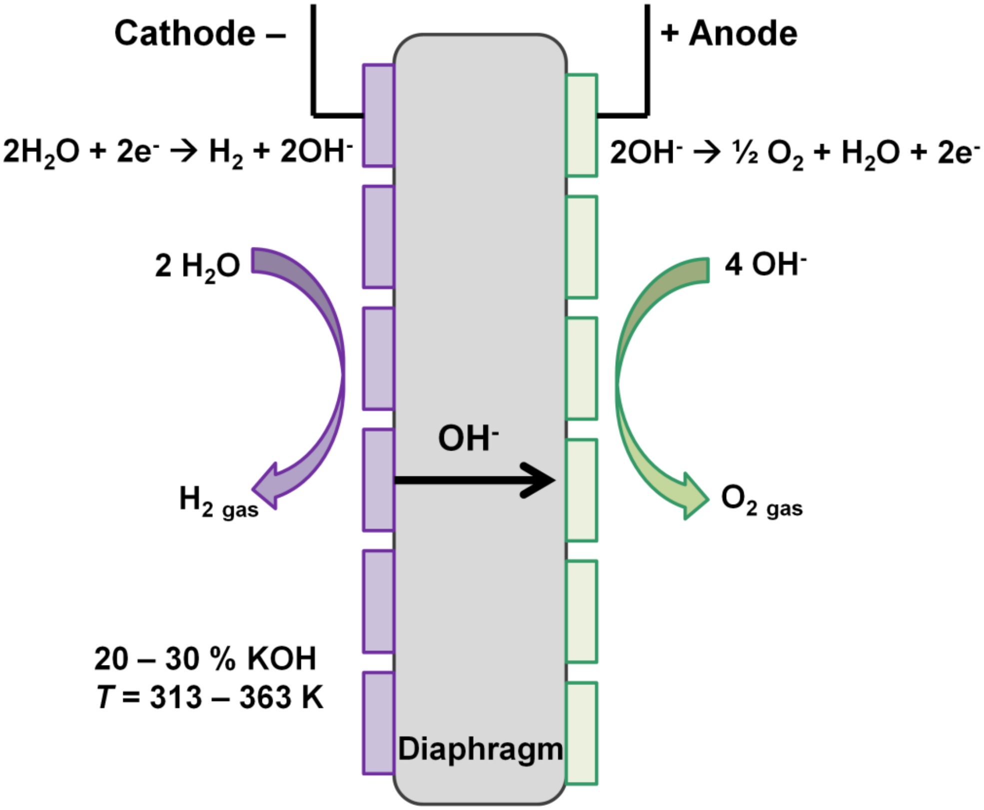

Figure 2.1. Schematic representation of an alkaline water electrolyser.

There are two major drawbacks associated with the use of pure Ni electrodes in alkaline electrolyzers; the first being a high operating cell potential, and the second being a decrease in cathodic activity with time [23]. The gradual decrease in HER activity in commercial electrolyzers is suspected to arise from the formation of an inactive surface hydride layer that is generated at high HER overpotential in the presence of hydrogen [23, 35 – 38]. There are a large number of studies examining the effect of adding various metals to the Ni electrodes to improve the efficiency of alkaline water electrolyzers by lowering the cell potential. Multi-component materials such as Ni/Fe [39 – 41], Ni – Zn alloy [28, 40], Ni – Fe – Zn alloy [40], Ni – P alloy [42], Co – P alloy [42], Ni – P – Fe alloy [42], Ni – Mo [40, 43], Ni – Mo – Cd alloy [43], Ni/NiFeS [44], and Raney-Ni/Mo [31] have been studied in an effort to reduce the overpotential at the cathode. The presence of certain metals, such as Fe, within the cathode also helps to mitigate the problem of cathode deactivation with time [23, 37]. Similar strategies are applied to increase O_2 gas production at the anode; reductions in OER overpotential are achieved with Ni + spinel-type Co_3O_4 and Ni + La-doped Co_3O_4 anodes [45]. The development of modern electrode materials focuses on low-cost materials with high efficiencies and long life cycles; in this respect Ni-based materials continue to be relevant electrocatalysts for alkaline water electrolysers.

2.2.2 Alcohol Fuel Fells

Direct alcohol fuel cells (DAFC) are predicted to be of use in the automotive industry where they are considered an attractive alternative to hydrogen fuel cells to power electric vehicles [46]. In this respect, DAFC have the following advantages over H_2 fuel cells: (i) the fuels are simple alcohols which can be produced in large quantities; (ii) the fuels are compatible with existing fuel-delivery infrastructure; and (iii) the fuel is introduced directly to the fuel cell as an aqueous solution (1 – 2 M). In the case of systems that utilize H_2 as a fuel, there is an engineering challenge associated with of implementing on-board H_2 storage or incorporating a hydrogen reformer [46, 47]. Currently, methanol is the fuel of choice for the DAFC because it is highly efficient and has a theoretical energy density of 6 kWh/kg (compare to gasoline at 10 kWh/kg) [46, 48, 49]. However, methanol is produced using natural gas as a starting material, so it is not a renewable resource. Methanol is also toxic and corrosive to certain metals such as aluminum; this makes it difficult to handle and transport. Furthermore, methanol crossover through the Nafion membrane from the anode to the cathode presents a major challenge in the development of these systems [50 – 52]. There are several other small alcohols that are attractive fuels for the DAFC. Ethanol, for example, is a promising fuel option because its full oxidation produces 12 electrons per molecule (as compared to 6 electrons from one molecule of methanol) [53]. Ethanol can be produced in large quantities from renewable biomass [54 – 56]. Isopropyl alcohol (IPA) is also considered as an alternative fuel to methanol for the DAFC because it is non-toxic, easy to handle, and easy to store [46, 47, 57]. Recent studies comparing the performance of an IPA fuel cell to a methanol fuel cell with a similar anode electrocatalyst concluded that the system utilizing IPA shows higher performance at current densities lower than 200 mA cm^{-2} [58, 59]. The crossover of IPA through the Nafion membrane is about 1/7th that of methanol [59]. Under fuel cell conditions, the complete oxidation of IPA to CO_2 and H_2O is unrealistic because of a high overpotential required to drive this reaction [47]. Instead, IPA is oxidized to acetone through a two electron process [60, 61]. The competitive adsorption of acetone which accumulates in the system is a concern for the use of certain electrocatalysts, such as Pd, as it results in a poisoning effect [62, 63]. Any anode material of practical significance for this system must tolerate the presence of acetone. Since no CO_2 is generated in the process, it is logical to design IPA fuel cells to operate in alkaline media where the kinetics of the alcohol oxidation and the oxygen reduction reaction (ORR) are faster, compared to acidic media [64].

Currently, Pt and Pt alloys are the best performing electrocatalyst materials for DAFC applications [48, 50, 65, 66]. However, Ni and Ni-based electrode materials are also under investigation for DAFC systems for the following reasons: (i) they are effective electro-oxidation catalysts for many alcohols [60, 61, 67 – 70]; (ii) they are not subject to poisoning through the adsorption of oxidation products [63, 71]; (iii) they are stable in alkaline media. The oxidation of organic molecules using a Ni electrode occurs at potentials slightly superior to the formation of β-NiOOH. There is also a higher oxide that forms on Ni at potentials concurrent with the OER; this oxide is NiO_2 [67, 72]. At this time it is not clear whether it is β-NiOOH or NiO_2 that participates directly in the alcohol oxidation reaction. Reasonable mechanisms based on both β-$Ni(OH)_2$ [60, 61, 69, 73] and NiO_2 [67, 72] are present in the literature. It is possible that both of these species function as electrocatalysts. The potential regions for β-NiOOH formation, NiO_2 formation, alcohol oxidation, and oxygen evolution are all very close together. The composition of the electrolyte, as well as the presence of alcohol in the system, can shift these potential regions. The following series of reactions (equations 2.5 – 2.13, illustrated in Figure 2.2) demonstrates the electrochemical oxidation of ethanol through the participation of β-NiOOH or NiO_2 [67]. Equations 2.5, 2.6, and 2.7 demonstrate the processes that take place in the absence of added alcohol to the system.

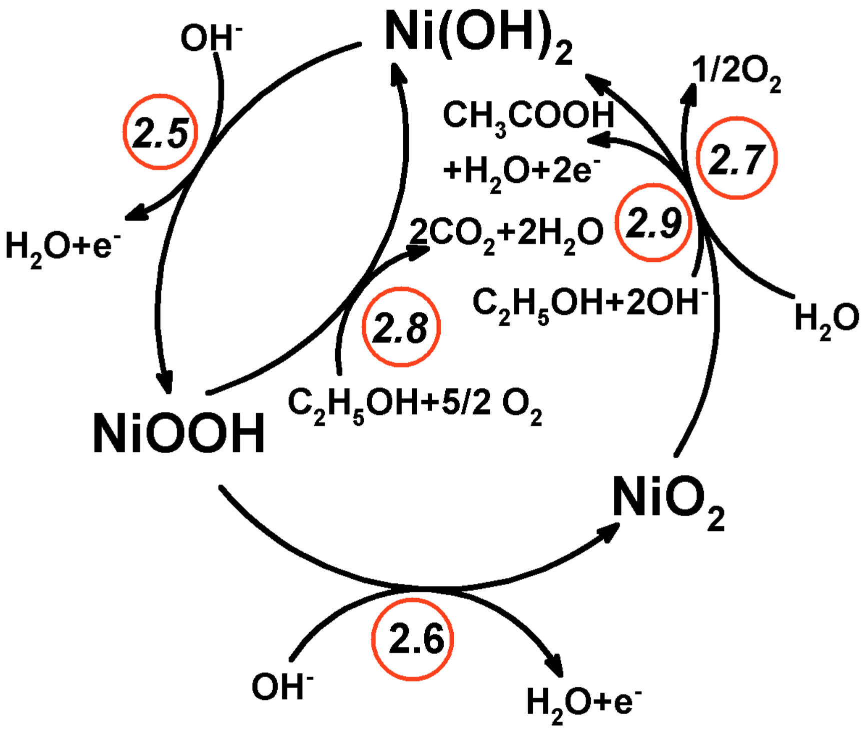

Figure 2.2. Catalytic cycle for the electrochemical oxidation of ethanol using a nickel electrode. The numbers within the red circles indicate the chemical reaction number.

$$\beta\text{-Ni(OH)}_2 + \text{OH}^- \longrightarrow \beta\text{-NiOOH} + \text{H}_2\text{O} + \text{e}^- \tag{2.5}$$

$$\beta\text{-NiOOH} + \text{OH}^- \longrightarrow \text{NiO}_2 + \text{H}_2\text{O} + \text{e}^- \tag{2.6}$$

$$\text{NiO}_2 + \text{H}_2\text{O} \longrightarrow \beta\text{-Ni(OH)}_2 + 1/2\ \text{O}_2 \tag{2.7}$$

Equation 2.8 shows the proposed reaction between ethanol and β-NiOOH, equation 2.9 shows the proposed process for ethanol reacting with NiO_2 from key papers by Fleischmann, Comninellis, and Motheo [61, 62, 72]. Equations 2.10 – 2.11 to demonstrate another process that is likely to take place [62, 72]. An analogous process for the electrochemical oxidation of isopropanol using a Ni electrocatalyst is the topic of Chapter 5.

$$2\ \beta\text{-NiOOH} + C_2H_5OH + 5/2\ O_2 \longrightarrow 2\ \beta\text{-Ni(OH)}_2 + 2\ CO_2 + 2\ H_2O \tag{2.8}$$

$$NiO_2 + C_2H_5OH + 2\ OH^- \longrightarrow \beta\text{-Ni(OH)}_2 + CH_3COOH + H_2O + 2\ e^- \tag{2.9}$$

$$(CH_3CH_2OH)_{sol} \rightleftarrows (CH_3CH_2OH)_{ads} \tag{2.10}$$

$$(CH_3CH_2OH)_{ads} + OH^- + \beta\text{-NiOOH} \longrightarrow (CH_3C^{\bullet}OH)_{ads} + \beta\text{-Ni(OH)}_2 + H_2O + e^- \tag{2.11}$$

$$(CH_3C^{\bullet}OH)_{ads} + OH^- \longrightarrow CH_3C^{\bullet}O + H_2O + e^- \tag{2.12}$$

$$CH_3C^{\bullet}O + OH^- \longrightarrow CH_3COOH + e^- \tag{2.13}$$

2.2.3 Electrochemical Hydrogenation Reactions

Hydrogenation refers to a group of reactions where hydrogen atoms are added to unsaturated organic species. In these processes, double and triple bonds undergo a decrease in bond order. Hydrogenation reactions are commonly applied in the food and pharmaceutical industries as well as in the production of chemicals [74 – 76]. These reactions are carried out in the presence of a catalyst because H_2 will generally not react with organic species unless the temperature is very high (> 750 K) [75]. The field of hydrogenation chemistry is extremely broad and involves many catalyst systems; herein the focus is on electrochemical hydrogenation reactions carried out using Ni-based catalysts.

During electrochemical hydrogenation, the electrocatalyst performs several key functions that provide a lower activation energy pathway that facilitates the reaction. First, the electrocatalyst brings the reactants in close proximity of each other while they are in a high-energy state. For example, organic species physisorbed at an electrode surface will experience bond weakening due to their interaction with the electrode [76, 77]. Metals with low hydrogen evolution overpotential values, such as Ni, allow hydrogen to be electrochemically adsorbed and evolved at the cathode through the electrolysis of water. This puts the hydrogen that is necessary for hydrogenation exactly where it is needed, i.e. in close proximity to the organic species [78]. Finally, the electrode (cathode) facilitates electron transfer by providing an electron source for the reduction of the organic species [78].

Pure Ni, Ni-based alloys, and Raney Ni have been investigated as hydrogenation electrocatalysts since the 1960's [79]. Raney Ni, also known as "sponge-metal catalyst" due to its high surface area and porosity, is a Ni – Al alloy. It is prepared by dissolving Ni into molten Al, followed by cooling; the alloy is then subjected to a selective leaching process that removes Al from certain Ni_xAl_y phases [80]. There are several types of Raney Ni materials that are used as industrial heterogeneous catalysts for hydrogenation processes. Raney Ni electrocatalysts have been successfully applied to the electrochemical hydrogenation of several phenanthrene moieties with the conversion of C=C within the six-member rings ranging from 78 to 100 % [81]. Raney Ni materials with various metal promoters (Fe, Sn, Mo, Cr) were developed for the electrochemical hydrogenation of glucose. Although the presence of promoter metal does enhance the activity of the electrocatalyst, certain promoters (Fe, Sn) deactivate quickly because they are leached into the electrolyte [76]. A comparison of the electrochemical hydrogenation of styrene, benzonitrile, and acetophenone using Raney Ni, palladised carbon, and platinised platinum demonstrated that Raney Ni is the more versatile hydrogenation electrocatalyst of the these three by accomplishing the reduction of each organic species with greater or equal conversion rates [82]. More recently, $LaNi_5$ was successfully applied to the electrochemical conversion of various alkenes to their respective alkanes with current efficiencies reaching 100% [83]. These studies demonstrate some of the many hydrogenation reactions where Ni-based electrocatalysts are applied.

2.3 The Significance of Platinum in Electrochemistry and Electrocatalysis

2.3.1 The Importance of Platinum as an Electrode Material

Global interest in the electrochemical properties of Pt continues to increase as the demand for new energy conversion and storage options drives research in the field of polymer electrolyte membrane fuel cells (PEMFCs) and hydrogen production systems. Platinum, in the form of nanoparticles, is the principal electrocatalyst used in both the anode and cathode of PEMFCs [84]. The electrochemical processes taking place at the Pt electrode in aqueous acidic media (generally H_2SO_4) are studied extensively. Ongoing research topics include the mechanism of platinum oxide formation (PtO, and PtO_2) [85 – 91] and the underpotential deposition (UPD) of hydrogen [92 – 95]. Recently, the phenomenon of Pt electro-dissolution has gained interest because of implications to PEMFC technology [96 – 100]. Reactions occurring through the interaction of Pt with the electrolyte include the oxygen reduction reaction (ORR) [101], hydrogen oxidation reaction (HOR) [53], hydrogen evolution reaction (HER) [102, 103], and oxygen evolution reaction (OER) [34, 104, 105]. These reactions are of extreme importance for the design and improvement of fuel cell technologies; for this reason they are generally studied in acidic media. Studies are also available that focus on Pt electrochemistry and electrocatalysis in alkaline media for applications in alkaline fuel cells, alcohol alkaline fuel cells, and alkaline water electrolysis [31, 66, 103, 106 – 109].

2.3.2 The Electrochemical Behavior of Platinum in Aqueous Alkaline Media

The electrochemical behaviour of Pt in alkaline media is studied far less than its behaviour in acidic media; however there are a few fundamental studies available on the topic [106, 110 – 114]. The features of a CV profile for a clean polycrystalline Pt electrode in 0.50 M KOH or similar alkaline electrolyte are listed in Table 2.2. The appearance of the CV profile of Pt in alkaline electrolyte is very similar to the profile collected in acidic electrolyte; an example CV profile of Pt in 0.50 M H_2SO_4 with s = 50 mV s^{-1} and T = 293 K is located in Chapter 3 (Figure 3.3). Additional discussion of the electrochemical behaviour of Pt in alkaline media is presented in Chapter 6 along with a discussion of Pt deposited on a Ni foam substrate.

Table 2.2. Features in the CV profile for polycrystalline Pt in aqueous alkaline media*.

CV Feature	*E* range (V / RHE)	Chemical Reaction	Anodic or Cathodic
Hydrogen Evolution Reaction	$E < 0.00$	$2\ H_2O + 2\ e^{-} \rightarrow H_2 + 2\ OH^{-}$	Cathodic
UPD of Hydrogen	$0.05 < E < 0.45$	$Pt + H_2O + e^{-} \rightarrow Pt\text{-}H_{UPD} + OH^{-}$	Cathodic
Desorption of UPD Hydrogen	$0.05 < E < 0.45$	$Pt\text{-}H_{UPD} + OH^{-} \rightarrow Pt + H_2O + e^{-}$	Anodic
Formation of PtO	$E > 0.80$ V	$Pt + 2\ OH^{-} \rightarrow PtO + H_2O + 2\ e^{-}$	Anodic
PtO Reduction	$0.50 < E < 1.20$	$PtO + H_2O + 2\ e^{-} \rightarrow Pt + 2\ OH^{-}$	Cathodic
Oxygen Evolution Reaction	$E > 1.23$	$4\ OH^{-} \rightarrow O_2 + 2\ H_2O + 4e^{-}$	Anodic

*References [34, 92, 93, 110, 114]

2.3.3 Alkaline Fuel Cells Utilizing Pt Electrocatalysts

Fuel cell (FC) devices convert chemical energy into electricity through electrochemical reactions [115]. There are many types of fuels cells based on different fuels (H_2 gas, alcohols, borohydride) and on different design characteristics (PEMFC, solid oxide fuel cell) [46]. The general operating principle of a FC is simple; the anode and cathode are in electrolytic contact with each other through the electrolyte and in electrical contact through an external circuit. A fuel is supplied into the system that undergoes oxidation at the anode. At the cathode, a reduction reaction occurs; this is generally the reduction of oxygen from supplied O_2 or air [84, 115]. As a result of these two reactions taking place in electrolytic contact, electrons flow through the external circuit [84, 116, 117]. A schematic diagram of an alkaline fuel cell is presented in Figure 2.3. Research on the topic of fuel cells is extremely broad, and indeed one of the most exciting topics in modern electrochemistry [118]. A discussion of fuel cells in their entirety is beyond the scope of this thesis. Herein, I include only a brief overview of systems that utilize Ni and / or Pt among the electrocatalyst materials. Since this thesis focuses on Ni and Ni / Pt electrode materials, and all experimental work is carried out in alkaline solution, the comparison is limited to fuel cell systems that operate in alkaline conditions. Table 2.3 compares three selected types of fuel cells, as examples. It is important to stress that the fuel cell systems presented in Table 2.3 are not necessarily the best systems available in terms of power or efficiency; they are simply examples of systems with relevance to this work.

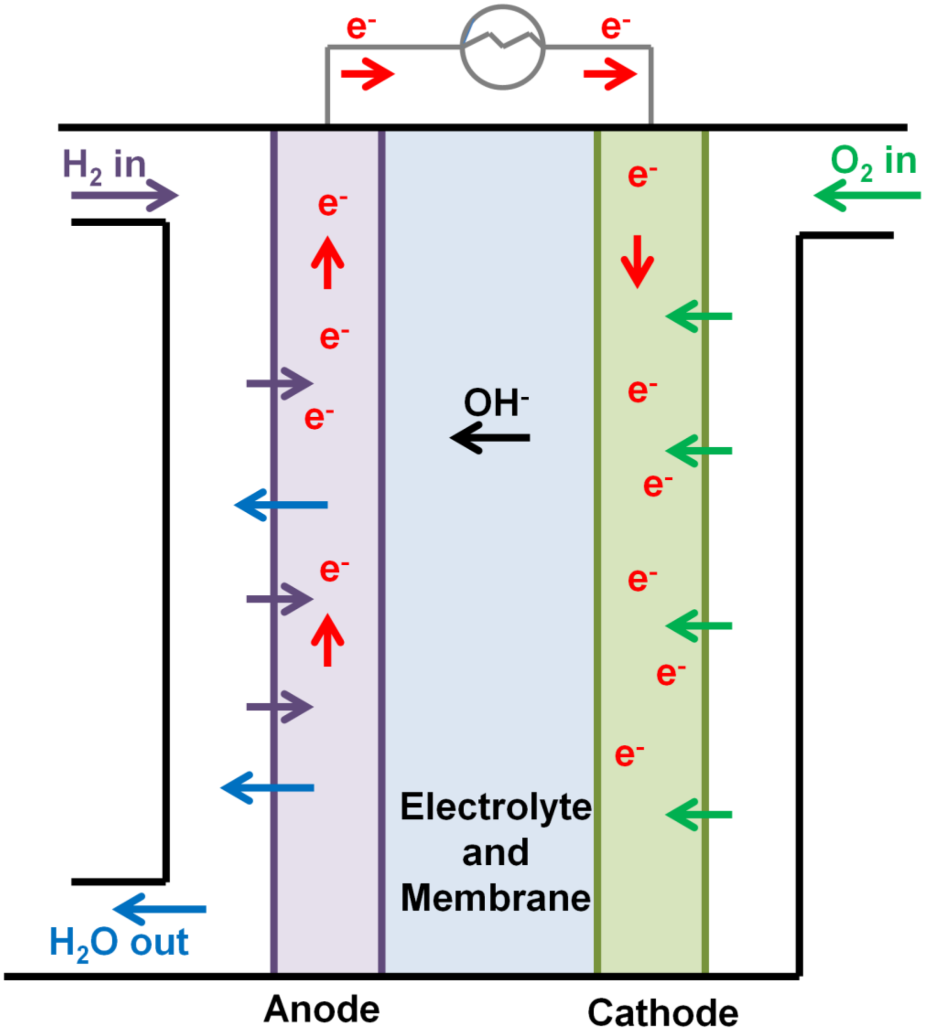

Figure 2.3. A schematic representation of an alkaline fuel cell.

Table 2.3. Selected examples of fuel cell systems and their operating parameters.

Common Name of Fuel Cell	**Alkaline (AFC)**	**Direct Alkaline Alcohol (DAAFC)**	**Direct Borohydride (DBFC)**
Fuel Source	H_2 (gas)	Methanol, ethanol, isopropanol, ethylene glycol, glycerol	$NaBH_4$ aq. Solution (10 wt. %)
Anode Material	Pt, Pd, PtPd, Ni, Raney Ni,	Pt, PtRu, Pd, Au, PdNi,	Ni, Pt, Pd, Au, Ag, Ni/Pt
Anode Reaction	$2\ H_2 + 4\ OH^- \rightarrow 4\ H_2O + 4\ e^-$	$CH_3OH + 6\ OH^- \rightarrow CO_2 + 5\ H_2O + 6\ e^-$ (methanol)	$BH_4^- + 8\ OH^- \rightarrow BO_2^- + 6\ H_2O + 8\ e^-$
Cathode Material	Pt, PtRu, MnO2,	Pt, Fe-Co, MnO_2	Pt, Pd, Ag, Ni, MnO_2
Cathode Reaction	$O_2 + 2\ H_2O + 4\ e^- \rightarrow 4\ OH^-$	$3/2\ O_2 + 3\ H_2O + 6\ e^- \rightarrow 6\ OH^-$	$2\ O_2 + 4\ H_2O + 8\ e^- \rightarrow 8\ OH^-$
Overall Reaction	$O_2 + 2\ H_2 \rightarrow 2\ H_2O$	$CH_3OH + 3/2\ O_2 \rightarrow CO_2 + 2\ H_2O$	$BH_4^- + 2\ O_2 \rightarrow BO_2^- + 2\ H_2O$
Electrolyte Environment	Aqueous alkaline (KOH, 5 – 8 M)	Aqueous alkaline (KOH), or solid electrolyte membrane	Aqueous alkaline (KOH, 20 wt. %)
Operating Temperature	70 – 200˚ C	40 – 90˚ C	60 – 85˚ C
Cell Voltage	1.23 V	1.21 V	1.64 V
Power Density	10 – 50 mW cm^{-2}	40 – 45 mW cm^{-2}	20 – 150 mW cm^{-2}
Status	Commercial / Research	Commercial / Research	Research
Applications	Aerospace energy needs, transportation	Portable energy systems, standby power, possible transportation	Possible aerospace energy needs, transportation
References	[46, 103, 119, 120]	[46, 47, 52, 121]	[103, 122, 123]

2.4 Open-Cell Nickel-Containing Foam Electrode Materials

Metal solid foam materials with high porosity and a cellular structure have interesting physical and mechanical properties that make them attractive engineering materials. Many of the advantageous properties (i.e. structural integrity combined with low specific mass, gas permeability, thermal and electrical conductivities) are related to their low mass and low material usage [124]. There are several methods used to manufacture open-pore metallic materials such as foaming of metal melts, powder compaction melting techniques, or through chemical vapour deposition (CVD), physical vapour deposition (PVD), and / or electrochemical deposition of the metal on an open pore substrate [124, 125]. The method of preparation determines the material's physical, mechanical, and chemical properties. The Ni foams examined in this study are formed through CVD and electroplating of Ni on a reticulated polymer substrate, followed by sintering of the polymer at high temperature in a controlled atmosphere [124, 126]. These materials were manufactured by former Inco Technical Services Ltd; this company has gone through a series of changes in their business platform and no longer produces these materials. The fabrication of Ni-based foams is further discussed in Chapter 4 where a full characterization is presented based on their materials science and electrochemical properties [19]. Other characterization studies, focusing mainly on engineering properties of Ni-based foams, are available in the literature [18, 126 – 133].

Open-cell metallic foams, similar to those that are the topic of this thesis, have been commercially available since the early 1980's [20]. The original use of open-cell Ni foams in the field of electrochemistry was as a support and current collector for pasted alkaline battery electrodes [124]. Early studies also recognized the potential of these materials as flow-through electrodes for electrochemical reactors [20, 134, 135] and as a support for other high-surface area materials such as electrochemical capacitors and pseudocapacitors [136, 137, 138]. Recently a number of papers were published describing the use of Ni-based foams as an electrode support materials for other electrocatalysts including Pt [139, 141], Rh [140, 142], Pd [63, 143, 144], Ag [145], Sn – Co [146], and Co – W – B [21]. The concept of using Ni foams as a support material for Pt electrocatalysts applications is the topic of Chapter 6.

Multi-component Ni-based foams were developed over the past fifteen years for specialty applications that demand stability at elevated temperatures, in acidic environments, and in highly oxidizing conditions. Generally, elements such as Cr, Al, Mo, Fe, Nb, and others are introduced in the form of a powder onto pre-fabricated Ni foam. A controlled-atmosphere heat treatment is then applied that allows the elements of the metallic powder to diffuse into the Ni-foam struts [129, 132, 133]. Other fabrication methods include plasma spraying of metal powder onto the pre-formed Ni foam [131], or layer-by-layer electrodeposition of different metals onto a polymer substrate, followed by sintering [133]. Two multi-component foam materials are included in the characterization studies described in Chapter 4.

The few characterization studies available that investigate Ni-based foams in terms of their structure and engineering properties are geared towards their use as battery electrodes [18, 126 – 133]. These studies do not provide the necessary information regarding the chemical composition or the micro and nanoscopic characteristics of Ni foams that is required by researchers in the field of electrocatalysis who wish to investigate Ni foam as an electrocatalyst material. The studies presented herein provide a foundation of knowledge regarding the properties of Ni-based foams and extend the current research on applications of these materials as electrocatalysts.

2.5 References

(1) Peter H. Kuck, *Nickel*, **2012**.

(2) Peter H. Kuck, *Nickel*, 51, **2008**.

(3) A. Anani, A. Visitin, K. Petrov, S. Srinivasan, J. J. Reilly, J. R. Johnson, R. B. Schwarz and P. B. Desch, *J. Power Sources,* **1994**, 47, 261–275.

(4) K. Watanabe and T. Kikuoka, *J. Appl. Electrochem.,* **1995**, 25, 219–226.

(5) F. Feng, M. Geng and D. O. Northwood, *Int J Hydrogen Energy,* **2001**, 26, 725–734.

(6) J. B. Goodenough, *J. Solid State Electrochem.,* **2012**, 16, 2019–2029.

(7) Gold Peak Batteries, *Nickel Cadmiun Technical Handbook*, **2006**.

(8) T. R. Crompton, *Battery Reference Book Third Edition*, Newnes, Oxford, England, **2000**.

(9) I. Rexed, M. Behm and G. Lindbergh, *Modelling of ZEBRA Batteries*, **2010**.

(10) H. Bode, K. Dehmelt and J. Witte, *Electrochim. Acta,* **1966**, 11, 1079–1087.

(11) L. M. M. de Souza, F. P. Kong, F. R. McLarnon and R. H. Muller, *Electrochim. Acta,* **1997**, 42, 1253–1267.

(12) F. Hahn, B. Beden, M. J. Croissant and C. Lamy, *Electrochim. Acta,* **1986**, 31, 335–342.

(13) M. Alsabet, M. Grden and G. Jerkiewicz, *Electrocatalysis,* **2011**, 2, 317–330.

(14) W. Visscher and E. Barendrecht, *Electrochim. Acta,* **1980**, 25, 651–655.

(15) M. Grden and K. Klimek, *J. Electroanal. Chem.,* **2005**, 581, 122–131.

(16) P. Oliva, J. Leonardi, J. F. Laurent, C. Delmas, J. J. Braconnier, M. Figlarz, F. Fievet and A. de Guibert, *J. Power Sources,* **1982**, 8, 229–255.

(17) S. Maximovitch and R. Durand, *J. Electroanal. Chem.,* **1983**, 149, 273–277.

(18) M. Grden, M. Alsabet and G. Jerkiewicz, *ACS Appl. Mater. Interfaces,* **2012**, 4, 3012–3021.

(19) J. van Drunen, B. Kinkead, M. C. P. Wang, B. D. Gates, E. Sourty and G. Jerkiewicz, *ACS Appl. Mater. Interfaces,* **2013**, 5, 6712–6722.

(20) S. Langlois and F. Coeuret, *J. Appl. Electrochem.,* **1989**, 19, 43–50.

(21) H. Dai, Y. Liang, P. Wang, X. Yao, T. Rufford, M. Lu and H. Cheng, *Int J Hydrogen Energy,* **2008**, 33, 4405–4412.

(22) G. F. Naterer, M. Fowler, J. Cotton and K. Gabriel, *International Journal of Hydrogen Energy,* **2008**, 33, 6849–6857.

(23) K. Zeng and D. Zhang, *Prog Energ Combust,* **2010**, 36, 307–326.

(24) H. Carmo, D. L. Fritz and J. S. Mergel D., *Int J Hydrogen Energy,* **2013**, 38, 4901–4934.

(25) J. Divisek, *J Electroanal Chem,* **1986**, 214, 615–632.

(26) D. Harrington and B. E. Conway, *J. Electroanal. Chem.,* **1987**, 221, 1–12.

(27) A. Lasia and A. Rami, *J. Electroanal. Chem.*, **1990**, 294, 123–141.

(28) L. Chen and A. Lasia, *J. Electrochem. Soc.*, **1991**, 138, 3321–3328.

(29) S. A. S. Machado and L. A. Avaca, *Electrochim. Acta*, **1994**, 39, 1385–1391.

(30) N. Krstajic, K. D. Popovic, B. N. Grgur, M. Vojnovic and D. Sepa, *J Electroanal Chem*, **2001**, 512, 16–26.

(31) S. Marini, P. Salvi, P. Nelli, R. Presenti, M. Villa, M. Berrettoni, G. Zangari and Y. Kiros, *Electrochim. Acta*, **2012**, 82, 384–391.

(32) D. E. Hall, *J. Electrochem. Soc.*, **1985**, 132, 42C–48C.

(33) D. L. Floner and J. -M. Leger, *Surface Science*, **1990**, 243, 87–97.

(34) M. H. Miles and Y. H. Huang, *J. Electrochem. Soc.*, **1978**, 125, 1930–1933.

(35) D. Soares, O. Teschke and I. Torriani, *J. Electrochem. Soc.*, **1992**, 139, 98–105.

(36) H. Rommal and P. Morgan, *J. Electrochem. Soc.*, **1988**, 135, 343–346.

(37) D. W. Kirk and S. Thorpe, *ECS Transactions*, **2007**, 2, 71–76.

(38) D. S. Hall, C. Bock and B. R. MacDougall, *J. Electrochem. Soc.*, **2013**, 160, F235–F243.

(39) J. de Carvalho, G. Tremiliosi-Filho, L. A. Avaca and E. R. Gonzalez, *Int J Hydrogen Energy*, **1989**, 14, 161–165.

(40) E. R. Gonzalez and M. J. de Giz, *Chem. Ind.*, **2000**, 54, 123–132.

(41) F. Rosalbino, G. Scavino and M. A. Grande, *J. Electroanal. Chem.*, **2013**, 694, 114–121.

(42) M. J. de Giz, G. Tremiliosi-Filho, E. R. Gonzalez, S. Srinivasan and A. J. Appleby, *Int J Hydrogen Energy*, **1995**, 20, 423–427.

(43) R. Simpraga and B. E. Conway, *J. Appl. Electrochem.*, **1995**, 25, 628–641.

(44) N. A. Assuncao, M. J. de Giz, G. Tremiliosi-Filho and E. R. Conzalez, *J. Electrochem. Soc.*, **1997**, 144, 2794–2800.

(45) R. N. Singh, D. Mishra, A. Anindita, A. S. K. Sinha and A. Singh, *Electrochem. Commun.*, **2007**, 9, 1369–1373.

(46) C. Lamy, J.-M. Léger and S. Srinivasan, in *Modern Aspects of Electrochemistry*, ed. J. O.M. Bockris, Kluwer Academic / Plenum Publishers, New York, **2001**.

(47) S. Song, V. Maragou and P. Tsiakaras, *J. Fuel Cell Sci. Technol.*, **2007**, 4, 203–209.

(48) C. Lamy, E. M. Belgsir and J. -M.. Leger, *J. Appl. Electrochem.*, **2001**, 31, 799–809.

(49) E. H. Yu, K. Scott and R. W. Reeve, *J. Electroanal. Chem.*, **2003**, 547, 17–24.

(50) C. Lamy, S. Rousseau, E. M. Belgsir, C. Coutanceau and J. -M. Léger, *Electrochim. Acta*, **2004**, 49, 3901–3908.

(51) M. E. P. Markiewicz, D. M. Hebert and S. H. Bergens, *J. Power Sources,* **2006**, 161, 761–767.

(52) L. Dubau, C. Coutanceau, E. Garnier, J. -M. Leger and C. Lamy, *J. Appl. Electrochem.,* **2003**, 33, 419–429.

(53) J. Friedl and U. Stimming, *Electrochimica Acta*, **2013**, 101, 41–58.

(54) J. Zaldivar, J. Neilson and L. Olsson, *Appl. Microbiol. Biotechnol.,* **2001**, 56, 17–34.

(55) F. M. Girio, C. Fonseca, F. Carvalheiro, L. C. Duarte, S. Marques and R. Bogel-Lukasik, *Bioresource Technol,* **2010**, 101, 4775–4800.

(56) D. Chiaramonti, M. Prussi, S. Ferrero, L. Oriani, P. Ottonello, P. Torre and F. Cherchi, *Biomass Bioenerg,* **2012**, 46, 25–35.

(57) C. Lamy, A. Lima, V. LeRhun, F. Delime, C. Coutanceau and J. -M. Leger, *J. Power Sources,* **2002**, 105, 283–296.

(58) D. Cao and S. H. Bergens, *J. Power Sources,* **2003**, 124, 12–17.

(59) Z. Qi and A. Kaufman, *J. Power Sources,* **2002**, 112, 121–129.

(60) M. Fleischmann, K. Korinek and D. Pletcher, *J. Electroanal. Chem. Interfacial Electrochem.,* **1971**, 31, 39–49.

(61) M. Fleischmann, K. Korinek and D. Pletcher, *J. Chem. Soc. , Perkin Trans.,* **1972**, 2, 1396–1403.

(62) G. Tremiliosi-Filho, E. R. Gonzalez, A. J. Motheo, E. M. Belgsir, J. -M. Leger and C. Lamy, *J. Electoanal. Chem.*, **1998**, 444, 31–39.

(63) Y. Cheng, Y. Liu, D. Cao, G. Wang and Y. Gao, *J. Power Sources*, **2011**, 196, 3124–3128.

(64) A. V. Tripkovic, K. D. Popovic, B. N. Grgur, B. Blizanac, P. N. Ross and N. M. Markovic, *Electrochim. Acta*, **2002**, 47, 3707–3714.

(65) R. Parsons and T. VanderNoot, *J. Electroanal. Chem.*, **1988**, 257, 9–45.

(66) E. Antolini and E. R. Gonzalez, *J. Power Sources*, **2010**, 195, 3431–3450.

(67) A. J. Motheo, S. A. S. Machado, F. S. B. Rabelo and J. R. J. Santos, *J. Braz. Chem. Soc.*, **1994**, 5, 161–165.

(68) F. Gobal, Y. Valadbeigi and L. M. Kasmaee, *J. Electroanal. Chem.*, **2011**, 650, 219–225.

(69) V. L. Oliveira, C. Morais, K. Servat, T. W. Napporn, G. Tremiliosi-Filho and K. B. Kokoh, *J. Electoanal. Chem.*, **2013**, 703, 56–62.

(70) J. van Drunen, T. W. Napporn, K. B. Kokoh and G. Jerkiewicz, *J. Electroanal. Chem.*, **2013**, http://dx.doi.org/10.1016/j.jelechem.2013.08.003.

(71) A. Budniok and E. Kozlowska, *Thin Solid Films*, **1991**, 204, 341–347.

(72) C. Comninellis and C. Pulgarin, *J. Appl. Electrochem.*, **1993**, 23, 108–112.

(73) P. M. Robertson, *J. Electoanal. Chem.*, **1980**, 111, 97–104.

(74) M. J. Lain and D. Pletcher, *Electrochim. Acta*, **1987**, 32, 99–107.

(75) M. J. Lain and D. Pletcher, *Electrochim. Acta*, **1987**, 32, 109–113.

(76) P. Gallezot, P. J. Cerino, B. Blanc, G. Fleche and P. Fuertes, *J Catal*, **1994**, 146, 93–102.

(77) J. K. Norskov, *Nature,* **2001**, 414, 405.

(78) V. Anantharaman and P. N. Pintauro, *J. Electrochem. Soc.*, **1994**, 141, 2729–2741.

(79) O. R. Brown and J. A. Harrison, *J. Electroanal. Chem.*, **1969**, 21, 387–407.

(80) European Space Agency, *Catalysts*. http://www.spaceflight.esa.int/impress/text/education/Catalysis/index.html. 10 / **2013.**

(81) B. Mahdavi, A. Lafrance, A. Martel, J. Lessard, H. Menard and L. Brossard, *J. Appl. Electrochem.*, **1997**, 27, 605–611.

(82) M. A. Casadei and D. Pletcher, *Electrochim. Acta*, **1988**, 33, 117–120.

(83) van Duten, G. M. R., E. Labbe, V. Paul-Boncour, J. Perichon and A. Percheron-Guegan, *J. Electoanal. Chem.*, **2000**, 487, 31–36.

(84) M. K. Debe, *Nature*, **2012**, 486, 43–51.

(85) S. Trasatti and O. A. Petrii, *J Electroanal Chem*, **1992**, 327, 353–376.

(86) M. Alsabet, M. Grden and G. Jerkiewicz, *J. Electroanal. Chem.*, **2006**, 589, 120–127.

(87) V. I. Birss, M. Chang and J. Segal, *J Electroanal Chem,* **1993**, 355, 181–191.

(88) D. A. Harrington, *J. Electroanal. Chem.,* **1997**, 420, 101–109.

(89) van der Geest, M. E., N. J. Dangerfield and D. A. Harrington, *J. Electroanal. Chem.,* **1997**, 420, 89–100.

(90) B. E. Conway, *Prog. Surf. Sci.,* **1995**, 49, 331–452.

(91) G. Jerkiewicz, G. Vatankhah, J. Lessard, M. P. Soriaga and Y. Park, *Electrochim. Acta,* **2004**, 49, 1451–1459.

(92) G. Jerkiewicz , *Prog. Surf. Sci.,* **1998**, 57, 137–186.

(93) G. Jerkiewicz, *Electrocatalysis,* **2010**, 1, 179–199.

(94) S. Kim and J. P. Meyers, *Electrochimica Acta,* **2011**, 56, 8387–8393.

(95) B. Losiewicz, R. Jurczakowski and A. Lasia, *Electrochimica Acta,* **2012**, 80, 292–301.

(96) S. Mitsushuma, Y. Koizumi, S. Uzuka and K. Ota, *Electrochimica Acta,* **2008**, 54, 455–460.

(97) A. A. Topalov, I. Katsounaros, M. Auinger, S. Cerevko, J. C. Meier, S. O. Klemm and K. J. J. Mayrhofer, *Agnew. Chem. Int. Ed.,* **2012**, 51, 1–4.

(98) D. A. J. Rand and R. Woods, *J. Electroanal. Chem. Interfacial Electrochem.,* **1972**, 35, 209–218.

(99) G. Inzelt, B. Berker and A. Kriston, *Pure Appl. Chem.,* **2011**, 2, 269–279.

(100) L. Xing, G. Jerkiewicz and D. Beauchemin, *Analytica Chimica Acta*, **2013**, http://dx.doi.org/10.1016/j.aca.2013.04.048.

(101) N. M. Markovic, T. J. Schmidt, V. Stamenkovic and P. N. Ross, *Fuel Cells,* **2001**, 2, 105–116.

(102) J. A. V. Butler, *Prof. R. Soc. Lond. A.,* **1936**, 157, 423–433.

(103) D. M. F. Santos, C. A. C. Sequeira, D. Maccio, A. Saccone and J. L. Figueiredo, *Int J Hydrogen Energy,* **2013**, 38, 3137–3145.

(104) K. J. Vetter and J. W. Schultze, *Electroanal. Chem. Intertacial Electrochem.*, **1973**, 34, 141–159.

(105) J. Willsau, O. Wolter and J. Heitbaum, *J Electroanal Chem,* **1985**, 195, 299–306.

(106) T. J. Schmidt, P. N. Stamenkovic, J. R. Ross and N. M. Markovic, *Phys. Chem. Chem. Phys. B,* **2003**, 5, 400–406.

(107) K. J. J. Mayrhofer, G. K. H. Wiberg and M. Arenz, *J. Electrochem. Soc.*, **2008**, 155, 1–5.

(108) N. Aleceyeva, K. Tammeveski, A. Lopez-Cudero, J. Solla-Gullon and J. M. Feliu, *Electrochimica Acta*, **2010**, 55, 794–803.

(109) W. Sheng, H. A. Gasteiger and Y. Shao-Horn, *J. Electrochem. Soc.*, **2010**, 157, B1529–B1536.

(110) M. M. Jaksic, B. Johansen and R. Tunold, *Int J Hydrogen Energy,* **1993**, 18, 817–837.

(111) L. Genies, R. Faure and R. Durand, *Electrochimica Acta*, **1998**, 44, 1317–1327.

(112) N. Furuya and M. Shibata, *J Electroanal Chem,* **1999**, 467, 85–91.

(113) S. J. Xia and V. I. Birss, *Electrochimica Acta*, **2000**, 45, 3659–3673.

(114) T. J. Schmidt, P. N. Ross and N. M. Markovic, *J Electroanal Chem*, **2002**, 524, 252–260.

(115) J. O.M. Brockris and S. Srinivasan, *Fuel Cells: Their Electrochemistry*, McGraw-Hill, New York, United States, **2001**.

(116) C. Lefrou, P. Fabry and J. Poignet, *Electrochemistry. The Basics, With Examples*, Springer, Berlin, Germany, **2012**.

(117) A. J. Bard and L. R. Faulkner, *Electrochemical methods fundamentals and applications,* John Wiley & Sons, Toronto, **1980**.

(118) V. Ramani, *Interface,* **2006**, 2, 41–44.

(119) F. Bidault, D. J. L. Brett, P. H. Middleton and N. P. Brandon, *J. Power Sources*, **2009**, 187, 39–48.

(120) Y. Kiros and S. Schwartz, *J. Power Sources*, **2000**, 87, 101–105.

(121) E. H. Yu, U. Krewer and K. Scott, *Energies,* **2010**, 3, 1499–1528.

(122) B. Sljukic, D. M. F. Santos and C. A. C. Sequeira, *J Electroanal Chem*, **2013**, 694, 77–83.

(123) J. Ma, N. A. Choudhury and Y. Sahai, *Renew Sust Energ Rev*, **2010**, 14, 183–199.

(124) J. Banhart, *Prog. Mater. Sci.*, **2001**, 46, 559–632.

(125) I. J. Brown and S. Sotiropoulos, *J. Appl. Electrochem.*, **2001**, 31, 1203–1212.

(126) V. Paserin, S. Marcuson, J. Shu and D. S. Wilkinson, *Adv. Eng. Mater,* **2004**, 6, 454–459.

(127) P. Liu and K. Liang, *Materials Science and Technology*, **2000**, 16, 575–578.

(128) G. Carpenter, Z. Wronski and M. Phaneuf, *Materials Science and Technology*, **2004**, 20, 1421–1426.

(129) H. Choe and D. C. Dunand, *Materials Science and Engineering: A*, **2004**, 384, 184–193.

(130) B. Ozmat, B. Leyda and B. Benson, *Mater. Manuf. Process.*, **2004**, 19, 839–862.

(131) F. Azarmi, J. Saaedi, T. W. Coyle and J. Mostaghimi, *Advanced Engineering Materials*, **2008**, 10, 459–465.

(132) G. Walther, B. Kloden, T. Buttner, T. Weissgarber, B. Kieback, A. Bohm, D. Naumann, S. Saberi and L. Timberg, *Advanced Engineering Materials*, **2008**, 10, 803–811.

(133) Q. Pang, G. Wu, Z. Xiu, G. Chen and D. Sun, *Materials Science and Engineering: A*, **2012**, 534, 699–706.

(134) A. Montillet, J. Comiti and J. Legrand, *J. Appl. Electrochem.*, **1993**, 23, 1045–1050.

(135) P. Cognet, J. Berlan, G. Lacoste, P. Fabre and J. Jud, *J. Appl. Electrochem.*, **1996**, 26, 631–637.

(136) M. Kummer and J. R. Kirchhoff, *Anal. Chem.*, **1993**, 65, 3720–3725.

(137) A. Bello, K. Makgopa, M. Fabiane, D. Dodoo-Ahrin, K. Ozoemena and N. Manyala, *J. Mater. Sci*, **2013**, 48, 1–6.

(138) J. Huang, J. Zhu, K. Cheng, Y. Xu, D. Cao and G. Wang, *Electrochim. Acta,* **2012**, 75, 273–278.

(139) S. A. Francis and S. H. Bergens, *J. Power Sources,* **2011**, 196, 7470–7480.

(140) S. Cimino, L. Lisi, G. Mancino, M. Musiani, L. Vázquez-Gómez and E. Verlato, *Int J Hydrogen Energy,* **2012**, 37, 17040–17051.

(141) S. Fiameni, I. Herraiz-Cardona, M. Musiani, V. Pérez-Herranz, L. Vázquez-Gómez and E. Verlato, *Int J Hydrogen Energy,* **2012**, 37, 10507–10516.

(142) E. Verlato, S. Cattarin, N. Comisso, L. Mattarozzi, M. Musiani and L. Vazquez-Gomez, *Electrocatalysis,* **2013**, DOI 10.1007/s12678-013-0129-2.

(143) E. Verlato, S. Cattarin, N. Comisso, A. Gambirasi, M. Musiani and L. Vazquez-Gomez, *Electrocatal.*, **2012**, 3, 48–58.

(144) B. Yang, G. Yu and D. Shuai, *Chemosphere*, **2007**, 67, 1361–1367.

(145) J. Chen, C. X. Zhao, M. M. Zhi, K. Wang, L. Deng and G. Xu, *Electrochim. Acta,* **2012**, 66, 133–138.

(146) C. Yang, D. Zhang, Y. Zhao, Y. Lu, L. Wang and J. B. Goodenough, *J. Power Sources*, **2011**, 196, 10673–10678.

Chapter 3

Experimental Methods

The specific details for each experiment are provided in a separate *Experimental Section* located within each chapter of the results section (Chapters 4 through 6) according to the analyses presented within that section. This Experimental Methods chapter serves to provide the reader with the appropriate information for a general understanding of the most important methods used in this thesis.

3.1 Apparatus for Electrochemical Measurements

3.1.1 Three-Electrode System

A variety of electrochemical techniques are applied throughout the studies described in this thesis. Table 3.1 outlines some commonly used electrochemical methods; upcoming subsections (sections 3.2.1 to 3.2.3) provide detailed descriptions of the three important techniques utilized within this thesis: cyclic voltammetry (CV), chronoamperometry (CA), and Tafel plots. All of the electrochemical studies herein are carried out using a three-electrode set-up comprised of a working electrode (WE), counter electrode (CE), and reference electrode (RE). The WE is the electrode that is being studied; it is at the WE where the potential (E) is controlled and the current (I) is measured (or vice versa). The transfer of electrons that takes place at the interface of the WE and the electrolyte during an electrochemical process, makes-up the measured current of the electrochemical system. The CE (or auxiliary electrode) serves to complete the electrochemical circuit as I flows between the WE and the CE. When a potential is applied at the WE, the potential of the CE adjust spontaneously to allow for the same overall current to flow. The RE allows the potential at the WE to be controlled and measured relative to a well-defined reaction determined by a redox couple occurring at the RE. It is necessary for the potential of the reference electrode to remain practically constant in order to have a precise value for the potential at the WE. This is accomplished by maintaining stable activities of the species in the RE half-cell reaction quotient (eq. 3.1 – 3.2) [1 – 3].

Table 3.1 Popular methods in physical and analytical electrochemistry.

	Potentiostat	**Galvanostat**
Parameter controlled:	Potential (E in V), static vs. time Potential (E in V), swept vs. time (V s^{-1})	Current (I in A), static vs. time Current (I in A), swept vs. time (A s^{-1})
Parameter measured:	Current (I, in A)	Potential (E, in V)
Examples	Chronoamperometry E static, I vs. t response Cyclic Voltammetry E swept, I vs E response	Chronopotentiometry I static, E vs. t response Galvanodynamic sweep I swept, E vs. I response

A reversible hydrogen electrode (RHE) was applied as the RE in many of the electrochemical measurements. This reference electrode consists of an inert metal, platinized platinum or "Pt black", in contact the electrolyte, which was typically aqueous KOH, while hydrogen gas was passed through the system with a pressure of 10^5 Pa. This RE utilizes the half cell reaction in equation 3.1.

$$2H^+ (aq) + 2e^- \rightleftharpoons H_2 (g) \tag{3.1}$$

The potential of this reference reaction is dependent on the conditions present in the reference electrode compartment of the electrochemical cell. The Nernst equation is applied to determine the reference electrode potential (equation 3.2); this takes into account the composition of the electrolyte, the presence of H_2 (g), and the temperature of the system. By bubbling pure H_2(g) through the reference compartment of the cell until the electrolyte is saturated, and maintaining a flow of H_2(g) at a constant pressure throughout the measurement, the fugacity of H_2(g) is assumed to be equal to 1.

$$E_{RHE} = E^0 - \frac{RT}{2F} \times ln\left(\frac{a_{H2}}{(a_{H+})^2}\right) \tag{3.2}$$

The standard potential (E^0) is exactly 0.00 V (by definition), R is the ideal gas constant, T is the temperature, F is Faraday's constant, a_{H2} is the activity of H_2 (g) and a_{H+} is the activity of protons. For the electrochemical experiments described in this thesis, the RHE is a practical and convenient RE because it is used in the same electrolyte as the working electrode compartment of the electrochemical cell; this ensures that there is no contamination of the system through the diffusion of ions from the RE. Instead of using a salt bridge to connect the RE compartment to the main electrode compartment, the RE and WE are in electrolytic contact via a Luggin capilliary that is filled with the same electrolyte. This set-up also minimizes the junction potential between the RE and WE [4].

Electrochemical experiments are carried out using a potentiostat, which has the ability to control the E at the WE, or a galvanostat, which has the ability to control the I at the WE. The studies herein utilize a multi-functional instrument, Autolab PGSTAT, which is capable of both of these methods, as well as other electrochemical techniques that are beyond the scope of this discussion. This instrument is capable of operating in the10 $nA < I < 1$ A range with ± 0.2 % accuracy and of applying E up to 10 V with a resolution of 0.3 μV and an accuracy of ± 0.2%. The practical limitations of the potentiostat / galvanostat instrument are generally not a major factor in the experimental uncertainty.

3.1.2 Electrochemical Cell

The majority of electrochemical experiments were carried out in an all-Pyrex glass two-compartment electrochemical cell. Figure 3.1 shows a simplified representation of the three-electrode set-up in the electrochemical cell. The WE and CE are both in the main compartment, separated by a distance of about 3 cm; they are in electrolytic contact via the electrolyte. The RE is placed in a separate reference compartment that is in electrolytic contact with the main compartment via a Luggin capillary.

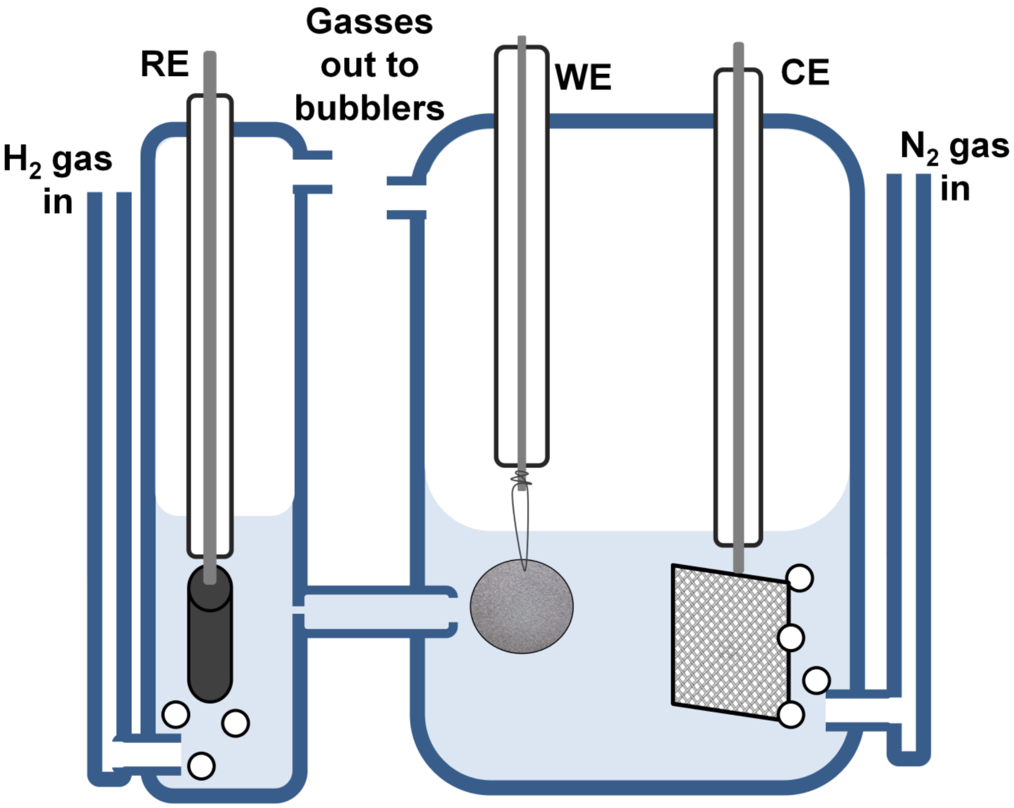

Figure 3.1. Schematic representation of a two-compartment electrochemical cell with a Ni foam working electrode (WE), a Pt mesh counter electrode (CE), and a Pt black reversible hydrogen reference electrode (RE).

3.1.3 Preparation of Ni Foam Electrodes

Nickel and Ni-based metallic foam working electrodes are prepared using the following method. A metal foam disk having a diameter of 10.0 ± 0.1 mm is attached to a thin nickel wire (Alfa Aesar Puratronic®, 99.994% in purity, 0.10 mm diameter) by passing the wire through the porous foam structure then twisting the wire to establish electrical contact. The opposite end of the wire is attached to a second thick Ni wire (Alfa Aesar Puratronic®, 99.994% in purity, 0.5 mm diameter) which is sealed in a glass tube (see WE in Figure 3.1). When the Ni foam WE is submerged in the electrolyte, only a very small section of the thin Ni wire is in contact with the electrolyte; the contribution of the wire to the electrochemical signal is less than 1% and assumed to be negligible [5,6]. By using this method, is it possible to remove the Ni WE while it is still attached to the thin Ni wire from the main electrode support (the thick Ni wire in the glass tube), thus the foam electrode can be stored in a clean environment and reused, as necessary, for multiple experiments. Several sets of experiments within this thesis are preformed with the same WE to allow for an accurate comparison between data sets, for example the CV results presented in Chapter 5. For this reason, it is important to use an electrode set-up which allows the removal and preservation of the WE to ensure that the Ni foam sample is not damaged or contaminated between electrochemical experiments.

3.2 Electrochemical Techniques

3.2.1 Cyclic Voltammetry

Cyclic voltammetry (CV) is a commonly used electroanalytical method that provides the researcher with a large amount of information from the electrochemical system; it is generally a good first analysis when facing an unknown system. In a CV experiment, the potential (E) is varied cyclically between an upper and lower E limit (Figure 3.2). The rate at which the potential is varied is referred to as a scan rate (s). In practice, s values of 1 mV s^{-1} to several hundred V s^{-1} are common but very fast scan rates introduce experimental difficulties that are beyond the scope of this discussion [7]. As the *E* is varied, the *I* is measured; the CV profile is a plot that displays the *I* response as a function of *E*, for a given *s* value. Since the *E* is swept at a defined rate, the *E* axis is also a time axis when divided by the scan rate. The CV profile of a given system can be thought of as an electrochemical spectrum, indicating at what *E* value an electrochemical process takes place. To facilitate comparison between electrodes of different size and surface morphology, the *I* signal is often converted to current density (*j*) by dividing *I* by the electrochemically active surface area (A_{ecsa}) of the WE. The *I* measured in a CV experiment is a combination of Faradic *I* from electrochemical processes and non-Faradic (capacitive) *I* due to charging of the electrochemical double-layer at the interface of the electrode and the electrolyte. Figure 3.2 shows a schematic representation of the CV method and Figure 3.3 shows an example of a CV profile collected at $s = 50$ mV s^{-1} that corresponds to a polycrystalline Pt electrode in 0.50 M aqueous sulfuric acid electrolyte.

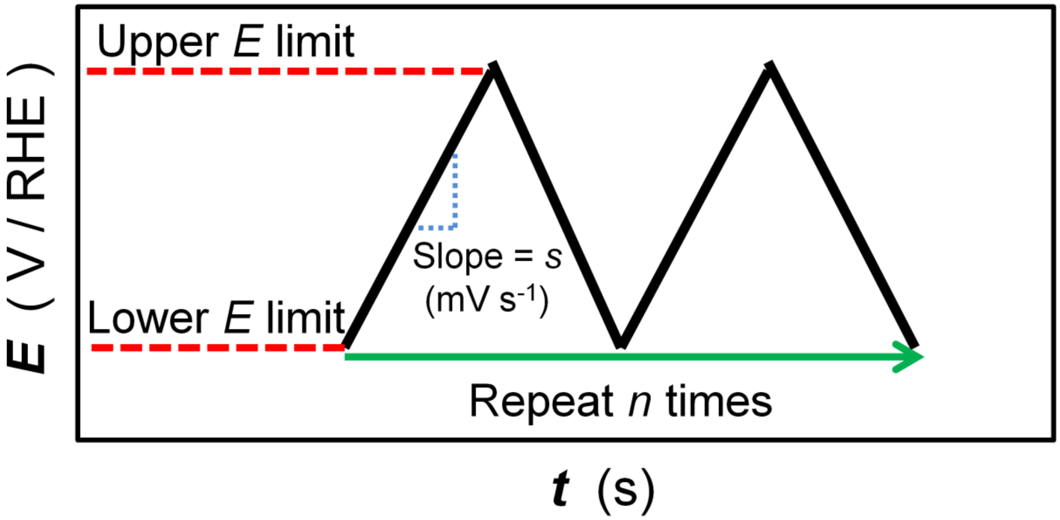

Figure 3.2. Schematic representation of the CV method.

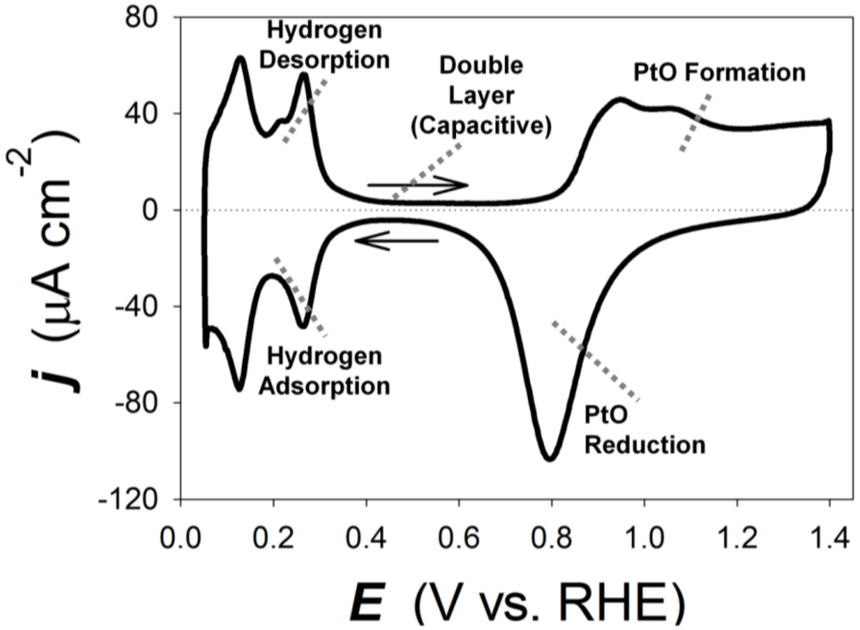

Figure 3.3. CV profile for polycrystalline Pt in 0.50 M aqueous H_2SO_4, at s = 50 mV s^{-1}, and T = 293 K.

Cyclic voltammetry is the dominant electroanalytical method applied within this thesis; it is used to study a variety of different processes some of which are outlined in Table 3.2, which demonstrates the versatility of this technique. Many of the reactions studied using CV involve reactants and products that are freely soluble in the electrolyte but undergo a reaction that occurs with some involvement of the WE, either as a source (or sink) of electrons, or as an electrocatalyst. Other processes studied using CV occur directly on the surface of the WE, such as the formation or reduction of surface oxides on a metal; these processes generally involve the participation of species from the supporting electrolyte. A brief description of CV as applied to each type of reaction is provided herein; Table 3.2 includes examples of both of these types of reactions.

Table 3.2. Electrochemical processes studied using CV throughout this thesis.

Processes Studied	**Reaction**	**Goal**	**Chapter**
Formation and reduction of α-$Ni(OH)_2$ on Ni foam	Anodic: $Ni^0 + 2OH^- \rightarrow \alpha\text{-}Ni(OH)_2 + 2\,e^-$ Cathodic : $\alpha\text{-}Ni(OH)_2 + 2\,e^- \rightarrow Ni^0 + 2OH^-$	Estimate the electrochemical surface area (A_{ecsa}) of Ni foam using the charge (Q) of α-$Ni(OH)_2$ formation	Chapter 4
Formation and reduction of β-NiOOH on Ni foam and Inconel foam, hydrogen evolution, oxygen evolution	Anodic: $\beta\text{-}Ni(OH)_2 + OH^- \rightarrow \beta\text{-}NiOOH + H_2O + e^-$ $2\,OH^- \rightarrow \frac{1}{2}\,O_2 + H_2O + 2e^-$ Cathodic: $\beta\text{-}NiOOH + H_2O + e^- \rightarrow \beta\text{-}Ni(OH)_2 + OH^-$ $H_2O + e^- \rightarrow \frac{1}{2}\,H_2 + OH^-$	Obtain an electrochemical spectrum for Ni and Inconel foams in alkaline media	Chapter 4
Oxidation of isopropanol to acetone using a Ni foam electrode in a variety of conditions	Anodic: $(CH_3)_2CHOH + \beta\text{-}NiOOH + OH^- \rightarrow (CH_3)_2CO + \beta\text{-}Ni(OH)_2 + H_2O + e^-$	Use CV analysis to improve mechanistic understanding of the system	Chapter 5
Hydrogen adsorption and desorption on the surface of Pt	Anodic: $H_{ads} + OH^- \rightarrow H_2O + e^-$	Estimate A_{ecsa} of Pt on Ni foam using Q of hydrogen desorption	Chapter 6

To understand the situation where freely soluble species react at the surface of the WE and then diffuse back into the electrolyte, we will consider a generic, reversible process whereby a species (A) is reduced (R), as shown in equation 3.3 [8].

$$A + n\,e^{-} \rightleftharpoons R \tag{3.3}$$

Figure 3.4 shows the *I* response in the *E* region where this process takes place. The *E* axis has been converted to the overpotential (η). The overpotential is the difference between the applied potential (*E*) at which an overall non-zero current passes through the electrode and the potential at which the overall current or current density (*j*) is zero ($E_{j\,=\,0}$) because the rate of the forward process is equal to that of the reverse process (equation 3.4). The value of $E_{\mathrm{j=0}}$ is determined by applying the Nernst equation; the Nernst equation is outlined earlier in the experimental techniques (section 3.1.1) as equation 3.2 [8].

$$\eta = E - E_{j=0} \tag{3.4}$$

Figure 3.4 demonstrates several features: (i) a maximum peak *I*, marked by the red dotted line, (ii) an increase in the peak *I* and change in the peak shape as the *s* is increased, and (iii) increase in the non-Faradic current as the *s* is increased, marked by the green dashed box. The curve with the lowest *s* value (bottom, light blue line) does not have a defined peak shape, but instead displays steady-state *I* vs. *E* behaviour. The concentrations of reactants and products at a certain distance from the electrode are constant; thus, we are mainly concerned with the concentrations of species in the vicinity of the electrode, a region referred to as the *Nernst diffusion layer*. Within the Nernst diffusion layer, there is a concentration gradient that depends on the relative rates of the reduction process (that depletes the concentration of reactant A) and the diffusion of fresh reactant A into this region. For the steady-state situation, the s value is sufficiently low that the concentration of reactant A in the Nernst diffusion layer is replenished at a rate equivalent to that of the reduction process. As the s is increased, a peak shape is defined. Increase in η results in the increase of I up to a maximum value, then the I begins to decrease. This behaviour is the consequence of two competing factors. First, as the η is increased, the rate of the reduction process increases, leading to the increase in I. Second, as the reduction reaction proceeds, the thickness of the Nernst diffusion layer increases resulting in a decrease in the rate of the reaction. As the s increases, the Nernst diffusion layer has less time to become replenished in the concentration of reactant A, thus higher s values give rise to maximum I values in less time. Finally, the non-Faradic current associated with the charging of the electrochemical double-layer increases with increasing s. Since the measured I is a combination of Faradic and non-Faradic I, the entire curve is also shifted upwards due to this increase in double-layer current [2,3,9].

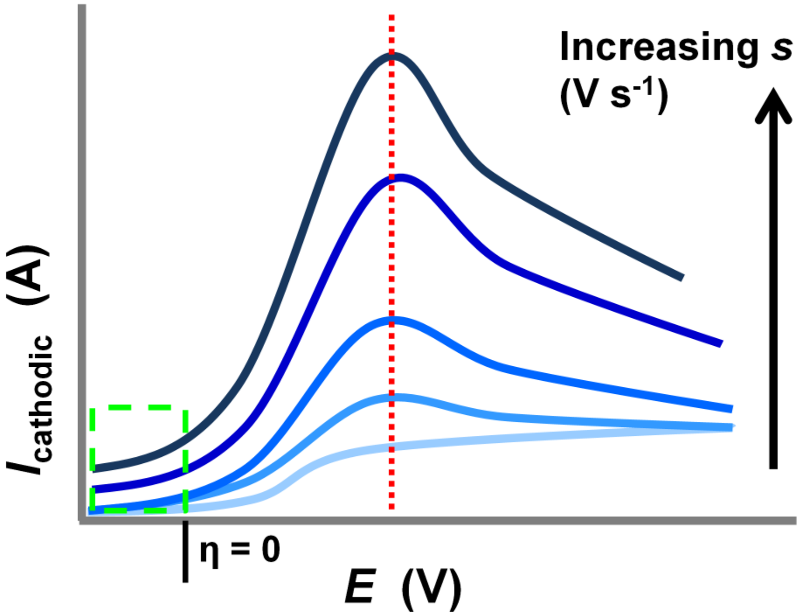

Figure 3.4. A series of cathodic CV profiles with increasing scan rates (*s*) for a reversible reduction process.

Processes occurring directly at the surface of the electrode including the adsorption of species and the formation of surface oxides, are also studied with CV. In this situation there is no concentration gradient of reactive species, instead the process is limited by the coverage of the species at the electrode surface. The appearance of CV peaks corresponding to a surface process is different from those involving dissolved species in the electrolyte. Surface processes often give rise to sharp, symmetrical CV features. If the surface process is reversible, there is little or no peak *E* separation for the anodic and cathodic processes. The charges associated with the anodic and cathodic processes are equal. Figure 3.5 shows the forward-going (anodic peak) and reverse-going (cathodic peak) CV scans for a reversible surface process. The adsorption and desorption of hydrogen on Pt is a classic example of a reversible surface process. In contrast, the formation of β-$Ni(OH)_2$ on the surface of Ni is an irreversible surface process, which gives rise to anodic current in the forward scan, but no corresponding reduction peak upon scan reversal [3,9].

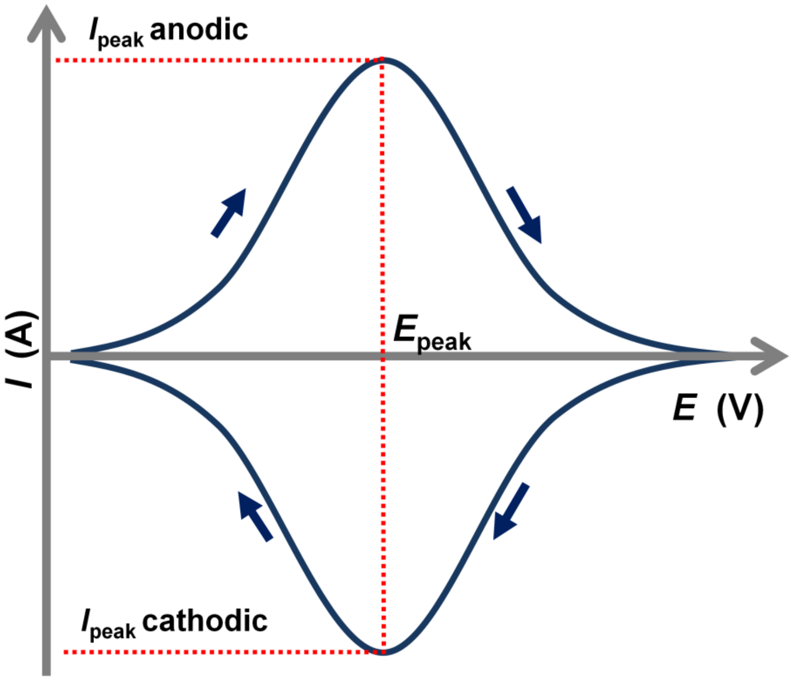

Figure 3.5. Anodic and cathodic CV peak shapes characteristic of a reversible surface process.

3.2.2 Chronoamperometry

Chronoamperometry (CA) is an important method in electrochemistry used to measure the current or current density of a system at a fixed potential. In this method, the E of the WE is held at a fixed value and the I response is measured as a function of t. The time scale of CA measurements can be from a few milliseconds up to several hours or longer. In Chapter 5 of this thesis, the electrochemical oxidation of an alcohol was carried out using CA over the course of 9 hours. The top section of Figure 3.6 shows the E vs. t profile for a typical potential-step CA experiment; E_1 is generally chosen such that no Faradaic electrochemical reaction takes place whereas E_2 should be in the potential region where the process of interest takes place. A CV experiment, performed prior to CA analysis, is useful for selecting appropriate E_1 and E_2 values. The potential-step from E_1 to E_2 is assumed to be instantaneous; generally this approximation is appropriate. However, it is important to understand that a potential-step cannot be instantaneous; it is better thought of as a very fast linear sweep on the order of ten million (10^6) V s^{-1} [10]. As is the case with any transient technique, the measured I is affected by the perturbation of the potential. In addition to Faradic I from the electrochemical process, there is also I due to the charging of the electrochemical double-layer that gives rise to a sharp spike in I just after the potential-step. Approximately the first hundred microseconds of a CA measurement display a I response where the Faradic current is completely masked by the contribution of the electrochemical double-layer [9, 11].

Analysis of the I vs. t profile from a CA potential step measurement provides qualitative information about the reaction taking place. For an electrode with planar geometry in an unstirred and thermostatic electrolyte environment, the relationship between I and t is given by equation 3.5 [8,9].

$$|I| = \frac{nFAD^{1/2}C^{\infty}}{\pi^{1/2}t^{1/2}} \tag{3.5}$$

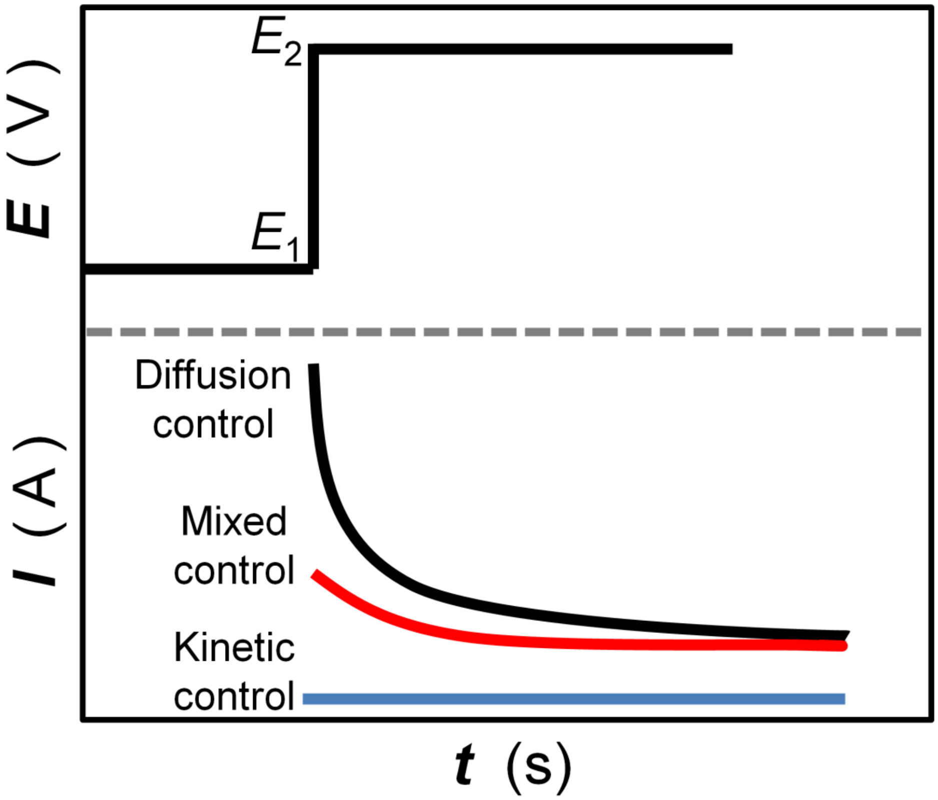

Figure 3.6. Potential (*E*) vs. time (*t*) profile for a potential-step CA experiment (top); Current (*I*) vs. *t* profiles for potential-step measurements of various systems (bottom).

In this equation, *n* is the number of electrons transferred in the process, *F* is Faraday's constant (C mol^{-1}), *A* is the surface area of the electrode (cm^2), *D* is the diffusion coefficient (m^2 s^{-1}), C^{∞} is the bulk concentration of the diffusion species (mol cm^{-3}), and *t* is the time (s). If the process is under diffusion control, a plot of *I* vs. t $^{-1/2}$ will be linear. It is practical to use data in the range of 1 ms to 10 s for this type of analysis. The CA *I* vs. *t* response for a diffusion controlled reaction will have an appearance similar to the black curve in the bottom section of Figure 3.6. The blue curve in this figure demonstrates the I vs. t response for a system under kinetic control with a small rate constant. The straight line with a low I value indicates that the surface concentration of the reaction-limiting species has not changed significantly with the application of the potential step. This behavior shows that diffusion does not significantly affect the rate of reaction and that the system is essentially at steady-state conditions. Finally, the red curve in Figure 3.6 shows the I vs t response for a system that is under a mixture of diffusion and kinetic control. This type of behavior indicates that the rate of diffusion and the rate of electron transfer may be comparable [9, 11].

Quantitative information can also be obtained from CA measurements. The I response may be integrated and converted to charge (Q) and plotted as a function of time. This curve can then be integrated in order to determine the total charge transferred, which can be compared to product yields or other analytical information from the system. Alternatively, many potentiostat instruments have the ability to measure Q directly using a built-in capacitor for real-time charge integration. This technique is called chronocoulometry (CC).

3.2.3 Tafel Plots

The relationship between the I and the E at an electrode is described by the Butler-Volmer equation, which is one of the most important equations in electrochemical kinetics. This equation can be written in several forms depending on the details of the electrochemical system to which it is applied. The version written below (equation 3.6) is applicable to systems where the charge-transfer step is rate-determining, the mass transport is very high and so the concentration of reactants at the electrode surface is approximately the same as in the bulk of the electrolyte. This version of the equation can be applied to a system where the solution is well-stirred and the current is kept low [2, 3].

$$j = j_0 \times \left(exp\left[\frac{\alpha_a nF\eta}{RT}\right]\right) - exp\left[-\frac{\alpha_c nF\eta}{RT}\right] \tag{3.6}$$

where $\eta = E - E_{j=0}$

In this equation, j is the current density (A m^{-2}), j_0 is the exchange current density (A m^{-2}), α_a is the anodic charge transfer coefficient (dimensionless), α_c is the cathodic charge transfer coefficient (dimensionless), n is the number of electrons in the reaction, F is Faraday's constant (C mol^{-1}), R is the universal gas constant (J mol^{-1} K^{-1}), T is the temperature (K), and η is the overpotential (V), which was described in an earlier section. This equation applies to both the anodic and cathodic process, with the distinction between the two being in the sign of the η. When $\eta < 0$, the j from the cathodic portion of the equation will be larger than that of the anodic portion and the resulting total j will be cathodic; when $\eta > 0$ the resulting j will be anodic. In the case where $|\eta|$ is large ($\eta > 25.7 / n$ mV), the Bulter-Volmer equation can be rewritten in another form that is also known as the Tafel equation. The Tafel equation, as written for a cathodic process, is shown in equation 3.7. Other common forms of the Tafel equation are shown in equations 3.8 and 3.9. The b term from the Tafel equation, as written in equation 3.8, is the Tafel slope (equation 3.10) [2, 3, 7, 9].

$$\eta = \left(\frac{2.3RT}{\alpha_c nF} log j_c\right) - \left(\frac{2.3RT}{\alpha_c nF} log j_0\right) \tag{3.7}$$

$$\eta = A + b \times log|j| \tag{3.8}$$

$$log|j| = logj_0 + \frac{\alpha_c nF}{2.3\ RT}|\eta| \tag{3.9}$$

$$b = \frac{\alpha nF}{2.3RT} \tag{3.10}$$

A Tafel plot is a graph of log j vs. η that is used to determine kinetic and mechanistic information about an electrochemical reaction. Figure 3.7 demonstrates the key features of a Tafel plot. The slope of a Tafel plot can help in determining the number of electrons transferred in the rate determining step of the electrochemical process. For example, solving equation 3.9 for n = 1 and T = 298 K, assuming α = 0.5 gives a slope of 118 mV for a one electron process. The value of j_0 is the current density at η = 0; it corresponds to an electrode at equilibrium (the rates of the cathodic and anodic processes are equal). The j_0 is an important kinetic parameter because it reflects the intrinsic rate of the process under study. The value of j_0 is determined experimentally by extrapolating the linear portion of the Tafel plot to the y-axis [3, 9].

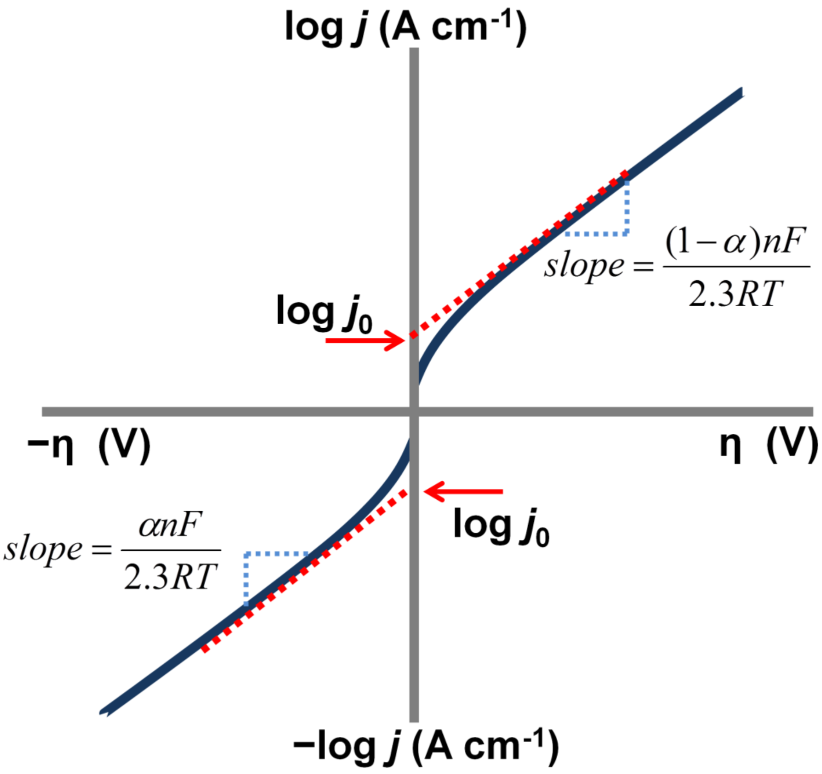

Figure 3.7. Key features of anodic and cathodic Tafel plots.

3.3 Material Characterization Techniques

3.3.1 XPS

X-ray photoelectron spectroscopy (XPS) is a qualitative and quantitative analysis technique that is capable of determining the elemental composition of a material's near surface region and provides additional information regarding the chemical bonding state of the species detected. All elements, with the exception of hydrogen and helium, can be detected with XPS. Commercial XPS instruments have been available since the 1970's and this technique is applied to the study of a wide range of solid materials including metals, alloys, ceramics, polymers, minerals, and others. XPS is a surface-sensitive technique that probes the near-surface region of the sample (top few Å). As it is a widely used technique, XPS is the topic of many textbooks and review articles; the reader is referred to the following resources for detailed descriptions of the method [12 – 16]. Herein, the utilization of XPS towards the analysis of Ni and Inconel foams is described in Chapter 4.

The necessary components of an XPS instrument consist of an ultrahigh vacuum chamber containing the sample stage, an electron energy analyzer and detection system, an X-ray source (typically Mg or Al), and an ion gun (used for sample cleaning and depth profiling). The surface of the sample is irradiated with photons of a characteristic energy from the X-ray source, which interact with the core-shell electrons of the atoms at the surface of the sample. As a result of these interactions, core electrons are ejected as photoelectrons (Figure 3.8); the sample is grounded to prevent charging. The kinetic energy (E_K) of the photoelectron is dictated by the amount of energy that was transferred from an incident photon in order to excite this electron from its electronic level to the vacuum level. The schematic diagram in Figure 3.8 demonstrates this process for a solid material; equation 3.11 shows the conservation of energy within the process.

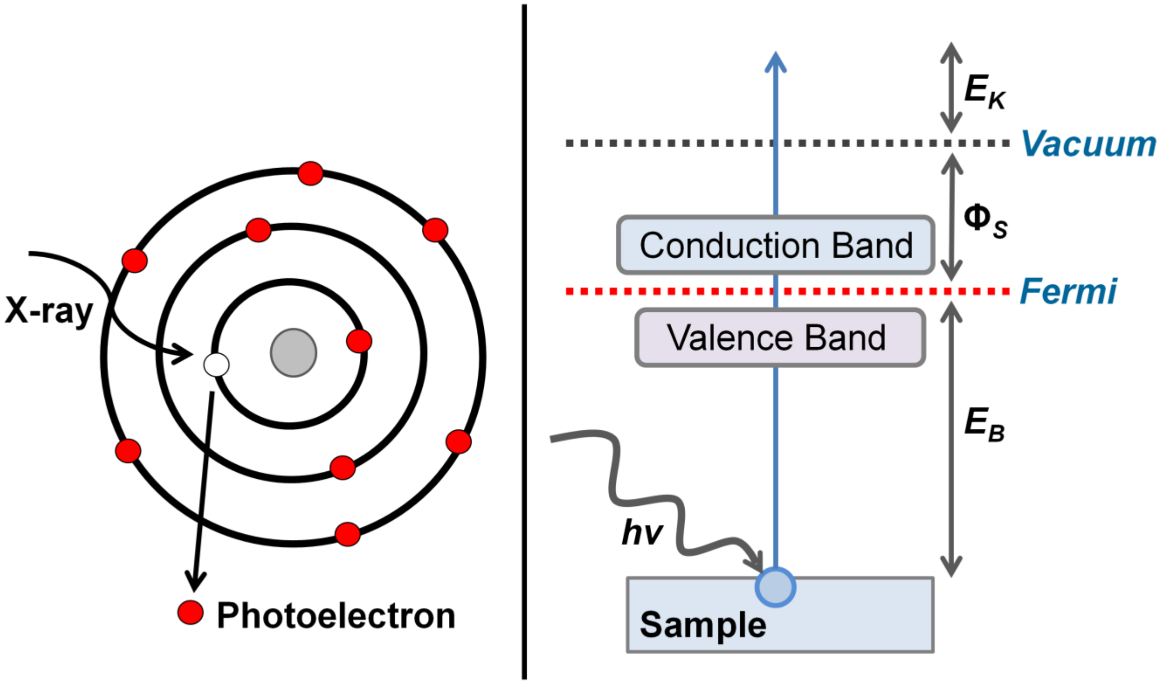

Figure 3.8. Photoelectron generated from an incident X-ray photon (left), schematic representation of the energy transfer during the XPS process (right).

$$E_K = hv - E_B - \Phi_S \tag{3.11}$$

In equation 3.10, E_B is the binding energy of the core electron with reference to the Fermi level, hv is the characteristic energy of the incident photon, E_k is the kinetic energy of the resulting photoelectron, and Φ_S is the work function of the sample atom. The E_B of each core electron is unique for a given element, therefore the emission of multiple photoelectrons from an element will give rise to multiple peaks at characteristic energy values in a spectrum. Photoelectrons from atomic levels higher than the s level (p, d, f) give rise to doublet peaks, with different binding energy values in the XPS spectrum, as a result of a process called spin-orbit coupling [15, 16]. This interaction occurs between the spin of the electron and the magnetic field generated by the movement of the electron around the nucleus. The unpaired electron left after photoemission has either a parallel or anti-parallel spin orientation relative to the orbital momentum resulting in the possibility of two different energy states and thus two different binding energy values.

Any changes in the bonding state of an atom will give rise to changes in its spectral features such as the binding energy of the peak, the peak width and shape, and sometimes contribute bonding satellite peaks to the spectrum. These changes allow chemical information, such as the oxidation state of an element, to be determined from the XPS spectrum. For example, when one atom bonds to a more electronegative element, the charge transfer results in a more positive effective charge on the original atom; this interaction increases the binding energy of electrons and results in an observable chemical shift of the XPS peak. In practice, experimental XPS spectra are often compared to tabulated reference spectra from databases or software in order to aid with peak assignment and interpretation of peak shifts [13].

3.3.2 Scanning Electron Microscopy

Scanning electron microscope (SEM) images are used within this thesis, in combination with other techniques, to characterize Ni-containing foams (Chapter 4) and Pt-modified Ni foams (Chapter 6). Detailed description of SEM instrumentation and SEM image interpretation can be found in a variety of textbooks [17 – 19] and is beyond the scope of this thesis.

SEM images are generated by scanning the surface of a sample with a focused beam of electrons that interact with the sample to produce a several types of signals that are detected by the instrumentation to generate images. Incident electrons interact with the electrons of the sample through elastic and inelastic collisions, characteristic X-rays are also emitted as a result of these collisions, all of these can be used to generate useful information about the sample. Electrons ejected from the sample as a result of inelastic scattering interactions are referred to as secondary electrons (SE). Secondary electron imaging is the most commonly-used imaging mode for SEM. The SE detected in SEM are generally low-energy electrons (<50 eV) originating from the K-shell of atoms located in the top 10 nm of the sample. The SE SEM images provide topographic contrast, as the brightness of any location on the resulting image depends on how many SE reach the detector. Regions of the sample that are lower (farther from the detector) and regions that are physically blocked from the detector (shadowed) will appear darker in the resulting image [17, 19].

Electrons that are scattered elastically at an angle of 90˚ or greater are called backscattered electrons (BSE); these electrons are also useful for imaging the sample. The detectors for BSE are placed in a “doughnut” type arrangement concentric with the electron beam, in order to efficiently collect these electrons. Images generated with BSE offer chemical composition contrast because high atomic number elements backscatter electrons more effectively. Backscattered electrons are higher in energy than SE and as such the region of the specimen from which BSE are detected is significantly deeper than simply the top 10 nm. Back-scattered electrons are detected from depths up to 1 μm within the sample [17].

Characteristic X-rays are generated when an inner-shell electron is displaced through a collision and an outer-shell electron drops down to fill the resulting hole. The difference in energy between the outer and inner shell is released in the form of an X-ray. The energy of this X-ray is characteristic of the atom that is undergoing the relaxation process, thus the information from characteristic X-rays offers important chemical information. Many SEM instruments are equipped with spectrometers that are capable of analyzing these X-rays based on their energy (energy-dispersive X-ray spectroscopy, EDS) or on their wavelength (wavelength-dispersive X-ray spectroscopy, WDS). The EDS or WDS signal can be generated from regions of the sample deeper than SE and BSE, the interaction volume for the detected X-rays is on the order of several cubic µm. Practically speaking, these techniques are generally qualitative and extremely useful in obtaining quick and non-destructive chemical information on the micrometer scale to compliment the SEM images [17, 18].

3.3.3 Focused Ion Beam Methods

A focused ion beam (FIB) instrument was used for the following applications throughout the course of this thesis: (i) electron and ion imaging, (ii) ion milling to generate specimen cross-sections, and (iii) fabrication of a TEM specimen. Table 3.3 describes some useful features of FIB analysis and provides images to illustrate these features. Due to the importance of the FIB instrument to the studies presented in Chapters 4 and 6, a general introduction to the FIB instrument is provided. For detailed information regarding the FIB apparatus and techniques involving FIB, the reader is referred to the following textbook and review articles [20 – 22].

Briefly, the FIB is very similar in design to a SEM microscope; however the beam in a FIB instrument is made up of ions instead of electrons. The main components of the FIB instrument are the ion source, column, sample chamber, vacuum pumping systems and user interface. The most common ion source is gallium. For the remainder of this document, a Ga^+ beam should be assumed unless otherwise stated. The Ga^+ ions are accelerated through the column and focused using electrostatic lenses. In most modern instruments the ion beam has an energy of 30-50 keV. The Ga^+ ions strike the surface of the sample causing a collision cascade (see Figure 3.9) that results in the ejection of the secondary ions (SI), and secondary electrons (SE) which can be used for imaging [23]. Sample material is sputtered off the surface, which gives the FIB the ability to mill away sections of material. The ion current or “dose” of the beam is controlled through the user interface, allowing the instrument to be used for imaging (at low dose), rough milling (high dose) or precision milling (moderate dose). Modern FIB systems can achieve 4 nm imaging resolution when they are operated at low beam currents [24, 25].

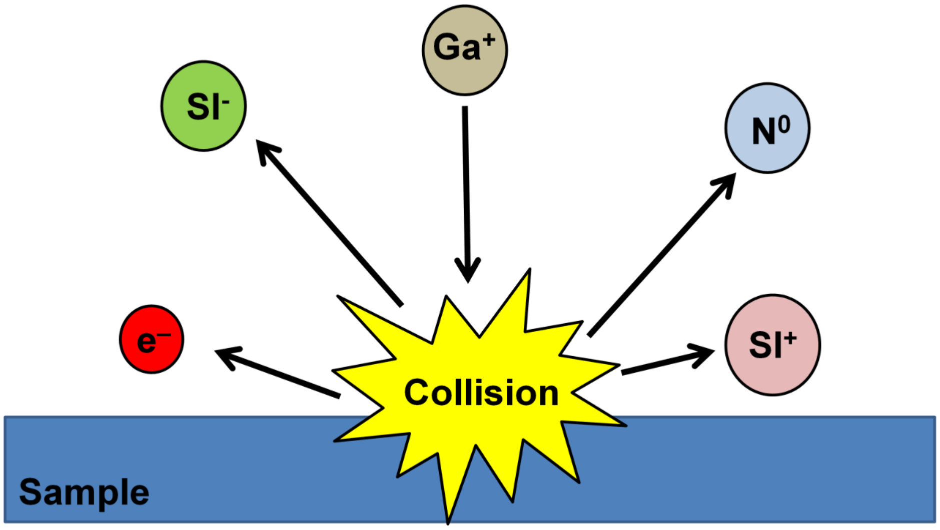

Figure 3.9. Species generated from the collision of incident Ga^+ ions with a sample in an FIB experiment.

The use of both SI and SE imaging modes is advantageous because of the different contrast mechanisms that contribute to the appearance of these images. Images in Table 3.3 illustrate the dissimilar appearance of FIB SI and FIB SE images by showing the same section of a Pt – modified Ni foam specimen imaged with both methods. Secondary electron imaging produces good depth of field for imaging three-dimensional structures, such as foams, and gives excellent grain orientation contrast in polycrystalline materials. The crystallographic orientation contrast results from incident Ga^+ ions channeling through interplanar spacing of metal grains. The depth of penetration for the incident Ga^+ ion depends on the relative angle of the ion beam and the grain [25, 26]. The channeling contrast induced by FIB is more than four times as intense as that observed in SEM backscatter images [27]. Secondary ion images are better than SE images for assessing differences in material composition because the secondary ion yield (or brightness) of a region depends strongly on the material. For example, oxidized regions on a metal generally appear bright in a secondary ion image because ions are more easily sputtered off an oxide than a pure metal. The same oxide may appear dark in the SE image because of charging; as the Ga^+ beam interacts with the sample, a region of positive charge may build up on less conductive materials, trapping the secondary electrons generated at this location which results in a darkened area on the SE image. It is important, however, to note that the appearance of a SE or SI image is often the result of a combination of topographic, crystallographic, and material contrast mechanisms and therefore the interpretation of these images, while very useful, should be supported with other analytical methods [25, 28].

The FIB is a valuable multipurpose tool for imaging solids on the $1 – 10^3$ µm scale and machining on the $1 – 10^2$ µm scale. It is a powerful instrument for the preparation and analysis of cross-section specimens for micro-structured, multiphase or delicate materials. The use of a FIB instrument in the preparation of TEM samples affords several benefits in comparison to more traditional methods: the FIB is faster than argon ion milling, more site specific than the tripod polisher, more gentle than the ultra-microtome, cleaner than chemical or electrochemical methods, and more versatile than any one of these aforementioned techniques [20, 29].

Table 3.3. Examples of material analysis using a FIB instrument.

Feature	**Image**
- SE FIB image of the strut of a Ni foam specimen. - Excellent grain orientation contrast is observed in FIB secondary electron images.	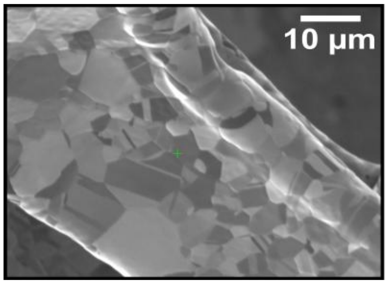
- SE FIB image of the strut of a Ni foam specimen. - A rectangular area has been milled away using the FIB.	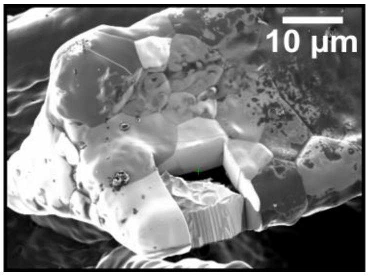
- SE FIB image of a section of Pt-modified Ni foam. - The thin layer of Pt (present as PtO from electrochemical oxide formation) on the surface of the Ni foam is difficult to see in the SE image.	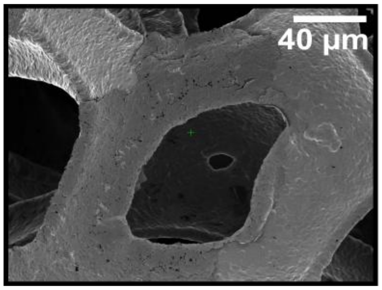
- SI FIB image of a section of Pt-modified Ni foam. - The thin layer of Pt (present as PtO from electrochemical oxide formation) on the surface of the Ni foam is easy to see in SI imaging mode due to material contrast.	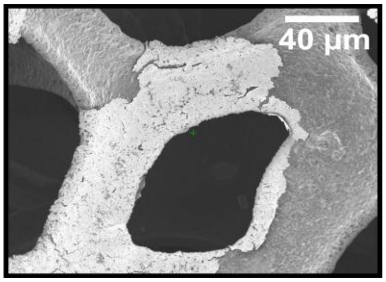

3.4 References

(1) J. A. V. Butler, *Prof. R. Soc. Lon*d. A. **1936**, 157, 423-433.

(2) A. J. Bard, L. R. Faulkner, *Electrochemical Methods Fundamentals and Applications*. John Wiley & Sons, Toronto, **1980**.

(3) A. J. Bard, G. Inzelt, F. Scholz, Eds, *Electrochemical Dictionary*. Springer-Verlag, Berlin, **2008.**

(4) G. Inzelt, A. Lewenstam, F. Scholz, *Handbook of Reference Electrodes*. Springer-Verlag, Berlin, **2013**.

(5) M. Grden, M. Alsabet, G. Jerkiewicz, *ACS Appl. Mater. Interfaces* **2012**, 4, 3012-3021.

(6) J. van Drunen, B. Kinkead, M. C. P. Wang, B. D. Gates, E. Sourty, G. Jerkiewicz, *ACS Appl. Mater. Interfaces* **2013**, 5, 6712-6722.

(7) C. Lefrou, P. Fabry, J. Poignet, *Electrochemistry. The Basics, With Examples*. Springer, Berlin, **2012**.

(8) W. Schmichler, E. Santos, *Interfacial Electrochemistry*, Springer-Verlag, Berlin, **2010**.

(9) D. Pletcher, R. Greef, R. Peat, L. M. Peter, J. Robinson, *Instrumental Methods in Electrochemistry*. Horwood Publishing Ltd., Chichester, **2001**.

(10) Z. Nagy, *Electrochim. Acta* **1982**, 129, 1943-1950.

(11) C. H. Hamann, A. Hamnett, W. Vielstich, *Electrochemistry*. Wiley-VCH, Darmstadt, **2007**.

(12) S. Hufner, Ed., *Very High Resolution Photoelectron Spectroscopy*. Springer, Berlin, **2007**.

(13) S. Hofmann, Ed., *Auger and X-ray Photoelectron Spectroscopy in Materials Science*. Springer-Verlag, Berlin, **2013**.

(14) F. Hippert, E. Geissler, J. L. Hodeau, E. Lelievre-Berna, J. Regnard, Eds., *Neutron and X-Ray Spectroscopy*. Springer, Dordrecht, **2006**.

(15) F. De Groot, *Coord. Chem. Rev*. **2005**, 249 31-63.

(16) C.D. Wagner, *Anal. Chem*. **1977**, 49, 1282-1290.

(17) J. Goldstein, D. E. Newbury, P. Echlin, D. C. Joy, A.D. Romig, C. E. Lyman, C. Fiori, E. Lifshin, *Scanning Electron Microscopy and X-Ray Microanalysis: A Text for Biologists, Materials Scientists, and Geologists*. Spinger, New York, **1992**.

(18) A. T. Hubbard, Ed., *The Handbook of Surface Imaging and Visualization*. CRC Press, London, **1995**.

(19) W. Zhou, Z. L. Wang, Eds., *Scanning Microscopy for Nanotechnology. Techniques and Applications*. Springer, New York, **2006**.

(20) L. A. Gianuzzi, F. A. Stevie, *Micrion* **1999**, 30, 197-204.

(21) F. A. Stevie, T. C. Shane, P. M. Kahora, R. Hull, D. Bahnck, V. C. Kannan, E. David, *Surf. Inter. Anal*. **1995**, 23, 61-68.

(22) F. A. Stevie, L. A. Giannuzzi, B. I. Prenitzer, *The focused ion beam instrument*. In: L. A. Giannuzzi, F. A. Stevie, Eds., *Introduction to Focused Ion Beams: Instrumentation, Theory, Techniques and Practice*. Springer, Ney York, **2005.**

(23) L. A. Giannuzzi, B. I. Prenitzer, B. W. Kempshall, *Ion – Solid Interactions*. In: L. A. Giannuzzi, F. A. Stevie, Eds., *Introduction to Focused Ion Beams: Instrumentation, Theory, Techniques and Practice*. Springer, New York, **2005**.

(24) F. A. Stevie, D. P. Griffis, P. E. Russell, *Focused Ion Beam Gasses for Deposition and Enhanced Etching.* In. L. A. Giannuzzi, F. A. Stevie, Eds., *Introduction to Focused Ion Beams: Instrumentation, Theory, Techniques and Practice*. Springer, New York, **2005**.

(25) M. Phaneuf, *Micrion* **1999**, 30, 277-288.

(26) L. A. Giannuzzi, J. R. Michael, *Microsci. Microanal*. **2013**, 19, 344-349.

(27) M. Phaneuf, *Grain Orientation Contrast - Fibics Tutorial*. Available at: http://www.fibics.com/fib/tutorials/grain-orientation-contrast/6/. Accessed 08/24, **2013**.

(28) M. Phaneuf, *FIB Chemical Contrast - Fibics Tutorial*. Available at: http://www.fibics.com/fib/tutorials/fib-chemical-contrast/1/. Accessed 08/24, **2013**.

(29) D. B. Williams, C. B. Carter, *Transmission Electron Microscopy: A Textbook for Materials Science*. Springer, New York, **2004**.

Chapter 4

Comprehensive Structural, Surface-Chemical and Electrochemical Characterization of Nickel-Based Metallic Foams [1]

4.1 Introduction

Nickel is an important metal applied in various industries due to several desirable physical, metallurgical and chemical properties (e.g. excellent electrical and thermal conductivities, malleability, ductility, ability to form stable alloys with different transition metals, corrosion resistance in alkaline and saline media). It is widely used in energy-storing and energy-delivering devices, such as rechargeable batteries [1], alkaline fuel cells [2], and electrochemical supercapacitors [3,4]. Nickel alloys and superalloys were developed specifically to exhibit excellent stability in harsh environments [5] (corrosive, high-temperature and high-stress). Nickel oxides showed to be effective catalysts for the electro-oxidation of alcohols and amines [6,7]. In all of these applications, the surface chemistry of the Ni-based material impacts the performance, catalytic activity, efficiency, and stability [4,8,9].

---

[1] The work presented in this chapter is published. J. van Drunen. *ACS Applied Materials and Interfaces*, 5 (2013) 6712 – 6722.

Porous metallic materials possessing high specific surface area (A_s in cm^2 g^{-1}) offer a beneficial combination of properties such as large surface area for heterogeneous catalysis, low material usage, low mass density, and ease of manufacture. There are several methods of manufacturing open-pore metallic materials, such as foaming of metal melts, powder compaction and melting, chemical vapor deposition (CVD), physical vapor deposition (PVD), and electrochemical deposition of one or several metals on a pre-formed, open-pore substrate [10 – 12].

The nickel foams used in this work were provided by Vale INCO (*former INCO Technical services*). They are prepared in two stages: (step 1) CVD of Ni by the decomposition of $Ni(CO)_4$ on an open-cell polyurethane substrate and (step 2) a high temperature (~1000 ˚C) burnout of the polymeric template together with sintering and annealing of the Ni deposit [12]. A variation of the process involves the formation of a thin Ni layer through PVD on a polyurethane substrate, followed by electrodeposition of Ni to thicken the struts. Multi-component foams (see Table 4.1 for their chemical composition) are produced through a powder metallurgical process, which involves spraying of pre-made Ni foam with a binding agent followed by coating with a pre-alloyed powder that has the desired composition. The final stage is heat treatment at a selected temperature, which results in sintering and interdiffusion of the component metals [13]. Such produced Ni foams are used to manufacture rechargeable batteries [10] and electrochemical supercapacitors [12], optically transparent electrodes [14], and permeable electrodes for flow electrolysis systems [2,10]. The multi-component foams examined in this study were developed specifically for

Table 4.1. Structural characteristics of Ni–containing foams [10, 13].

Chemical Composition	Sheet Density ($g\ m^{-2}$)	Bulk Density ($g\ cm^{-3}$)	Range of Grain Size (μm)	Average Strut Wall Thickness (μm ± σ μm)	Thickness of InnerWall Structure (μm)
Ni	320	0.16	1 – 12	2.5 ± 0.5	0.3
Ni	420	0.21	1 – 12	2.5 ± 0.5	0.2
Ni	510	0.26	4 – 12	3.5 ± 0.5	0.2
Ni	640	0.32	4 – 12	4.0 ± 1.0	0.3
NiCrMoFe(Nb+Ta) (Inconel)	1320	0.66	4 – 20	6.0 ± 2.0	0.7
NiFeCrAl (FE2)	1200	0.60	4 – 20	5.0 ± 1.0	0.6

elevated temperature, highly corrosive, and strongly oxidizing environments (e.g. diesel engine particulate filters) [13]. The Inconel 625 alloy (Table 4.1) was designed to offer acid resistance and high temperature stability, whereas the FE2 alloy (Table 4.1) was designed to withstand oxidation at high temperatures [13].

This study presents a structural, surface, and electro-chemical characterization of open-cell Ni and Inconel foams using scanning and transmission electron microscopies (SEM, TEM), focused ion beam (FIB), X-ray photoelectron spectroscopy (XPS), and cyclic voltammetry (CV). It discusses the applicability of chemical etching as a means of removing a native oxide layer, increasing the surface area, and activating the electrode towards a specific electrochemical reaction without compromising the integrity of three-dimensional (3D) structure.

4.2 Experimental Section

4.2.1 Electrochemical Measurements

Electrochemical measurements were carried out using a two-compartment Pyrex electrochemical cell and three electrodes. The working electrode (WE) was either a nickel or Inconel foam (supplied by the former Inco Technical Services Ltd.), attached to a Ni wire sealed in a glass tube (Alfa Aesar Puratronic®, 0.25 mm in diameter) for electrical contact. The contribution of the Ni wire to the overall surface area, and thus to the electrochemical signal, was less than 1% and assumed to be negligible. Each metal foam WE was degreased with acetone under reflux in order to remove organic impurities. The counter electrode (CE) consisted of high-purity Pt gauze (99.98% in purity, Alfa Aesar) spot-welded to a Pt wire (99.98% in purity, Alfa Aesar) and covered with electro-deposited Pt (Pt black). The surface area of CE was at least ten times larger than that of the WE. The reference electrode (RE) was a reversible hydrogen electrode (RHE); it was made in the same manner as the CE. Hydrogen gas of ultra-high purity (UHP) (Praxair 5.0 grade) was bubbled through the RE compartment at a pressure of 1 bar. The separation between WE and CE was approximately 3 cm. Electrochemical characterization was carried out in 0.5 M aqueous KOH solution (Sigma-Aldrich KOH pellets of 85% in purity, A.C.S. reagent grade). The electrolyte solution was prepared using UHP water (Millipore, 18.2 MΩ cm). The reference electrode was in electrolytic contact with the main compartment via a Luggin capillary. All potentials are reported with respect to RHE. Prior to each experiment, the electrolyte solution was degassed by bubbling UHP N_2(g) (Praxair 5.0 grade) for 30 minutes. Throughout the duration of electrochemical measurements, UHP N_2(g) was passed over the electrolyte to maintain the inert gas environment and to expel any gases that might be generated during electrochemical experiments. Glassware was cleaned according to well-established procedures [15, 16]. The electrochemical measurements were carried out at a temperature of T = 298 ± 1 K. CV profiles were collected using an Autolab model PGSTAT302 potentiostat (Metrohm). All experimental parameters were controlled and data acquired using the NOVA Advanced Electrochemical Software (Metrohm).

4.2.2 Chemical Etching

Nickel develops a native surface oxide (β-Ni(OH)$_2$) upon contact with moist air [17]. For certain experiments, Ni foams were pre-treated by chemical etching in order to remove the β-Ni(OH)$_2$ layer and produce a metallic Ni surface. The etching solution employed in this research was made from 30 cm^3 of conc. HNO_3, 10 cm^3 of conc. H_2SO_4, 10 cm^3 of conc. H_3PO_4, and 50 cm^3 of glacial CH_3COOH [18]. The Ni-containing foams were submerged in the solution at T = 298 ± 1 K for a typical etching time of 120 s and then thoroughly rinsed, sonicated and again rinsed with UHP water.

4.2.3 Electron Microscopy and Focused Ion Beam Characterization

Electron and ion imaging techniques were used to analyze the surface morphology and the 3D structure of the Ni-containing metallic foams. SEM characterization was performed using a Strata DB235 FESEM/FIB instrument operated at 5 kV equipped with an energy dispersive spectrometer (EDS) for elemental analysis (EDAX). FIB experiments were also conducted using a Micrion 2500 instrument (FEI Company). Samples were viewed at varying tilt angles adjusted by moving the SEM stage. A FIB instrument was used to mill and image cross-sections of the foams. This instrument employed a focused beam of Ga^+ ions to selectively etch regions of the sample and had the ability to mill with a precision of ca. 1 µm. It was also used to acquire images using secondary ion (SI) and secondary electron (SE) detection modes, which generate different topographical and chemical information. Specimens for the TEM analysis were extracted from the inner wall of the Ni foam with a dual beam FESEM/FIB instrument using an in-situ lift-out technique [19]. High resolution TEM and 3D electron tomography (ET) analyses were performed. These measurements were conducted using a Tecnai G2 F20 X-Twin TEM equipped with a Fischione™ high tilt holder, which allows for tilting of the specimen up to ± 80˚.

4.2.4 X-Ray Photoelectron Spectroscopy Characterization

XPS analysis was carried out using an Analytical Axis Ultra DLD spectrometer (Kratos) equipped with a monochromatic aluminum source (AlKα 1486.6 eV) operating at a power of 150 W (10 mA emission current and 15 kV voltage). The analysis was conducted on a 700 µm × 300 µm area of the sample. High resolution scans were obtained at a 50 meV step size with a dwell time of 500 ms per step, a pass energy of 20 eV, and averaged over 3 scans. The energy scale linearity was calibrated using Al and Mg X-ray sources through the analysis of Ar sputter-cleaned Au and Cu substrates (ISO 15472 procedure). The samples were mounted on the sample holder using a conductive copper tape (EMS). Compositional analysis with depth profiling of the samples was performed by ion etching with an Ar ion beam having energy of 4 kV for specific periods of time.

4.3 Results and Discusion

4.3.1 Electrochemical Characterization of Ni-Containing Foams

CV was used to examine the electrochemical properties of Ni-containing foams in aqueous alkaline electrolyte and to relate such acquired insight to their chemical composition and surface characteristics. A typical CV profile for bulk Ni in aqueous KOH or NaOH solution in the –0.20 to 1.60 V potential (*E*) range shows the following anodic features: (i) oxidation of metallic Ni to α-$Ni(OH)_2$ at $0.20 < E < 0.40$ V (eq 4.1); (ii) concurrent conversion of α-$Ni(OH)_2$ to β-$Ni(OH)_2$ (eq 4.2) and oxidation of metallic Ni to β-$Ni(OH)_2$ (eq. 4.3) at $0.50 < E < 1.30$ V; (iii) increase of the oxidation state of Ni from +2 to +3 through the oxidation of β-$Ni(OH)_2$ to β-NiOOH at $1.30 < E < 1.55$ V (eq 4.4); and (iv) oxygen evolution reaction (OER) at $E \geq 1.55$ V (eq 4.5) [20, 21].

$$Ni^0 + 2\,OH^- \longrightarrow \alpha\text{-}Ni(OH)_2 + 2\,e^- \tag{4.1}$$

$$\alpha\text{-}Ni(OH)_2 \longrightarrow \beta\text{-}Ni(OH)_2 \tag{4.2}$$

$$Ni^0 + 2\,OH^- \longrightarrow \beta\text{-}Ni(OH)_2 + 2\,e^- \tag{4.3}$$

$$\beta\text{-}Ni(OH)_2 + OH^- \longrightarrow \beta\text{-}NiOOH + H_2O + e^- \tag{4.4}$$

$$2\,OH^- \longrightarrow \tfrac{1}{2}\,O_2 + H_2O + 2\,e^- \tag{4.5}$$

A scan reversal at $E = 1.55$ V generates the following cathodic features: (v) reduction of β-NiOOH to β-$Ni(OH)_2$ at $1.10 < E < 1.40$ V (eq. 4.6) and (vi) hydrogen evolution reaction that gives rise to an appreciable current density at $E < -0.20$ V (eq. 4.7).

$$\beta\text{-NiOOH} + H_2O + e^- \longrightarrow \beta\text{-Ni(OH)}_2 + OH^- \tag{4.6}$$

$$H_2O + e^- \longrightarrow \tfrac{1}{2} H_2 + OH^- \tag{4.7}$$

In the case of metallic Ni being cycled at $-0.20 < E \leq 0.50$ V in addition to the anodic peak corresponding to the α-Ni(OH)$_2$ formation, there is also a cathodic peak at $-0.12 < E \leq 0.12$ V representing the reduction of α-Ni(OH)$_2$ to Ni^0 (eq 4.8).

$$\alpha\text{-Ni(OH)}_2 + 2\ e^- \longrightarrow Ni^0 + 2\ OH^- \tag{4.8}$$

The β phase of Ni(OH)$_2$ is the most stable and thermodynamically favored oxide of Ni; it is the passive layer that develops on the surface of metallic Ni upon contact with the ambient environment [21]. The conversion of α-Ni(OH)$_2$ to β-Ni(OH)$_2$ is irreversible and once it has taken place, the cathodic peak corresponding to the reduction of α-Ni(OH)$_2$ is not observed anymore [18]. The reduction of β-Ni(OH)$_2$ cannot be accomplished electrochemically and can be achieved at elevated temperatures in the presence of H_2(g). Alternative methods of preparing a metallic Ni surface involve the removal of the native oxide through chemical etching or mechanical polishing, but these are destructive approaches.

Figure 4.1 displays two overlaid CV profiles, one for Ni (red line) and the other for Inconel (black line) foams at $-0.15 < E < 1.60$ V in 0.50 M aqueous KOH solution obtained at $T = 298$ K and a potential scan rate of $s = 50$ mV s^{-1}. The anodic and cathodic peaks characteristic of α-Ni(OH)$_2$ formation and reduction are not observed because a layer of β-Ni(OH)$_2$ has

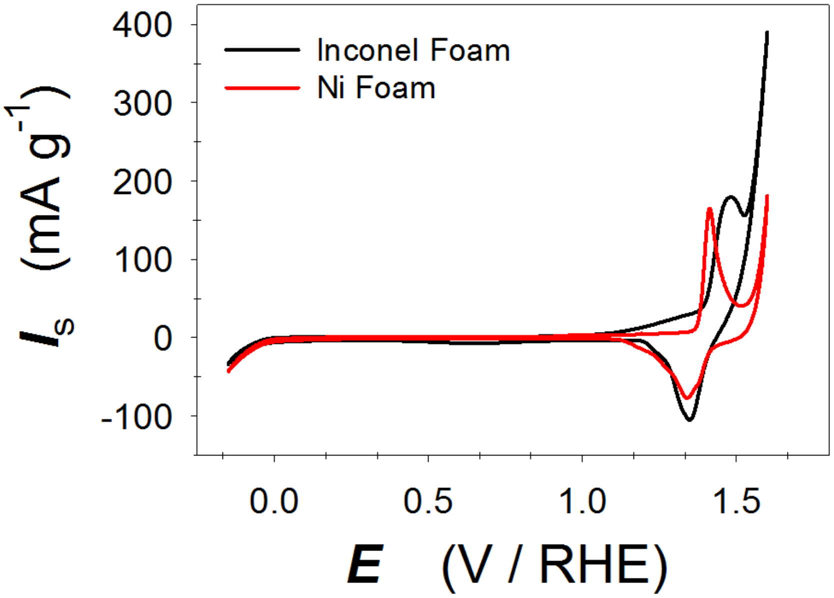

Figure 4.1. CV profiles of Ni and Inconel foams in 0.5 M aqueous KOH solution obtained at $T = 298$ K and $s = 50$ mV s^{-1} in the $-0.15 \leq E \leq 1.6$ V range. I_s is the specific current.

developed as the result of several prior CV scans. The most prevalent feature in these CV profiles is the formation and reduction of β-NiOOH and the specific current (I_s, where $I_s = I/m$ and its unit is A kg^{-1} or mA g^{-1}; I is the current and m is the sample mass) increase at $E > 1.50$ V due to the onset of OER. The CV profile for Ni foam displays the same features as those observed for bulk Ni in alkaline media [21]. The CV profile for Inconel foam reveals pronounced differences as compared to the CV profile for Ni foam, especially in the anodic scan. As it is concluded on the basis of spectroscopic measurements (see section 4.3.5. Spectroscopic Analysis of the Chemical Composition of Ni-Containing Foams), the surface of Inconel foam is rich in Ni and the broad anodic peak ($1.18 < E < 1.55$ V) with a shoulder at lower potentials corresponds mainly to the formation of β-NiOOH. Compared to the Ni foam, the peak is shifted towards higher potentials and overlaps the region of OER. The value of I_s for OER is greater than in the case of Ni foam; the specific current for the cathodic feature is greater than in the case of Ni foam but the difference is small. Nickel and Inconel foams have very different surface morphologies (see section 4.3.3. Surface Morphology of Ni-Containing Foams) and the rough, bubbly surface of Inconel foam gives rise to a larger surface area than Ni foam. Because the ratio I_s(Inconel) / I_s(Ni) ≤ 2 in the OER region and because the real surface area of the Inconel foam is much greater than that of the Ni foam, the results suggest that the Inconel foam is less active towards OER than the Ni foam. The cathodic scans reveal only one, asymmetric peak (reduction of β-NiOOH to β-$Ni(OH)_2$ (eq 4.6)) for both foams and their peak potentials and specific currents are comparable. Integration of the cathodic peaks demonstrates that the specific charge (Q_s, where $Q_s = Q / m$ in C kg^{-1} or mC g^{-1}; Q is the peak charge and m is the sample mass) is 592 mC g^{-1} for the Ni foam and 816 mC g^{-1} for the Inconel foam. The charges under the two cathodic peaks are similar, thus indicating that both samples have similar amounts of β-NiOOH on the surface. Bearing in mind that the difference in Q_s values for Ni and Inconel foams is less than 40% and that Inconel foam has a significantly larger real surface area, we conclude that β-NiOOH does not make up the entire surface of Inconel foam. This behavior is expected because Inconel foams contain other elements within the surface region (see section 4.3.5 Spectroscopic Analysis of the Chemical Composition of Ni-Containing Foams).

Inconel foam is a multi-component material made from Ni, Cr, Mo, Fe, Nb and Ta (Table 4.1). Constituent elements such as Cr and Fe display their own electrochemical behavior in alkaline media, thus the CV profile for Inconel foam cannot be interpreted by considering only the behavior of Ni. Chromium is well known to segregate to the surface region and to form chemically stable, passive oxide layers, which are not reduced in the cathodic scan [22 – 24]. Marioli and Soreno compared the electrochemical formation of surface oxides on pure Ni and on Ni-Cr alloy (80%-20%) and observed a larger CV feature in the anodic scan than in the cathodic one for the Ni-Cr alloy [24]. The electrochemical behaviour of Inconel foams gives rise to CV features characteristic of an alloy containing Ni and Cr.

4.3.2 Electrochemically Active Surface Areas of Ni-Containing Foams

Knowledge of the electrochemically active surface area (A_{ecsa}) is important because it specifies the actual surface being in contact with electrolyte and where electron transfer can take place. In the case of Ni materials, estimates of A_{ecsa} and the specific surface area (A_{s}, where $A_{\mathrm{s}} = A_{\mathrm{ecsa}} / m$ in $\mathrm{cm}^2\ \mathrm{g}^{-1}$) utilize the charge ($Q$) of the CV peak corresponding to α-$\mathrm{Ni(OH)_2}$ formation [18]. The electrochemically active surface area is then determined using eq. 4.9:

$$Q = \left(q_{\mathrm{Ni(OH)2}} \times A_{\mathrm{ecsa}}\right) + \left(C_{\mathrm{dl}} \times A_{\mathrm{ecsa}} \times \Delta E\right) \tag{4.9}$$

where $q\mathrm{Ni(OH)_2}$ is the charge density associated with the formation of 1 monolayer (ML) of α-$\mathrm{Ni(OH)_2}$ and equals 514 $\mu\mathrm{C\ cm^{-2}}$, C_{dl} is the double layer capacitance and equals 20 $\mu\mathrm{F\ cm^{-2}}$, and ΔE is the CV peak potential range [25 – 27]. This approach was adopted to determine A_{ecsa} of four Ni foams having different densities. In order to determine A_{ecsa} of each foam, it was first necessary to chemically etch the samples to prepare a metallic surface, which was then oxidized to α-$\mathrm{Ni(OH)_2}$. Details of the etching procedure are discussed in a subsequent section (see section

4.3.6 Surface Modification of Ni-Containing Foams through Chemical Etching), but it is important to specify that a fresh etching solution was used for each foam and the etching time was 120 s. Such determined A_{ecsa} values were then used to calculate A_s for each foam.

The manufacturer's material specifications list the Ni foam density in g m^{-2} (Table 4.1); the thickness of the Ni foam sheet is 2.0 mm [12]. Thus, these numbers are converted to bulk density (ρ) values in g cm^{-3} (Table 4.1). Figure 4.2 A presents a graph of A_s as a function of ρ, and reveals that A_s decreases as ρ increases. This trend seems counterintuitive because an increase in mass is expected to enhance the foam surface area, however the SEM images for three Ni foams of different densities (Figure 4.2 B, C, and D) show that their pores are identical in size and the amount of pore space is the same. This behavior is anticipated because the same

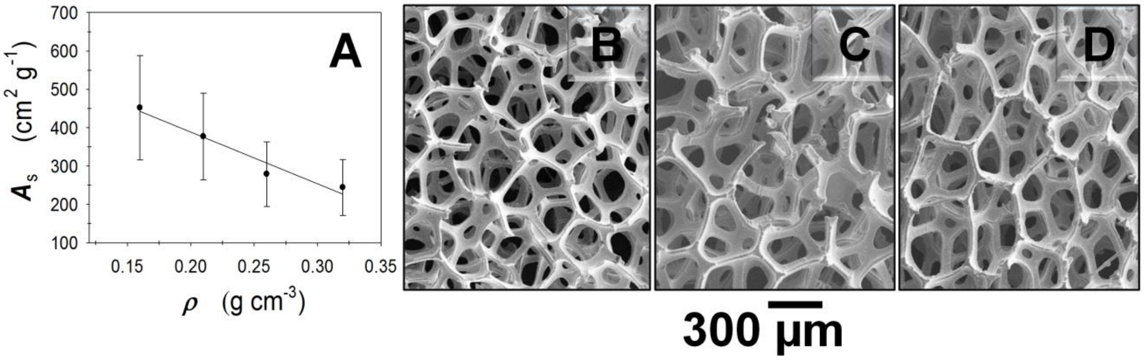

Figure 4.2. Relationship between the specific surface area (A_s) of etched Ni foams and the bulk density (ρ) of the foam (A). SEM images at a magnification of 125× for Ni foams with various bulk densities: (B) ρ = 0.16 g cm^{-3}; (C) ρ = 0.21 g cm^{-3}; and (D) ρ = 0.32 g cm^{-3} .

polyurethane substrate is used to manufacture foams of various densities. The density increase is accomplished by thickening the Ni struts, which results in an overall increase in mass without altering other characteristics. Table 4.1 displays the mean value of the strut wall thickness as determined on the basis of FIB cross-section measurements; three FIB cross-sections were milled for each type of foam and the thickness of the strut wall was measured at 5 locations on each cross-section for a total of 15 measurements. The average strut wall thickness increases from ca. 2 μm for the least dense foam to ca. 5 μm for the densest foam. Therefore, the A_{ecsa} values for the various foams are comparable but their masses gradually increase resulting in a decrease of A_{s}. The ability to control the density of Ni foams without changing A_{ecsa} is of importance to applications that require very robust materials (e.g. electrodes for large-scale electrolysis). The A_{ecsa} values (Figure 4.2 A) are subject to large uncertainty that has several origins which are discussed elsewhere [18]. An important source of error stems from the difficulty to maintain identical fabrication conditions when manufacturing hundreds of square meters of Ni foam in a continuous process [12]. As a result, there are some inherent differences in the thickness of struts and the thickness of native Ni oxide from batch to batch. A thorough discussion of different etching solutions and their impact on the 3-D structure of Ni foams and A_{ecsa} is reported in a recent paper from this research group [18].

4.3.3 Surface Morphology of Ni-Containing Foams

Figure 4.3 shows SEM images of Ni, Inconel, and FE2 foams at two levels of magnification. The images in the left-hand column (scale bars of 200 μm) are suitable for evaluating their overall structure and the images in the right-hand column (scale bars of 20 μm) reveal details of the surface morphology. It is apparent that all of the foams have the same general structure, which resembles a 3D network of roughly pentagonal macroscopic pores and struts ranging in width from 25 to 80 µm. The struts have a concave, triangular shape that is an exact cast of the polyurethane substrate upon which Ni is deposited. Table 4.1 summarizes the main structural properties of the foams determined from SEM and FIB measurements. The higher magnification images reveal differences in the surface morphology between Ni and multi-component foams (Inconel and FE2). The surface of Ni foam is smooth with some visible grains and grain boundaries. The surface morphology of Inconel and FE2 foams reveals rough and bubbly surfaces; they have a rougher surface because they are manufactured by binding and annealing metallic powders to a Ni foam substrate. Even after high temperature annealing, the metallic powder particles still retained some of their initial shape. The rough, bubbly surfaces of Inconel and FE2 foams give rise to the large A_{ecsa} reported above.

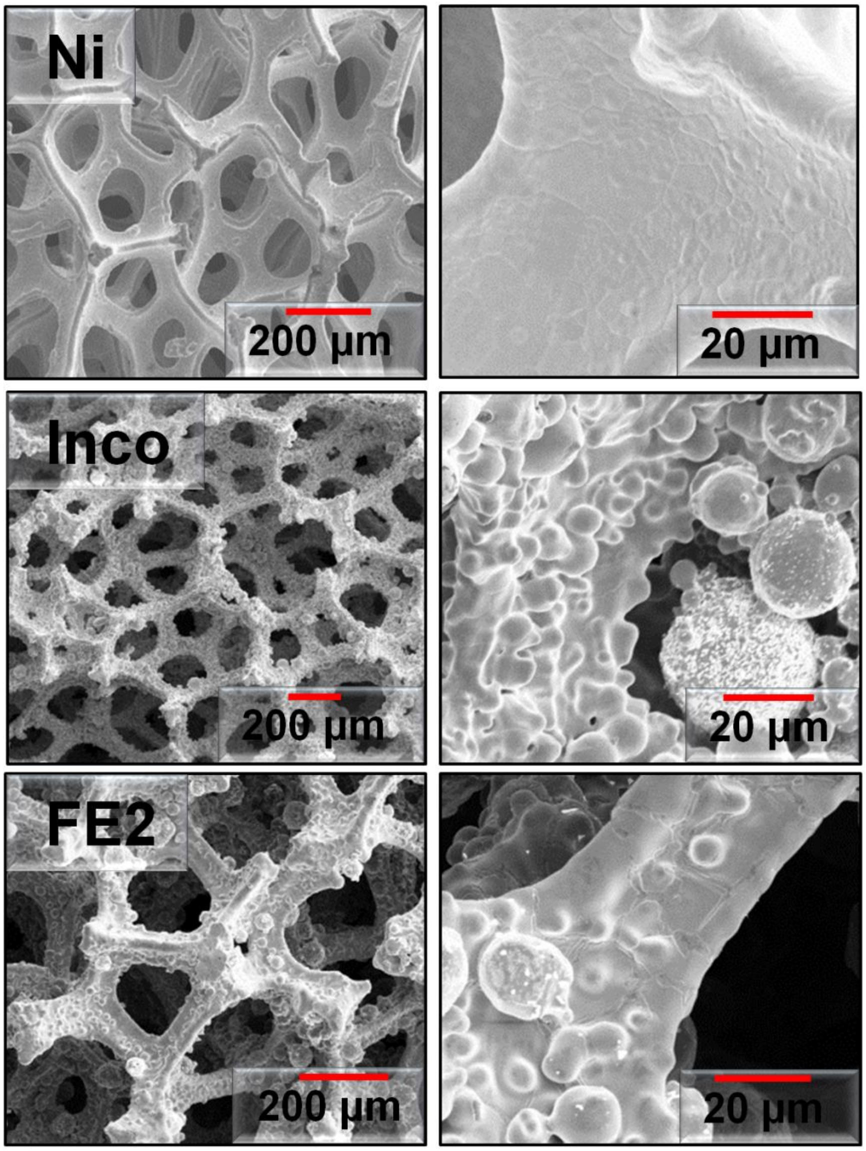

Figure 4.3. SEM images of Ni, Inconel, and FE2 foams at two levels of magnification showing the porosity of the foams (left column) and their surface morphology (right column).

4.3.4 Structural Characterization of Ni-Containing Foams

The manufacturing process used to fabricate Ni foams leaves a porous metallic material that mimics the structure of the polyurethane foam substrate. The individual macroscopic metallic struts have a 3D structure encompassing the cavity left behind by the polymer. Figure 4.4 shows three FIB images for Ni foams at various stages of preparation. Image A presents the polyurethane substrate with a very thin layer of Ni prepared by CVD. The Ni deposit is uniform

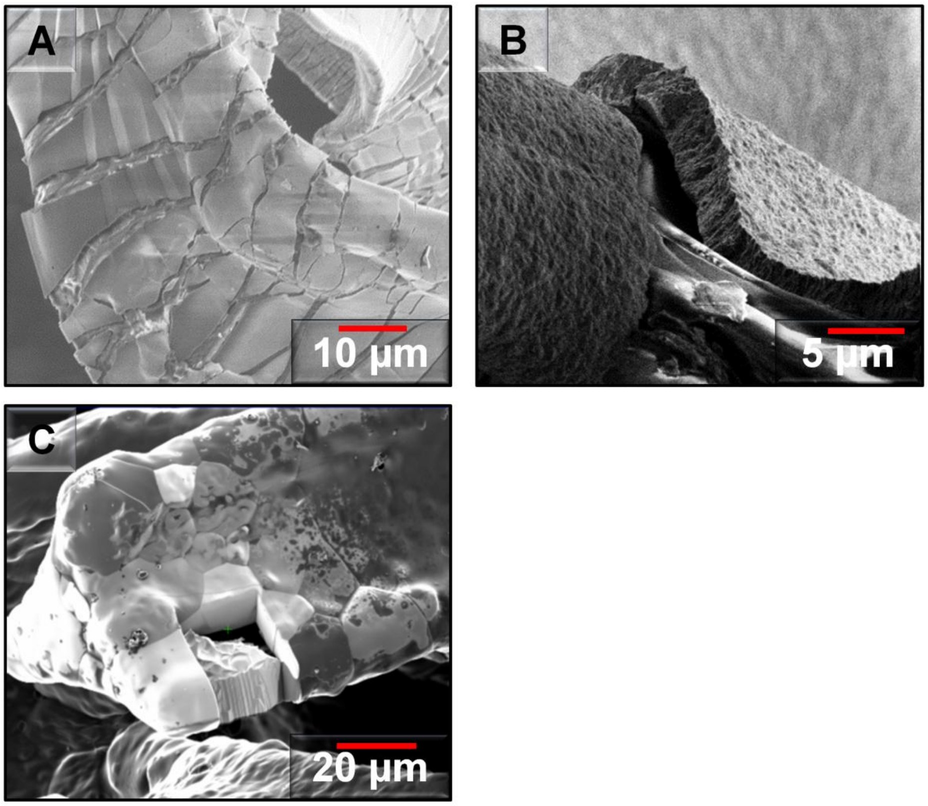

Figure 4.4. FIB images of Ni foam at various stages of fabrication: (A) polyurethane substrate with a thin layer of PVD Ni; (B) polyurethane substrate with a thick layer of PVD Ni before sintering; and (C) sintered Ni foam.

but reveals cracks; the latter develop during handling because the polyurethane foam with a thin layer of Ni is flexible. Image B shows a thick layer of Ni deposit on polyurethane foam prior to the sintering and annealing step. There is a crack in the thick Ni deposit and one of its sections is lifted showing the polyurethane substrate. The Ni deposit is porous and most likely polycrystalline with a small grain size because FIB images do not reveal any grain structure. Image C shows Ni foam after sintering and burnout. A section of the foam was milled out using a focused beam of Ga^+ ions. The rectangular, milled section exposes a hollow cavity, which once housed the polyurethane template. The Ni deposit looks very different in image C as compared to image B, and shows well-defined grains that are clearly visible because they have different crystallographic orientations with respect to the Ga^+ ion beam. We conclude that the sintering transforms the porous, fine-grained Ni deposit through thermal grain growth.

FIB was used to ion-mill cross-section from struts of Ni and Inconel foams in order to examine their inner structure. These cross-sections were used to estimate the thickness of the Ni strut walls for each foam density and to measure the grain size; these parameters are summarized in Table 4.1. Figure 4.5 shows four FIB images of cross-sections from Ni (images A and B) and Inconel (images C and D) foams. In image B, three features are labeled 1 through 3; 1 corresponds to the hollow cavity within the struts; 2 corresponds to an inner porous Ni layer at the interface between the cavity and the Ni strut; and 3 corresponds to a boundary between two metallic grains having different crystallographic orientations. It is much easier to detect the inner, porous layer using ion beam imaging than by SEM, because these two techniques employ different imaging modes. Images C and D demonstrate that Inconel foam has significantly thicker strut walls and that their thickness is less uniform. The fabrication of multi-component foams (e.g. Inconel, FE2) begins with pure Ni foams on which multi-component metallic powders are placed using a binding agent and subsequently annealed, thus, it is no surprise that the inner cavity of Inconel foam has similar structural characteristics to those of Ni foam.

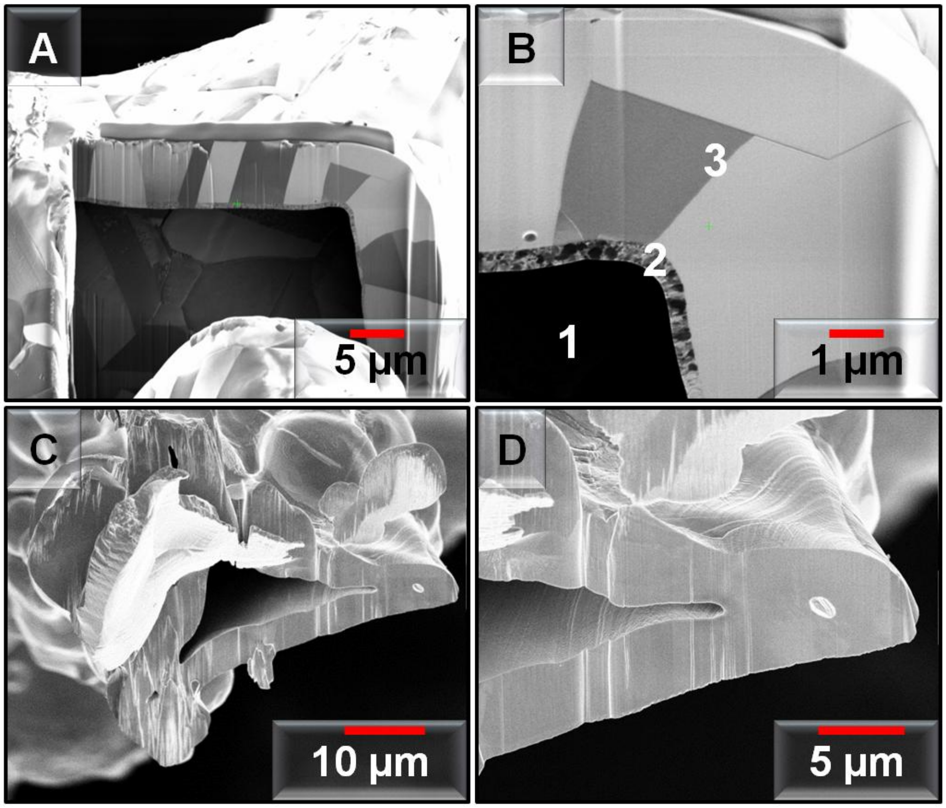

Figure 4.5. FIB images of cross-sections of Ni foam (A and B) and Inconel foam (C and D).

The inner, porous wall observed in Ni foams was further investigated using TEM and ET. These measurements were performed on a small section of Ni foam removed from the inner wall of a strut. A FIB instrument was used to prepare the TEM lamella having dimensions ca. 20 µm × 10 µm × 100 nm that was then placed on a specialized tilt manipulator for TEM and ET experiments. A TEM image of the inner, porous wall is shown in the top image of Figure 4.6; the bottom image shows a 3D ET reconstruction of the inner, porous wall as generated by collecting, aligning, and combining a series of TEM micrographs at various tilt angles. The two images clearly reveal a polycrystalline and granular nanostructure. Combined SEM, TEM and ET results show that the material has three levels of structure and two levels of porosity. The inner nanostructure reported for the first time in this study is not accessible to electrolyte with the exception of very small sections that are present near the natural cracks in the Ni foam structure. However, its discovery suggests that future modification of the fabrication process may be applied to create struts that are entirely nanostructured and possess significantly larger A_s and A_{ecsa}.

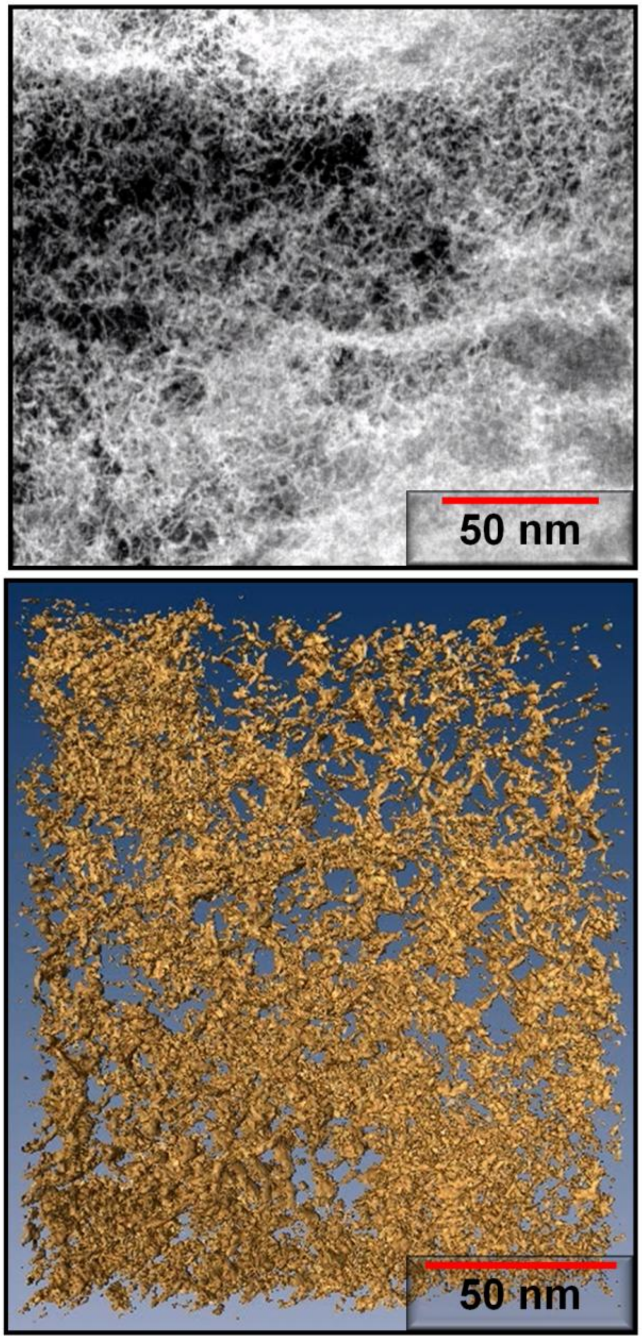

Figure 4.6. TEM image (top) and ET 3D reconstruction (bottom) of the inner, porous structure present within the struts of Ni foam.

4.3.5 Spectroscopic Analysis of the Chemical Composition of Ni-Containing Foams

XPS and EDS were employed to study the chemical composition of Ni and Inconel foams. XPS analysis coupled with Ar^+ ion sputtering was used to provide surface and near-surface chemical composition of these foams at different stages of ion etching. The spectroscopic signal obtained from XPS measurements corresponds to an analysis area of 700 μm × 300 μm. EDS analysis of an area measuring 10 μm × 10 μm or 20 μm × 20 μm provides information about bulk chemical composition because the signal is generated within 2 μm from the outer surface. Thus, by employing EDS we probed between 25% and 100% of the struts' depth because their thickness ranges from 2 to 8 μm.

Figure 4.7 presents the EDS spectrum collected from a 10 μm × 10 μm area of a Ni foam strut. Only C, O and Ni are detected; the C and O peaks are small as compared to the Ni peak and are due to the sample transfer via air. The O signal is also present as part of the native surface oxide, β-$Ni(OH)_2$.

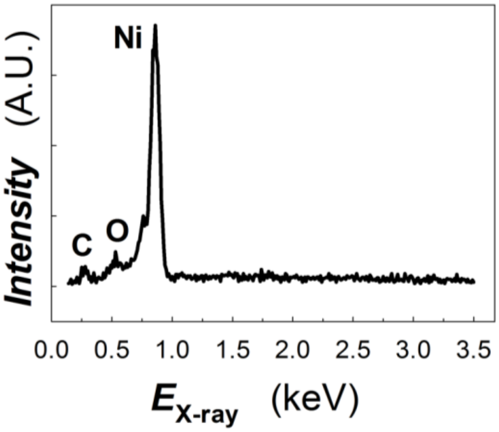

Figure 4.7. EDS spectrum collected from a 10 μm × 10 μm area of a Ni foam strut.

Figure 4.8 presents four XPS survey spectra for Ni foam, which underwent Ar^+ ion etching for various lengths of time ($t_{\text{Ar-etch}}$) in the 0 to 80 s range: (spectrum A) $t_{\text{Ar-etch}}$ = 0 s; (spectrum B) $t_{\text{Ar-etch}}$ = 20 s; (spectrum C) $t_{\text{Ar-etch}}$ = 40 s; and (spectrum D) $t_{\text{Ar-etch}}$ = 80 s. The XPS spectra display peaks that are assigned to the following binding energy (*BE*) values: C(1s) at 284.7 eV; O(1s) at 531.6 eV; Ni($2p_{1/2}$) and Ni($2p_{3/2}$) at 874.2 eV and at 856.3 eV; Ni(3p) at 66.1 eV; one Ni(Auger) peak at 497.0 eV; and several Ni(Auger) peaks in the 800 – 600 eV range. In the spectrum for $t_{\text{Ar-etch}}$ = 0 s, the O(1s) and C(1s) peaks are more prevalent than after Ar^+ ion etching because C is a surface contaminant and O originates not only from the native β-$Ni(OH)_2$ layer but also from adsorbed H_2O. The intensity of Ni($2p_{1/2}$) and Ni($2p_{3/2}$) peaks increases appreciably after the first 20 s of Ar^+ ion etching (spectrum B). The Ni, O, and C XPS signals were studied in detail using high resolution XPS (HRXPS) throughout Ar^+ ion depth profiling.

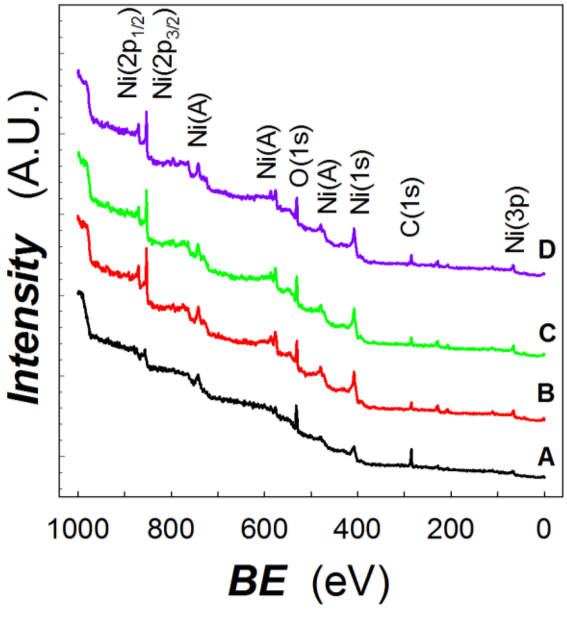

Figure 4.8. XPS survey spectra of Ni foam exposed to Ar^+ ion etching for various lengths of time: (A) $t_{\text{Ar-etch}}$ = 0s; (B) $t_{\text{Ar-etch}}$ = 20s; (C) $t_{\text{Ar-etch}}$ = 40s; and (D) $t_{\text{Ar-etch}}$ = 80s.

Figure 4.9 shows HRXPS spectra for the Ni($2p_{3/2}$) and Ni($2p_{1/2}$), O(1s), and C(1s) bands for $t_{\text{Ar-etch}}$ = 0, 20, 40, 80, 160 and 320 s, respectively. The HRXPS signals for Ni($2p_{1/2}$) and Ni($2p_{3/2}$) increase steadily as $t_{\text{Ar-etch}}$ is extended. The Ni($2p_{3/2}$) peak contains contributions from both the Ni(0) and the Ni(2+) oxidation states. The contribution from Ni(0) is observed at a binding energy of *BE* = 852.7 eV, with a satellite peak at *BE* = 857 – 858 eV. The contribution from Ni(2+) is present at *BE* = 855 – 856 eV, with a satellite peak at *BE* = 861 eV [18, 22, 28]. In spectrum A, the small Ni($2p_{3/2}$) peak at *BE* = 856 eV indicates that mostly the Ni(2+) oxidation state is present. As Ar^+ ion etching proceeds for 20 and 40 s, the Ni($2p_{3/2}$) signal at *BE* = 856 eV increases because H_2O and CO_2 become desorbed from the Ni foam surface. As the Ar^+ ion etching continues for 80, 160 and 320 s, the Ni($2p_{3/2}$) peak continues to grow, but also shifts towards lower *BE* values until it reaches a value of *BE* = 853 eV. This shift in *BE* indicates that the contribution of Ni(0) increases relative to the contribution of Ni(2+) because the native surface oxide is removed. The conversion of $t_{\text{Ar-etch}}$ to the thickness of the sputtered material is not straightforward for porous materials. Argon ion bombardment erodes polycrystalline bulk Ni with a rate of 13 nm min^{-1}, when a potential of 10 kV is applied [29]. If the sputter rate of 13 nm min^{-1} were employed to the native oxide layer on Ni foams, then $t_{\text{Ar-etch}}$ = 320 s would correspond to the erosion of about 70 nm of the material. In our case, Ar^+ ion bombardment is accomplished by applying a voltage of 3 kV when sputtering Ni foams and 4 kV when sputtering Inconel foams. Because the application of a lower voltage reduces the erosion rate, we conclude that the thickness of the removed native oxide does not exceed 70 nm and is most likely significantly lower. Because the Ni-containing foams are not flat, the Ar^+ ion beam reaches different parts of the 3D structure at different angles of incidence and gives rise to different sputter rates. Inner portions of the foams are blocked from the Ar^+ ions (shadow effect) and remain covered with the native oxide. Due to the porous nature of Ni-containing foams and the above-mentioned limitations, the thickness of the native oxide layer was not obtained from the Ar^+ ion etching and XPS analysis and only an estimate is provided.

Figure 4.9 presents HRXPS spectra for the O(1s) band as a function of $t_{\text{Ar-etch}}$. The O(1s) band at BE = 528 – 534 eV has contributions from O in different chemical environments; O in the form of H_2O gives rise to a peak at BE = 533 eV, O from $Ni(OH)_2$ at BE = 531.5 eV, and O from NiO at BE = 529.5 eV [22, 28]. The O(1s) band shifts towards lower BE values as the duration of Ar^+ ion etching progresses. The broad peak in spectrum A at BE = 532 eV is assigned to H_2O and $Ni(OH)_2$, and the small shoulder at BE = 529.5 eV to NiO. Spectra B, C, and D display two overlapping peaks with maxima at BE = 531.8 eV and BE = 529.8 eV, respectively; the first peak is assigned to $Ni(OH)_2$ and the other to NiO. The intensity of the O(1s) peak in spectrum E (for $t_{\text{Ar-etch}}$ = 160 s) is significantly lower indicating that a majority of H_2O, $Ni(OH)_2$ and NiO is removed from the surface.

Figure 4.9 also presents a HRXPS spectrum for the C(1s) peak at BE = 284.7 eV for different $t_{\text{Ar-etch}}$ values. The HRXPS spectra display a decrease in the intensity of the C(1s) peak because Ar^+ ions clean the surface; however, even after 80 s of Ar^+ ion etching (spectra D) there is still a detectable C(1s) signal. Because Ni-containing foams are porous materials, it is conceivable that some of the carbon detected by XPS originates from inner struts that are not etched with Ar^+ ions.

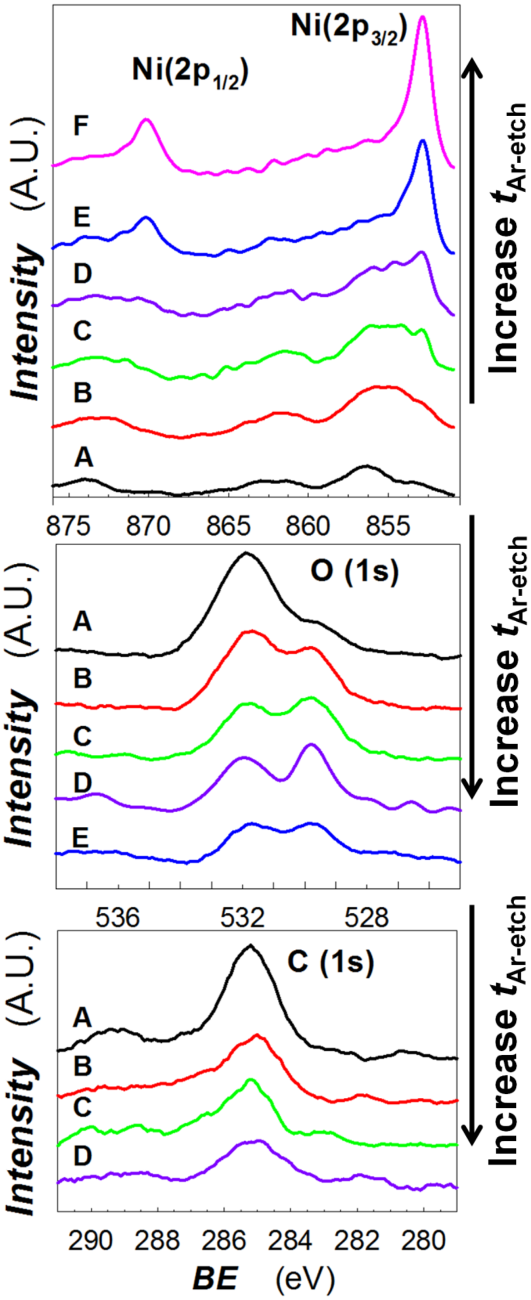

Figure 4.9. HRXPS spectra of the Ni(2p$_{1/2}$), Ni(2p$_{3/2}$), O(1s), and C(1s) bands for Ni foam exposed to Ar$^+$ ion etching for various lengths of time: (A) $t_{\text{Ar-etch}}$ = 0 s; (B) $t_{\text{Ar-etch}}$ = 20 s; (C) $t_{\text{Ar-etch}}$ = 40 s; (D) $t_{\text{Ar-etch}}$ = 80 s; (E) $t_{\text{Ar-etch}}$ = 160 s; and (F) $t_{\text{Ar-etch}}$ = 320 s.

It is important to discuss some possible experimental limitations that are unique to the analysis of micro and nano-structured materials. The design of a surface analysis instrument is such that an X-ray gun, an electron energy analyzer and an Ar^+ ion gun are permanently mounted at different angles to each other and to the sample. In the case of a flat sample, the focal point of the three devices is the same and the emitted photoelectrons originate from a very thin surface region (1-2 nm). When the sample is irregular and has extended 3D structure, the geometry of the three devices is not ideally optimized anymore and slightly different sections of the sample are analyzed and sputtered. The porous nature of the material explains why the O(1s) and C(1s) peaks are observed even after prolonged Ar^+ ion etching.

Surface chemical analysis of Inconel foam is more complicated than that of Ni foam because Inconel foam has several constituents, and each of them can be either in a metallic state or present as a compound. We employed EDS and XPS to examine the bulk and surface chemical composition of Inconel foam. Figure 4.10 shows an SEM image of Inconel foam and two EDS spectra from regions having different morphologies. The white box corresponds to a typical strut having a bubbly but smooth surface and the red box corresponds to a sphere of material attached to a strut; the sphere has characteristic small bright flecks. In general, areas which appear bright in an SEM image correspond to heavy materials that scatter more electrons. Because the bright flecks appear only in certain regions, the SEM images indicate that either the heavy elements never mixed with other constituents or that the heavy elements underwent segregation during the fabrication process. Thus, we may conclude that the composition of

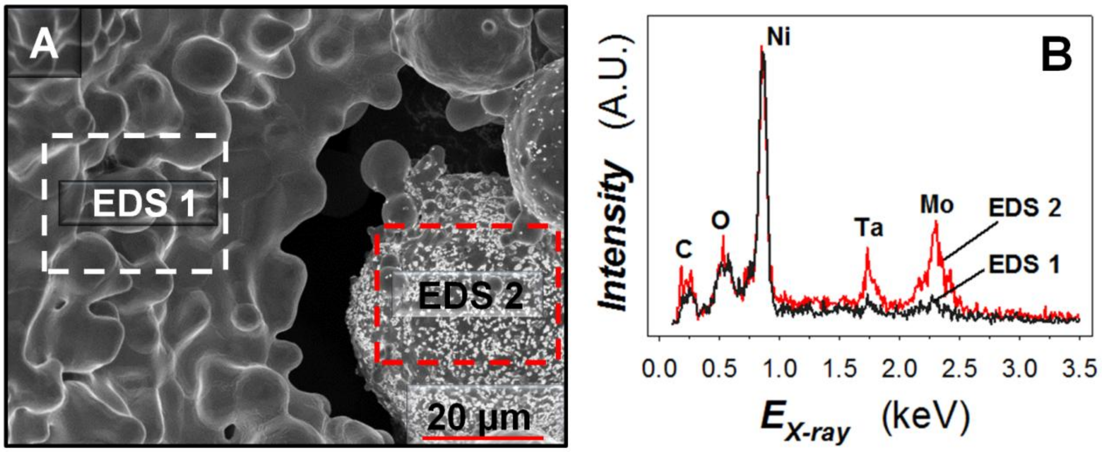

Figure 4.10. SEM image of Inconel foam (A) and EDS spectra (B) corresponding to two areas designated in the SEM image.

Inconel foam is heterogeneous. The EDS spectra collected from the strut and the sphere demonstrate that the latter is enriched in Ta and Mo; these two constituents of Inconel are barely observed in the spectrum collected from the strut. Precipitation of intermetallic phases occurs when Inconel alloys are subjected to heat treatment in the 800 – 1000 K temperature range. Two of the phases formed in these conditions are the γ″-phase [Ni_3(Nb, Al, Ti)] and the δ-phase [Ni_3(Nb, Mo)] [32]. During the fabrication of Ni-based metallic foams there is a sintering step that involves exposing the foams to temperatures up to 1300 K. It is likely that the elevated temperature during sintering results in the precipitation of phases similar to the γ″-phase and δ-phase within the microstructure of Inconel foams.

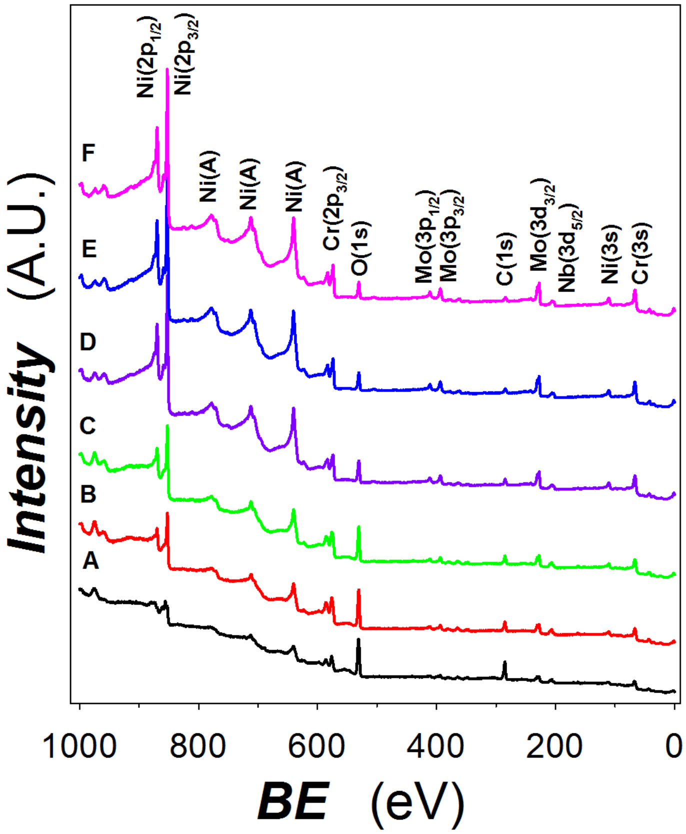

Figure 4.11. XPS survey spectra of Inconel foam exposed to Ar^+ ion etching for various lengths of time: (A) $t_{\text{Ar-etch}}$ = 0 s; (B) $t_{\text{Ar-etch}}$ = 5 s; (C) $t_{\text{Ar-etch}}$ = 10 s; (D) $t_{\text{Ar-etch}}$ = 30 s; (E) $t_{\text{Ar-etch}}$ = 70 s; and (F) $t_{\text{Ar-etch}}$ = 100 s.

XPS and Ar^+ ion depth profiling were employed to analyze the surface and near-surface chemical composition of Inconel foam. Figure 4.11 presents six XPS survey spectra for various Ar^+ ion etching times in the 0 to 100 s range: (spectrum A) $t_{\text{Ar-etch}} = 0$ s; (spectrum B) $t_{\text{Ar-etch}} = 5$ s; (spectrum C) $t_{\text{Ar-etch}} = 10$ s; (spectrum D) $t_{\text{Ar-etch}} = 30$ s; (spectrum E) $t_{\text{Ar-etch}} = 70$ s; and (spectrum F) $t_{\text{Ar-etch}} = 100$ s. They display peaks that are assigned as follows: C(1s) at 284.7 eV; O(1s) at 531.6 eV; Ni($2p_{1/2}$) and Ni($2p_{3/2}$) at 874.2 eV and at 856.3 eV; Ni(3s) at 110.5 eV; Cr($2p_{1/2}$) and Cr($2p_{3/2}$) at 583.4 and 574.2 eV; Cr(3s) at 68.1 eV; Mo($3p_{1/2}$) and Mo($3p_{3/2}$) at 410.6 and 394.8 eV; Mo($3d_{3/2}$) at 228.4 eV; Nb($3d_{5/2}$) at 204.4 eV; and several Ni(Auger) peaks in the 800 – 600 eV range. Iron is a component of Inconel and as such should be detected using XPS. However, the Fe(2s) band at 845 eV falls very near the Ni($2p_{3/2}$) band and the Fe($2p_{3/2}$) band at 707 eV overlaps one of the Ni(Auger) peaks; thus, there is no compelling evidence for its presence or absence on the basis of XPS measurements. Cobalt and tantalum are also as components of Inconel; however, there is no XPS evidence for the presence of these elements. We cannot confirm that Co is absent because its XPS peaks overlap with Ni(Auger) peaks. As in the case of Ni foam, the spectrum for $t_{\text{Ar-etch}} = 0$ s (spectrum A) reveals O(1s) and C(1s) peaks that are more prevalent than after Ar^+ ion etching (spectra B through F) because C is a surface contaminant and O originates from several surface oxides and adsorbed H_2O. The intensity of the peaks corresponding to Ni, Cr, Mo, and Nb increases appreciably after 30 seconds of Ar^+ ion etching and then levels off. HRXPS spectra were collected for the Ni($2p_{3/2}$), Cr($2p_{1/2}$) and Cr($2p_{3/2}$) bands for each $t_{\text{Ar-etch}}$ and are presented in Figure 4.12; the spectra A through F refer to the same $t_{\text{Ar-ion}}$ values as in Figure 4.11. The intensity of Ni($2p_{3/2}$) peak increases within the initial 30 s of Ar^+ ion etching and then levels off. Unlike in the case of Ni foam, there is practically no change in *BE* of the Ni($2p_{3/2}$) peak brought about by the Ar^+ ion etching. In spectrum A, the peak centers at

BE = 852.7 eV and in spectrum F at *BE* = 853.1 eV; thus, the entire peak shift is less than 0.5 eV. The binding energy of the Ni($2p_{3/2}$) peak is very close to the characteristic value for metallic Ni, i.e. *BE* = 853.5 eV. Metallic Ni is also expected to yield a peak at *BE* = 859 eV. This feature is observed in spectra D, E and F, but not in spectra A through C. Spectrum A shows a small peak at *BE* = 856 eV that is characteristic of Ni(2+), but disappears already after 5 s of Ar^+ ion etching. On the basis of HRXPS measurements, we may conclude that Ni within Inconel foam is present mostly as Ni(0) with a small amount of Ni(2+) on the foam surface.

High resolution spectra of the Cr($2p_{1/2}$) and Cr($2p_{3/2}$) bands are shown in Figure 4.12. The Cr($2p_{3/2}$) band appears as two overlapping peaks with *BE* = 576.9 and *BE* = 574.0 eV corresponding to Cr(3+) in the form of Cr_2O_3 and Cr(0), respectively. The Cr($2p_{1/2}$) band also appears as two overlapping peaks with *BE* = 586.4 and *BE* = 583.4 eV that also correspond to Cr(3+) and Cr(0) [22, 30, 31]. The intensity of the Cr(3+) peaks decreases and that of Cr(0) increases as Ar^+ ion etching progresses. This evolution of XPS spectra is attributed to the removal of Cr_2O_3, which forms naturally on metallic Cr upon its contact with the ambient. The presence of Cr_2O_3 on the surface of Inconel foam is important because Cr-rich metallic alloys are known to offer corrosion resistance. Chromium is also known to form $Cr(OH)_3$ as a surface compound giving rise to an XPS peak at *BE* = 578 eV [22, 31]. Contributions from Cr_2O_3 and $Cr(OH)_3$ to the XPS spectra cannot be separated only on the basis of Cr($2p_{3/2}$) band measurements because their respective peaks overlap. However, we may conclude that Cr within Inconel foam is present mostly as Cr(3+) with a small amount of Cr(0) on the foam surface.

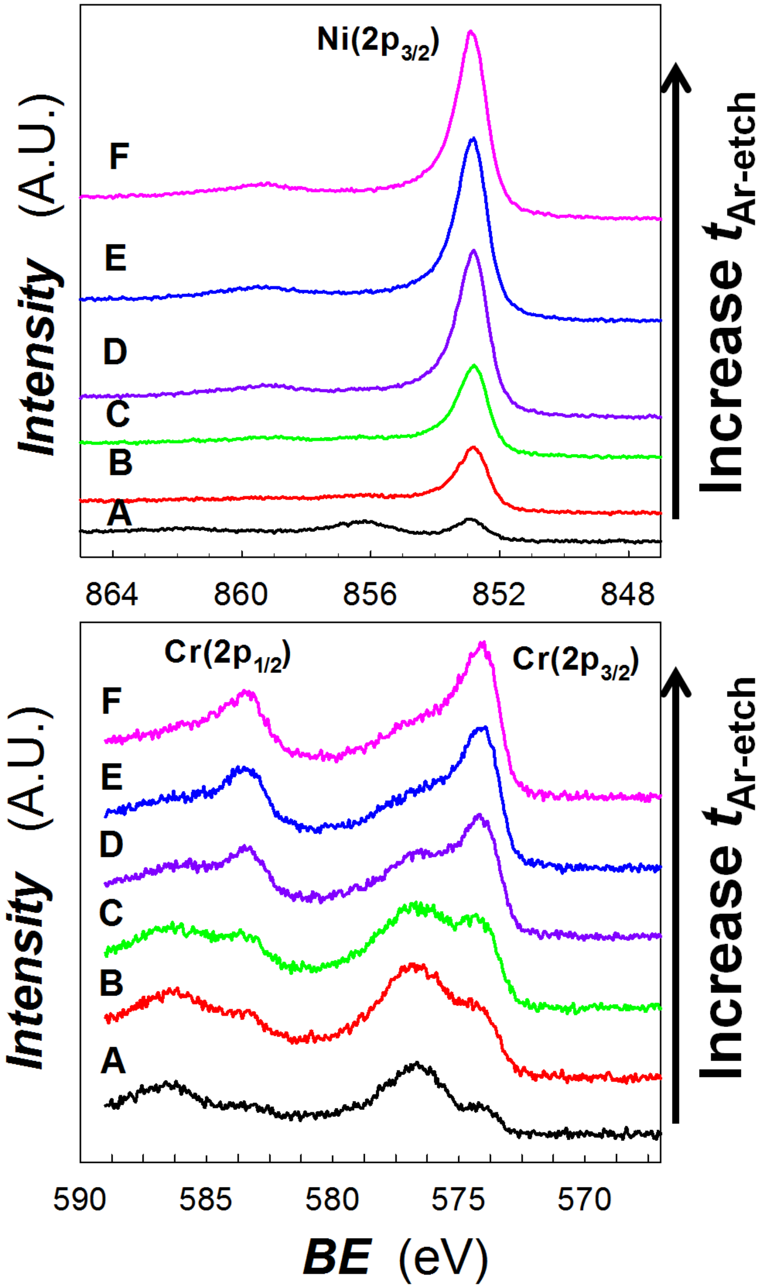

Figure 4.12. HRXPS spectra of the Ni($2p_{3/2}$), Cr($2p_{1/2}$), and Cr($2p_{3/2}$) bands for Inconel foam exposed to Ar^+ etching for various lengths of time: (A) $t_{Ar\text{-}etch}$ = 0 s; (B) $t_{Ar\text{-}etch}$ = 5 s; (C) $t_{Ar\text{-}etch}$ = 10 s; (D) $t_{Ar\text{-}etch}$ = 30 s; (E) $t_{Ar\text{-}etch}$ = 70 s; and (F) $t_{Ar\text{-}etch}$ = 100 s.

4.3.6 Surface Modification of Ni-Containing Foams through Chemical Etching

Chemical etching was applied to remove β-$Ni(OH)_2$ from the surface of Ni foam without altering its 3D structure [18]. For bulk Ni materials, typical methods of removing β-$Ni(OH)_2$ are polishing, sand-blasting, ion etching, and chemical etching. Mechanical methods are not applicable to micro-structured and porous materials because the structure will be deformed. A reliable chemical etching procedure for removing β-$Ni(OH)_2$ from Ni foam with minimal alteration to the micro-structure is described elsewhere [18,33]. The SEM images in Figure 4.13 show that chemical etching results in roughening of the surface of the Ni foam struts and occurs preferentially at grain boundaries. The images also reveal that chemical etching for short periods of time does not cause any damage to the material and preserves its unique micro-structure.

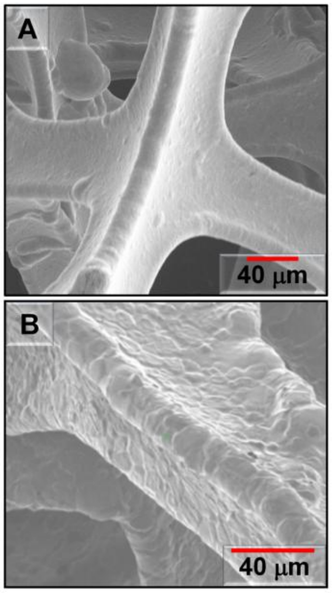

Figure 4.13. SEM images of Ni foam before (A) and after (B) chemical etching for t_{etch} = 120 s at T = 298 K.

Figure 4.14 presents a series of CV profiles collected in the α-$Ni(OH)_2$ potential region ($-0.15 \le E \le 0.55$ V) at $T = 298$ K and $s = 100$ mV s^{-1} for the same electrode that was etched in intervals for a total $t_{etch} = 235$ s. The experimental procedure was as follows: (i) the first chemical etching was performed for $t_{etch} = 130$ s and a CV profile was recorded; (ii) the second etching was

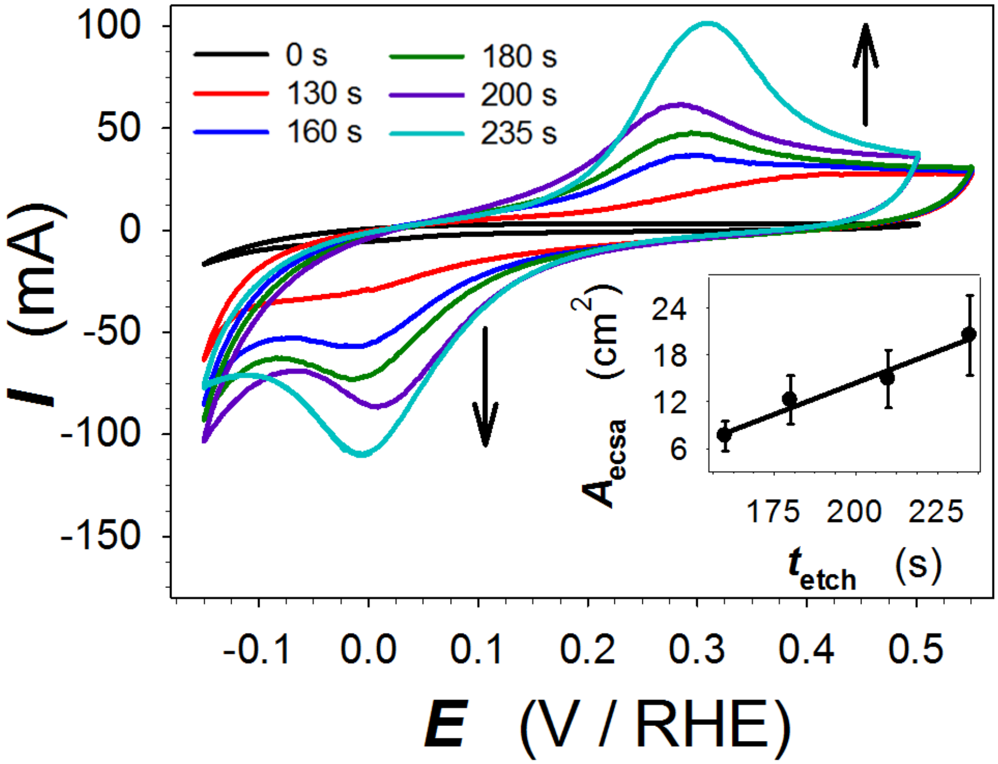

Figure 4.14. CV profiles for a Ni foam electrode at various chemical etching times (t_{etch} = 0 s, 130 s, 160 s, 180 s, 200 s, and 235 s) collected in 0.5 M aqueous KOH solution at $T = 298$ K and $s = 100$ mV s^{-1} in the α-$Ni(OH)_2$ potential region. The inset shows the relationship between the electrochemically active surface area (A_{ecsa}) of etched Ni foam and the etching time (t_{etch}).

performed for additional 30 s for a total t_{etch} = 160 s and a CV profile was recorded; and (iii) the experiment continued in this manner up to a cumulative t_{etch} = 235 s. Continuous chemical etching results in a faster removal of β-$Ni(OH)_2$ than etching in intervals.

The CV profiles in Figure 4.14 reveal α-$Ni(OH)_2$ formation and reduction features, which increase in size as the cumulative t_{etch} increases. The α-$Ni(OH)_2$ formation CV features were used to determine the surface area of metallic Ni generated by chemical etching; it is equivalent to A_{ecsa} and is plotted as a function of t_{etch} in the inset of Figure 4.14. The A_{ecsa} values were only calculated for $t_{\mathrm{etch}} > 160$ s because, in the case of shorter t_{etch}, this CV feature was too small and its integration would result in large uncertainty. There is a linear increase in A_{ecsa} with extension of t_{etch}; the increase in surface area is a combination of two factors: (i) more of the native oxide is removed generating a greater portion of metallic surface and (ii) chemical etching increases the surface roughness.

The chemical etching of multi-element Ni-containing foams is challenging because each metallic phase has its own reactivity with the etching solution, thus dissolves at different rates. The objectives of chemical etching for Ni foams are to: (i) obtain a metallic surface; (ii) increase the surface area through roughening; (iii) activate the Ni foam for application as an electrode material; and (iv) determine A_{ecsa}. In the case of multi-component Ni-containing foams, the objective (iv) cannot be accomplished because there does not exist a single electrochemical reaction that can probe the surface area of each component present at the material surface. We exposed Inconel and FE2 foams to chemical etching in order to evaluate their stability in a strongly acidic environment. The terms “Inconel” refers to a family of alloys with slightly different compositions and contain Ni as the main element, up to 25% of Cr, Fe, Mo, and Nb, and other metals in varied amounts [34]. The other elements are added to accomplish specific characteristics such as corrosion resistance, grain structure, high temperature stability, strength hardness, and elasticity [13, 35, 36]. Previous research on these acid resistant materials focused on bulk materials. Since Inconel and FE2 foams are not bulk materials, their behavior in strongly acidic solutions cannot be easily related to previous studies.

The applicability of the above-mentioned solution as an etching medium was examined by submerging in it Inconel foam specimens at three temperatures, namely T = 293, 313 and 353 K. In the case of T = 293 K, there was no visible degradation of the material over the course of even several days and the etching solution remained colorless. Chemical etching at T = 313 K resulted in gradual dissolution of the material within 700 s and the etching solution gradually developed yellowish green coloration characteristic of Ni and Cr ions in an aqueous medium. Figure 4.15 shows FIB images of Inconel foam for several values of t_{etch} that reveal progression of the evolution of surface morphology and 3D structure during chemical etching. The six pictures refer to the following etching times: image A: t_{etch} = 0 s (no chemical etching); image B: t_{etch} = 30 s; image C: t_{etch} = 60 s; image D: t_{etch} = 80 s; E: t_{etch} = 240 s; and image F: t_{etch} = 600 s. Images B, C, and D demonstrate that there is no visible degradation of Inconel foam structure within the initial 80 s of etching. Image E reveals that in the case of t_{etch} = 240 s the struts become thinner and their surface smoother. Image F shows that in the case of t_{etch} = 600 s there is an extensive damage to the 3D structure of Inconel foam and its surface morphology is significantly changed; we observe complete dissolution of some struts and thinning of the remaining ones. The resultant structure is no longer an extended network of interconnected struts with pentagonal openings. The sample shown in image F was the last recoverable sample of Inconel foam upon chemical etching because further extension of t_{etch} led to a loss of structural integrity. In the case of chemical etching at $T = 353$ K, immersion of Inconel foam in the etching solution resulted in an immediate and intense dissolution of the material.

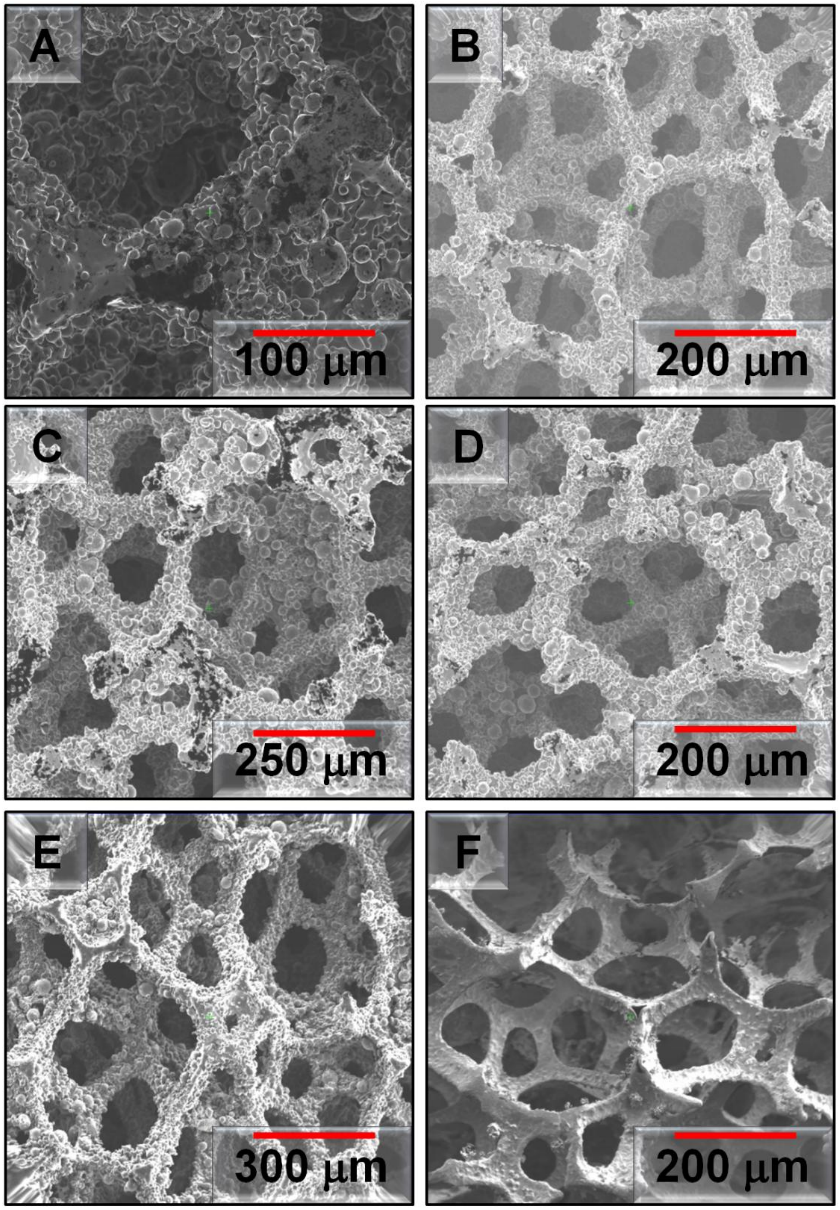

Figure 4.15. FIB images of Inconel foam exposed to chemical etching for various lengths of time: (A) t_{etch} = 0 s; (B) t_{etch} = 30 s; (C) t_{etch} = 60 s; (D) t_{etch} = 80 s; (E) t_{etch} = 240 s; and (F) t_{etch} = 600 s.

FE2 alloy was developed to withstand strongly oxidizing environments [13]. Although the compositions of Inconel and FE2 are alike (Table 4.1), the difference between them is that FE2 contains Al but lacks Mo, Ta, or Nb. The addition of Al enables the material to form a passive alumina (Al_2O_3) layer on the surface, which contributes to its long-term oxidation resistance in gaseous environments [13]. We tested the stability of FE2 foam in the etching solution as an example of a strongly oxidizing environment. Chemical etching of FE2 was studied at T = 293 K because at this temperature FE2 dissolved readily, as indicated by a change in the color of the solution from colorless to green; thus, heating was not required to initiate the etching process. Figure 4.16 presents three FIB images of FE2 foam at various stages of chemical etching: image A for t_{etch} = 0 s (no chemical etching); image B for t_{etch} = 120 s; and image C for t_{etch} = 240 s. After 120 s of chemical etching (image B), there is severe damage to the foam structure; the bubbly surface morphology disappears, struts become thinner, and the 3D network of struts is partially damaged. After 240 s of chemical etching (image C), entire struts are dissolved and the structure is almost completely broken down; at this point the sample barely holds together during rinsing with de-ionized water. Attempts of etching of FE2 foam at higher temperatures than 293 K resulted in the complete dissolution of the foam in less than 30 s.

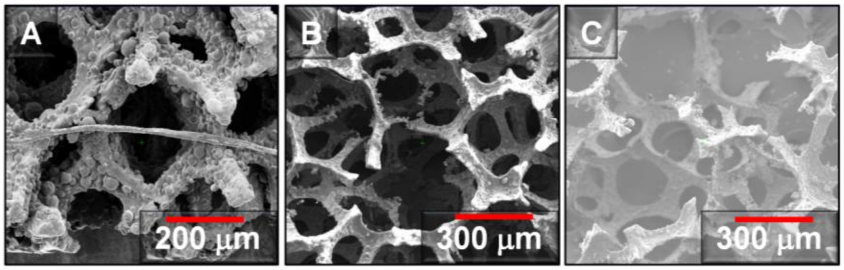

Figure 4.16. FIB images of FE2 exposed to chemical etching for various lengths of time: (A) t_{etch} = 0 s; (B) t_{etch} = 120 s; and (C) t_{etch} = 240 s.

4.4 Conclusions

The results presented within this chapter and their analysis contributes to a greater understanding of Ni-containing foams, which are important materials in electrochemical technologies. Cyclic voltammetry can be used to examine the electrochemical properties of Ni-containing foams in aqueous alkaline media. The electrochemical behavior of Ni foam is similar to that of bulk Ni, and the electrochemical behavior of Inconel foam is similar to that of an alloy containing Ni and Cr. Application of CV to chemically etched Ni foams of various densities allows the determination of their A_{ecsa}; the values of A_{ecsa} are in the 250–450 $\mathrm{cm}^2\ \mathrm{g}^{-1}$ range. SEM images of Ni, Inconel, and FE2 foams show similar 3D structures comprising interconnected struts (25–80 μm in width); the 3D network mimics the pentagonal arrangement of the polyurethane template. Correlation of CV and SEM data reveals that the Ni foams possessing different densities and A_{ecsa} values have similar 3D structures and pore volumes; the increase in Ni foam density is related to the increase of strut wall thickness. The struts within Ni foams are smooth with visible metallic grains, whereas the struts within Inconel and FE2 foams have rough and bubbly surfaces. Although in the case of Inconel and FE2 foams A_{ecsa} cannot be determined using CV, the analysis of SEM and FIB images leads to the conclusion that these two foams have higher values of A_{ecsa} than those of Ni foams. Both EDS and XPS analyses of Ni foam detected only Ni, O, and C; the latter two were present as adsorbed H_2O and CO_2 on the surface of the foam; some O is also assigned to β-$Ni(OH)_2$ covering the material. HRXPS coupled with Ar^+ ion etching shows that the surface of untreated Ni foam is almost entirely covered with β-$Ni(OH)_2$. Etching of Ni foams with Ar^+ ions removes the surface layer of β-$Ni(OH)_2$ and exposes the underlying metal. SEM and EDS analyses of Inconel foam demonstrate that different surface regions have different chemical compositions. Two constituents, Ta and Mo, are non-uniformly distributed and accumulate preferentially on spheres attached to struts. HRXPS measurements coupled with Ar^+ ion etching reveal that in the case of Inconel foam Ni is present mostly as Ni(0) with a small amount of Ni(2+), whereas Cr is present mostly as Cr(3+) with a small amount of Cr(0). Chemical etching can be successfully applied to pretreat Ni-containing foams without destroying their 3D structure. It increases the strut surface roughness of Ni foams but decreases the strut surface roughness of Inconel and FE2 foams. Chemical etching of Ni foams is required in order to determine the A_{ecsa} of the Ni. FIB can be effectively employed to image Ni-containing foams at various stages of their fabrication and to monitor changes in the materials' porosity, crystallinity and dimensions. FIB can also be employed to prepare cross-sections, which are then used to measure the thickness of strut walls and to analyze the inner wall structure. FIB reveals the existence of inner nanostructure that can be further examined by TEM and ET. Nickel, Inconel and FE2 foams have a unique structure encompassing pentagonal macropores within 3D network of struts, hollow cavities within struts, and nanostructured inner walls. Thus, we conclude that Ni-containing foams have three levels of structure and two level of porosity. In conclusion, these combined studies offer a very comprehensive analysis of Ni-containing foams that discusses their materials science, surface science and electrochemical characteristics.

4.5 References

(1) K. Watanabe, T. Kikuoka, *J. Appl. Electrochem.* **1995**, 25, 219–226.

(2) A. Montillet, J. Comiti, J. Legrand, *J. Appl. Electrochem.* **1993**, 23, 1045–1050.

(3) P. Simon, Y. Gogotsi, *Nature Mater.* **2008**, 7, 845–854.

(4) J. Kleperis, G. Wójcik, A. Czerwinski, J. Skowronski, M. Kopczyk, M. Beltowska-Brzezinska, *J. Solid State Electrochem.* **2001**, 5, 229–249.

(5) A. Chyrkin, S. L. Schulze, J. Piron-Abellan, W. Bleck, L. Singheiser, W. Quadakkers, *J. Adv. Eng. Mater.* **2010**, 12, 873–883.

(6) M. Fleischmann, K. Korinek, D. Pletcher, *J. Chem. Soc., Perkin Trans*. **1972**, 2, 1396–1403.

(7) A. J. Motheo, S. A. S. Machado, F. S. B. Rabelo, J. R. J. Santos, *J. Braz. Chem. Soc*. **1994**, 5, 161–165.

(8) J. K. Norskov, *Nature* **2001**, 414, 405–406.

(9) P. M. Robertson, *J. Electroanal. Chem.* **1980**, 111, 97–104.

(10) J. Banhart, *Prog. Mater. Sci.* **2001**, 46, 559–632.

(11) I. J. Brown, S. Sotiropoulos, *J. Appl. Electrochem.* **2001**, 31, 1203–1212.

(12) V. Paserin, S. Marcuson, J. Shu, D. S. Wilkinson, *Adv.Eng. Mater*. **2004**, 6, 454–459.

(13) G. Walther, B. Kloden, T. Buttner, T. Weissgarber, B. Kieback, A. Bohm, D. Naumann, S. Saberi, L. Timberg, *Adv. Eng. Mater.* **2008**, 10, 803–811.

(14) M. Kummer, J. R. Kirchhoff, *Anal. Chem.* **1993**, 65, 3720–3725.

(15) B. E. Conway, W. B. A. Sharp, H. Angerstein-Kozlowska, E. E. Criddle, *Anal. Chem.* **1973**, 45, 1331-1336.

(16) H. Angerstein-Kozlowska, *Surfaces, Cells, and Solutions for Kinetic Studies*; Yeager E, Ed.; Comprehensive Treatise of Electrochemistry Volume 9; Plenum Press, NY, **1984**.

(17) P. Oliva, J. Leonardi, J. F. Laurent, C. Delmas, J. J. Braconnier, M. Figlarz, F. Fievet, A. de Guibert, *J. Power Sources* **1982**, 8, 229–255.

(18) M. Grden, M. Alsabet, G. Jerkiewicz, *ACS Appl. Mater. Interfaces* **2012**, 4, 3012–3021.

(19) L. A. Giannuzzi, B. W. Kempshall, S. M. Schwarz, J. K. Lomness, B. I. Prenitzer, F. A. Stevie, *FIB Lift-Out Specimen Preparation Techniques*; L. A. Giannuzzi, F. A. Stevie, Eds.; Introduction to Focused Ion Beams; Springer: NY, **2005**.

(20) M. Alsabet, M. Grden, G. Jerkiewicz, *Electrocatalysis* **2011**, 2, 317–330.

(21) A. Jouanneau, M. Keddan, M. C. Petit, *Electrochim. Acta* **1976**, 21, 287–292.

(22) D. Addari, B. Elsener, A. Rossi, *Electrochim. Acta* **2008**, 53, 8078–8086.

(23) J. H. Garretsen, J. H. W. de Wit, *Corros. Sci.* **1990**, 30, 1075–1084.

(24) J. M. Marioli, L. E. Sereno, *Electrochim. Acta* **1994**, 40, 983–989.

(25) B. E. Conway, L. Bai, *J. Electroanal. Chem.* **1986**, 198, 149–175.

(26) A. Lasia, A. Rami, *J. Electroanal. Chem.* **1990**, 294, 123–141.

(27) S. A. S. Machado, L. A. Avaca, *Electrochim. Acta* **1994**, 39, 1385–1391.

(28) N. Kitakatsu, V. Maurice, C. Hinnen, P. Marcus, *Surf. Sci.* **1998**, 407, 36–58.

(29) Y. Okajima, *J. Appl. Phys.* **1980**, 51, 71–717.

(30) N. Fairley, *CasaXPS* Version 2.3.14. Casa Software Ltd **2008**, 2.3.14.

(31)R. P. Gupta, S. K. Sen, *Phys. Rev. B: Condens. Matter* **1974**, 10, 71–77.

(32) V. Shankar, K. B. S. Rao, S. L. Mannan, *J. Nuclear Mater.* **2001**, 288, 222–232.

(33) J. L. Weininger, M. W. Breiter, *J. Electrochem. Soc.* **1963**, 110, 484–490.

(34) P. Zoltowski, *Electrochim. Acta* **1993**, 38, 2129–2133.

(35) F. Azarmi, J. Saaedi, T. W. Coyle, J. Mostaghimi, *Adv.Eng. Mater.* **2008**, 10, 459–464.

(36) R. W. Revie, Ed.; *Uhlig's Corrosion Handbook*; Volume 3; John Wiley & Sons: Hoboken, NJ, **2011**.

(37) M. F. Ashby, D. R. H. Jones, *Engineering Materials*; Pergamon Press: Oxford, **1989**.

Chapter 5

Electrochemical Oxidation of Isopropanol Using a Nickel Foam Electrode [2]

5.1 Introduction

Although electrochemical methods are not often applied in the synthesis of organic compounds, there has been growing interest in organic electrochemical processes since the second half of the twentieth century [1, 2]. A simple oxidation or reduction process between an electrode and an organic molecule can accomplish many of the key functional group interconversions (FGI) that are necessary in organic synthesis [1, 3, 4]. Often, there are advantages of the electrochemical approach to FGI over the use of a chemical redox reagent such as the ability to precisely select the potential (E) of the reaction, allowing a specific functional group of the molecule to be targeted while other groups remain unaffected. This can significantly shorten a synthesis route by avoiding the addition, and subsequent removal, of a protecting group [1, 5]. Electrochemical FGI methods are also often more economical because they eliminate the need for expensive electron-transfer agents such as lead OsO_4 and $Pb(OAc)_4$, and, since the electrode material is not consumed in the reaction, it can be re-used indefinitely [1, 4, 6]. However the economic gain is greatly dependant on the cost of the electrode material as some electrodes can be very expensive (e.g. Pt). Perhaps the most important advantage of the

---

[2] The work presented in this chapter is in press. J. van Drunen. *Journal of Electroanalytical Chemistry*, (2013).

electrochemical approach to FGI lies in the ease of scale-up from the laboratory to the industrial setting. Many electrochemical FGI reactions can be run in a continuously-operating cell with little or no work-up required since additional oxidizing, reducing, and protecting agents have not been added to the system [7, 8]. However, electrolysis treatments developed under potentiostatic conditions at the laboratory scale must be converted to galvanostatic conditions for effective scale-up to an economically viable industrial application. With the growing global shift towards environmentally conscious methods in science and industry, electrochemical methods are more relevant than ever in organic synthesis.

The study presented in this chapter investigates the conversion of a secondary alcohol (isopropanol, IPA) to a ketone (acetone) using a nickel foam anode, which is a low-cost electrode material. The reaction takes place in aqueous alkaline electrolyte. The first and most extensive mechanistic studies for the electrochemical oxidation of small alcohols, including IPA, using a nickel anode in alkaline media were carried out by Fleischmann et al. [9, 10]. These two studies resulted in a good understanding of the system; however there are some inconsistencies [11] in the detailed mechanistic understanding of the reaction which are noted below in the Results and Discussion section (section 5.3). Using a non-noble metal electrocatalyst material such as nickel, most species (organic acids, linear, branched, and cyclic alcohols, and amines) oxidize at approximately the same potential that is simultaneous or very close in potential to the formation of an oxide or hydroxide species on the metal surface [9 - 14]. It is generally accepted that this oxide or hydroxide is essential to the oxidation of the organic species and participates directly in the reaction [9, 10, 12, 14]. In the case of IPA oxidation with a Ni anode, the reaction occurs just above the potential of β-NiOOH formation and just below the onset potential of the oxygen evolution reaction (OER) [3, 9, 10]. Although it is clear from previous research [9, 10, 11] that the oxidation of IPA requires the presence of β-NiOOH, it is uncertain whether these two processes proceed simultaneously [11]. Regardless of the mechanistic details, it is also clear that Ni is an effective electrocatalyst for this FGI; IPA is oxidized to acetone with a current yield of 90% [3, 9, 10, 15]. The goals of the present study are twofold; (i) to use cyclic voltammetry (CV) to re-examine the process of IPA oxidation with a nickel anode under a range of well-controlled experimental conditions, and (ii) to evaluate nickel foam as an anode which could be applied to this and other FGI reactions.

5.2 Experimental Section

5.2.1 Electrochemical Measurements

Electrochemical measurements were carried out using a two-compartment Pyrex electrochemical cell and three electrodes. The working electrode (WE) was a disk of nickel foam having a thickness of ca. 3 mm and a diameter of 12 mm. (supplied by the former Inco Technical Services Ltd.), attached to a Ni wire (99.98% in purity, 0.25 mm diameter, Alfa Aesar) sealed in a glass tube for electrical contact. The contribution of the Ni wire to the overall surface area, thus to the electrochemical signal, was less than 1% and is assumed to be negligible. The electrochemically active surface area (A_{ecsa}) of a Ni foam sample cannot be determined without chemically etching and therefore altering the sample [16, 17]. Thus, the differences in A_{ecsa} values between samples are accounted for in the following ways: (i) whenever possible, studies are carried out using the exact same electrode so that the current (I) can be compared directly, or

(ii) the current was normalized to an estimate of A_{ecsa} based on the mass of the Ni foam electrode to yield the current density (j) [16]. Each Ni foam WE was degreased with acetone under reflux for 2 hours in order to remove organic impurities. The counter electrode (CE) consisted of a 1.5 cm × 2.5 cm sheet of glassy carbon attached to a high-purity gold wire (99.98% in purity, Alfa Aesar). The surface area of CE was at least ten times larger than that of WE and the separation between WE and CE was about 3 cm. The reference electrode (RE) was a reversible hydrogen electrode (RHE); it consisted of a platinised Pt wire in contact with a bubble of $H_2(g)$ and in electrolytic contact with the WE compartment through a Luggin capillary tip. All potentials are reported with respect to RHE. All electrochemical experiments were carried out in a 0.50 M aqueous KOH supporting electrolyte (Sigma-Aldrich KOH pellets, A.C.S. reagent grade), unless indicated otherwise in the Results and Discussion section (section 5.3). Isopropanol (Sigma-Aldrich, 99.7% purity) was added to the electrolyte to reach a concentration of 0.10 M, unless indicated otherwise in the Results and Discussion section (section 5.3). The electrolyte solution was prepared using ultra high purity (UHP) water (Millipore) the resistivity of which was 18.2 MΩ cm. Prior to each experiment, the electrolyte was degassed by bubbling UHP $N_2(g)$ (Praxair 5.0 grade) through the solution for 30 minutes. Throughout the duration of electrochemical measurements, UHP $N_2(g)$ was passed over the electrolyte to ensure a neutral gas environment and to expel any gases that might be generated during electrochemical experiments. Glassware was cleaned according to well established procedures [18, 19]. The electrochemical measurements were carried out at a temperature of $T = 298 \pm 1$ K, unless otherwise indicated in the Results and Discussion section (section 5.3).

The electrolysis was carried out in a two compartment electrolysis cell divided by an ion exchange membrane that is stable in aqueous alkaline media (fumapem® FAA by Fumatech). The anode consisted of a Ni foam electrode as described above. The cathode was a sheet of glassy carbon attached to a gold wire, as described above. The electrolyte in the anode compartment was 1.00 M aqueous KOH solution with 0.10 M of isopropanol; the electrolyte in the cathode compartment was 1.00 M aqueous KOH. Each compartment had a working volume of 20.0 ± 0.5 mL. Both compartments of the cell were degassed with UHP N_2(g) gas; the cell was allowed to equilibrate for 30 minutes prior to experimentation. The electrolysis experiments employed a Hg/HgO RE (Radiometer Analytical, XR440) filled with 1.00 M KOH solution, connected to the anode compartment with a Luggin capillary. For consistency in reporting WE potential values, the potentials are converted from the Hg/HgO RE and are reported with respect to the RHE (*E* shift of approximately 0.85 V). The CV and electrolysis experiments were carried out using the Radiometer Analytical Voltalab® PGZ 100 All-In-One instrument and VoltaMaster 4 software (Radiometer Analytical).

5.2.2 High-Performance Liquid Chromatography Measurements

High-performance liquid chromatography (HPLC) measurements were used to quantitatively analyze the concentrations of IPA and acetone throughout the electrolysis experiment. The concentrations of these species were determined in fixed aliquots of electrolyte removed from the anode compartment at various times during electrolysis. HPLC analysis was carried out using a Dionex system equipped with an ASI 1000 Automated Sample Injector. The automated sampler delivered 20 µL of sample, which was transported to the column (Aminex

HPX-87H, 300 mm) using a 8 mM aq. H_2SO_4 mobile phase with a flow rate of 0.6 mL min^{-1}. The species eluted from the column were detected using an absorbance spectrometer (Dionex AD20) in the ultraviolet detection mode (deuterium light source) and a refractive index detector (IOTA 2); the latter was coupled with the spectrometer. The detectors were calibrated using a two point calibration method. Chromeleon 6.50 software was used to control experimental parameters and collect data.

5.3 Results and Discussion

5.3.1 Nickel Foam Electrode Materials

Open-cell Ni foams are attractive electrode materials for the oxidation of small organic molecules and potentially other FGIs because: (i) they are chemically stable in aqueous alkaline media [16, 17]; (ii) they are electrically conductive [20, 21]; (iii) they have an open-pore structure (displayed in Figure 5.1) that allows the electrolyte to flow through the electrode [20, 22, 23]; (iv) they have large specific surface area (A_s, in cm^2 g^{-1}) and electrochemically active surface areas (A_{ecsa} in cm^2) [16, 17]; (v) they are manufactured on a large scale (e.g. sheets that are many m^2) and can be cut to virtually any size or shape for convenient use in large-scale electrolysis [23]; and (vi) the oxides formed on Ni are effective electrocatalysts for the oxidation of organic compounds [9, 12, 13, 15]. The open-cell Ni foam used in this study has A_s of approximately 300 ± 75 cm^2 g^{-1} [16]; it has a large pore volume which corresponds to low material use and consequently, low cost. Despite its low density of $\rho = 0.26 \pm 0.01$ g cm^{-3}, the Ni foam is remarkably robust towards handling and cutting, and stable in alkaline media [17].

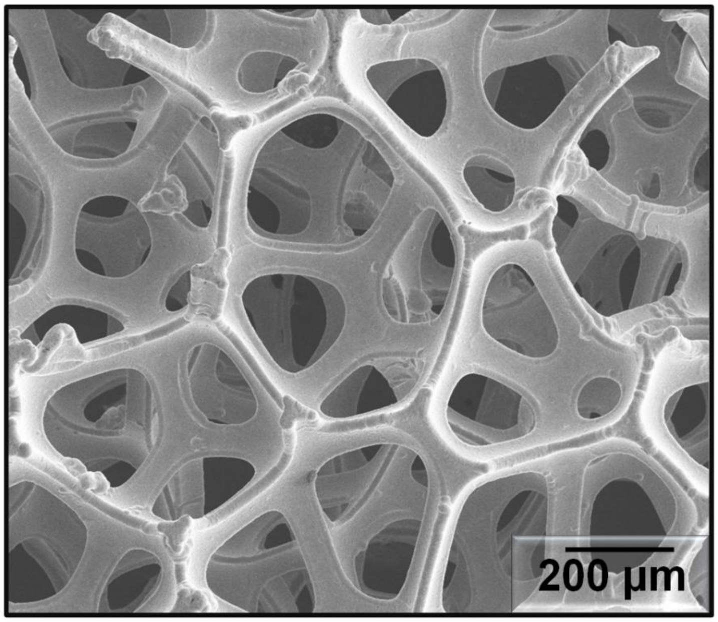

Figure 5.1. Scanning electron microscope image of Ni foam.

The surface chemical composition and surface oxidation state of any electrode material are of upmost importance to its electrocatalytic properties. The formation of Ni surface oxides is key to the oxidation of IPA because it was demonstrated that the β-$Ni(OH)_2$ / β-NiOOH redox couple participates directly in the process (see equations 5.8 to 5.12) [9, 10, 14]. The surface chemistry of a Ni electrode depends on the electrode history prior to electrochemical measurements and on the electrochemical conditions imposed during the oxidation reaction [24 – 26]. Nickel forms a native surface hydroxide, β-$Ni(OH)_2$, when exposed to the ambient or when in contact with aqueous alkaline solutions; this surface hydroxide cannot be reduced electrochemically. Removal of β-$Ni(OH)_2$ from the surface of Ni can be achieved through mechanical polishing or chemical etching in aqueous acidic solutions. The electrochemical behavior of Ni in aqueous alkaline solutions is summarized in equations 5.1 to 5.7; these surface electrochemical processes give rise to unique features in a CV profile. A typical CV profile for bulk Ni in aqueous KOH solution in the –0.20 to 1.60 V potential (E) range shows the following anodic characteristics: (i) oxidation of Ni^0 to α-$Ni(OH)_2$ at $0.20 < E < 0.40$ V (eq. 5.1); (ii) concurrent conversion of α-$Ni(OH)_2$ to β-$Ni(OH)_2$ (eq. 5.2) and oxidation of Ni^0 to β-$Ni(OH)_2$ (eq. 5.3) at $0.50 < E < 1.30$ V; (iii) oxidation of β-$Ni(OH)_2$ to β-NiOOH at $1.30 < E < 1.55$ V (eq. 5.4); and (iv) OER at $E > 1.55$ V (eq. 5.5) [24 – 27].

$$Ni^0 + 2\,OH^- \longrightarrow \alpha\text{-}Ni(OH)_2 + 2\,e^- \qquad (5.1)$$

$$\alpha\text{-}Ni(OH)_2 \longrightarrow \beta\text{-}Ni(OH)_2 \qquad (5.2)$$

$$Ni^0 + 2\,OH^- \longrightarrow \beta\text{-}Ni(OH)_2 + 2\,e^- \qquad (5.3)$$

$$\beta\text{-}Ni(OH)_2 + OH^- \longrightarrow \beta\text{-}NiOOH + H_2O + e^- \qquad (5.4)$$

$$2\,OH^- \longrightarrow \tfrac{1}{2}\,O_2 + H_2O + 2\,e^- \qquad (5.5)$$

The reverse CV scan from E of 1.55 V to –0.20 V displays two cathodic features: (v) a reduction peak for the conversion of β-NiOOH to β-$Ni(OH)_2$ at $1.10 < E < 1.40$ V (eq. 5.6) and (vi) hydrogen evolution reaction (HER) that gives rise to an appreciable current density at $E < -0.20$ V (eq. 5.7).

$$\beta\text{-}NiOOH + H_2O + e^- \longrightarrow \beta\text{-}Ni(OH)_2 + OH^- \qquad (5.6)$$

$$H_2O + e^- \longrightarrow \tfrac{1}{2}\,H_2 + OH^- \qquad (5.7)$$

Analysis of the electrochemical behaviour and surface chemical composition of Ni foams demonstrates that their response is very similar to that of bulk Ni; their CV profiles display all of the features listed above in equations 5.1 through 5.7 [16, 17]. Knowledge of the electrode history (e.g. prior passivation or electrochemical treatment) and electrochemical reactions that take place at the electrode surface in the presence of supporting electrolyte facilitates the analysis of CV profiles when IPA is added to the system.

5.3.2 General Comments on the Oxidation of IPA on Ni Electrodes in Alkaline Media

As mentioned in the Introduction section, the anodic oxidation of small organic molecules using a Ni electrode was studied by several groups [3, 9 – 12]. A general mechanism for the conversion of alcohols to aldehydes or ketones was proposed by Fleischmann et al.; equations 5.8 to 5.12 illustrate this mechanism specifically for the oxidation of IPA to acetone [9, 10, 14].

$$\beta\text{-Ni(OH)}_2 + \text{OH}^- \rightleftharpoons \beta\text{-NiOOH} + \text{H}_2\text{O} + e^- \qquad (5.8)$$

$$((\text{CH}_3)_2\text{CHOH})_{sol} \rightleftharpoons ((\text{CH}_3)_2\text{CHOH})_{ads} \qquad (5.9)$$

$$((\text{CH}_3)_2\text{CHOH})_{ads} + \beta\text{-NiOOH} \longrightarrow ((\text{CH}_3)_2\text{C}^{\bullet}\text{OH})_{ads} + \beta\text{-Ni(OH)}_2 \qquad (5.10)$$

$$((\text{CH}_3)_2\text{C}^{\bullet}\text{OH})_{ads} + \text{OH}^- \longrightarrow (\text{CH}_3)_2\text{CO} + \text{H}_2\text{O} + e^- \qquad (5.11)$$

$$((\text{CH}_3)_2\text{C}^{\bullet}\text{OH})_{ads} + \beta\text{-NiOOH} \longrightarrow \beta\text{-Ni(OH)}_2 + (\text{CH}_3)_2\text{CO} \qquad (5.12)$$

Equation 5.8 presents the interconversion of β-Ni(OH)$_2$ to β-NiOOH, which is described by Fleischmann et al. as a fast equilibrium [9]; equation 5.9 shows the adsorption of isopropanol on the electrode surface; equation 5.10 refers to the rate-determining hydrogen extraction step; equations 5.11 and 5.12 both present the formation of acetone, but only the reaction shown in equation 5.11 proceeds with an electron release. Based on rotating disc electrode studies performed by Fleischmann et al. [10], in which the *I* was not affected by the electrode rotation speed, it was proposed that the entire process as presented in equations 5.8 through 5.12 was under kinetic control. Based on their log *i* vs. *E* plots (Tafel plots) collected in the presence of varied concentrations of IPA, it was determined that the process was governed by first-order kinetics with respect to the concentration of the IPA at all potentials [9, 10]. Experiments carried out in varied concentrations of KOH indicated first order kinetics with respect to the concentration of OH^- at potentials that were in the narrow, linear Tafel region [9, 10]; the Tafel region corresponded to the potential region of β-NiOOH formation (eq. 5.4). The Tafel plots revealed a limiting-current plateau, where increase in *E* offered no increase in *I* at potentials slightly above the potential of β-NiOOH formation; in this potential range, *I* was also independent of the concentration of OH^-; the plateau is in the potential range of IPA oxidation. In their criticism of the Fleishmann et al. mechanistic and kinetic studies, Vertes and Horanyi [11] observed that the oxidation of the alcohol and the reduction of β-NiOOH to β-$Ni(OH)_2$ proceed in different potential ranges and concluded that the limiting-current plateau region may be a superposition of two independently occurring phenomena. Vertes and Horanyi performed CV experiments in which the anodic scan covered the potential range of β-NiOOH formation and IPA oxidation, but the cathodic scan did not extend into the region of β-NiOOH reduction; they observed an increase in *j* with an extension of *E*. Because under such conditions the surface coverage of β-NiOOH changes very little, the increase in *j* was assigned to IPA oxidation. This important experiment allowed the separation of theβ-NiOOH formation and IPA oxidation electrode processes

In a separate study, Robertson [12] examined the oxidation of small organic molecules at Ni electrodes in alkaline media and observed separate CV peaks for the β-NiOOH formation and alcohol oxidation. He was also the first researcher to observe: (i) an appreciable anodic current due to the oxidation of the alcohol in the reverse CV scan; (ii) a dependence of the limiting-current plateau on the rate of electrolyte stirring for low OH^- concentrations, pointing to a process under diffusion control; (iii) an independence of the peak current for alcohol oxidation on the concentration of the alcohol when the concentration of OH^- is low; and (iv) a dependence of the peak current for alcohol oxidation on the concentration of the alcohol when the concentration of OH^- is high. The results of Vertes and Horanyi [11] and of Robertson [12] clearly show that the current understanding of the mechanism and kinetics of electrochemical alcohol oxidation is lacking.

5.3.3 CV Analysis of IPA Oxidation on Ni Foam Electrodes

Herein, the oxidation of IPA on Ni foam anodes is studied using CV in order to analyze factors affecting the reaction, such as concentration of IPA, concentration of KOH, temperature (T), and scan rate (s). Figure 5.2 shows two overlaid CV profiles; the black curve corresponds to Ni foam in 0.50 M aqueous KOH and the red curve corresponds to Ni foam in 0.50 M aqueous KOH + 0.10 M IPA. The black CV profile for Ni foam in the supporting electrolyte displays the following features: (i) an anodic peak at $E = 1.30$ V in the forward-going scan corresponding to the formation of β-NiOOH (eq. 5.4); (ii) a sharp increase in anodic current at $E = 1.50$ V in the forward-going scan corresponding to the OER (eq. 5.5); and (iii) a cathodic peak at $E = 1.15$ V in

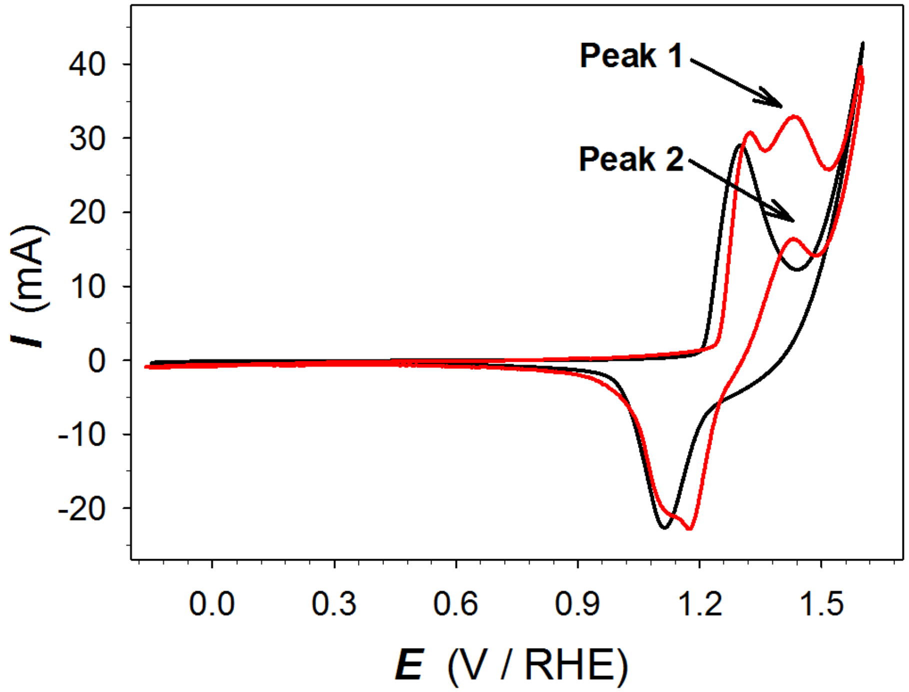

Figure 5.2. CV profiles of Ni foam collected in 0.50 M aqueous.KOH (black scan) and 0.50 M aqueous KOH + 0.10 M IPA (red scan) at $T = 298$ K and with $s = 50$ mV s^{-1}.

the reverse-going scan corresponding to the reduction of β-NiOOH (eq. 6). When 0.10 M IPA is added to the system (the red CV profile), these same CV features are observed along with additional features assigned to IPA oxidation, namely a new anodic peak in the forward-going scan that reaches its maximum peak current (I_{peak}) at peak potential (E_{peak}) values superior to those of β-NiOOH formation and slightly inferior to the E value of OER onset; this peak shall be denoted peak 1 from here on. There is also a new anodic peak in the reverse-going scan with E_{peak} and I_{peak} values slightly lower than those of peak 1; this peak shall be denoted peak 2 from now on. Peaks 1 and 2 are both attributed to the oxidation of IPA to acetone [9, 10, 12]. In early studies on the oxidation of IPA the β-NiOOH formation peak and peak 1 were regarded as one single CV feature [9, 10]. Yet in a subsequent study [11] it was suggested that the predominant anodic CV feature may be a superposition of two phenomena; this observation lays the foundation for the detailed study of the influence of several experimental parameters on IPA oxidation in the present contribution. Although anodic current for IPA oxidation in the reverse-going CV scan was observed by Robertson [12], the behavior of peak 2 has not yet been analyzed in detail.

5.3.4 Effect of KOH Concentration

The effect of changes in KOH concentration ([KOH]) was studied by acquiring CV profiles for Ni foam electrodes in electrolytes ranging from 0.20 to 2.00 M aqueous KOH, each containing 0.10 M IPA. Figure 5.3 A presents overlaid CV profiles collected in each electrolyte at T = 293 K and at s = 50 mV s^{-1}; we present CV profiles for the 0.60 to 1.60 V range because there are no features at E < 0.60 V (see Figure 5.2). Changes in [KOH] do not appear to have a significant effect on the I_{peak} or E_{peak} of IPA oxidation peaks 1 or 2. However, the overlaid CV profiles in Figure 5.3 A demonstrate qualitative changes in the β-NiOOH formation and reduction features caused by the increased [KOH]; these changes are more easily discernible in the reverse-going scans than in the forward-going ones. The onset of the anodic β-NiOOH formation peak shifts towards high E values as [KOH] is increased and the peak becomes more narrow, giving rise to a higher I value. The same qualitative behavior is observed for the cathodic β-NiOOH reduction peak, here the peak potential shift is greater. It is interesting to observe that the charge (q) due β-NiOOH formation and reduction is unaffected; q = 65 ± 4 mC. Figure 5.3 B shows the values of I_{peak} for peaks 1 and 2 plotted as a function of [KOH]; we do not show I_{peak} values for [KOH] = 0.20 M because the peaks are not well-defined and appear as shoulders. Because the peaks 1 and 2 overlap with the CV features due to β-NiOOH formation and reduction, and because the morphology of the latter peaks changes with modification of [KOH], there is uncertainty associated with I_{peak} determination which is reflected by the error bars. We observe

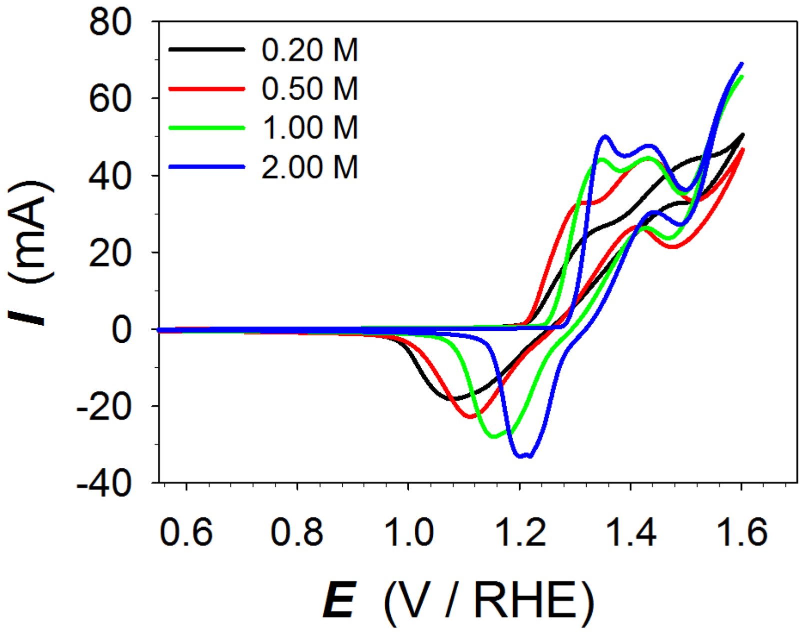

Figure 5.3 A. CV profiles of Ni foam in supporting electrolyte with various KOH concentrations (0.20 M, 0.50 M, 1.00 M, and 2.00 M), each containing 0.10 M IPA collected at T = 298 K and with s = 50 mV s^{-1}.

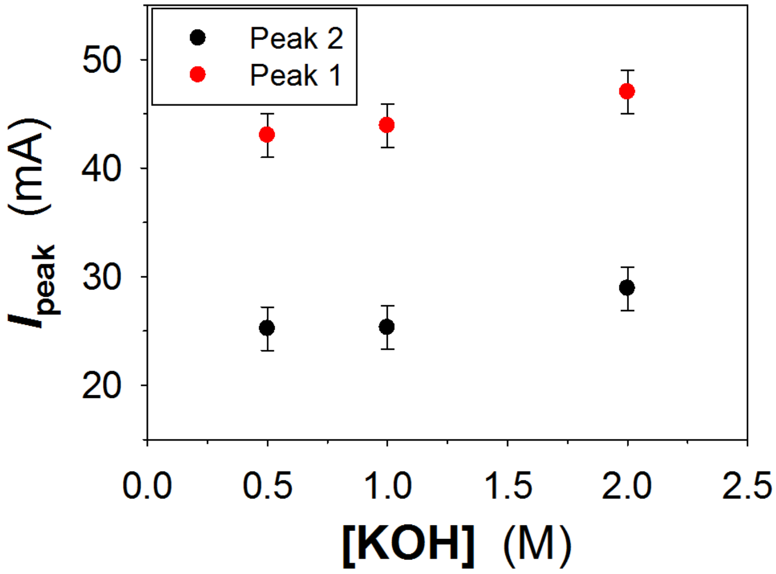

Figure 5.3 B. Relationship between the maximum peak current (I_{peak}) of IPA oxidation peaks 1 and 2 and the concentration of KOH within the supporting electrolyte.

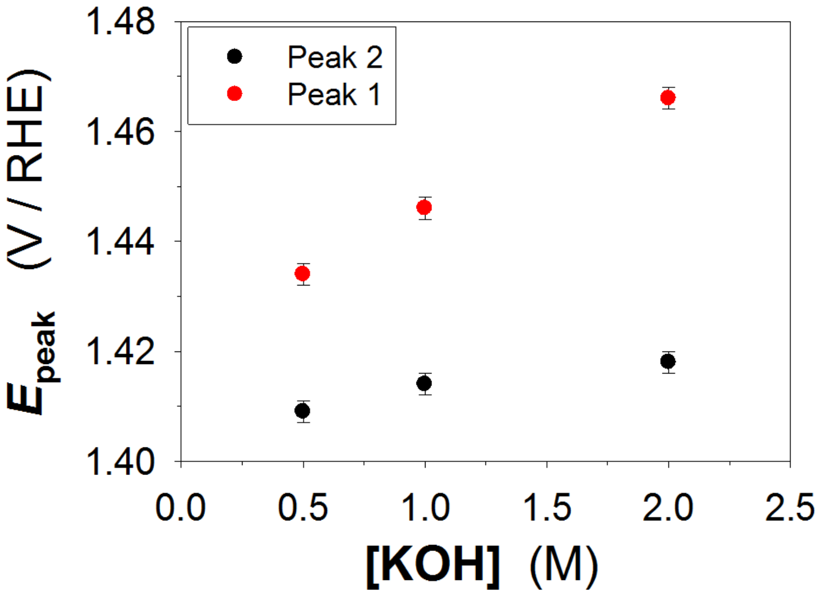

Figure 5.3 C. Relationship between the peak potential (E_{peak}) of IPA oxidation peaks 1 and 2 and the concentration of KOH within the supporting electrolyte.

that I_{peak} for peak 1 increases slightly from 43 to 48 mA, and that I_{peak} for peak 2 is in the 26 to 29 mA range and reveals no clear trend as a function of [KOH]. Figure 5.3 C shows the E_{peak} values for peaks 1 and 2 as a function of [KOH]; again, we do not show E_{peak} values for [KOH] = 0.20 M because the peaks are not well-defined. In both cases, E_{peak} slightly increases as [KOH] is raised; the change is ca. 30 mV for peak 1 and ca. 10 mV for peak 2.

5.3.5 Effect of Isopropanol Concentration

The effect of changes in IPA concentration ([IPA]) is examined by collecting CV profiles for Ni foam electrodes in 0.50 M aqueous KOH + IPA having different concentrations in the 0.05 to 2.00 M range; these CV profiles are shown in Figure 5.4 A. As in the case of the effect of KOH concentration, we present CV profiles commencing at E = 0.60 V because there are no features at E < 0.60 V (see Figure 5.2). Increased [IPA] alters the CV features in several ways; most notably there is an increase in the I_{peak} and E_{peak} of peaks 1 and 2. We also observe that an increase in [IPA] shifts the onset of OER towards higher potentials. The I_{peak} versus [IPA] and E_{peak} versus [IPA] relationships for peaks 1 and 2 are shown in Figures 5.4 B and 5.4 C, respectively. The inset in Figure 5.4 B shows the linear relationship between I_{peak} and log([IPA]). Figure 5.4 B reveals that an initial increase of [IPA] significantly raises I_{peak} but as high [IPA] values are reached, the increase in I_{peak} becomes gradually less pronounced. For instance, in the case of [IPA] = 1.00 M, the I_{peak} value is ca. 80 mA, which corresponds to a current density (j) value of about 10 mA cm^{-2}. Figure 5.4 B also illustrates the difference in I_{peak} values for peaks 1 and 2. In the case [IPA] < 0.50 M, I_{peak} of peak 2 is lower than I_{peak} of peak 1; however, in the case of [IPA] > 0.50 M, I_{peak} values for peaks 1 and 2 are similar and the two plots overlap. This observation indicates that, at low [IPA], the IPA oxidation occurring in the forward-going scan likely depletes the concentration of IPA near the electrode surface to the point that the process cannot yield the same I for peak 2 in the reverse-going scan. However, as [IPA] reaches higher values, the reaction seems to be limited by the amount of active catalytic sites on the electrode surface, as opposed to the [IPA] near the electrode surface. Figure 5.4 C demonstrates a linear increase in E_{peak} of peaks 1 and 2 as a function of increasing [IPA]. At [IPA] = 0.05 M (the lowest value), E_{peak} value is 1.42 V and at [IPA] = 2.00 M (the highest value), E_{peak} is 1.86 V. It is important to add that the onset potential of IPA oxidation remains practically the same for the gradually increasing [IPA] values, but it is the values of I_{peak} and E_{peak} that strongly depend on the IPA concentration. The shift towards higher E as the concentration of the organic species is increased is frequently observed for the anodic oxidation of organic compounds, although the origin of this behavior is not well understood. The logarithmic dependence of I_{peak} on [IPA] agrees with the results of Fleishmann et al. [10] who reported that the oxidation of various organic compounds follows a first order dependence on the compound’s concentration for a wide potential range.

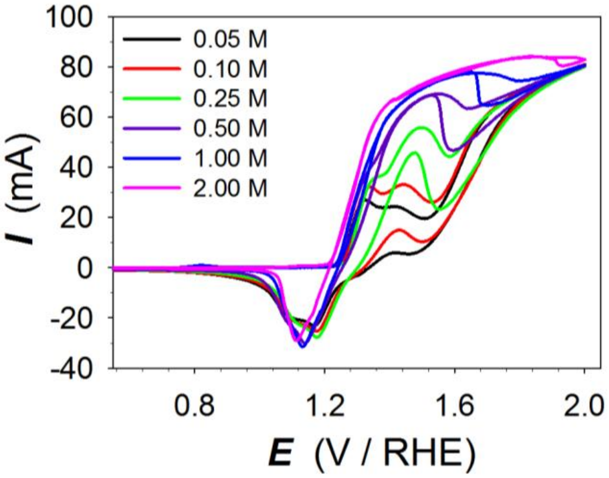

Figure 5.4 A. CV profiles of Ni foam in 0.50 M aqueous KOH with various concentrations of IPA (0.05 M, 0.10 M, 0.25 M, 0.50 M, 1.00 M, and 2.00 M) collected at T = 298 K and with s = 50 mV s^{-1}.

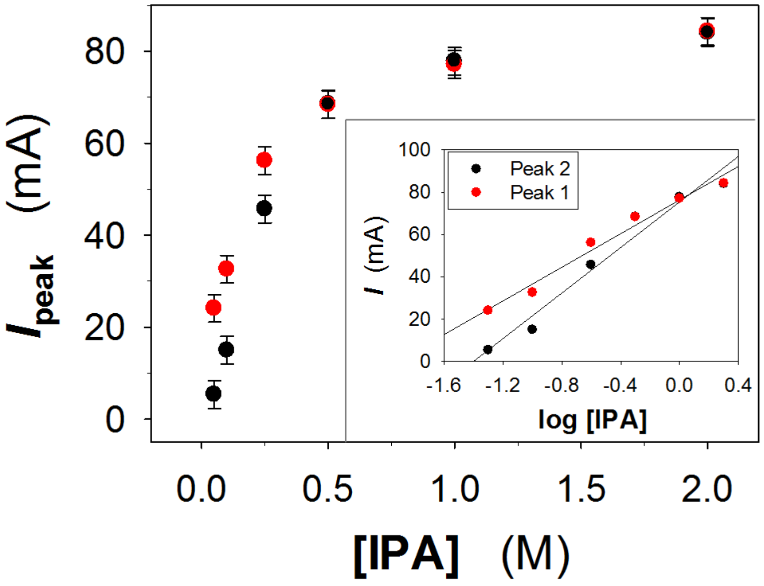

Figure 5.4 B. Relationship between the maximum peak current (I_{peak}) of IPA oxidation peaks 1 and 2 and the concentration of IPA within the electrolyte; the inset shows the relationship when [IPA] is plotted on a log scale.

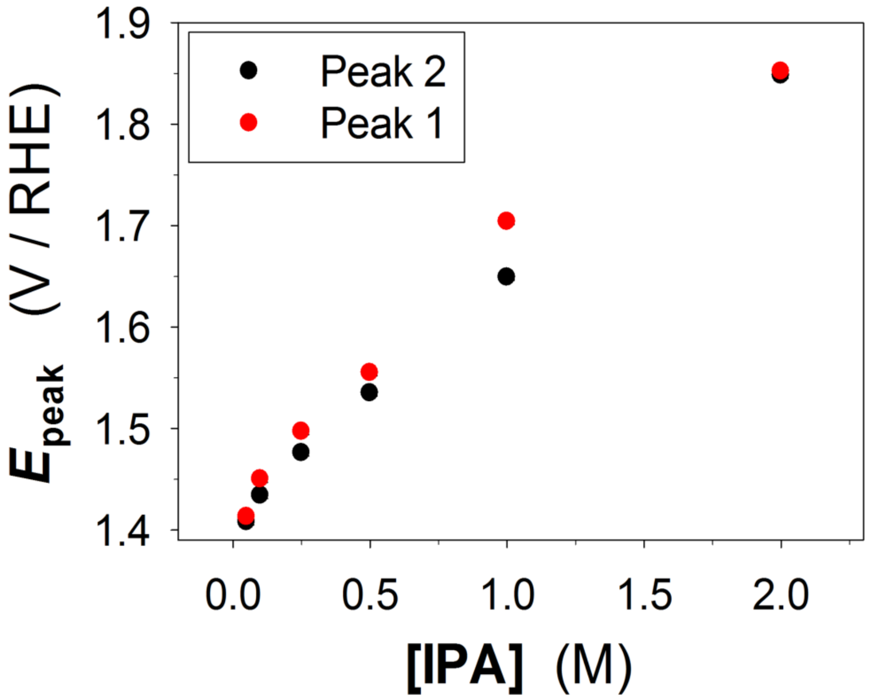

Figure 5.4 C. Relationship between the peak potential (E_{peak}) of IPA oxidation peaks 1 and 2 and the concentration of IPA within the electrolyte.

5.3.6 Effect of Presence of Dissolved O_2

As discussed at the beginning of Results and Discussion (section 5.3), OER occurs almost concurrently with the alcohol oxidation. In addition, Figure 5.4 A shows that the onset potential of OER shifts towards higher values as [IPA] increases. In this series of experiments we analyze if the presence of dissolved molecular oxygen near the electrode surface has any effect on the oxidation of IPA. The molecular oxygen is generated in situ by extending the potential limit of the CV scan into the region where OER takes place and by cycling the electrode several times.

The amount of dissolved O_2 is related to the upper scan reversal potentials ($E_{\mathrm{up,rev}}$), which range from $E_{\mathrm{up,rev}} = 1.60$ V to 2.00 V. The application of $E_{\mathrm{up,rev}} = 1.60$ V generates only a small amount of O_2 because the rate of OER on Ni electrodes at this potential is very low, while the application of $E_{\mathrm{up,rev}} = 2.00$ V generates a significant amount of O_2. The high surface area and porous structure of the Ni foam electrode facilitates the production of small oxygen bubbles that remain either attached to the electrode surface or are trapped within the macro-pores of the material. Thus, OER at the electrode surface results in an environment in which the electrolyte in the immediate vicinity of the electrode has a significant amount of O_2. Figure 5.5 shows overlaid CV profiles for three different values of $E_{\mathrm{up,rev}}$, namely 1.60, 1.80 and 2.00 V, for a Ni foam electrode in 0.50 M aqueous KOH + 0.10 M IPA acquired at $T = 293$ K and $s = 50$ mV s^{-1}. The only observable difference between these three CV profiles is the expected increased I due to OER as $E_{\mathrm{up,rev}}$ increases; peaks 1 and 2 as well as the CV features due to the formation and reduction of β-NiOOH overlap for the three CV scans. On the basis of this experiment, we may conclude that the presence of dissolved O_2 within the electrode vicinity has no effect on the oxidation behavior of IPA.

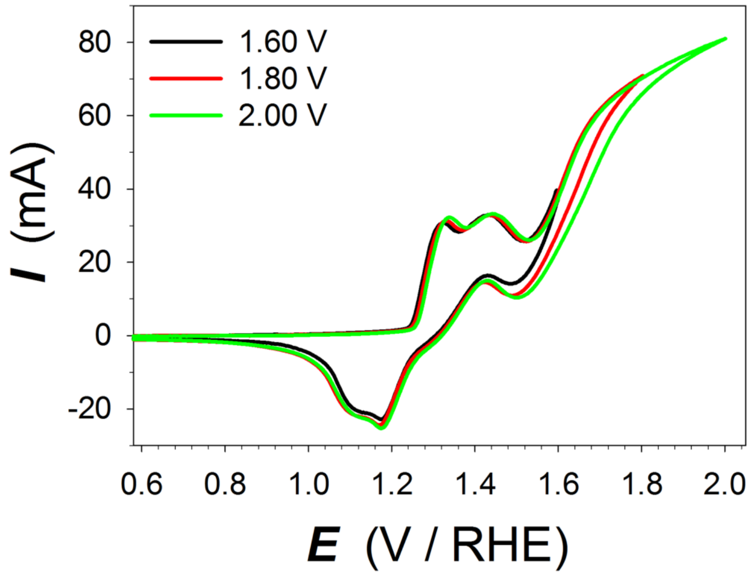

Figure 5.5. CV profiles with various upper scan reversal potentials ($E_{\mathrm{up,rev}}$ = 1.60 V, 1.80 V, and 2.00 V) for Ni foam in 0.50 M aqueous KOH + 0.10 M IPA collected at T = 298 K and with s = 50 mV s^{-1}.

5.3.7 Effect of Temperature

In industrial electrocatalysis applications, the relationship between the efficiency of the reaction and the temperature is a key design consideration [7, 8, 27]. In order to analyze if T variation has any impact on IPA oxidation, we performed a series of experiments at different T values. Figure 5.6 A shows the CV profiles for Ni foam electrodes in 0.50 M KOH + 0.10 M IPA collected at several temperatures ranging from T = 298 ± 1 to 343 ± 1 K, with the first interval being 5 K and the subsequent intervals being 10 K. The CV profiles reveal the following changes that arise upon T increase: (i) a significant increase in the I_{peak} values for peaks 1 and 2; (ii) a gradual merger of the I_{peak} values for peaks 1 and 2 (iii) a shift of the onset of OER towards

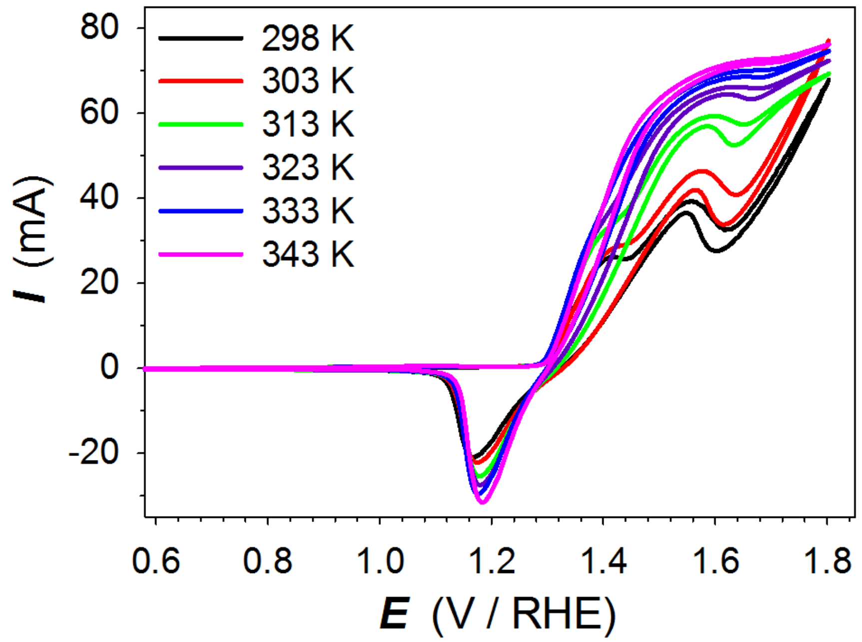

Figure 5.6 A. CV profiles of Ni foam in 0.50 M aqueous KOH + 0.10 M IPA collected at various *T* values ranging from 298 K to 343 K with *s* = 50 mV s^{-1}.

higher *E* values; and (iv) an increase in the amount of β-NiOOH (*q* for β-NiOOH reduction increases from ca. 45 to 56 mC) and a slight shift of the β-NiOOH reduction peak towards higher *E* values. An analysis of the anodic CV scans is complicated, because three electrode processes occur concurrently. However, the shift of the onset potential of OER towards higher values and the change in the amount of β-NiOOH allow us to conclude that the increase in *I* brought about by *T* rise is mainly due to a greater rate of IPA oxidation. These changes in the CV profiles indicate that the *T* increase accelerates IPA oxidation through the formation of a thicker β-NiOOH surface layer and through faster diffusion of IPA from the bulk of electrolyte to the interfacial region. Figure 5.6 B shows the I_{peak} values of peaks 1 and 2 as a function of T, and demonstrates that the increase in I_{peak} as a function of T is not linear. The I_{peak} values for peak 1 range from 38 mA (j = 8.2 mA cm^{-2}) at T = 298 K to 73 mA (j = 16 mA cm^{-2}) at T = 343 K. The results reveal that, at higher temperatures, the I_{peak} values for peak 1 and 2 are almost the same. The same trend is observed when the concentration of IPA is increased (see Figure 5.4 B). We assign this behavior to the enhanced diffusion of IPA from the electrolyte bulk to the interfacial region, thus replenishing IPA that has been consumed in its oxidation in the forward-going scan. Figure 5.6 C presents the relationship between the E_{peak} values of peaks 1 and 2 and T; the values of E_{peak} for peaks 1 and 2 are almost the same. There is a slight shift in the E_{peak} values for peaks 1 and 2 of about 11 mV as T is raised from 298 to 343 K.

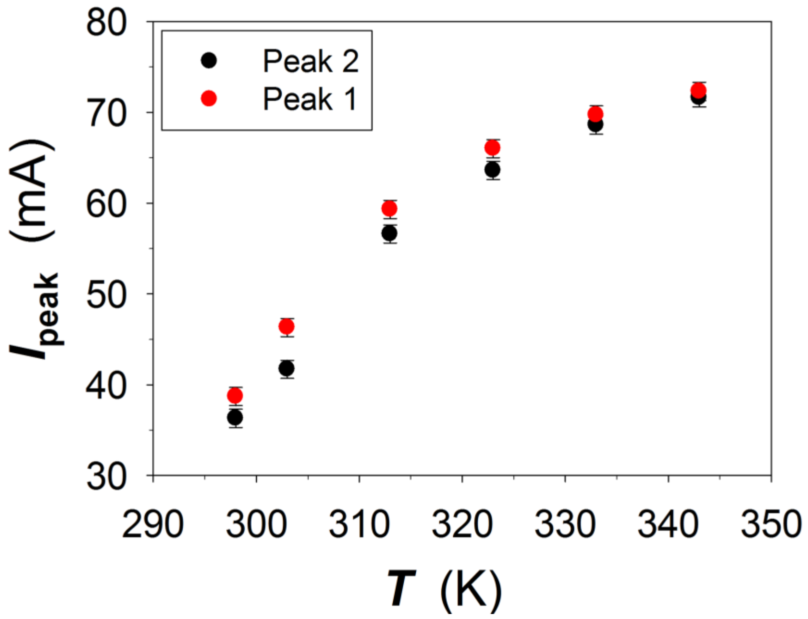

Figure 5.6 B. Relationship between the maximum peak current (I_{peak}) of IPA oxidation peaks 1 and 2 and the temperature.

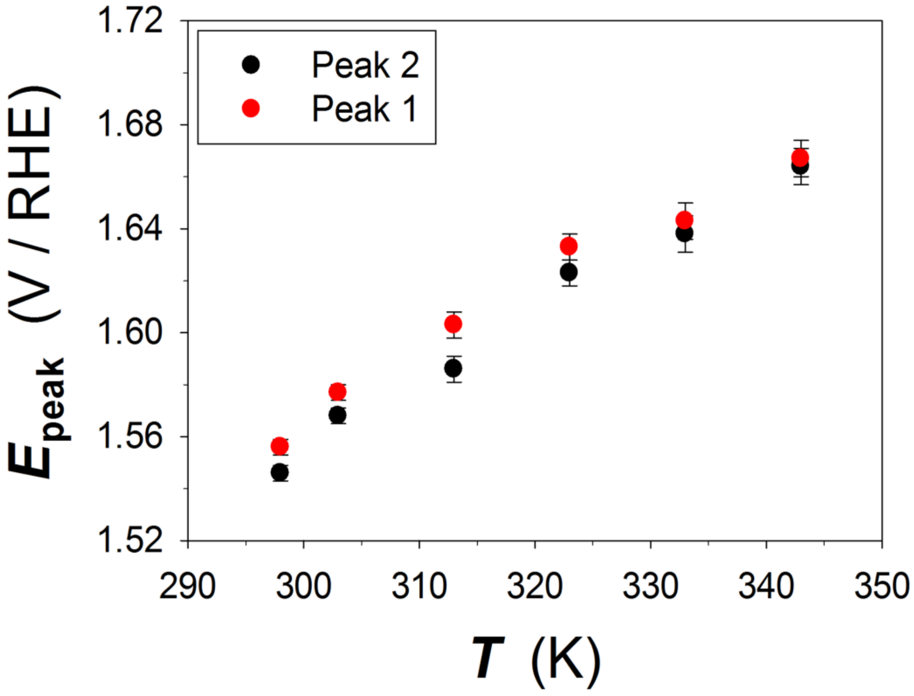

Figure 5.6 C. Relationship between the peak potential (E_{peak}) of IPA oxidation peaks 1 and 2 and the temperature.

5.3.8 Effect of CV Scan Rate

The effect of potential scan rate on the IPA oxidation peaks 1 and 2 as well as on the β-NiOOH formation and reduction CV features is investigated in order to gain further insight into these processes. Figure 5.7 displays six CV profiles acquired at six different s values (s = 5, 10, 25, 50, 100 and 150 mV s^{-1}) for Ni foam electrodes in 0.50 M aqueous KOH + 0.10 M IPA at T = 298 K. The increase of s gives rise to qualitative changes in CV features associated with IPA oxidation and β-NiOOH formation and reduction, we discuss these features separately. As regards the CV features for β-NiOOH formation and reduction, the following changes are observed: (i) as s increases the β-NiOOH formation and reduction peaks become progressively larger; (ii) the increase of I is proportional to $\sqrt{s}$; and (iii) as s increases the β-NiOOH formation peak shifts towards higher E values and the β-NiOOH reduction peak shifts towards lower E values (the separation between these two peaks increases). At $s = 5$ mV s^{-1}, the separation in E for these two peaks is ca. 54 mV, whereas at $s = 150$ mV s^{-1} the peak separation is ca. 180 mV. As regards IPA oxidation, an increase in s brings about no changes to I of IPA oxidation ($I = 20$ mA, corresponding to $j = 6.5$ mA cm^{-2}), as it is apparent from the first four graphs for $s \leq 50$ mV s^{-1}. In the case of $s = 100$ and 150 mV s^{-1}, the value of I for IPA oxidation seems to be higher than at lower s values; this behavior is due to overlap with the current associated with β-NiOOH formation and the concurrently-occurring shift of β-NiOOH formation peak towards higher E values. Thus, we conclude that for $5 \leq s \leq 150$ mV s^{-1} the current of IPA oxidation is independent of the potential scan rate.

Our data agree with previously published results that demonstrate the linear relationship between I of β-NiOOH formation and reduction peaks and $s^{1/2}$, and the increase in E separation between the β-NiOOH formation and reduction peaks as s increases [28 – 30]. These CV characteristics are typical of an irreversible surface electrochemical process and indicate that

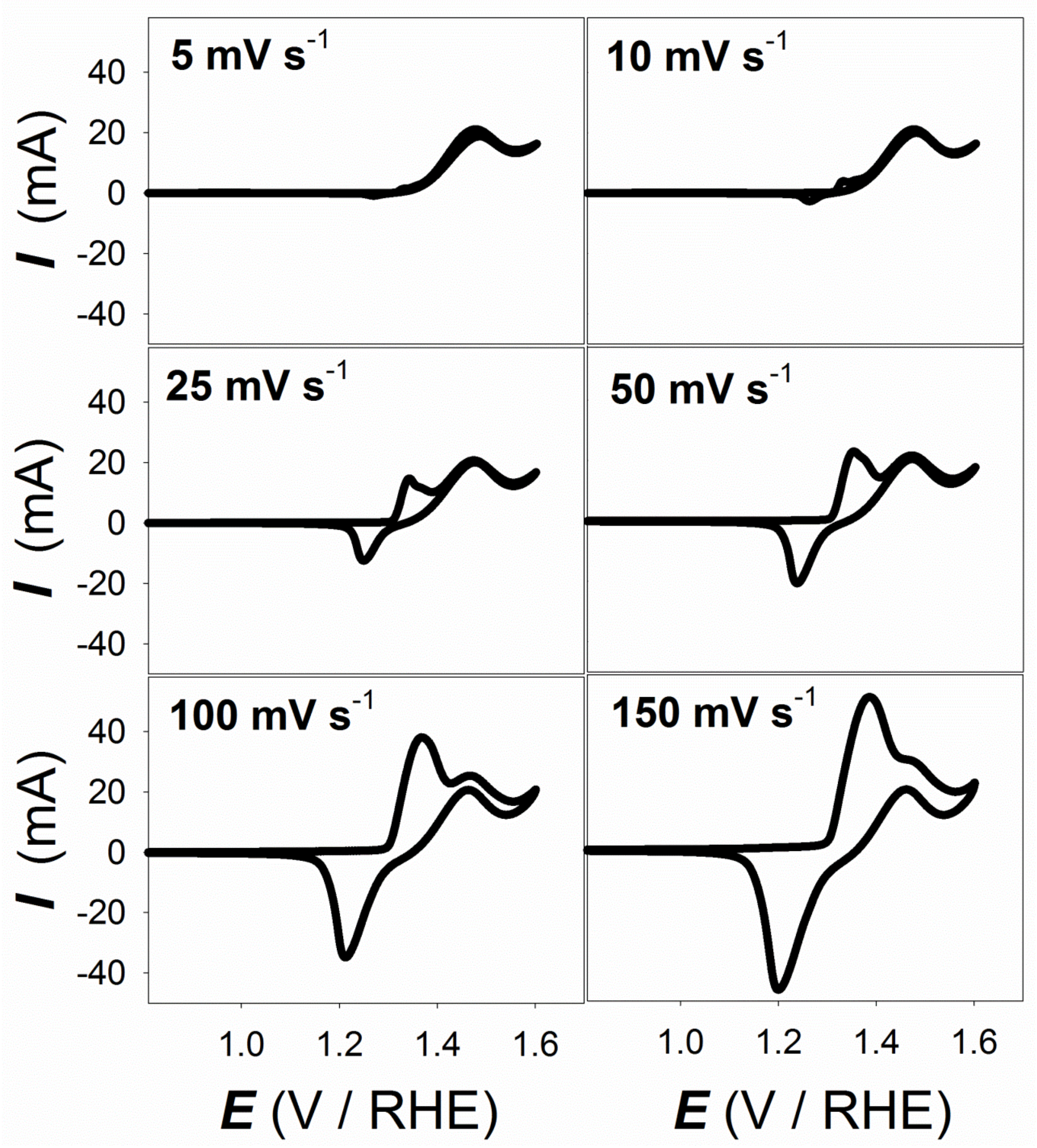

Figure 5.7. CV profiles of Ni foam in 0.5 M aqueous KOH + 0.1 M IPA collected with various potential scan rates (*s* = 5, 10, 25, 50, 100, and 150 mV s^{-1}) at *T* = 298 K.

there is no equilibrium between β-NiOOH formation and reduction. This observation is important because the mechanistic and kinetic analysis of IPA oxidation proposed by Fleischmann et al. [9, 10] included a rate determining step (eq. 5.10) that involves β-NiOOH as a reactant and β-$Ni(OH)_2$ as a product. In this mechanism the assumption that an equilibrium exists between β-$Ni(OH)_2$ and β-NiOOH (eq. 5.8) implies that β-$Ni(OH)_2$ produced in equation 5.10 becomes right away converted to β-NiOOH, making further oxidation of IPA possible. Because β-$Ni(OH)_2$ and β-NiOOH are formed and reduced at different potentials, and therefore there is no equilibrium between β-$Ni(OH)_2$ and β-NiOOH, the mechanism proposed by Fleishmann et al. cannot be correct. At present, we are unable to propose an alternative mechanism of IPA oxidation based on CV data alone.

5.3.9 Electrolysis of Isopropanol Using a Nickel Foam Anode

Chronoamperometric electrolysis was performed to study the oxidation of isopropanol as a function of time with the objective of determining whether Ni foams were suitable electrocatalysts for the conversion of IPA to acetone; the initial electrolyte composition was 1.0 M aqueous KOH + 0.1 M IPA. The electrolysis was conducted at E = 1.45 V vs. RHE because this potential corresponds to the E_{peak} of IPA oxidation in CV profiles reported in Figure 5.4 A. The temperature was maintained constant (T =298 K) and the anolyte was continuously agitated using a magnetic stirrer; the duration of electrolysis was 600 min (10 hrs). Sample aliquots of 100 μL in volume were removed approximately every hour to measure the concentration of IPA and acetone with HPLC. Figure 5.8 A shows the concentrations of IPA and acetone as a function of electrolysis time ($t_{electrolysis}$); figure 5.8 B shows the HPLC chromatogram before and after 10 hours of electrolysis. In the first 100 min of electrolysis, there is no significant, measurable

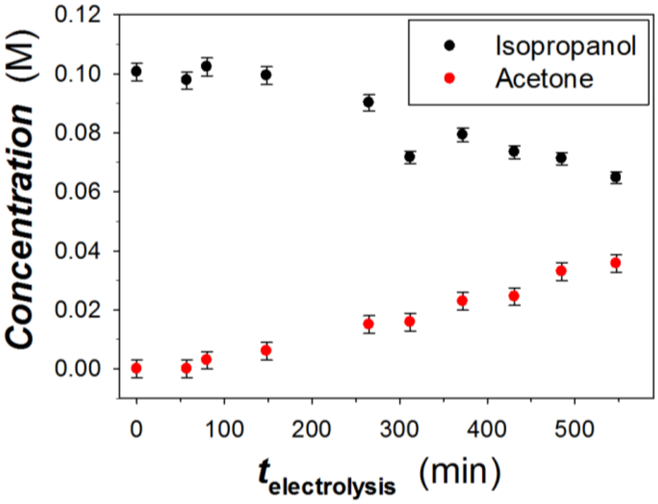

Figure 5.8A. Concentration of IPA and acetone at various times ($t_{electrolysis}$) during the electrolysis of IPA in 1.00 M aqueous KOH using a Ni foam electrode; E = 1.45 V, T = 298 K.

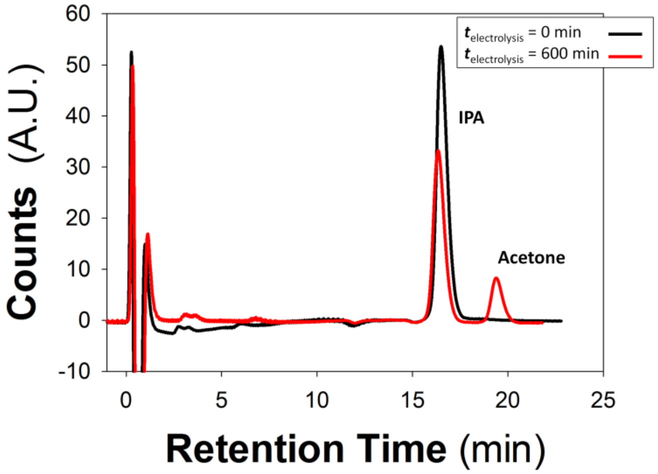

Figure 5.8 B. HPLC chromatograms corresponding to IPA electrolysis samples collected at $t_{electrolysis}$ = 0 min and $t_{electrolysis}$ = 600 min.

decrease in the concentration of IPA. After this initial 100 min, the concentration of IPA decreases steadily at a rate of ca. 5.5 ± 0.3 mM per hour and the concentration of acetone increases at a steady rate of 5.7 ± 0.3 mM per hour. Throughout the ten hour electrolysis, the *j* of IPA oxidation decreases slightly from an initial value of j = 3.5 mA cm^{-2} to a final value of j = 2.6 mA cm^{-2}. It is unlikely that this decrease in *j* is the outcome of electrode poisoning, but rather a result of the decrease in concentration of IPA from 0.1 M at $t_{\text{electrolysis}}$ = 0 min to 0.064 M at $t_{\text{electrolysis}}$ = 600 min. Electrode poisoning can be ruled out for this system because (i) there is no decrease in the rate of conversion of IPA to acetone over the course of this long term electrolysis, and (ii) CV profiles acquired prior to and after the electrolysis were identical.

Isopropanol oxidation using various electrocatalyst materials was a subject of several studies; Table 5.1 compares the *j* values for the oxidation of IPA in aqueous KOH solutions for different electrode materials from studies employing conditions comparable this study. We examine and discuss *j* values from CV profiles and CA electrolysis experiments. It is important to note that many of those studies used a higher concentration of IPA and KOH; [KOH] is expected to have little effect on the comparison of *j* values but an increase in [IPA] gives rise to higher *j* values for IPA oxidation. As regards Ni-based materials, the *j* values measured from CV profiles for IPA oxidation using a Ni foam electrodes (our results) and bulk Ni electrodes (results referenced in Table 5.1) are approximately the same, namely 5.8 mA cm^{-2} for Ni foams and 6 mA cm^{-2} for bulk Ni. However, our electrolysis study demonstrated that Ni foam electrodes can sustain a significantly higher *j* value (2.6 mA cm^{-2}) than bulk Ni electrodes (0.08 mA cm^{-2}). As regards other electrode materials, it is important to add that the mechanism for IPA oxidation using anode materials such as Pt, Au, and Pd is completely different from the mechanism presented above for Ni electrocatalysts [27, 31, 32]. Table 5.1 shows that Pt is a poor electrocatalyst for the oxidation of IPA to acetone. On the other hand, Pd and Au anodes appear to be good electrocatalysts for IPA oxidation because they produce high *j* values in CV and CA experiments. However, these materials are subject to poisoning due to the strong adsorption of acetone and acetone oxidation products [33, 34]. Table 5.1 reveals that Ni-Ni_5P_2 anode appears to be a suitable electrocatalyst for IPA oxidation [15] because it shows a fourfold increase in *j* as compared to bulk Ni and Ni foams. In addition, Ni-Ni_5P_2 is also expected to resist poisoning because acetone does not adsorb strongly to Ni materials.

Table 5.1. Current density values for oxidation of IPA using various anode materials.

Anode	***j* IPA Oxidation (mA cm^{-2})**	***E* (V / reference)**	**Conditions**	**Reference**
Ni Foam	5.8 (CV, s = 50 mV s^{-1}) 2.6 (CA)	1.45 V / RHE	[IPA] 0.1 M ; [KOH] 0.5 M	This study
Ni (bulk)	6 (CV, s = 10 mV s^{-1}) 0.08 (CA)	0. 6 V / Hg/HgO	[IPA] 0.1 M; [KOH] 0.87 M;	[9, 12]
Ni-Ni_5P_2	23 (CV, s = 50 mV s^{-1})	0.38 V / SCE	[IPA] saturation; [KOH] 5.0 M	[15]
Pd – Ni foam	64 (CV, s = 50 mV s^{-1}) 9 (CA)	–0.4 V / Ag/AgCl	[IPA] 1.0 M; [KOH] 2.0 M	[34]
Pt (bulk)	4 (CV, s = 5 mV s^{-1}) < 2.5 (CA)	–0.4 V / SCE	[IPA] 1.0 M; [KOH] 1.0 M	[33]
Pd (bulk)	52 (CV, s = 5 mV s^{-1}) < 2.5 (CA)	–0.4 V / SCE	[IPA] 1.0 M; [KOH] 1.0 M	[33]
Au (bulk)	32 (CV, s = 5 mV s^{-1}) < 2.5 (CA)	–0.4 V / SCE	[IPA] 1.0 M; [KOH] 1.0 M	[33]

5.4 Conclusions

In this contribution, the electrochemical conversion of isopropanol to acetone using a Ni foam electrode is examined using CV in well-defined experimental conditions that include variation of the IPA concentration and the concentration of the KOH supporting electrolyte, the presence of O_2(g), several different temperatures, and several CV scan rates. The CV data obtained from these experiments is compared with previous studies to yield the following conclusions:

(i) The formation of a β-NiOOH species at the surface of the electrode is necessary for the conversion of IPA to acetone, however the two processes do not proceed simultaneously in all conditions.

(ii) Increase in the [KOH] does not affect the I of IPA oxidation.

(iii) There is a logarithmic increase in I of IPA oxidation as a function of [IPA].

(iv) IPA oxidation is unaffected by the presence of oxygen within the electrolyte and interfacial electrode region.

(v) The I of IPA oxidation increases if the system is heated; however a large increase in temperature is not necessary to be of benefit to the reaction.

(vi) The I of IPA oxidation is unaffected by the potential scan rate; however the scan has significant influence on the β-NiOOH formation and reduction CV features.

Controlled-potential electrolysis of IPA using a Ni foam anode successfully converts IPA to acetone at a rate of about 5.6 mM per hour; the Ni foam electrode sustains a j value of 2.6 mA cm^{-2}. In addition, these materials also offer many practical advantages over the use of bulk Ni such as their high A_{ecsa}, low mass, and low material use. Thus we conclude that Ni foams are promising electrode materials that can be applied to organic electrochemical processes for simple FGI such as the conversion of an alcohol to a ketone.

5.5 References

(1) L. Eberson, H. Schafer, *Organic Electrochemistry*; Springer, Berlin, **1971**.

(2) O.R. Brown, J. A. Harrison, *J. Electroanal. Chem.* **1969**, 21, 387–407.

(3) H. J. Schafer, *Oxidation of Organic Compounds at the Nickel Hydroxide Electrode*; Springer, Berlin, **1987**.

(4) H. J. Schafer, *Agnew. Chem. Int. Ed. Engl.* **1981**, 20, 911–934.

(5) A. J. Fry, M. A. Mitnick,, R. G. Reed, *J. Org. Chem*. **1970**, 35, 1232–1234.

(6) K. Sasaki, W .J. Newby, *Electroanal. Chem. Interfacial Electrochem*. **1969**, 20, 137–165.

(7) F. Goodridge, *Chem. and Proc. Eng*. **1968**, 49, 93.

(8) R. D. Armstrong, O. R. Brown, R. D. Giles, J. A. Harrison, *Nature* **1968**, 219, 94–94.

(9) M. Fleischmann, K. Korinek, D. Pletcher, *J. Chem. Soc., Perkin Trans*. **1972**, 2, 1396–1403.

(10) M. Fleischmann, K. Korinek, D. Pletcher, *J. Electroanal. Chem. Interfacial Electrochem*. **1971**, 31, 39–49.

(11) G. Vertes, G. Horanyi, *Electroanal. Chem. Interfacial Electrochem.* **1974**, 52, 47–53.

(12) P. M. Robertson, *J. Electoanal. Chem*. **1980**, 111, 97–104.

(13) A. J. Motheo, S. A. S. Machado, F. S. B. Rabelo, J. R. J. Santos, *J. Braz. Chem. Soc*. **1994**, 5, 161–165.

(14) A. Kowal, S. N. Port, R. J. Nichols, *Catal. Today* **1997**, 38, 483–492.

(15) A. Budniok, E. Kozlowska, *Thin Solid Films* **1991**, 204, 341–347.

(16) M. Grden, M. Alsabet, G. Jerkiewicz, *ACS Appl. Mater. Interfaces* **2012**, 4, 3012–3021.

(17) J. van Drunen, B. Kinkead, M. C. P. Wang, B. D. Gates, E. Sourty, G. Jerkiewicz, *ACS Appl. Mater. Interfaces* **2013**, 5, 6712–6722.

(18) H. Angerstein-Kozlowska, *Surfaces, Cells, and Solutions for Kinetic Studies*; E. Yeager, Ed.; Comprehensive Treatise of Electrochemistry Volume 9; Plenum Press, NY, **1984**.

(19) B. E. Conway, W. B. A. Sharp, H. Angerstein-Kozlowska, E. E. Criddle, *Anal. Chem.* **1973**, 45, 1331-1336.

(20) B. Yang, G. Yu, D. Shuai, *Chemosphere* **2007**, 67, 1361–1367.

(21) J. Banhart, *Prog. Mater. Sci*. **2001**, 46, 559–632.

(22) A. Montillet, J. Comiti, J. Legrand, *J. Appl. Electrochem*. **1993**, 23, 1045–1050.

(23) V. Paserin, S. Marcuson, J. Shu, D. S. Wilkinson, *Adv.Eng. Mater*. **2004**, 6, 454–459.

(24) H. Bode, K. Dehmelt, J. Witte, *Electrochim. Acta* **1966**, 11, 1079–1087.

(25) A. Jouanneau, M. Keddam, M. C. Petit, *Electrochim. Acta* **1976**, 21, 287–292.

(26) M. Alsabet, M. Grden, G. Jerkiewicz, *Electrocatalysis* **2011**, 2, 317–330.

(27) C. Lamy, J.-M. Léger, S. Srinivasan, *Direct methanol fuel cells: From a twentieth century electrochemist`s dream to a twenty-first century emerging technology*; J. O. Bockris Ed.; Modern Aspects of Electrochemistry, Plenum Press, NY, **2001**, p. 53–118.

(28) D. M. Mac Arthur, *J. Electrochem. Soc*. **1970**, 17, 422–426.

(29) C. Zhang, S. Park, *J. Electrochem. Soc*. **1987**, 134, 2966–2970.

(30) L. Bing, Y. Huatang, Z. Yunshi, Z. Zuoxiang, S. Deying, *J. Power Sources* **1999**, 79, 277–280.

(31) C. Lamy, E. M. Belgsir, J.-M. Leger, *J. Appl. Electrochem*. **2001**, 31, 799–809.

(32) J. B. Goodenough, B. L. Cushing, *Oxide-based ORR catalysts*; W. Vielstich, H. A. Gasteiger, A. Lamm Eds.; Handbook of Fuel Cells - Fundamentals, Technology and Applications, John Wiley & Sons, NY, **2003**, p. 520.

(33) J. Ye, J. Liu, C. Xu, S. P. Jiang, Y. Tong, *Electrochem. Commun*. **2007**, 9, 2760–2763.

(34) Y. Cheng, Y. Liu, D. Cao, G. Wang, Y. Gao, *J. Power Sources* **2011**, 196, 3124–3128.

Chapter 6

Nickel Foams as an Electrochemically Active Support Material for Platinum Electrocatalysts [3]

6.1 Introduction

The following four electrochemical reactions are of upmost importance to water electrolysis and hydrogen fuel cell technologies: (i) hydrogen evolution reaction (HER, eq. 6.1); (ii) hydrogen oxidation reaction (HOR, eq. 6.2); (iii) oxygen reduction reaction (ORR, eq. 6.3); and (iv) oxygen evolution reaction (OER, eq. 6.4). These reactions are studied extensively in the field of electrocatalysis towards the development of energy conversion and energy delivering devices. In alkaline water electrolyzers, alkaline fuel cells, and alkaline alcohol fuels cells, the following reactions occur.

$$2\,H_2O + 2\,e^- \longrightarrow H_2 + 2\,OH^- \qquad (6.1)$$

$$H_2 + 2\,OH^- \longrightarrow 2\,H_2O + 2\,e^- \qquad (6.2)$$

$$O_2 + 2\,H_2O + 4\,e^- \longrightarrow 4\,OH^- \qquad (6.3)$$

$$4\,OH^- \longrightarrow O_2 + 2\,H_2O + 4e^- \qquad (6.4)$$

---

[3] The work presented in this chapter is submitted to *ACS Applied Materials and Interfaces* for review.

The availability of high-purity hydrogen gas is one important challenge that must be addressed for the implementation of fuel cells as a viable energy delivering technology. The global demand for hydrogen gas grows at a rate of approximately 10% per year and is driven by the use of hydrogen in fertilizer production, food processing, metallurgical applications, and many other industries [1, 2]. Increased commercialization of fuel cells will contribute to the growing demand for high-purity hydrogen gas that is generated through a limited number of processes that includes the electrolysis of water (eq. 6.5) [2, 3]. It is generally accepted that the mechanism for cathodic hydrogen evolution in alkaline media proceeds through the steps outlined in eq. 6.6 – 6.8 [4 – 10].

$$H_2O_{\text{(liquid)}} \longrightarrow H_{2\,\text{(gas)}} + \tfrac{1}{2}\,O_{2\,\text{(gas)}} \tag{6.5}$$

$$M + H_2O + e^{-} \longrightarrow MH + OH^{-} \tag{6.6}$$

$$MH + H_2O + e^{-} \longrightarrow M + H_2 + OH^{-} \tag{6.7}$$

$$2\,MH \longrightarrow 2\,M + H_2 \tag{6.8}$$

Many commercial alkaline electrolyzers use Ni-based electrodes. This is a logical choice due to the stability of Ni in alkaline media [11, 12], the electrocatalytic activity of Ni [11, 13], and the relatively low cost of Ni-based materials. A large number of studies are available examining water electrolysis electrodes made-up of combinations of nickel and other metals, such as Ni/Fe [14 – 16], Ni – Zn alloy [7, 15], Ni – Fe – Zn alloy [15], Ni – P alloy [17], Co – P alloy [17], Ni – P – Fe alloy [17], Ni – Mo [15, 18], Ni – Mo – Cd alloy [18], Ni/NiFeS [19], Raney-Ni/Mo [10], Ni + spinel-type Co_3O_4, Ni + La-doped Co_3O_4 [20], and many others. The development of industrial electrode materials focuses on low-cost, high efficiency, and long lifetime; in this respect, Ni-based materials are relevant electrocatalysts for alkaline water electrolysis. Several types of fuel cells operate in alkaline conditions and utilize Pt or combined Pt / Ni electrocatalysts for HOR at the anode or ORR at the cathode [21 – 26]. The results presented herein are applicable to the development of water electrolyzers, alkaline fuel cells, alkaline alcohol fuel cells, and borohydride fuel cells.

Open-cell metallic foams are of interest for research in electrochemistry for applications in electrocatalysis and energy storage. The original use of open-cell Ni foams was as a support and current collector for alkaline battery electrodes [27]. A number of papers were published describing the use of Ni-based foams as an electrode support material for other electrocatalysts including Pt [28 – 30], Rh [29, 31], Pd [32 – 34], Ag [35], Sn – Co [36], and Co – W – B [37]. As an electrocatalyst support material, Ni foams offer a consistent open-pore 3-D structure [38] with tunable density and large surface area. In addition, because Ni is also an electrochemically active material, in some instances the Ni foam can behave as an electrocatalytically active support.

This study presents the fabrication and characterization of Pt / Ni foams and includes a discussion of their applicability as electrocatalysts for HER, HOR, ORR, and OER in alkaline media. Platinum particles are deposited on Ni foam via electroless deposition; the resulting material is characterized using a combination of materials science, electrochemical, and analytical techniques. Scanning electron microscopy (SEM) is used to examine the size and morphology of the Pt particles. Energy dispersive X-ray spectroscopy (EDS) is used to determine the chemical composition. Cyclic voltammetry (CV) is used to determine the electrochemically active surface area (A_{ecsa}) of the deposited Pt. Inductively coupled plasma optical emission spectroscopy (ICP-OES) is used to determine the mass loading of deposited Pt. Each of the above mentioned electrochemical reactions (HER, HOR, ORR, and OER) is carried out in alkaline media using Pt / modified Ni foams with various Pt loadings. The effectiveness of these electrocatalysts is studied using linear sweep voltammetry (LSV) and steady state polarization curves (Tafel plots). Unmodified Ni foam and polycrystalline Pt wire are also applied as electrocatalysts in the same experiments for comparison.

6.2 Experimental Section

6.2.1 Preparation of Pt Modified Ni Foams

Deposition of Pt on Ni foam was accomplished using an electroless deposition method that is similar to the impregnation method described in several other studies [39 – 43]. Uniform Ni foam disks, having diameters equal to 10 mm (ca. 3 mm in thickness), were first prepared using a punch. Prior to the deposition of Pt, each Ni foam disk is degreased with acetone under reflux for two hours in order to remove any organic impurities. The foam is then dried under ultra high purity (UHP) N_2 gas, and weighed using an analytical balance. To deposit Pt, the Ni foam disk was first placed in a glass vial and submerged in 10 mL of 0.20 M aqueous $NaBH_4$ (reducing agent) for 120 seconds, allowing the pores of the foam to become saturated with the solution. The foam was then removed from the $NaBH_4$ solution and, while still saturated with the $NaBH_4$ solution, placed in a glass vial with 10 mL of an aqueous solution of Pt salt containing 0.10 M KOH and allowed to soak for 120 seconds. Four different Pt salt solutions consisting of two Pt salts with different Pt oxidation states (Pt $^{2+}$ and Pt $^{4+}$) and two concentrations for each oxidation state were applied. Thus, the deposition solutions are as follows: 0.001 M K_2PtCl_4 (type A), 0.002 M K_2PtCl_4 (type AA), 0.001 M K_2PtCl_6, (type B), and 0.002 M K_2PtCl_6 (type BB). All solutions contained 0.10 M KOH, in addition to the dissolved Pt salt. After soaking for 120 seconds in the Pt salt solution, the foam was placed in fresh $NaBH_4$ for an additional 120 seconds and then again in fresh Pt salt solution for 120 seconds. The deposition steps are repeated 2, 5, or 10 times, as indicated by the number of times the Ni foam was soaked in the Pt salt solution. The nomenclature used herein refers to the concentration and type of Pt salt in the deposition solution, as well as the number of depositions. For example, samples of type AA10 are prepared using 0.002 M K_2PtCl_4 solution with 10 deposition events. The final step is always submersion in $NaBH_4$, followed by rinsing and sonicating in UHP water to remove deposition solution that may be trapped within the Ni foam pores, and drying in a stream of N_2 gas. All aqueous solutions are made with UHP water (Millipore).

6.2.2 Electrochemical Methods

Electrochemical analysis was carried out using a two-compartment Pyrex electrochemical cell and three electrodes. The working electrode (WE) was an unmodified nickel foam (supplied by the former Inco Technical Services Ltd.), a polycrystalline Pt wire, or a Pt / Ni foam prepared using the method described above. The foam materials were attached to a Ni wire sealed in a glass tube (Alfa Aesar Puratronic®, 0.25 mm in diameter) for electrical contact. The contribution of the Ni wire to the overall surface area in contact with the electrolyte, and thus to the electrochemical signal, is less than 1% and assumed to be negligible [44, 45]. The counter electrode (CE) consisted of high-purity Pt gauze (99.98% in purity, Alfa Aesar) spot-welded to a Pt wire (99.98% in purity, Alfa Aesar) and covered with electro-deposited Pt (Pt black). The surface area of CE was at least ten times larger than that of the WE. The reference electrode (RE) was a reversible hydrogen electrode (RHE) made in the same manner as the CE. Hydrogen gas (UHP, Praxair 5.0 grade) was bubbled through the RE compartment at a pressure of 1 bar. All potentials herein are reported with respect to RHE, unless otherwise noted. The RE was in electrolytic contact with the WE via a Luggin capillary; this minimizes the uncompensated resistance (R_Ω) of the solution. The separation between the WE and CE was approximately 3 cm. Electrochemical characterization was carried out in 0.50 M aqueous KOH solution (Sigma-Aldrich KOH pellets of 85% in purity, A.C.S. reagent grade) prepared using UHP water. Prior to each experiment, the electrolyte solution was degassed by bubbling UHP N_2(g) (Praxair 5.0 grade) for 30 minutes. Throughout the duration of electrochemical measurements, UHP N_2(g) was passed over the electrolyte to maintain the inert gas environment. Electrochemical impedance spectroscopy (EIS) was used to determine the value of R_Ω for this electrochemical set up at various potential values (E = –0.20, 0.00, 0.20, 0.80, and 1.50 V). The value of $R_\Omega = 0.68 \pm 0.04\ \Omega$ was determined by taking the average value from four separate measurements at each of the potentials mentioned (total of 20 measurements). Glassware was cleaned according to well established procedures [46]. The electrochemical measurements were carried out at a temperature of $T = 298 \pm 1$ K. An Autolab model PGSTAT302 potentiostat (Metrohm) equipped with NOVA Advanced Electrochemical Software (Metrohm) was used to control experimental parameters and acquire the data.

In the latter section of this thesis chapter we describe four reactions that are carried out in order to evaluate the electrocatalytic activity of Pt / Ni foams. The reactions are: (i) HER; (ii) HOR; (iii) ORR; and (iv) OER. They were carried out using two different experimental methods, linear sweep voltammetry (LSV) and a staircase-type Tafel polarization program. The Tafel polarization experiments were performed by pre-programming the potentiostat to apply a sequence of *E* steps, each with a magnitude of 5 mV. Each *E* value was held for 10 s, during this time the *I* was monitored and recorded. The *I* at each *E* value was determined by averaging the *I* values for the last 2 s of each *E* hold. This was done to represent the *I* at the given *E* value once the system is under steady-state or close to steady-state conditions. Figure 6. 1 illustrates the experimental program used for Tafel polarization. The applied *E* program is shown in blue and a typical *I* versus *t* profile is shown in red. Further details of the LSV and Tafel polarization analyses are provided in Table 6.1.

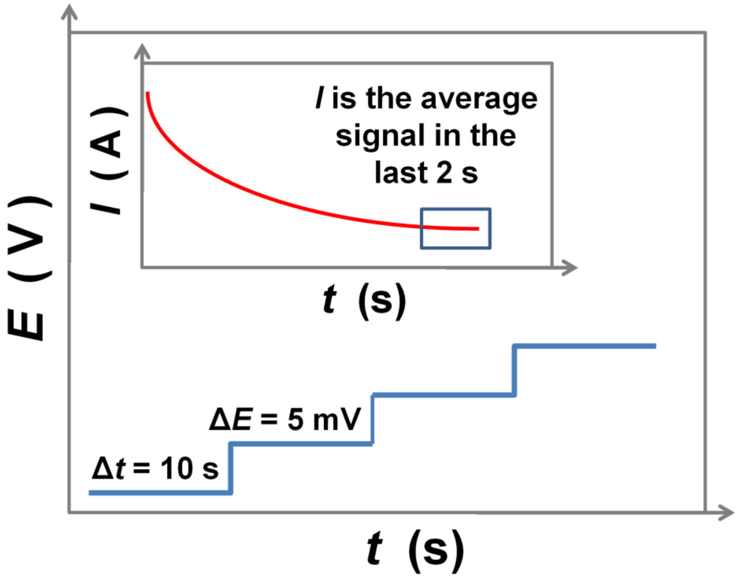

Figure 6.1 Experimental method used in the Tafel polarization experiments. The applied *E* program is shown in blue. A typical *I* vs. *t* plot is shown in red.

Before beginning each experiment with a new Pt / Ni electrode, fresh electrolyte was introduced into the electrochemical cell and purged with N_2 gas for 60 minutes. The electrolyte was then saturated with either H_2 gas (in the case of HER and HOR) or O_2 gas (in the case of ORR and OER) by bubbling the gas through the electrolyte for 30 minutes while stirring. Throughout the electrochemical measurements, the electrolyte was stirred and H_2 or O_2 gas was passed above the electrolyte to maintain saturation. The history of an electrode has an important influence on its electrochemical behavior [47]. Both Ni and Pt form oxides in *E* ranges that overlap with the ORR and OER; the presence of an oxide can influence the electrocatalytic activity. In an effort to control the history of the Pt / Ni foam electrodes, the electrocatalysis reactions were always performed in the following sequential order.

1. Electrolyte purged for 60 minutes with N_2 gas.
2. CV cycling for 100 cycles, $0.005 < E < 1.30$ V, $s = 100$ mV s^{-1} with N_2 gas purging.
3. Electrolyte saturated with H_2 gas for 30 minutes.
4. HER linear sweep voltammetry (LSV) experiment followed by HER Tafel polarization experiment.
5. HOR LSV experiment followed by HOR Tafel polarization experiment.
6. Electrolyte purged with N_2 gas for 60 minutes
7. CV cycling for 100 cycles, $0.005 < E < 1.30$ V, $s = 100$ mV s^{-1} with N_2 gas purging.
8. Electrolyte saturated with O_2 gas for 30 minutes.
9. ORR LSV experiment followed by ORR Tafel polarization experiment.
10. OER LSV experiment followed by OER Tafel polarization experiment.

Table 6.1. Procedures applied in the LSV and Tafel polarization experiments for the HER, HOR, ORR, and OER reactions.

Experiment	***E* Range (V vs. RHE)**	**Electrolyte Conditions**	**Scan Rate / Step Method**	**Duration (minutes)**
HER LSV	E = 0.00 to –0.20	H_2 saturated 0.50 M KOH, stirred, T = 293 K	s = 0.1mV s^{-1}	33
HER Tafel	E = 0.00 to –0.20	H_2 saturated 0.50 M KOH, stirred, T = 293 K	E step every 5 mV, E held for 10 s	7
HOR LSV	E = 0.00 to 0.25	H_2 saturated 0.50 M KOH, stirred, T = 293 K	s = 0.1mV s^{-1}	42
HOR Tafel	E = 0.00 to 0.25	H_2 saturated 0.50 M KOH, stirred, T = 293 K	E step every 5 mV, E held for 10 s	8
ORR LSV	E = 1.10 to 0.60	O_2 saturated 0.50 M KOH, stirred, T = 293 K	s = 0.1mV s^{-1}	83
ORR Tafel	E = 1.10 to 0.60	O_2 saturated 0.50 M KOH, stirred, T = 293 K	E step every 5 mV, E held for 10 s	17
OER LSV	E = 1.35 to 1.80	O_2 saturated 0.50 M KOH, stirred, T = 293 K	s = 0.1mV s^{-1}	75
OER Tafel	E = 1.35 to 1.80	O_2 saturated 0.50 M KOH, stirred, T = 293 K	E step every 5 mV, E held for 10 s	15

6.2.3 Electron and Ion Microscopy

Complementary electron and ion imaging techniques were used to analyze the Pt deposited on Ni foams. Scanning electron microscopy (SEM) characterization was performed using a Strata DB235 FESEM/FIB instrument operated at 5 kV equipped with an energy dispersive spectrometer (EDS) for elemental analysis (manufactured by EDAX). Focused ion beam (FIB) analysis was performed using a Micrion 2500 instrument (FEI Company). The FIB instrument was used to acquire images in the secondary ion (SI) and secondary electron (SE) detection modes, which provide different topographical and chemical information.

6.2.4 Inductively Coupled Plasma Optical Emission Spectroscopy Quantification of Platinum

Liquid samples for inductively coupled plasma optical emission spectroscopy (ICP–OES) quantification of Pt on Ni foams were prepared through the following steps: (i) Pt / Ni foam disks (three of each type) were weighed using an analytical balance; (ii) each disk was digested in 2.0 mL of aqua regia (mixture of HCl and HNO_3 in 3:1 proportion by volume) and sonicated for 30 minutes; (iii) the samples were diluted with 5 mL of UHP water; no further dilution was required. Sample blanks were prepared from unmodified Ni foam disks using the same method. The ICP–OES analysis was performed on the same day as the sample digestion. The analysis was performed using a radial view ARCOS ICP–OES instrument (SPECTRO Analytical Instruments, Kleve, Germany) fitted with a concentric nebulizer (Glass Expansion, Victoria, Australia) and a cyclonic spray chamber (SCP Science, Quebec, Canada). Platinum and nickel standard solutions

(0.1 – 500 mg L^{-1}) in ultrapure 2 % (v/v) HNO_3 with 2 % (v/v) HCl were prepared from commercially available 1000 mg L^{-1} single element standard solutions (SCP Science, Quebec, Canada) and UHP water. Optimization of the nebulizer flow rate was performed to arrive at a comprised set of conditions that maximizes sensitivity for the Pt II 214.423 nm emission line. The optimized conditions are outlined in Table 6.2. The intensities of the Pt II 214.423 nm and Ni II 221.648 nm optical emission lines were analyzed. Standard solutions were aspirated in order of increasing concentration, followed by the aspiration of sample blanks, and then the samples to be analyzed. The optical emission intensities were blank-subtracted and the elemental concentrations were determined by linear interpolation, using external calibration standards. The limit of detection for Pt and Ni were determined to be 0.04 and 0.01 µg L^{-1}, respectively. The limit of detection for Pt was at least 50 times lower than the amount of Pt in the least abundant sample. Three samples of each type (A2, A5, A10, B2, B5, B10, AA2, AA5, AA10, BB2, BB5, BB10) were analyzed and three replicates were performed for each sample.

Table 6.2. Optimal ICP operating conditions for the analysis of Pt in acid-digested Pt / Ni foam samples.

Operating Parameter	**Value**
Ar Plasma Coolant Flow Rate (L min^{-1})	12.0
Ar Auxiliary Flow Rate (L min^{-1})	1.0
Ar Nebulizer Flow Rate (L min^{-1})	1.0
R.F. Power (kW)	1.5
Sample Uptake Rate (mL min^{-1})	2.0
Plasma Observation Height A.L.C. (mm)	11

[*] A.L.C. refers to the plasma observation height in terms of millimeters *Above the Load Coil*.

6.3 Results and Discussion Part 1: Characterization of Pt / Ni Foam

This section presents the characterization of Pt / Ni foams with respect to size and morphology of the deposited Pt particles, as well as the electrochemical properties of the resulting Pt / Ni materials. The amount of Pt deposited on the Ni foam is quantified with respect to the electrochemical surface area of Pt and the mass of deposited Pt per gram of Ni foam substrate.

6.3.1 General Comments on the Deposition Method

6.3.2 Characterization of Pt / Ni Foam Using Scanning Electron Microscopy

Figure 6.2 displays three SEM images of Pt / Ni foam at various levels of magnification and one image of unmodified Ni foam for comparison. The Pt / Ni foam shown in these images is of type AA 10, meaning that the Pt was deposited from 2.0×10^{-3} M K_2PtCl_4 solution with 10 deposition events. As is discussed below, the AA 10 samples have the highest mass loading and highest surface area of Pt. The SEM images of AA 10 samples are the best ones for demonstrating the Pt particle morphology. Focused ion beam secondary ion (FIB SI) images of each sample type were also collected and are shown for reference in Figures 6.3 and 6.4, but will not be discussed in detail. Figure 6.2 Image A shows the surface microstructure of unmodified Ni foam; the surface is smooth with visible grain boundaries [45]. Image B shows Pt / Ni foam at a magnification of 2540×; at this level of magnification, the entire width of the struts that comprise the Ni foam structure is visible with Pt particles dispersed over the surface. Image C shows Pt / Ni foam at a magnification of 10 000×; at this magnification well-dispersed Pt particles are visible as small, bright specks. Some regions of the surface have larger clusters of deposited Pt that are ca. 1 µm in size. Image D shows Pt / Ni foam at 150 000× magnification. From images at the 150 000× and 200 000× level of magnification the size of the deposited Pt particles is estimated to be in the 5 – 30 nm range. However, we suspect that higher magnification images would reveal the presence of smaller particles that cannot be observed in these SEM images.

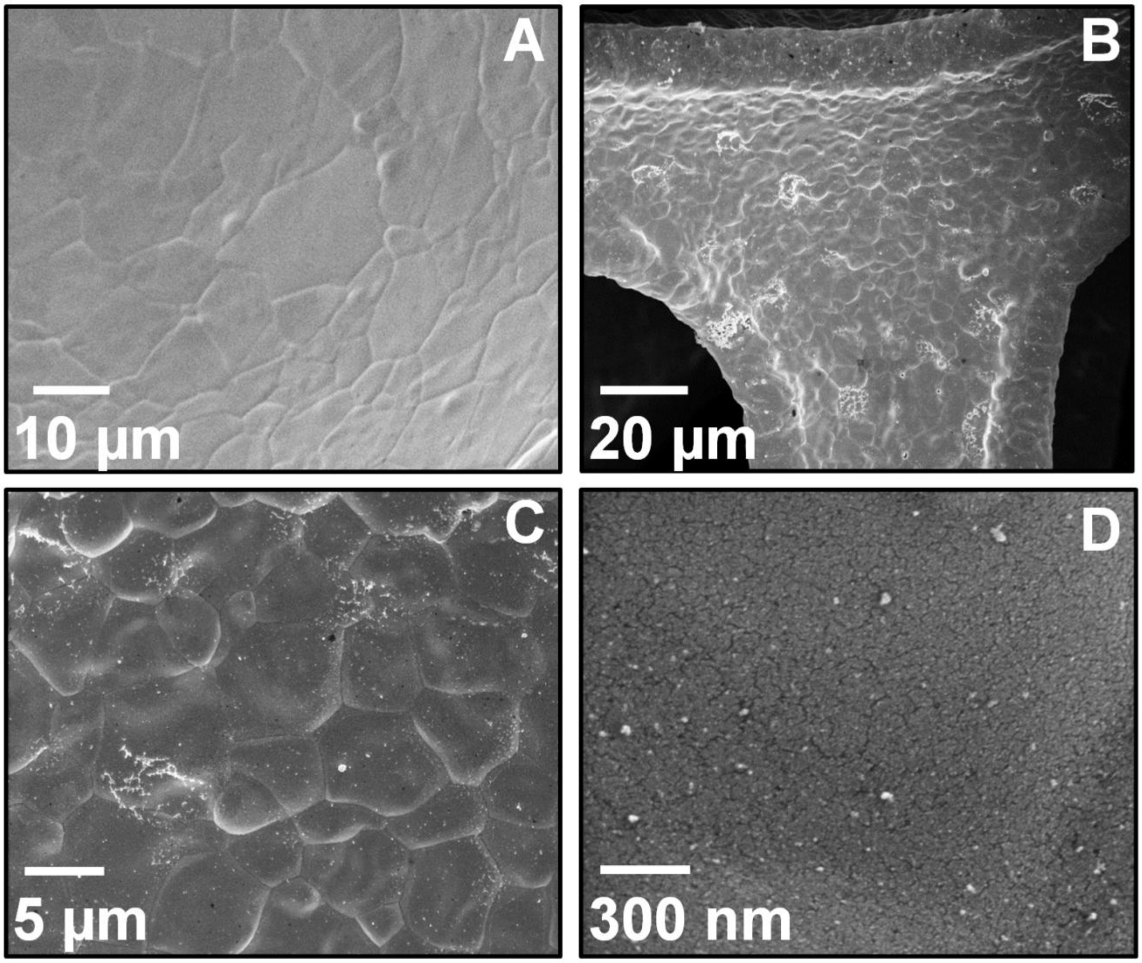

Figure 6.2. SEM image of unmodified Ni foam at 5000× magnification (A), and of Pt / Ni foam type AA 10 at various levels of magnification; 2540× (B), 10 000× (C), 150 000× (D).

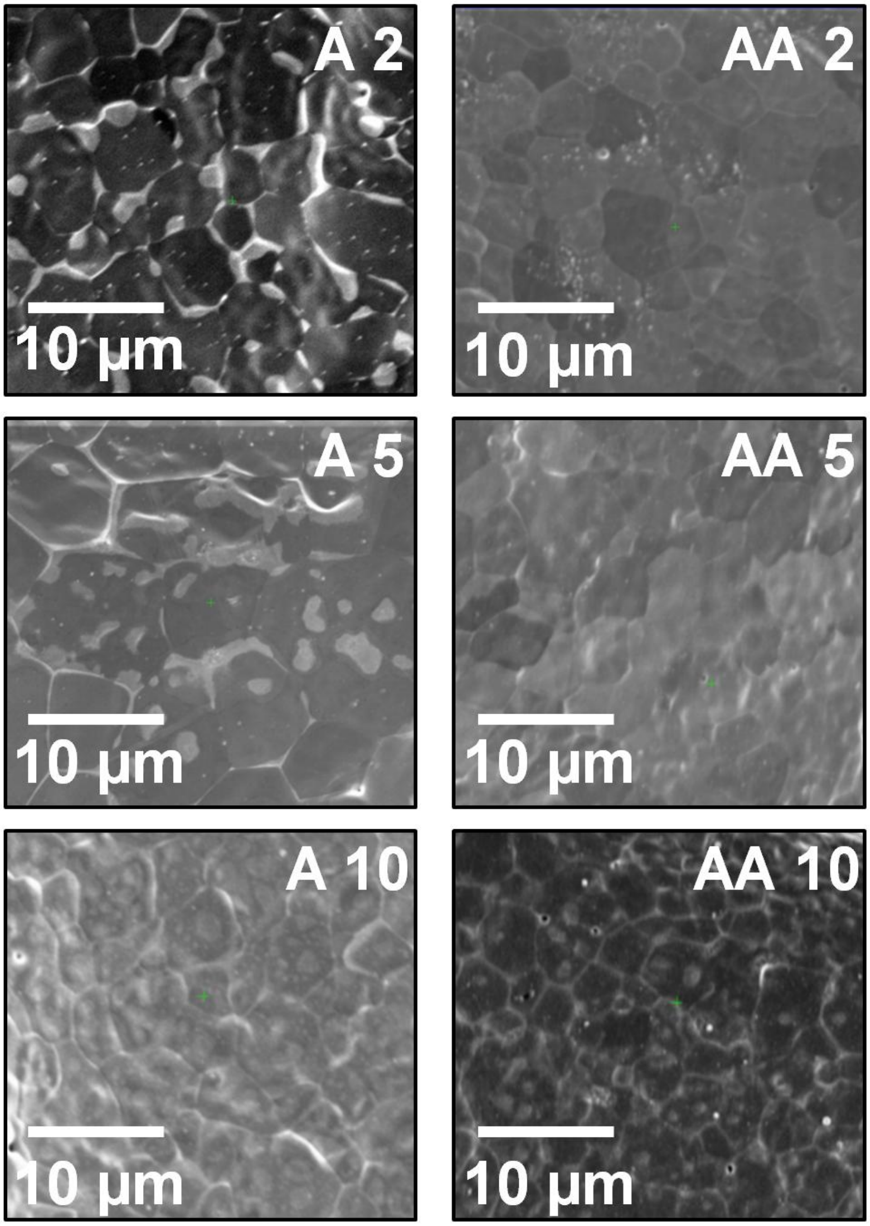

Figure 6.3. FIB SI images of the A and AA type Pt / Ni foams; Pt was deposited from K_2PtCl_4 aqueous solution.

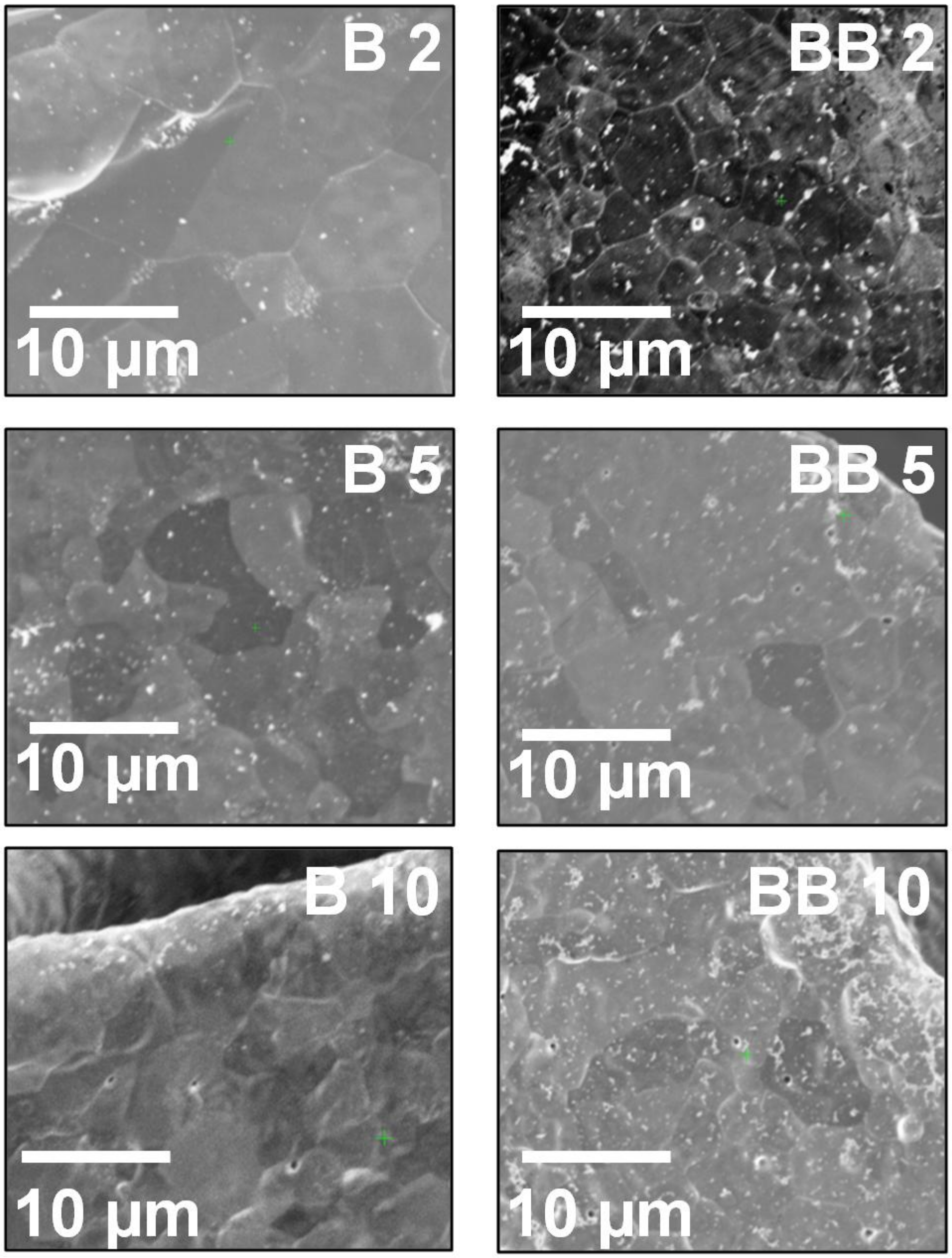

Figure 6.4. FIB SI images of the B and BB type Pt / Ni Foams; Pt was deposited from K_2PtCl_6 aqueous solution.

The Ni foams used in this study have a consistent 3-dimensional structure made up of struts that are 20 – 40 µm in width, and interconnecting, pentagonal shaped pores that are 300 – 500 µm across. The foams are manufactured in sheets that are ca. 3 mm or 3000 µm in thickness. A cross-section of the material reveals 5 – 6 layers of Ni struts through the depth of the foam. The struts in the center of the foam are up to 2 to 3 layers away from the outer face of the material. Figure 6.5 shows an optical microscopy image of a thin slice of unmodified Ni foam at 20× magnification. The foam is oriented such that the image is taken of the cut surface and shows full 3 mm thickness of the sheet. Three black dotted lines are drawn across the image and a red star is placed at each location where the line crosses a Ni strut that is in the same plane of view. Each line intersects 5 or 6 Ni struts that appear to be in the same plane. In experiments that are not described within this thesis, we have explored a variety of methods and conditions for depositing Pt on open-cell Ni foams and have encountered some issues with obtaining an even distribution of Pt throughout the depth of the material. Electrochemical deposition methods, for example, are particularly susceptible to the development of an uneven Pt deposition gradient from outer surfaces of the material to inner regions. Using the FIB instrument, which offers excellent depth of field and five-axis movement (x, y, z, rotation, and tilt up to 50˚) [48], samples of each type were imaged at various locations throughout their depth. We wish to emphasize that Pt is observed uniformly throughout the Ni foam structure when it is deposited using the method described herein. The reader is referred to Figures 6.2, 6.3, and 6.4 that show images which were collected at a variety of sample depths.

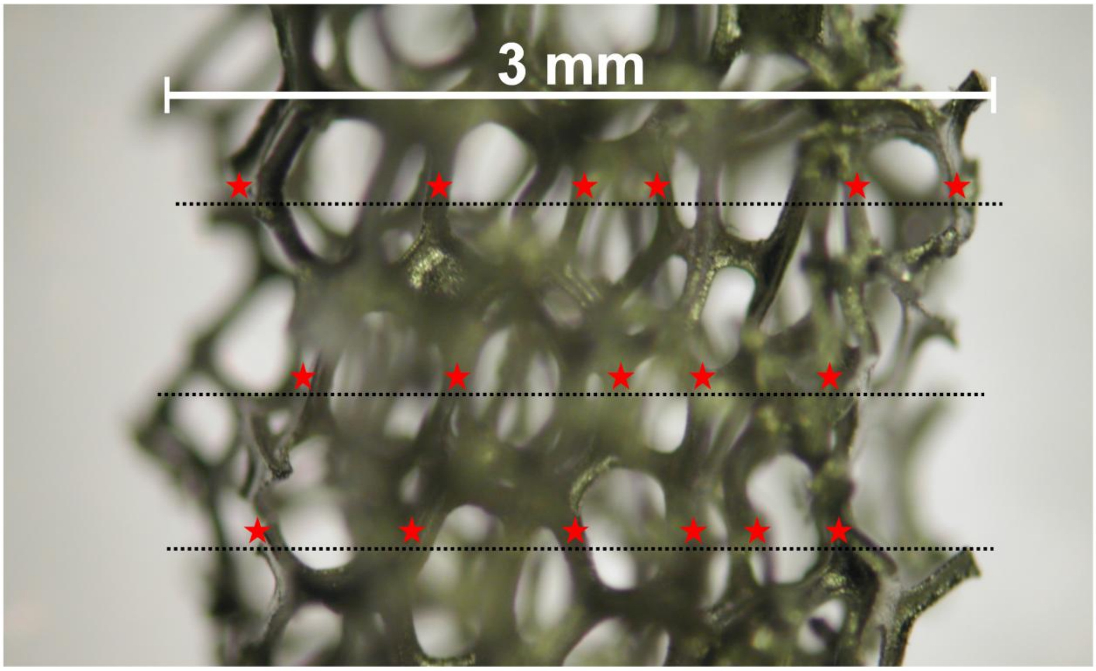

Figure 6.5. Optical microscope image at 20× magnification of the cross-section of a slice of unmodified Ni foam. The red stars indicate Ni struts that are in the same plane.

Energy dispersive X-ray spectroscopy (EDS) was applied in order to confirm the presence of Pt on the Pt / Ni foams. Figure 6.6 shows EDS spectra (on the right) collected from a Pt / Ni foam (type AA 10) at three regions that appear to have different amounts of Pt according to the SEM image (on the left). The black, red, and green colored boxes on the SEM image correspond to the EDS spectra of matching color. The largest analysis area is ca. 36 μm^2 (Region 1, large black rectangle). This region is meant to serve as a representative of the overall distribution of Pt over the surface. Region 1 has some places where the deposited Pt is clustered together and other places where only small Pt particles are observed. Region 2 (red rectangle) corresponds to an area of about 3 μm^2 that contains a cluster of deposited Pt on the surface.

Region 3 (green rectangle) corresponds to an area of about 3 μm^2 that, from the SEM image, does not appear to have very much Pt and only a few small particles are visible. In each region Ni, Pt, C, and O are detected in the EDS analysis. The C and O are present as adsorbed surface species (CO_2) and metal oxides (β-$Ni(OH)_2$). Carbon is a typical surface contaminant. Other than the peak corresponding to Pt, the EDS spectra for Regions 1, 2, and 3 are identical to the EDS spectra of an unmodified Ni foam [45]. The EDS spectra of the three regions displayed in Figure 6.6 are very similar to each other. In each region, the presence of Ni, C, O, and Pt is detected; Ni is the most abundant element in each spectrum. The peaks corresponding to C and O have similar intensities and shapes in the three spectra. The characteristic Pt peaks in the EDS spectra are comparable in height and size, even though Pt appears to be more abundant in Region 2 as compared to Region 3 from the SEM image. The observation that the Pt signal from region 3 is comparable to region 2 supports the idea that the surface of the Ni foam is evenly covered with small Pt particles, most of which are too small to observe in the SEM images.

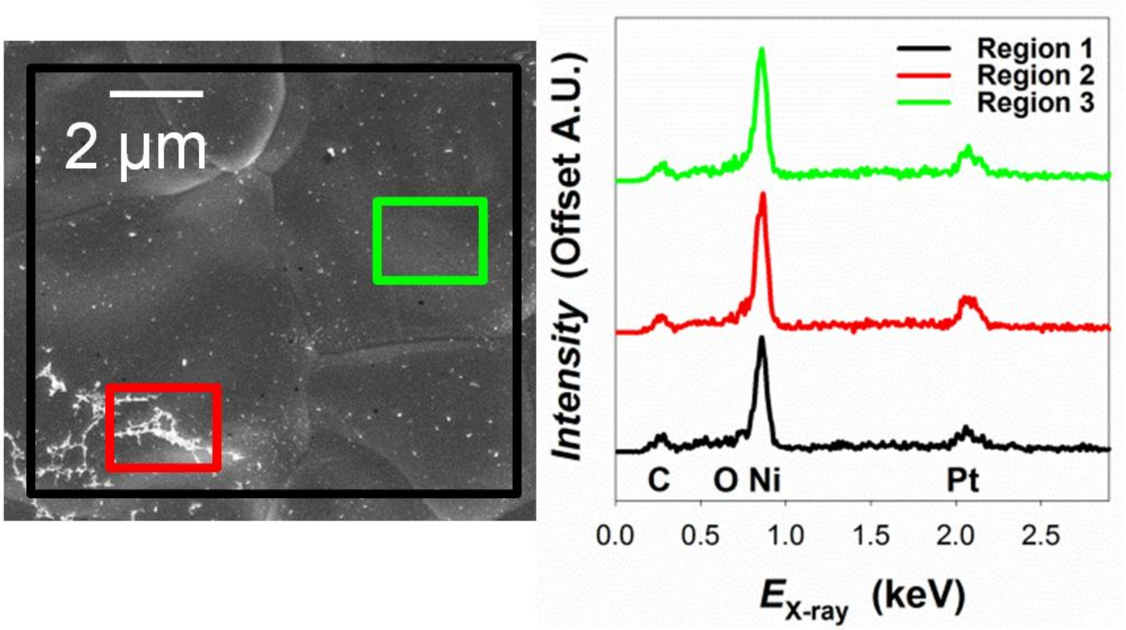

Figure 6.6. EDS analysis performed at three regions on a Pt / Ni foam (sample type AA 10). The three analysis regions are specified in the SEM images on the left using colored boxes that are matched with corresponding EDS spectra on the right.

6.3.3 Electrochemical Behavior of Pt / Ni Foam in Alkaline Media

Cyclic voltammetry was used to examine the electrochemical properties of Pt / Ni foams in aqueous alkaline electrolyte and to compare the electrochemical behavior of Pt / Ni foams to unmodified Ni foam and bulk polycrystalline Pt ($\mathrm{Pt_{poly}}$). Figure 6.7 shows overlaid CV profiles in the $0.05 < E < 1.30$ V region for unmodified Ni foam (black curve), Pt / Ni foam (sample type BB 10, blue curve), and $\mathrm{Pt_{poly}}$ (Ni wire, red curve), each collected in 0.50 M KOH electrolyte at $T = 298$ K and $s = 100$ mV $\mathrm{s^{-1}}$. A typical CV profile for $\mathrm{Pt_{poly}}$ in aqueous KOH or NaOH solution in the 0.05 to 1.30 V potential range displays the following features: (i) under-potential deposition of hydrogen (H_{UPD}) (cathodic) and desorption of H_{UPD} (anodic) at $0.05 < E < 0.45$ V; (ii) a capacitive double layer region, $0.45 < E < 0.80$ V; (iii) formation of PtO at $E > 0.80$ V (anodic); and (iv) reduction of PtO (cathodic) at $1.20 < E < 0.50$ V. The CV profile of unmodified Ni foam is essentially featureless in this potential range. From 0.05 V up to ca. 0.70 V a small, steady double-layer j is observed; there is a very gradual increase in j at $E > 0.70$ V that corresponds to the formation of β-$Ni(OH)_2$. The CV profile of Pt / Ni foam is plotted in blue and displays similar features to that of Pt_{poly} (red curve). Here, we observe the expected cathodic and anodic H_{UPD} features at $0.05 < E < 0.45$ V. The anodic j corresponding to the formation of PtO dominates the upper potential region, and the cathodic j corresponding to the reduction of PtO is observed at $E > 1.20$ V. However, in the case of Pt / Ni foam, the H_{UPD} peaks are broad indicating that the deposited Pt does not have well-defined crystal facets [49, 50]. It is difficult to discern a well-defined double layer region in the CV profile of Pt / Ni foam. In cathodic half of the CV profile, the reduction of PtO is spread out over a large E range that overlaps the expected double layer region and overlaps with the onset of H_{UPD}. In the anodic half of the CV profile, there is a minimum in j that consistently occurs between $E = 0.40$ and 0.50 V; the j begins to increase thereafter due to the onset of PtO formation which occurs at potentials lower than those observed for Pt_{poly}.

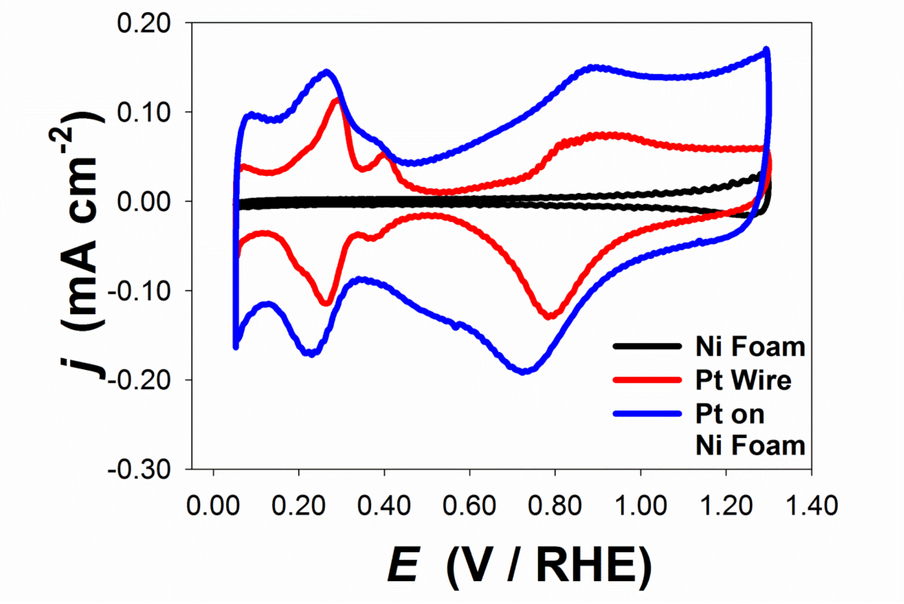

Figure 6.7. Overlaid CV profiles collected for Ni foam (black), Pt / Ni foam (blue), and Pt wire (red) each collected in 0.50 M KOH at T = 293 K with s = 100 mV s^{-1}.

6.3.4 Electrochemical Surface Area and Mass Loading of Pt on Pt / Ni Foams

The electrochemical surface area of deposited Pt was determined for at least three separate Pt / Ni foam disks of each sample type. The Pt / Ni disks were mounted as working electrodes using the procedure described in the Experimental Section. They were then subjected to a minimum of 200 CV cycles. The shape of the CV profile for Pt / Ni evolves significantly during the first 200 CV cycles; this phenomenon is analyzed in detail in an upcoming section. The 200th CV cycle was chosen for A_{ecsa} determination because, at this point, the most significant changes in the CV profile have already occurred. Further changes do occur after the 200th cycle as a result of Pt loss. From the CV profile, the charge corresponding to H_{UPD} desorption is determined by first isolating the anodic section from $E = 0.05$ V to 0.45 V, and then subtracting from this section the I value at $E = 0.45$ V. This I value corresponds to the I minimum observed in the expected double layer region; it is accepted as an estimate of the double-layer current (I_{DL}). By subtracting I_{DL}, the remaining I is attributed to Faradic current exchanged during desorption of H_{UPD}. This section of the CV profile is integrated to obtain the charge (Q), which is converted to A_{ecsa} using the value of 220 μC cm^{-2} which is the charge density of H_{UPD} on polycrystalline Pt[51, 52]. Since the CV profile for unmodified Ni foam displays no features overlapping with $H_{UPD,}$ all of the faradic I from this region is attributed to the combination of the H_{UPD} desorption process at the deposited Pt and double-layer charging. The H_{UPD} method the most popular and most reliable method for determining the A_{ecsa} of Pt_{poly} electrodes; it is considered reliable for Pt nanoparticles and high surface area Pt materials [52].

The mass loading of Pt on each type of Pt / Ni foam was determined using ICP OES, as described in the Experimental Section. In Figure 6.8 there are two graphs that show the A_{ecsa} of deposited Pt (in cm^2 Pt g^{-1} of Ni foam) and the mass loading of Pt (in μg Pt g^{-1} of Ni foam) for each sample type. The top graph displays all of the information for the type A and AA samples; the bottom graph displays the information for the type B and BB samples. Each point on these two graphs corresponds the value obtained from averaging three separate specimen; the error bars reflect the standard deviation. The top graph displays the results for A (circles) and AA (triangles) type samples, with Pt A_{ecsa} plotted in black, as a function of number of depositions. Platinum mass loading is plotted in red, as a function of number of depositions. The bottom graph uses the same format to display the same information for the B (circles) and BB (triangles) type samples. At this point we wish to remind the reader that type A samples are deposited from

0.001 M K_2PtCl_4 + 0.1 M KOH aqueous solution, AA samples from 0.002 M K_2PtCl_4 + 0.1 M KOH, B samples from 0.001 M K_2PtCl_6 + 0.1 M KOH, and BB samples from 0.002 M K_2PtCl_6 + 0.1 M KOH.

Careful analysis of the data presented in Figure 6.8 allows some general trends to be observed. For both the type A and type AA samples, there is a linear increase in the A_{ecsa} as the number of depositions increases from 2 to 5 to 10. The slope of the line representing the relationship between number of depositions and A_{ecsa} is steepest for the type AA samples, likely due to the higher concentration of Pt in the deposition solution used to make the AA samples. However, doubling the concentration of Pt in the deposition solution does not result in a two-fold increase in the A_{ecsa} of deposited Pt. The ratio between the A_{ecsa} of AA samples and the A_{ecsa} of A samples is slightly less than 1.5. The relationship between the mass of deposited Pt and the number of depositions is not linear for the type A sample set; in this case the mass of deposited Pt seems to level off after five depositions. With respect to the AA samples, the relationship between number of depositions and mass of Pt deposited is linear. After 10 deposition events the mass of Pt on the type AA samples is more than double the mass of Pt on the type A samples. However, this large difference in mass loading is not observed between the A and AA samples with 2 and 5 depositions; on the contrary, at 2 and 5 depositions, the mass loading of A and AA samples overlap within experimental uncertainty. Similar trends are observed in the bottom graph of Figure 6.8, which displays the data obtained for B and BB type samples. For both the type B and BB samples, the A_{ecsa} increases from 2 to 5 depositions, but levels off or decreases slightly for those samples with 10 deposition events. Comparison of the B and BB type samples demonstrates an approximately two-fold increase in A_{ecsa} of Pt by doubling the concentration in the deposition solution. The relationship between the mass loading of Pt and the number of depositions is not linear for the B or BB type samples. The average mass of deposited Pt levels off after five deposition events for the type B samples and increases for the BB type samples. Doubling of the concentration of Pt in the K_2PtCl_6 deposition solution results in a 2.5 to 3.5 fold increase in the mass of Pt deposited. Overall, the trends observed in both graphs of Figure 6.8 indicate that the A_{ecsa} and mass loadings achieved for various numbers of depositions are similar for the two Pt compounds used. The B and BB type samples, on average, have slightly lower A_{ecsa} of Pt and slightly lower loading than comparable A and AA type samples.

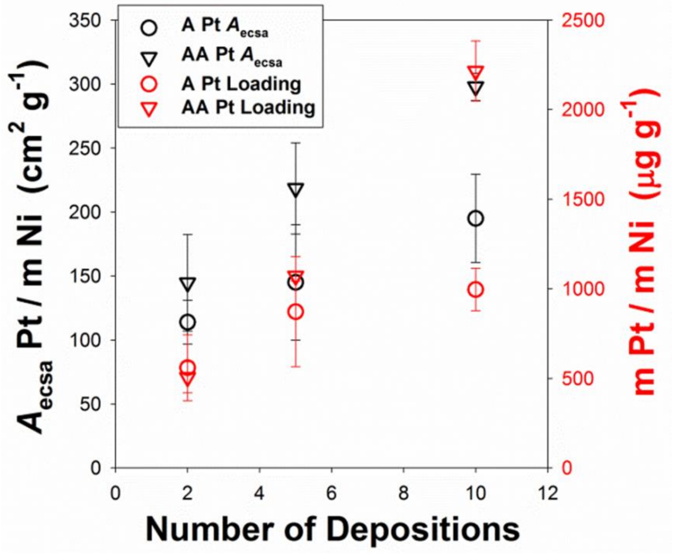

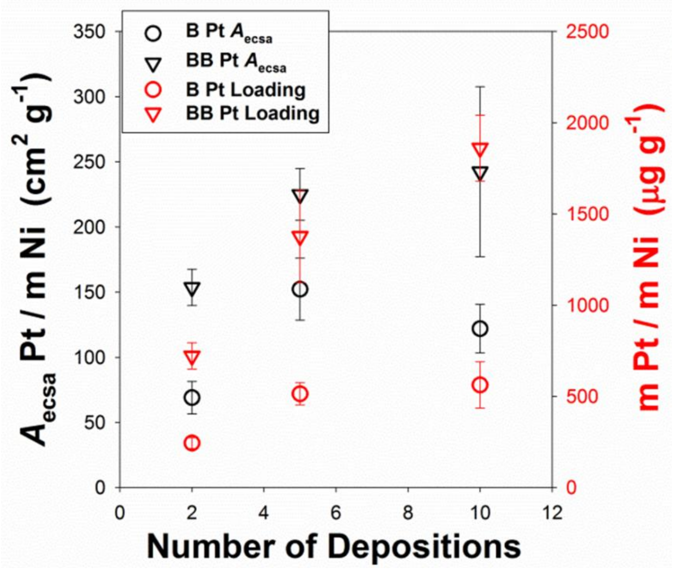

Figure 6.8. Relationship between the number of depositions to the A_{ecsa} of deposited Pt (black symbols) and also the mass of deposited Pt (red symbols) as measured by ICP-OES. The top graph shows the data for Pt deposited from K_2PtCl_4 salt solution (A and AA samples); the bottom graph shows the data for Pt deposited from K_2PtCl_6 salt solution (B and BB samples).

6.3.5 CV Stability of Pt / Ni Foams

As mentioned in the above discussion regarding the electrochemical behavior of Pt / Ni foams, there is a surprisingly large double-layer current observed in the CV profile for Pt / Ni foams. Figure 6.6 displays overlapping CV profiles for unmodified Ni foam, Pt_{poly}, and Pt / Ni foams, the j in the double-layer region of these materials are 2.41 µA cm^{-2}, 10.78 µA cm^{-2}, and 41.45 µA cm^{-2} respectively. The j values can be converted to double-layer capacitance (C_{dl}) by dividing them by the scan rate of the CV measurement. The C_{dl} values of Ni foam, Pt_{poly}, and Pt / Ni foam are 0.241 F m^{-2}, 1.08 F m^{-2}, and 4.15 F m^{-2}, respectively. The C_{dl} value for an electrode is affected by several factors including the roughness and geometry of the electrode, the surface area of the electrode, the nature of the electrolyte, and intrinsic properties of the electrode material that affect its interaction with the electrolyte [52, 53]. When comparing Pt / Ni foams to either Pt_{poly}, or unmodified Ni foams, we must keep in mind that there are multiple factors that differentiate these materials. By depositing Pt on the Ni foam, we have altered the roughness and surface area of the electrode, and have added a new material to the system. Thus, it is not unreasonable to observe a large change in the C_{dl} of the material. Nonetheless, we investigate the evolution of this feature over the course of the first 400 CV cycles in the upcoming discussion.

Changes in the CV profile for Pt / Ni foam during the first 400 CV cycles are examined in the three graphs of Figure 6.9. Graph A displays the first 400 CV cycles in the $0.05 < E < 1.30$ V range collected in 0.50 M KOH at $T = 293$ K and $s = 100$ mV s^{-1}. The scans are displayed by color in groups of 50 cycles; the first 50 cycles are in black, the next 50 cycles are in red, etc. Use of this method to display the data allows changes in the CV profile to be understood with respect to the number of CV cycles. It is evident from Figure 6.9 A that the majority of changes in the CV profile occur in the first 100 CV cycles. During the 400 CV cycles, the CV profile of Pt / Ni foam evolves from its original appearance to resemble more closely the shape expected for Pt_{poly} in aqueous alkaline media (Figure 6.7). The following changes are observed changes in the CV profile of Pt / Ni foam during the 400 CV cycles.

(i) Significant changes occur in the forward scan of the CV profile in the $0.60 < E < 0.90$ V region. A peak centered at about 0.8 V in the first few cycles decreases in intensity and eventually disappears with CV cycling, as indicated by the black arrow.

(ii) There is loss of anodic I throughout the entire PtO formation region. After approximately the first 200 cycles, the loss of I appears to be uniform in the 0.70 to 1.30 V E region.

(iii) In the reverse scan, within the potential range of $0.70 < E < 0.30$ V, I decreases significantly with CV cycling. This decrease is most significant in the first 100 CV cycles. This E region also gives the appearance of the PtO reduction peak shifting towards slightly higher potential values (indicated by the black arrow). The shape of the PtO reduction peak does not change on the upper-potential side of the peak maximum ($E > 0.75$ V).

(iv) Major changes are observed in the double-layer region of the CV profile (near $E = 0.45$ V). This is of particular importance because the A_{ecsa} of Pt on the Pt / Ni foams are calculated using the charge of H_{UPD} desorption in the CV profile. As described above, this calculation requires knowledge of the double-layer current (I_{DL}). In the forward scan, the thick double-layer region overlaps with the onset of PtO formation that occurs between $E = 0.60 – 0.80$ V. It is hard to define at which potential PtO formation begins from the CV profile. There is also the possibility of concurrently-occurring, poorly-defined reactions, such as the oxidation of impurities resulting from the deposition process.

(v) There is some loss of I in the H_{UPD} region (both anodic and cathodic). In the first 200 CV cycles, the peaks corresponding to H_{UPD} adsorption and desorption become shaper and more well-defined; this is indicative of restructuring of the deposited Pt and possible grain growth as the peaks in this region correspond to the particular crystal facets of a polycrystalline material [49, 50, 54]. After the first 200 cycles, loss of I in this region is uniform over the H_{UPD} potential range and the peak shapes stay constant. This is indicative of overall loss of Pt A_{ecsa}, likely via detachment of particles and dissolution of Pt [55, 56].

Figure 6.9 B shows the calculated A_{ecsa} and the measured value of I_{DL} (I at E = 0.45 V) plotted as a function of CV cycle number for a BB 10 type sample. This type of analysis was carried out for five different Pt / Ni foam samples; similar results were obtained for the other four samples. Graph B shows a decrease in the A_{ecsa} of Pt over the 400 CV cycles. After the 400 CV cycles, the A_{ecsa} of Pt has decreased by about 19 $cm^2\ g^{-1}$, which corresponds to ca. 8% of the initial A_{ecsa} of this sample. Within the five samples that were examined in this manner, the average loss of Pt A_{ecsa} was 13% over the course of 400 cycles. The decrease in Pt A_{ecsa} may have a number of different origins: (i) detachment of Pt particles; (ii) decrease in surface area through rearrangement, grain growth, and smoothing of the surface [54]; and (iii) electrochemical dissolution of Pt as a result of CV cycling [56, 57]. Figure 6.9 B also shows a decrease in the double-layer current (I_{DL}) as a function of CV cycle number. Here, we observe a steep decrease for the first 200 cycles and the I_{DL} begins to stabilize for cycle number 350 and 400. It is interesting to note that the decrease in I_{DL} and the decrease in A_{ecsa} do not reveal any correlation.

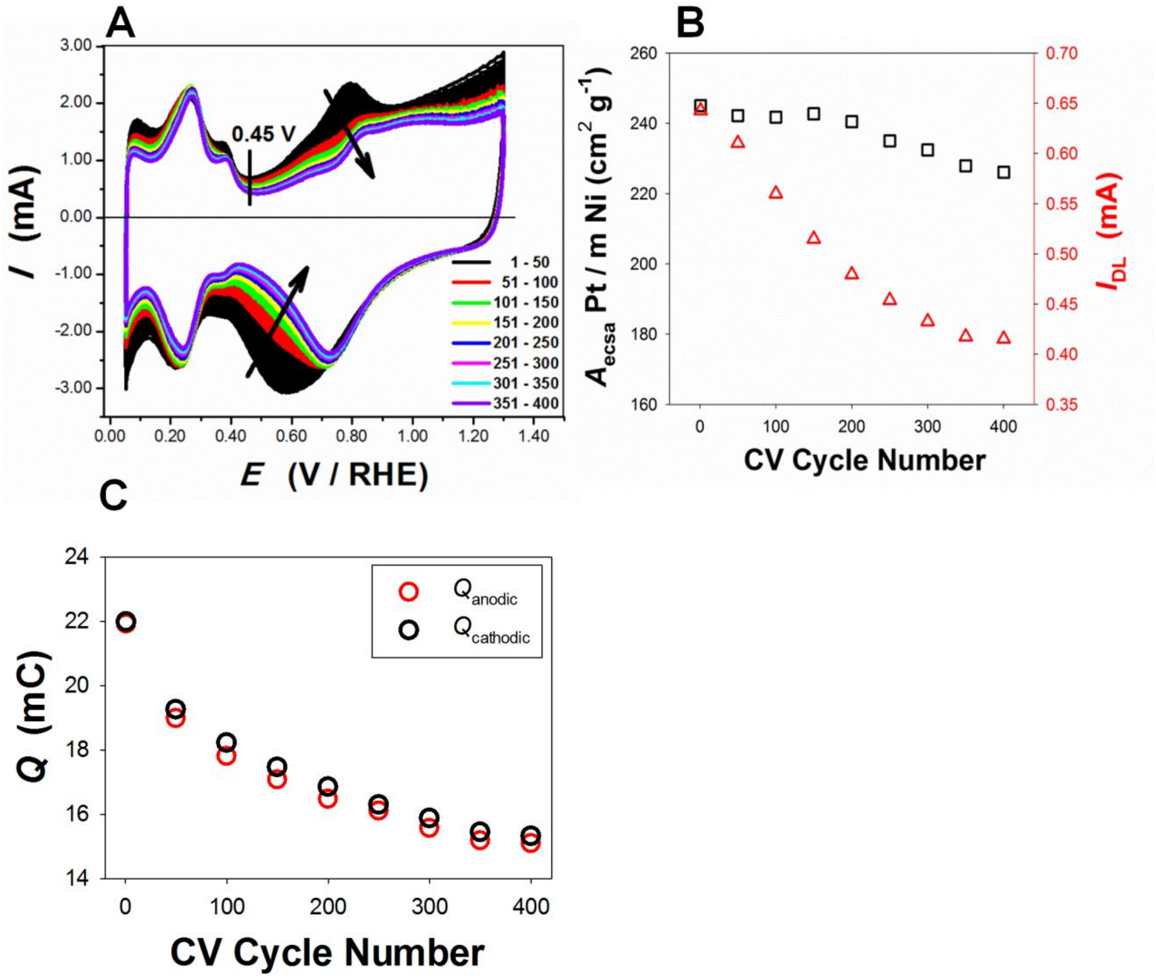

Figure 6.9. Four hundred CV cycles for Pt / Ni foam collected in 0.50 M KOH at T = 293 K with s = 100 mV s^{-1} (A). The CV profiles are in groups of 50 cycles, according to color. Relationship between the CV cycle number, the A_{ecsa} of Pt (black squares), and I_{DL} from the CV profile (red triangles) (B). The total anodic and cathodic charges (Q_{anodic}, Q_{cathodic}) from $0.05 < E < 1.30$ V as a function of CV cycle number (C).

Figure 6.9 C shows the total anodic charge (Q_{anodic}) and total cathodic charge (Q_{cathodic}) from the CV profile of Pt / Ni foam ($0.005 < E < 1.30$ V), plotted as a function of the CV cycle number. This plot demonstrates that the values of Q_{anodic} and Q_{cathodic} are very similar to each other throughout the 400 CV cycles, however, in all cases Q_{cathodic} is slightly higher than Q_{anodic}. In the CV profile for Pt / Ni foams, the onset of HER is visible at $E < 0.10$ V in the cathodic CV scans. The small difference between Q_{cathodic} and Q_{anodic} is attributed to onset of HER which contributes current to the cathodic section of the CV profile only. Both Q_{anodic} and $\text{Q}_{\text{cathodic}}$ decrease drastically in the first 200 cycles then begin to stabilize. Since Q_{anodic} and Q_{cathodic} are approximately equal, we cannot attribute the drastic changes in the CV profile over the 400 CV cycles to the oxidation of impurities because, in such a case, we would expect Q_{anodic} to be significantly larger than Q_{cathodic} for a given cycle number. From the evidence presented in the three graphs of Figure 6.9, we conclude that the changes observed in the CV profile of Pt / Ni foam as a function of CV cycling are the result of restructuring of the deposited Pt and loss of Pt through electrochemical dissolution and detachment. We wish to note that we did attempt to further confirm the restructuring and crystal grain growth of the deposited Pt using X-ray diffraction (XRD). The goal was to examine the average grain size of Pt as a function of CV cycle number using XRD data and the Scherrer formula [54, 58]. Unfortunately, due to the low loading of Pt on the Pt / Ni foams, the intensity of the Pt XRD peaks was too low for quantification.

Figure 6.10 shows FIB SI images of Pt / Ni foam before (A) and after (B) 400 CV cycles, as described above. These images show that Pt is still clearly visible on the Ni foams after 400 CV cycles. The appearance of the Pt deposit and the distribution of Pt over the surface of the Ni foam do not change significantly with CV cycling. As mentioned earlier, there is an average loss of 13 % of Pt A_{ecsa} over the course of 400 CV cycles that is attributed to particle detachment, Pt dissolution, or particle agglomeration. It is possible that all of these processes are occurring. The small, nanometer-sized Pt particles are not visible in the FIB image in Figure 6.10. This FIB SI image does not have sufficiently-high resolution to offer any insight on the origins of the Pt A_{ecsa} loss.

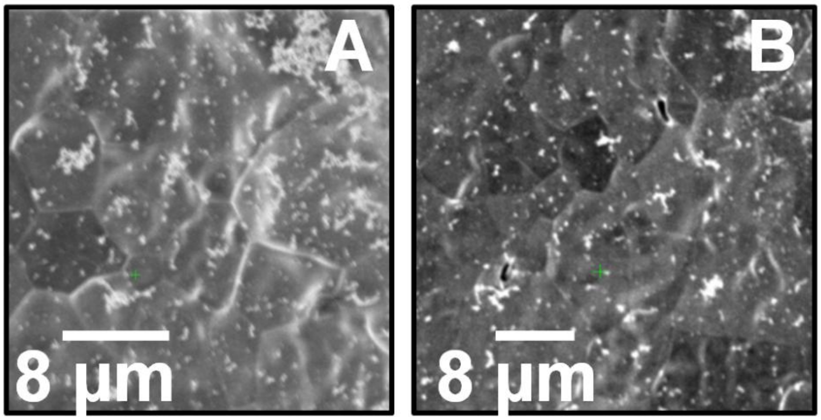

Figure 6.10. FIB ion images of Pt / Ni foam (type BB 10) before (A) and after (B) four hundred CV cycles in 0.50 M KOH at T = 298 K and s = 100 mV s^{-1}.

6.4 Results and Discussion Part 2: Electrocatalytic Activity of Pt / Ni Foams

In this section, we examine the electrocatalytic activity of Pt / Ni foams towards four reactions: hydrogen evolution, hydrogen oxidation, oxygen reduction, and oxygen evolution. The reactions were carried out using Pt / Ni foams of each type (A, AA, B, and BB for 2, 5, and 10 depositions). Unmodified Ni foam and $\mathrm{Pt_{poly}}$ wire were included in the analysis for comparison.

Each reaction was examined using both the LSV and Tafel polarization methods. The characterization presented in the previous section demonstrates that the Pt particles deposited from solutions containing either K_2PtCl_4 or K_2PtCl_6 are very similar in terms of particle size and morphology. The CV profiles obtained for the various Pt / Ni foams display identical behavior. With this in mind, we proceed to interpret the results by considering the four different electrode types (A, AA, B, and BB) with various numbers of deposition events (2, 5, and 10) as one large sample set. The variable that we consider within this sample set is the A_{ecsa} of Pt, which we determine for each Pt / Ni foam electrode. In the upcoming analysis, we quantify the amount of Pt on a Pt / Ni foam electrode in terms of the A_{ecsa} of Pt divided by the total A_{ecsa} of material (Pt + Ni foam).

The Pt / Ni foams are bimetallic materials that present a unique challenge in determining the electrochemically active surface area that should be used in normalizing I values. Generally, the I measured in an electrochemical experiment is converted to current density (j) by normalizing the I to the A_{ecsa} of the electrode. This allows comparisons to be made between electrodes that have different A_{ecsa} values. In the case of Pt / Ni foams, it is not difficult to estimate the total A_{ecsa} of the electrode material because the A_{ecsa} of Pt is determined using the H_{UPD} desorption charge, as outlined in the Characterization Section. From previous work that is presented in Chapter 4, we have the required information to estimate the A_{ecsa} of the Ni foam substrate. The Ni foam disks used in this study were weighed prior to the deposition of Pt. The specific surface area ($A_s = A_{\mathrm{ecsa}} / m$) of the Ni foam used in this study was previously estimated and is ca. 300 $\mathrm{cm}^2\ \mathrm{g}^{-1} \pm 90\ \mathrm{cm}^2\ \mathrm{g}^{-1}$ [45]. The total A_{ecsa} of a Pt / Ni foam electrode is determined by adding the A_{ecsa} of Pt, determined via H_{UPD}, to the A_{ecsa} of the Ni foam support, estimated based on its mass. For any given Pt / Ni foam electrode, the experimental uncertainty associated with the total A_{ecsa} value is dominated by the large uncertainty (30%) associated with the A_s of Ni foam. There is also some uncertainty associated with the determination of Pt A_{ecsa} using the H_{UPD} method described above. We propose that the main source of uncertainty in the H_{UPD} method as applied to Pt / Ni foams stems from the fact that the CV profile of Pt / Ni foams never completely stabilizes due to structural changes in the Pt deposit (particle detachment, agglomeration, and dissolution). In the Characterization Section, the 200th CV cycle is always used for the determination of the Pt A_{ecsa}. For the eletrocatalysis studies, the 200th CV cycle is also used to determine the A_{ecsa} of Pt. The electrocatalysis experiments were carried out according to the schedule of experiments presented in Section 6.2.2. Therefore, the 200th CV cycle occurs after the HER and HOR experiments. The A_{ecsa} of Pt for eight separate Pt / Ni electrodes was determined before, and after the HER and HOR experiments. These values differed by an average of 4 %, which is a very good agreement. As noted above, continuous CV cycling 400 times results in an average loss of Pt A_{ecsa} of 13 %. The determination of j for Pt / Ni foams is further complicated by the fact that both Pt and Ni are active electrocatalysts for some of the reactions studied. However, in these cases their activities differ significantly. In some cases, it is not obvious if the A_{ecsa} of the Ni foam substrate should be included in the calculation of j values. This issue is addressed independently for each of the reactions studied.

6.4.1 The Hydrogen Evolution Reaction

Both Ni and Pt are considered good electrocatalysts for the HER in alkaline media. The exchange current density of the HER ($j_{0,\ \mathrm{HER}}$) for a Pt cathode is about 2.5 orders of magnitude higher than that of a Ni cathode [59]. Figure 6.11 shows LSV profiles for the HER using Ni foam, Pt_{poly}, and three Pt / Ni foams with various Pt A_{ecsa}, indicated by the value of Pt A_{ecsa} / total electrode A_{ecsa}. The LSV profiles were collected in the 0.000 < E < –0.200 V region, in 0.50 M KOH aq. electrolyte saturated with H_2 gas, at T = 293 K and s = 0.1 mV s^{-1}; the electrolyte was stirred during the measurements. The E values for all electrocatalysis measurements presented herein are adjusted for the E drop due to uncompensated solution resistance (i.e. *IR* drop). The current density for the HER (j_{HER}) using a Ni foam (purple LSV profile) is very low compared that of Pt_{poly} (blue), and the Pt / Ni foams (black, red, and green). However, there is a small j due to HER that is observed as E values approach –0.15 V. Figure 6.11 B displays the 0.00 < E < –0.020 region from Figure 6.11 A at an enlarged scale. This graph allows the onset of HER for the various electrocatalysts to be examined in more detail. All of the materials that contain Pt (Pt_{poly}, and Pt / Ni foams) display j due to the HER beginning at E values very close to 0.000 V, which is the standard potential (E^0) for the HER. The Ni foam electrode does not produce any measurable current density for the HER in the first 20 mV of the LSV scan. Since both Ni and Pt are active electrocatalysts towards the HER, the LSV profiles for Pt / Ni foams are normalized by dividing the I value by the total A_{ecsa} (Pt + Ni foam). The LSV profiles for Pt / Ni demonstrate increasing j_{HER} with increase in the A_{ecsa} of deposited Pt; this is expected because Pt is more active towards this reaction than Ni.

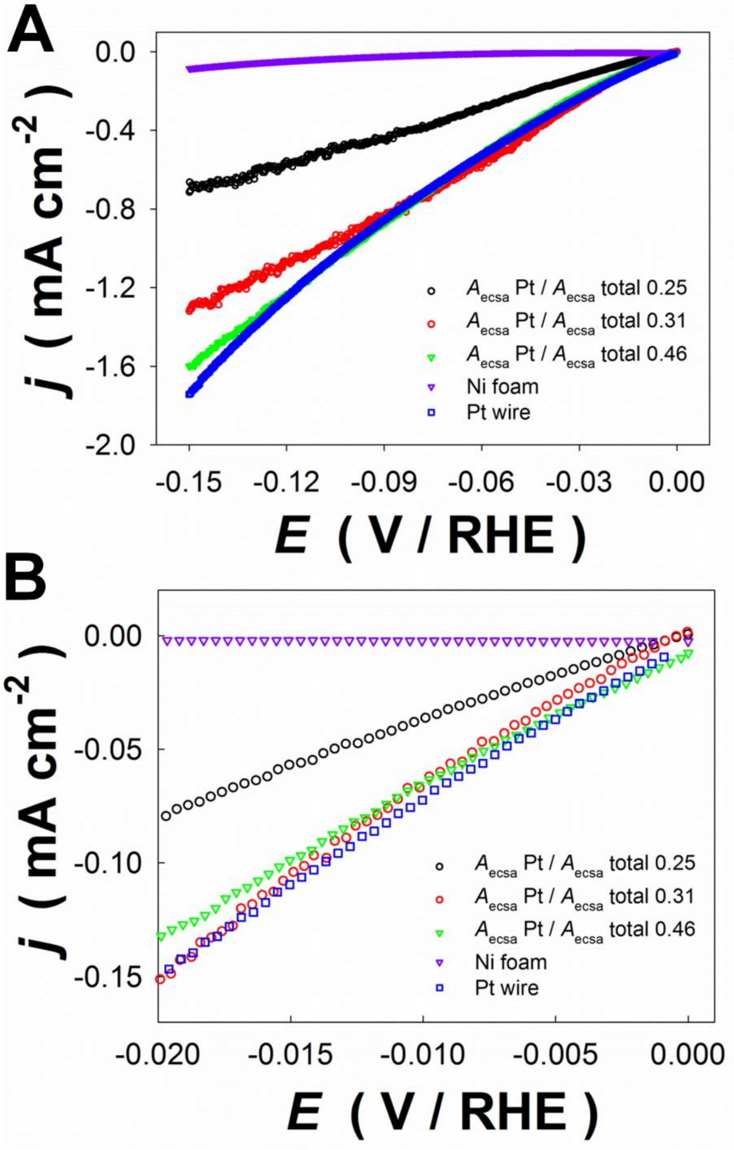

Figure 6.11. LSV profiles for the HER in 0.50 M KOH using the following electrodes: Ni foam (purple); $\mathrm{Pt_{poly}}$ (blue); and Pt / Ni foams with different fractions of Pt A_{ecsa}: 0.25 (black), 0.31 (red), 0.46 (green) (A). Enlarged version for the low E region of the graph above (B); s = 0.1 mV $\mathrm{s^{-1}}$, T = 293 K, E is corrected for IR drop. Current density values are normalized to the total A_{ecsa} of the electrode (Ni foam + Pt).

Figure 6.12 shows the j_{HER} values obtained at E = –0.150 V for various Pt / Ni foam electrode, as well as unmodified Ni foam and Pt_{poly}. These values are plotted as a function of A_{ecsa} Pt / A_{ecsa} total. The j_{HER} value for unmodified Ni foam is marked with a green line; the j_{HER} value for Pt_{poly} is marked with a blue line. Black circles represent the j_{HER} values obtained when I is divided by the total A_{ecsa} of the Pt / Ni foam electrode. In this instance, the deposited Pt and the underlying Ni foam substrate are both considered electrocatalytic materials. The red triangles represent the j_{HER} values obtained when I is divided by only the A_{ecsa} of Pt. In this case, the Ni foam is not considered electrocatalytically active and all I from the HER is attributed to the deposited Pt particles. In all cases, the j_{HER} obtained when the I is normalized to only the A_{ecsa} of Pt is greater than the j_{HER} of Pt_{poly}. This indicates that the Pt deposited on Ni foam is more active towards the HER than Pt_{poly}, or that the activity of the Ni foam substrate towards the HER reaction is significant. There are a number of studies that report increased electrocatalytic effects through the addition of Ni to Pt electrode materials. Similar effects are also observed when other precious metals or early transition metals are added to Pt. These multi-component Pt-based electrocatalysts are alloyed materials. These increases in electrocataytic activity are often attributed to changes in the Pt – Pt bond distance, or electronic effects opon the added metal such as an increase in its d – vacancy character [60]. Binary NiPt electrocatalysts are developed and studied for reactions such as HOR and ORR [61, 62], CO oxidation [63], methanol oxidation [60]. In the case of Pt / Ni foams, there is no step in the fabrication process that could lead to PtNi alloy formation. For this reason, an enhanced catalytic effect due to electronic interactions or atomic-level structural disruptions is not likely. The observation that j_{HER} for Pt / Ni foams is greater than for Pt_{poly} when the I is normalized to the A_{ecsa} of Pt demonstrates that the underlying

Ni foam substrate is active towards the HER, and that contribution of the Ni foam substrate to j_{HER} is significant.

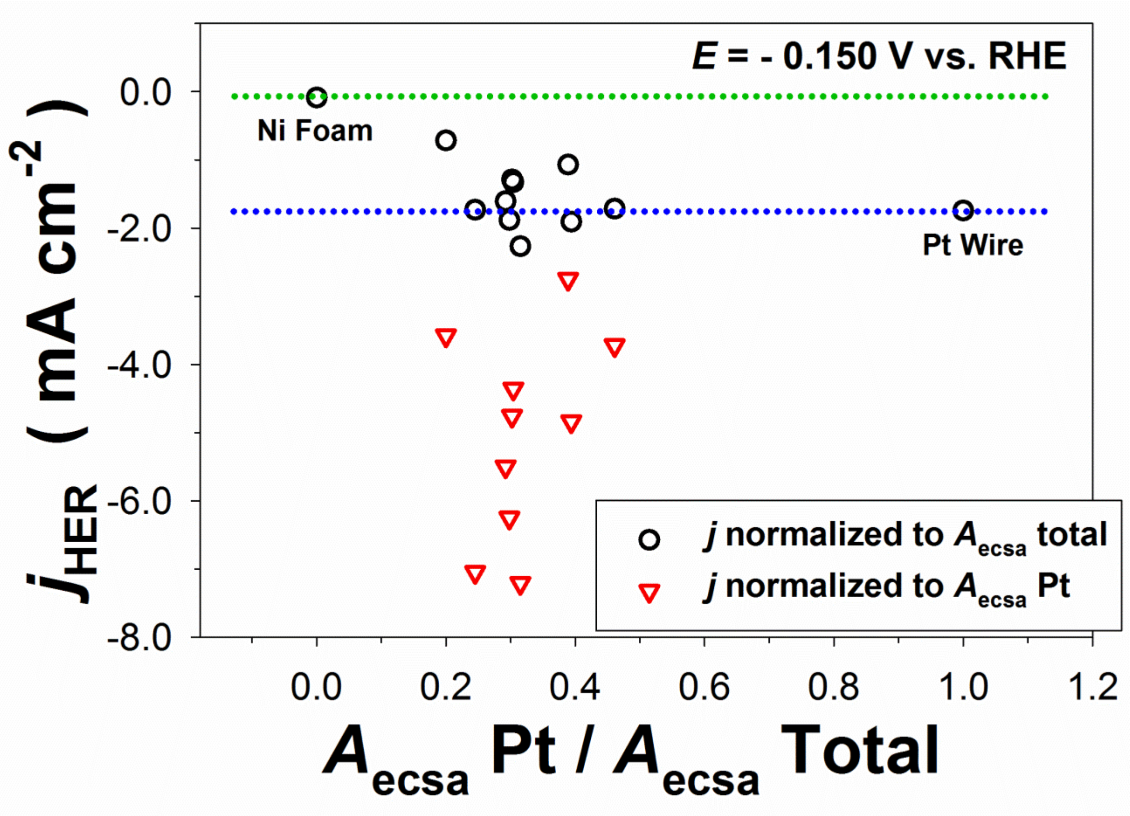

Figure 6.12. j_{HER} values at E = –0.150 V for $\mathrm{Pt_{poly}}$, Ni foam, and Pt / Ni foam electrodes with various fractions of Pt A_{ecsa} plotted as a function of the A_{ecsa} Pt / A_{ecsa} total. These values are obtained from LSV profiles carried out in 0.50 M KOH at T = 293 K with s = 0.1 mV s^{-1}. Black circles correspond to j_{HER} values normalized to the total A_{ecsa} of the electrode; red triangles correspond to j_{HER} values normalized to the A_{ecsa} of Pt.

Figure 6.13 A presents Tafel polarization plots for the HER taking place on Pt_{poly}, and three Pt / Ni foams with different Pt surface areas. From this graph, it is evident that Pt_{poly}, and Pt / Ni foams have different electrochemical behaviors. Figure 6.13 B shows the Tafel plot for Pt_{poly} and one Pt / Ni foam in more detail. The plot corresponding to Pt_{poly} has a linear region in the η = 100 – 200 mV range. The Tafel plot corresponding to Pt / Ni foam has two linear regions, one at lower η values ($\eta < 100$ mV) and one at higher η values ($\eta > 120$ mV). The information obtained from Tafel plots can be used to determine mechanistic information about an electrochemical process, and also to evaluate the activity of a given electrode. The *Tafel slope* is the slope of the linear portion of a η vs. log j curve. The presence of multiple linear regions in this type of plot is an indication that there are multiple reaction mechanisms taking place. Thus is it possible to calculate multiple Tafel slopes. The value of this slope can be used to calculate the number of electrons transferred in the rate determining step of the reaction mechanism. This linear region is extrapolated to the x – axis in order to determine the exchange current density (j_0) of the process. There may be other linear regions present in this type of plot, but only those linear regions that occur within the E range where I is entirely determined by the rate of electron transfer can be analyzed for mechanistic information. Once the η is such that mass transport phenomena begin to affect the I, it is no longer possible to relate the slope of this region to the rate determining step of the reaction. Complex systems, such as a multi-component electrode, are difficult to analyze in this manner because there may be several concurrently-occurring processes. In this case, deviations from linearity may occur in the low η region, and multiple linear regions may be observed corresponding to different mechanisms or entirely different processes. In the case of Pt / Ni foams, the Tafel plots are not analyzed for mechanistic information because of reactions occurring simultaneously on Pt and Ni. Other useful information can be obtained from the Tafel polarization plots. For example, the slope of the η vs. log j plots can be compared to evaluate the relative electrocatalytic activity of various electrode materials. A shallow slope indicates good electrocatalytic activity because significant increase in the j is observed with small increases in η; a steep slope is an indication of poor electrocatalytic activity [64].

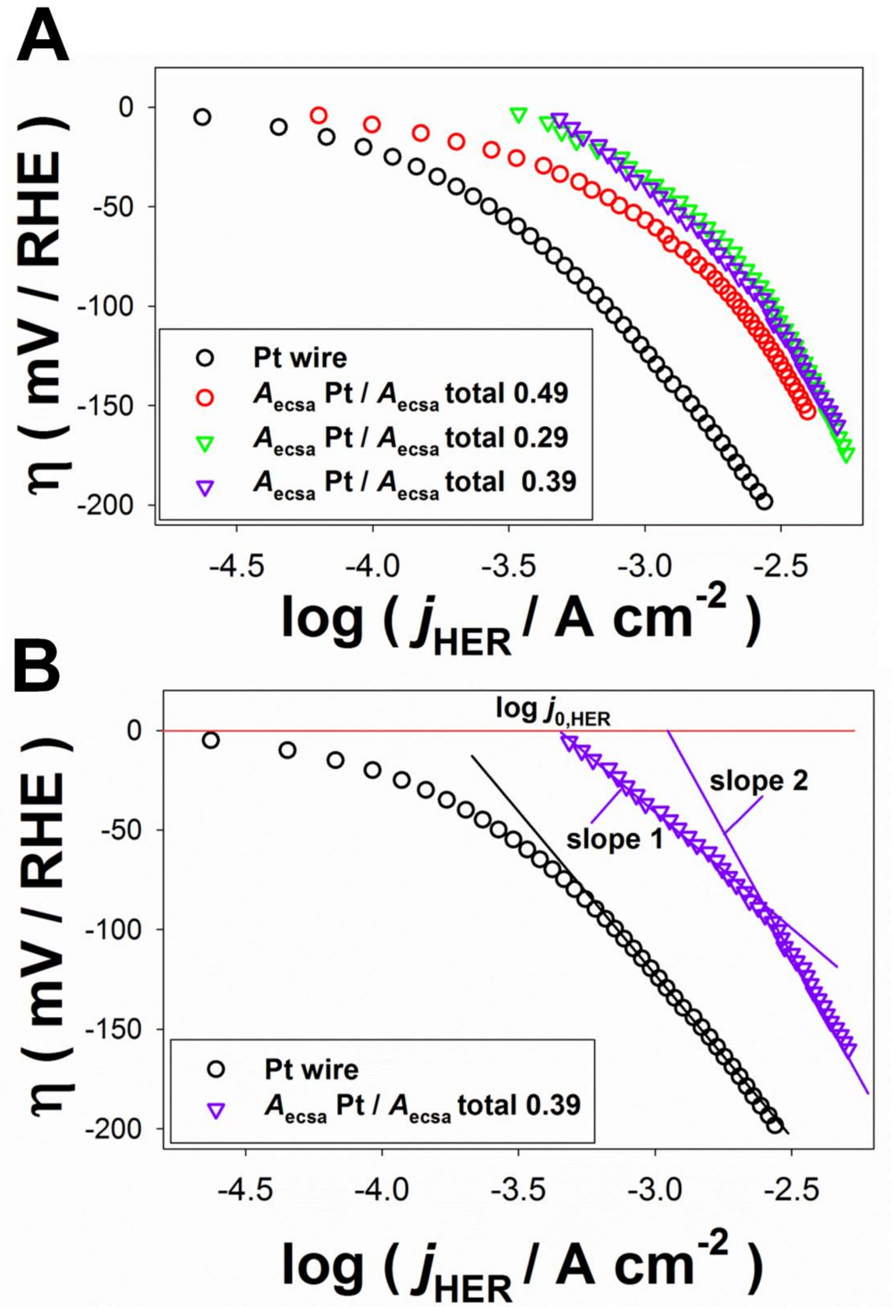

Figure 6.13. HER Tafel polarization plots for Pt_{poly}, and Pt / Ni foam electrodes with various fractions of Pt A_{ecsa} plotted as a function of the A_{ecsa} Pt / A_{ecsa} total. The data was obtained from staircase-type polarization experiments carried out in 0.50 M KOH at T = 293 K (A). Illustration for the determination of the Tafel slope (b) and exchange current density ($j_{0,\ HER}$) (B).

The linear regions of the Tafel polarization plot shown in Figure 6.13 are analyzed for the purpose of comparing the electrocatalytic activity of Pt / Ni foam to that of Pt_{poly}. Table 6.3 presents the slope values (b) calculated for linear regions 1 and 2. For those samples that display linear behavior in the low η region (region 1), the value of $j_{0,\ HER}$ is presented. The b value corresponding to Pt_{poly} is the lowest, which is expected due to the superior electrocatalytic activity of Pt towards the HER. The b values for Pt / Ni foams decrease with increasing Pt A_{ecsa}, as is expected. The $j_{0,\ HER}$ values presented for Pt / Ni foams are slightly less than half of the $j_{0,\ HER}$ value of 1.03 mA cm^{-2} that is expected for Pt_{poly} in alkaline solution at 293 K [22].

Table 6.3. Data obtained from the Tafel polarization plots for the HER.

Electrode	**$j_{0,\ HER}$ (1)** **mA cm^{-2}**	**b (1)** **mV / dec**	**b (2)** **mV / dec**
Pt_{poly}	-	-	–169
Pt / Ni foam A_{ecsa} Pt / A_{ecsa} total = 0.49	-	-	–209
Pt / Ni foam A_{ecsa} Pt / A_{ecsa} total = 0.39	0.44	–112	–227
Pt / Ni foam A_{ecsa} Pt / A_{ecsa} total = 0.29	0.34	–74	–268

6.4.2 The Hydrogen Oxidation Reaction

Figure 6.14 shows LSV profiles for the HOR taking place on Ni foam, Pt_{poly}, and three Pt / Ni foams with various Pt A_{ecsa}. The LSV profiles were collected in the $0.000 < E < 0.200$ V region, in 0.50 M KOH aq. electrolyte saturated with H_2 gas, at $T = 293$ K and $s = 0.1$ mV s^{-1}; the electrolyte was stirred during the measurement. The LSV profiles demonstrate that the unmodified Ni foams have no electrocatalytic activity towards the HOR. The LSV profile for Pt_{poly} shows that Pt is an active electrocatalyst for HOR. The LSV profiles corresponding to Pt / Ni foams display some unexpected behavior. The Pt / Ni foams show moderate activity towards the HOR as compared to Pt_{poly}. However, a large η of 50 to 100 mV is required before significant anodic j is observed. In the E region between 0.000 V and the onset of HOR, cathodic j values are observed for Pt / Ni foams. This unexpected behavior is reproducible for the majority of the Pt / Ni foam electrodes. In addition, the same behavior is observed in the HOR Tafel polarization measurements that are carried out directly following the completion of the HOR LSV measurements. As outlined in the Experimental Section of this chapter, the HOR experiments are performed after the electrode has been subjected to 100 CV cycles in the $0.05 < E < 1.30$ V range, and then applied the the LSV and Tafel HER experiments. No CV cycling was performed between the HER and HOR experiments; the measurements were carried out in the same electrolyte without the electrode being removed from the electrochemical cell. Knowledge of the electrode history allows us to conclude that this cathodic current is unlikely to be the result of the reduction of Pt or Ni oxides. It is also unlikely that there are any impurities from the Pt deposition process remaining on the electrode that could undergo reduction. At this time, the origin of this cathodic current is unknown. Figure 6.14 B displays the LSV profiles in the 0.00 <

$E < 0.015$ region from the top graph at an enlarged scale allowing the onset of HOR to be observed in more detail. Since unmodified Ni foam displays no electrcatalytic activity towards the HOR, the LSV profiles for Pt / Ni foams are normalized by dividing the I values by the A_{ecsa} of Pt only.

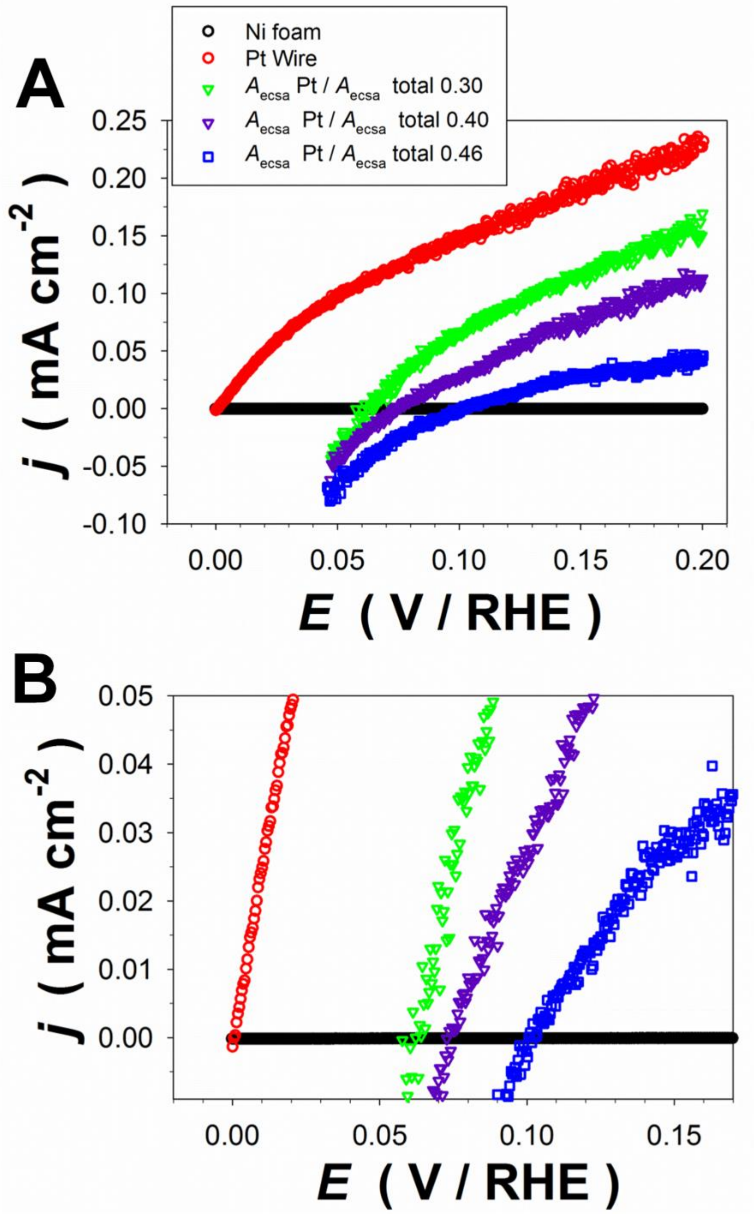

Figure 6.14. LSV profiles for the HOR in 0.50 M KOH using the following electrodes: Ni foam (black); Pt_{poly} (red); and Pt / Ni foams with different fractions of Pt A_{ecsa}: 0.30 (green), 0.40 (purple), 0.46 (blue) (A). Enlarged version for the low potential region of the graph above (B); $s = 0.1$ mV s^{-1}, $T = 293$ K, E is corrected for IR drop. Current density values are normalized to the A_{ecsa} of Pt only.

Figure 6.15 shows the current density values for the HOR (j_{HOR}) obtained at E = 0.150 V for Pt / Ni foam electrodes with various Pt A_{ecsa} fractions (A_{ecsa} Pt / A_{ecsa} total), as well as for unmodified Ni foam and Pt_{poly}. Black circles represent the j_{HOR} values obtained when I is divided by the total A_{ecsa} of the Pt / Ni foam electrode. The red triangles represent the j_{HOR} values obtained when I is divided by the A_{ecsa} of Pt only. The j_{HOR} for the unmodified Ni foam is marked with a green line; this value is essentially 0 mA cm^{-2} or below the detectable I limit of the potentiostat. Since the unmodified Ni foam is inactive towards the HOR, the A_{ecsa} of Ni foam should not be included when normalizing the I signal. If there were to be a contribution from the Ni foam substrate to the j_{HOR} of Pt / Ni foams, the j values determined by normalizing the I to A_{ecsa} of only Pt would be consistently above the A_{ecsa} of Pt_{poly}, which is not observed. Figure 6.15 also demonstrates that there is a correlation between the A_{ecsa} fraction of Pt and the j_{HOR} values at E = 0.015 V. The two Pt / Ni foams with A_{ecsa} Pt / A_{ecsa} total values near 0.5 produce j_{HOR} similar to that of Pt_{poly}. The j_{HOR} values decrease with decreasing A_{ecsa} of Pt. Since the Ni foam offers no electrocatalytic activity towards the HOR, it cannot be considered an electrochemically active support material. For this reason, and because of the strange behavior of the Pt / Ni foams in the $0.000 < E < 0.100$ V region (i.e. the cathodic current), the discussion of Pt / Ni foams as electrocatalysts for the HOR is not extended and does not include Tafel polarization curves.

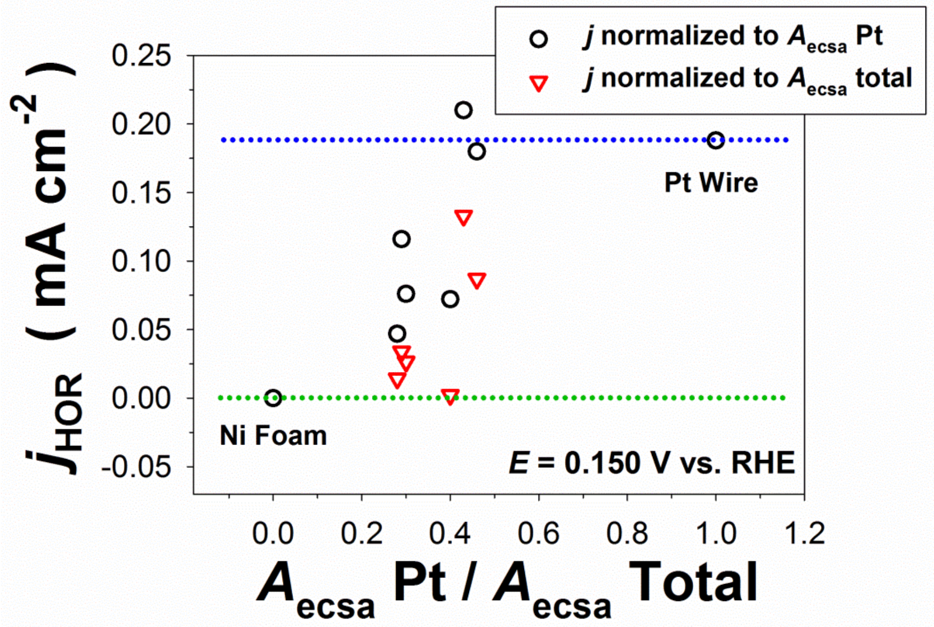

Figure 6.15. j_{HOR} values at E = 0.150 V for $\mathrm{Pt_{poly}}$, Ni foam, and Pt / Ni foam electrodes with various fractions of Pt A_{ecsa} plotted as a function of the A_{ecsa} Pt / A_{ecsa} total. These values are obtained from LSV profiles carried out in 0.50 M KOH at T = 293 K with s = 0.1 mV $\mathrm{s^{-1}}$. Black circles correspond to j_{HOR} values normalized to the total A_{ecsa} of the electrode; red triangles correspond to j_{HOR} values normalized to the A_{ecsa} of Pt.

6.4.3 The Oxygen Reduction Reaction

Figure 6.16 displays LSV profiles for the ORR using unmodified Ni foam, $\mathrm{Pt_{poly}}$, and three Pt / Ni foams with various Pt A_{ecsa} fractions. The LSV profiles were collected in the $1.100 < E < 0.600$ V region, in 0.50 M KOH aq. electrolyte saturated with O_2 gas, at T = 293 K and s = 0.1 mV $\mathrm{s^{-1}}$. Typically studies of the ORR are carried out using a rotating disk electrode (RDE) in order to increase the diffusion of oxygen to the electrode / electrolyte interface. The ORR experiments presented herein were carried out in stirred electrolyte with a stationary electrode. The reader is reminded that Ni foam and Pt / Ni foam working electrodes are prepared by attaching the foam material to a Ni wire (see Chapter 3 Experimental Methods). If the solution is agitated too vigorously, the connection between the Ni foam and the wire is loosened. The foam portion of the electrode moves as a result of the agitation of the electrolyte. The same experimental difficulty occurs when gases are bubbled through the electrolyte during electrochemical measurements. This is the reason why the reactant gasses (O_2 or H_2) were not continuously bubbled through the electrolyte during the measurements. Instead, they were introduced into the electrochemical cell over the electrolyte throughout the measurements. Movement of the electrode adds noise to the *I* response because the electrical connection between the foam and the wire is temporarily disturbed. For this reason, it was necessary to stir the solution gently which does not result in large improvements for the diffusion of oxygen within the electrolyte. The LSV profile for unmodified Ni foam demonstrates that this material has no electrocatalytic activity towards the ORR. Since unmodified Ni foam displays no electrcatalytic activity towards the ORR, the LSV profiles for Pt / Ni foams are normalized by dividing the *I* by the A_{ecsa} of Pt only. The LSV profile for $\mathrm{Pt}_{\mathrm{poly}}$ shows that Pt is an active electrocatalyst towards ORR. The LSV profiles corresponding to Pt / Ni foams display electrocatalytic behavior similar to that of $\mathrm{Pt}_{\mathrm{poly}}$, but with lower current density values towards the ORR (j_{ORR}). All of the LSV profiles display a significant amount of noise once the *E* is brought below ca. 0.85 V. This noise is most likely a result of the slow diffusion of oxygen in the system; the *j* in this *E* region is limited by mass transport phenomena [53].

The ORR LSV profiles for $\mathrm{Pt_{poly}}$ and Pt / Ni foams display similar features. Although the E^0 for ORR is 1.23 V, a large η is required for the ORR reaction [53]. Appreciable j for the ORR process (j_{ORR}) is observed only at $E = 0.93$ V. As the E decreases, the j_{ORR} increases up to approximately $E = 0.8$ V; at this point, mass-transfer effects limit the j_{ORR}. Figure 6.16 B displays the same data as in Figure 6.16 A, with the $0.81 < E < 0.96$ region enlarged. This plot allows some differences between the behavior of $\mathrm{Pt_{poly}}$ and Pt / Ni foam electrodes to be observed: (i) the increase in j_{ORR} with decreasing E is steeper for $\mathrm{Pt_{poly}}$; (ii) the influence of mass-transfer limitation is observed at a higher E value for $\mathrm{Pt_{polyt}}$ than for the Pt / Ni foam; and (iii) the j_{ORR} achieved at $E < 0.80$ V (mass transfer limited j) is higher for $\mathrm{Pt_{poly}}$ than for Pt / Ni foams In the case of $\mathrm{Pt_{poly}}$, there are two process that occur concurrently with the ORR: the formation of PtO in the $0.80 < E < 1.23$ V range and the reduction of PtO at $E < 1.10$ V. At the near-steady state conditions of this LSV experiment, the contributions of j from PtO formation and reduction are negligible. In the case of Pt / Ni foams, the PtO formation and reduction reactions occur as well. However it is the formation of $\beta\text{-Ni(OH)}_2$ that also occurs in this E region that has greater implications for the ORR behavior of Pt / Ni foam because this hydroxide species is not reduced electrochemically. The formation of $\beta\text{-Ni(OH)}_2$ gives rise to anodic j at $E > 0.50$ V. This could be the reason why Pt / Ni foams have a less pronounced j_{ORR} vs. E dependence relative to $\mathrm{Pt_{poly}}$ in the $0.85 < E < 90$ range. The high surface area, porous structure of Pt / Ni foams is likely the reason why these materials display lower j_{ORR} values as compared to $\mathrm{Pt_{poly}}$ in the mass-transport limited E range.

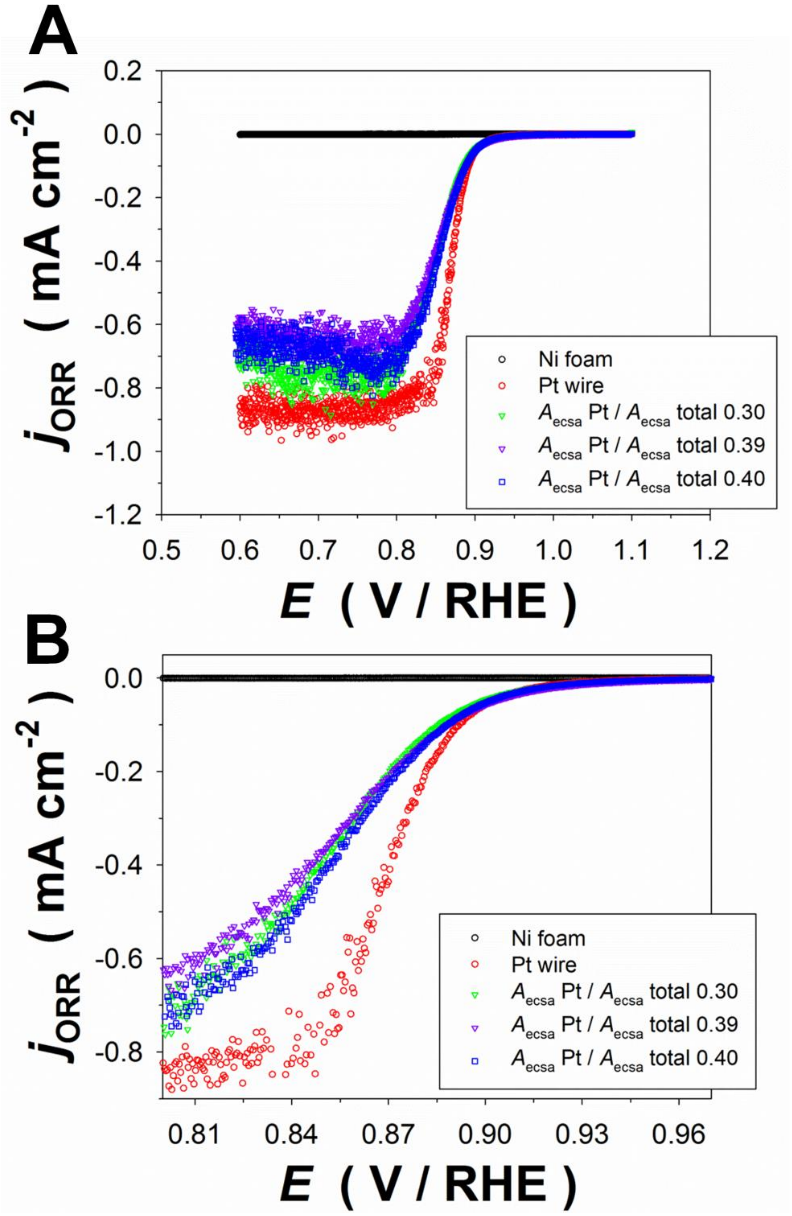

Figure 6.16. LSV profiles for the ORR in 0.50 M KOH using the following electrodes: Ni foam (black); Pt_{poly} (red); and Pt / Ni foams with different fractions of Pt A_{ecsa}: 0.30 (green), 0.39 (purple), 0.49 (blue) (A). Enlarged version for the low potential region of the graph above (B); s = 0.1 mV s^{-1}, T = 293 K, E is corrected for IR drop. Current density values are normalized to the A_{ecsa} of Pt only.

Figure 6.17 shows the current density values for the ORR (j_{ORR}) obtained at $E = 0.900$ V for Pt / Ni foam electrodes with various Pt fractions (A_{ecsa} Pt / A_{ecsa} total), as well as for unmodified Ni foam and $\mathrm{Pt_{poly}}$. Black circles represent the j_{ORR} values obtained when I is divided by the total A_{ecsa} of the Pt / Ni foam electrode. The red triangles represent the j_{ORR} values obtained when I is divided by the A_{ecsa} of Pt only. The j_{ORR} of unmodified Ni foam is marked with a green line. As is the case with the HOR, the activity of Ni foam towards the ORR is essentially 0 mA cm^{-2}, or below the detectable I limit of the potentiostat. Since unmodified Ni foam is inactive towards the ORR, the A_{ecsa} of Ni foam is not included when normalizing the I signal. Figure 6.17 shows that the j_{ORR} values for Pt / Ni foams at $E = 0.900$ V are very similar to that of $\mathrm{Pt_{poly}}$. There is no correlation observed between the j_{ORR} values and A_{ecsa} Pt / A_{ecsa} total fraction. Although Pt / Ni foam materials appear to be decent electrocatalysts towards the ORR, the Ni foam substrate is not an active electrocatalyst support for this reaction. Since the electrocatalytic behavior of Pt / Ni foams is similar to that of $\mathrm{Pt_{poly}}$, the discussion of Pt / Ni foams as electrocatalysts for the ORR is not extended and does not include the analysis of the Tafel polarization plots.

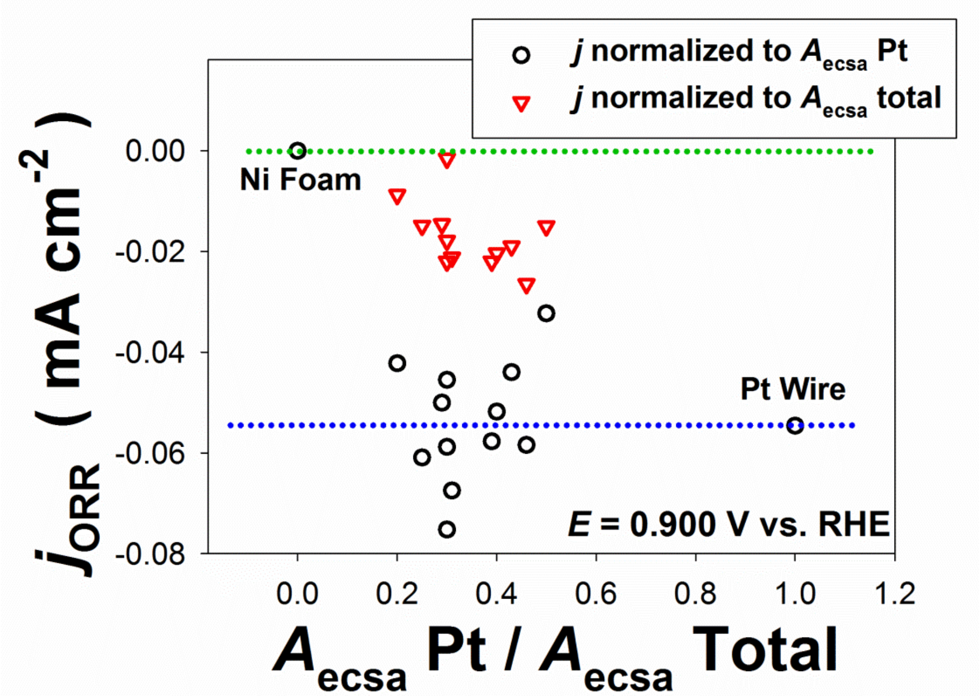

Figure 6.17. j_{ORR} values at E = 0.900 V for $\mathrm{Pt_{poly}}$, Ni foam, and Pt / Ni foam electrodes with various fractions of Pt A_{ecsa} plotted as a function of the A_{ecsa} Pt / A_{ecsa} total. These values are obtained from LSV profiles carried out in 0.50 M KOH at T = 293 K with s = 0.1 mV $\mathrm{s^{-1}}$. Black circles correspond to j_{ORR} values normalized to the total A_{ecsa} of the electrode; red triangles correspond to j_{ORR} values normalized to the A_{ecsa} of Pt.

6.4.4 The Oxygen Evolution Reaction

Figure 6.18 shows LSV profiles for the OER for the Ni foam, $\mathrm{Pt_{poly}}$, and three Pt / Ni foams with various Pt A_{ecsa} fractions. The LSV profiles were collected in the $1.350 < E < 1.800$ V region, in 0.50 M KOH aq. electrolyte saturated with O_2 gas, at T = 293 K and s = 0.1 mV $\mathrm{s^{-1}}$; the electrolyte was stirred during the measurement. The E values are adjusted for the E drop due to uncompensated solution resistance (i.e. *IR* drop). Due to the large *I* generated during the OER, the *IR* drop correction results in significant shifts of the *E*. The analysis of the OER differs slightly from those of the HER, HOR, and ORR because Ni is a more effective electrocatalyst towards this reaction than Pt [65]. In this case, the Pt / Ni foams are studied to determine if there are any electrocatalytic benefits that can be gained by depositing Pt on Ni foam. The current density for the OER (j_{OER}) using a Ni foam anode (black LSV profile) is significantly higher than that of $\mathrm{Pt_{poly}}$ (red LSV profile). The Pt / Ni foams yield j_{OER} values that are intermediate as compared with the values for the unmodified Ni foam and $\mathrm{Pt_{poly}}$. The LSV profiles demonstrate an increase in electrocatalytic activity with decreasing fraction of Pt A_{ecsa} on the Pt / Ni foam. This is likely due to the presence of Pt particles blocking regions of the Ni foam which results in a decreased A_{ecsa} of Ni foam. Figure 6.18 B displays LSV profiles in the $1.50 < E < 1.63$ region at an enlarged scale. This graph allows the onset of OER to be examined in greater detail. Of the five electrocatalyst materials shown in this plot, Ni foam demonstrates appreciable j_{OER} at the lowest η, which is about 290 mV. Large η values are typically required for the OER to proceed regardless of the electrocatalyst material [53]. Since both Ni and Pt are electrocatalytically active towards the OER, the j_{OER} is determined by dividing *I* by the total A_{ecsa} of the electrode (Pt + Ni foam).

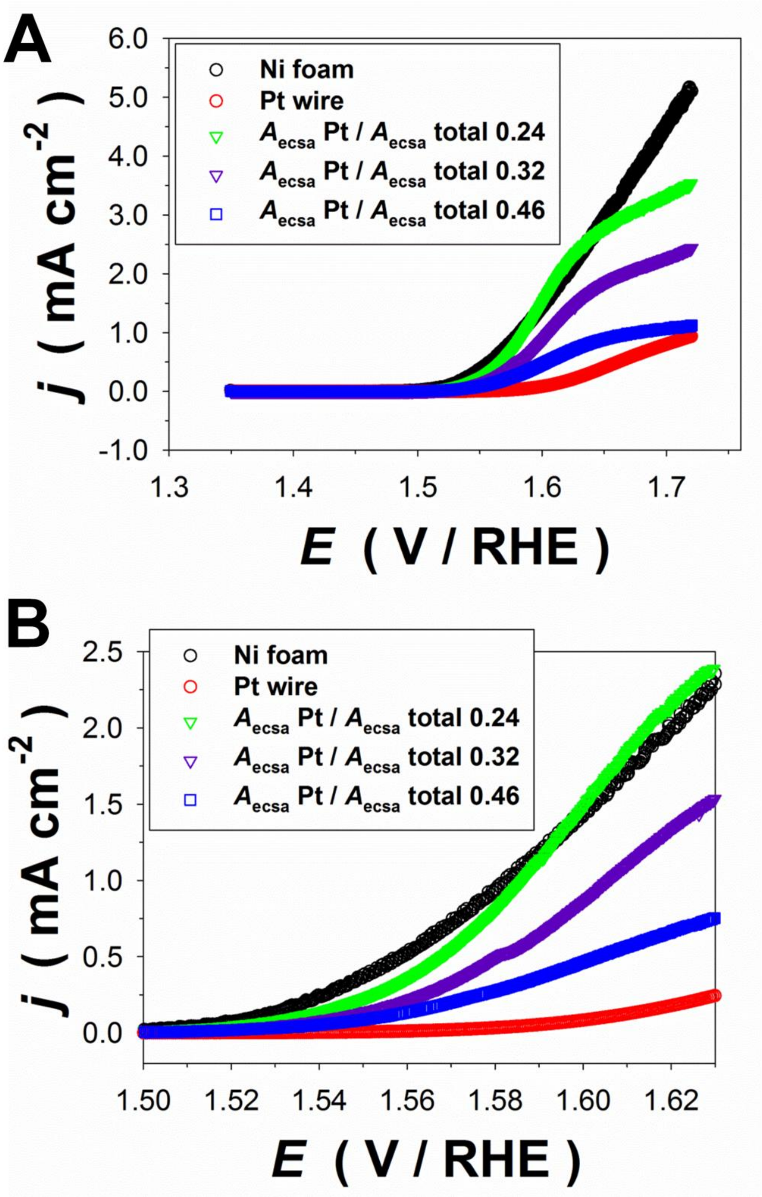

Figure 6.18. LSV profiles for the OER in 0.50 M KOH using the following electrodes: Ni foam (black); Pt_{poly} (red); and Pt / Ni foams with different fractions of Pt A_{ecsa}: 0.24 (green), 0.32 (purple), 0.46 (blue) (A). Enlarged version for the low potential region of the graph above (B); $s = 0.1$ mV s^{-1}, $T = 293$ K, E is corrected for IR drop. Current density values are normalized to the A_{ecsa} of Pt + Ni foam.

Figure 6.19 displays the j_{OER} values obtained at E = 1.65 V for various Pt / Ni foam electrodes, as well as for the unmodified Ni foam and $\mathrm{Pt_{poly}}$; the values are plotted as a function of A_{ecsa} Pt / A_{ecsa} total. The j_{OER} value for unmodified Ni foam is marked with a green line; the j_{OER} value for $\mathrm{Pt_{poly}}$ is marked with a blue line. Black circles represent the j_{OER} values obtained when I is divided by the total A_{ecsa} of the Pt / Ni foam electrode. The red triangles represent the j_{OER} values obtained when I is divided by only the A_{ecsa} of Ni foam. Since both Pt and Ni are electrocatalytically active towards the OER, it is logical to determine j_{OER} using the total A_{ecsa} of the Pt / Ni foam electrode. Figure 6.19 also demonstrates a decrease in j_{OER} as the A_{ecsa} of Pt on the Pt / Ni foam increases. As mentioned above, this is attributed to the presence of Pt particles that block regions of the Ni foam surface. The data obtained from the LSV profiles demonstrates that unmodified Ni foam is a better electrocatalyst for the OER than the Pt / Ni foams or $\mathrm{Pt_{poly}}$.

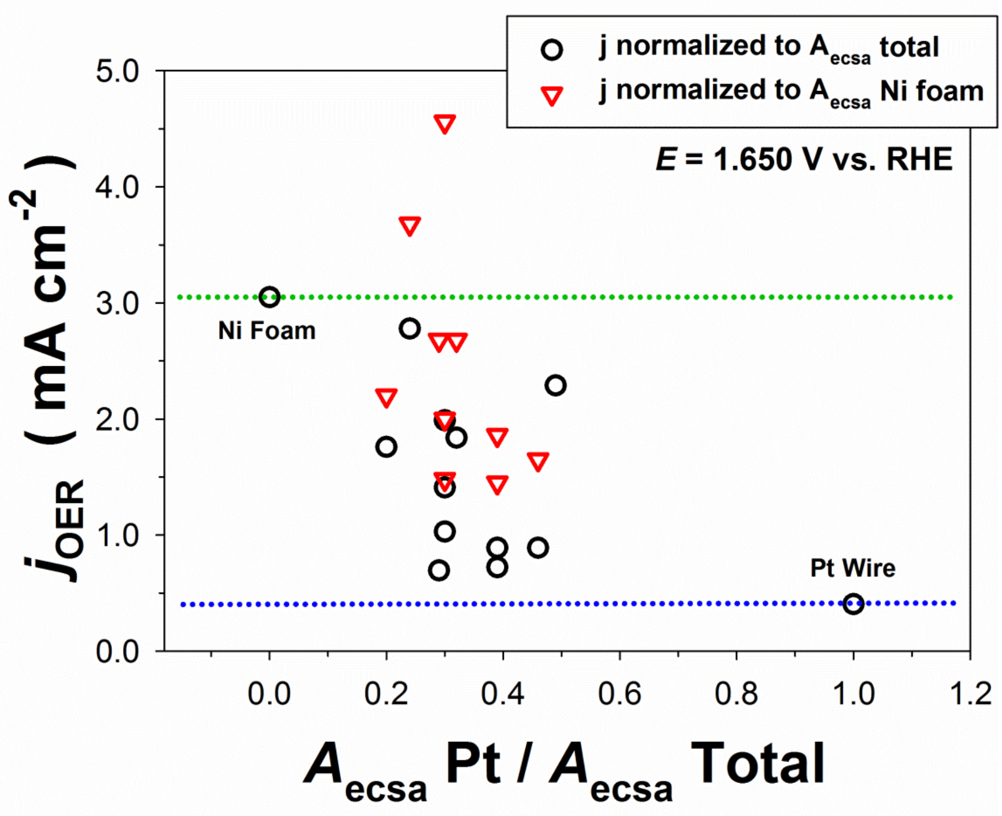

Figure 6.19. j_{OER} values at E = 1.650 V for $\mathrm{Pt_{poly}}$, Ni foam, and Pt / Ni foam electrodes with various fractions of Pt A_{ecsa} plotted as a function of the A_{ecsa} Pt / A_{ecsa} total. These values are obtained from LSV profiles carried out in 0.50 M KOH at T = 293 K with s = 0.1 mV $\mathrm{s^{-1}}$. Black circles correspond to j_{OER} values normalized to the total A_{ecsa} of the electrode; red triangles correspond to j_{OER} values normalized to the A_{ecsa} of the Ni foam only.

Figure 6.20 A presents Tafel polarization plots for the OER for the unmodified Ni foam, $\mathrm{Pt_{poly}}$, and three Pt / Ni foams with different Pt A_{ecsa} fractions. The Tafel plots for $\mathrm{Pt_{poly}}$ and Pt / Ni foam electrodes display similar features. There is a region at η values > 250 mV where the slope is very high and has an unusual shape; this region corresponds to the part of the LSV profile where no appreciable j_{OER} is observed. There is an intermediate η linear region where the Tafel slope is low (Slope 1), and there is a high η linear region where the slope is high (Slope 2). The Tafel polarization curve for unmodified Ni foam is similar to those of Pt / Ni foam and Pt_{poly}. In the case of Ni foam, the low η region reveals a moderate slope which is attributed to the formation of NiOOH in the $1.20 < E < 1.40$ V range occurring concurrently with the OER and affecting its rate. Figure 6.13 B shows Tafel plots for Pt_{poly} and unmodified Ni foam in order to demonstrate the two linear regions described above. The slope of linear region 1 is analyzed for the purpose of comparing the electrocatalytic activity of Ni foam, Pt_{poly}, and Pt / Ni foam electrodes. Table 6.4 presents the slope values (*b*) calculated for Region 1. The *b* value corresponding to Ni foam is the lowest, indicating that Ni foam has the highest electrocatalytic activity towards the OER. The *b* values corresponding to the Pt / Ni foams and Pt_{poly} are approximately the same.

Table 6.4. Data obtained from the Tafel polarization plots for the OER.

Electrode	***b* (1)** **mV / dec**
Pt_{poly}	0.057
Ni foam	0.043
Pt / Ni foam A_{ecsa} Pt / A_{ecsa} total = 0.30	0.056
Pt / Ni foam A_{ecsa} Pt / A_{ecsa} total = 0.35	0.055
Pt / Ni foam A_{ecsa} Pt / A_{ecsa} total = 0.46	0.056

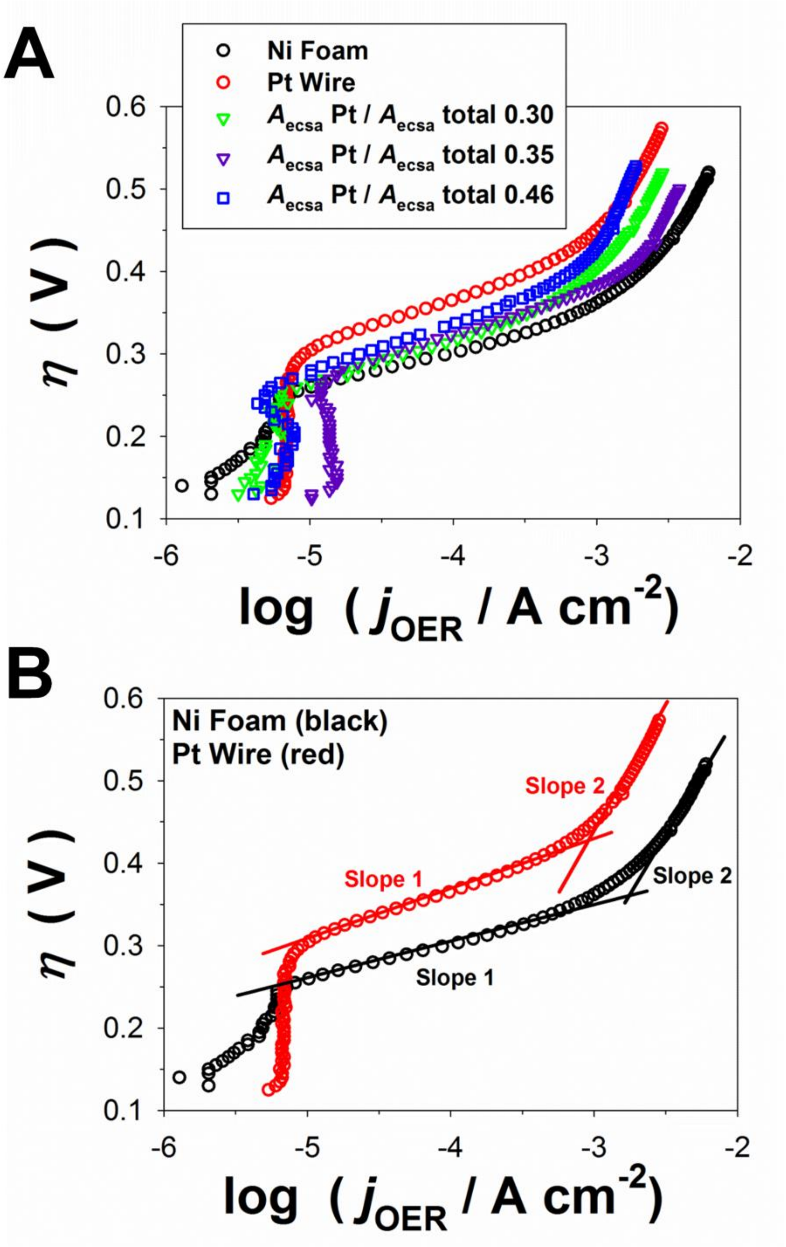

Figure 6.20. OER Tafel polarization plots for unmodified Ni foam, Pt_{poly}, and Pt / Ni foam electrodes with various fractions of Pt A_{ecsa} plotted as a function of the A_{ecsa} Pt / A_{ecsa} total (A). The data was obtained from staircase-type polarization experiments carried out in 0.50 M KOH at T = 293 K (A). Illustration of the two linear regions that are analyzed in this study.

6.5 Conclusions

The results presented in this chapter contribute towards a greater understanding of Ni foams as electrocatalysts, and as electrocatalyst support materials for Pt. The Pt / Ni foams can be prepared via an electroless deposition method. Platinum particles are deposited through the reduction of Pt^{2+} or Pt^{4+} ions using aqueous $NaBH_4$ solution as a reducing agent. The A_{ecsa} and mass loading of deposited Pt can be tailored by controlling the concentration of Pt cations in the deposition solution and by adjusting the number of deposition events. In this study, the two Pt salts used to make the deposition solutions are K_2PtCl_4 and K_2PtCl_6. The amount of Pt deposited on Ni foam can be quantified in terms of the A_{ecsa} of Pt ($\mathrm{cm}^2\ \mathrm{g}^{-1}$) and the mass loading of Pt (µg Pt / g Ni foam). The A_{ecsa} of deposited Pt is determined using the charge of H_{UPD} desorption obtained from CV profiles. The values of Pt A_{ecsa} with respect to the mass of the Ni foam substrate are in the 40 – 300 $\mathrm{cm}^2\ \mathrm{g}^{-1}$ range. The mass loading of deposited Pt can be determined by first dissolving the Pt / Ni foam in aqua regia, and then performing ICP-OES analysis to determine the concentration of Pt in the aqua regia solution. The mass loading of Pt is the range of 250 to 2200 µg of Pt / g of Ni foam. SEM and FIB can be used to study the morphology of the Pt deposit and to estimate the Pt particle size. EDS analysis, coupled with SEM imaging, provides information regarding the distribution of Pt over the surface of the Ni foam. The SEM images of Pt / Ni foam materials with Pt deposited from the two different deposition salt solutions demonstrate that the Pt particles have circular shapes and are in the 5 – 30 nm size range. Correlation of SEM and EDS results indicate that the surfaces of Pt / Ni foam struts are covered uniformly with small Pt particles. The electrochemical stability of Pt / Ni foams can be evaluated through careful analysis of CV profiles. In this study, four electrochemical parameters (A_{ecsa}, I_{DL},

Q_{anodic}, and Q_{cathodic}) were analyzed as a function of CV cycle number for 400 CV cycles. By comparing these four data sets, the evolution of CV features is analyzed with respect to surface and structural changes occurring at the Pt deposit. Over the course of CV cycling, the H_{UPD} peaks become sharper and the PtO formation and reduction E regions become more narrow. These changes in peak shape in the CV profile of Pt / Ni foams indicate an increase in structural reorganization in the Pt deposit. Electrochemical grain growth may be the phenomena responsible for this CV effect. Overall loss of j in all regions of the CV profile indicates a decrease in the A_{ecsa} of Pt. This may be attributed to several concurrently-occurring processes including: (i) Pt particle detachment; (ii) electro-dissolution of Pt; and (iii) surface smoothening as a result of electrochemical grain growth. Comprehensive characterization of the four types of Pt / Ni foams (A, AA, B, and BB) with respect to their Pt A_{ecsa}, Pt mass loading, particle distribution, particle morphology, and electrochemical behavior allows us to conclude that Pt / Ni foam materials fabricated using the Pt^{2+} or Pt^{4+} deposition solution cannot be distinguished from each other based on any of these parameters. The most important factor in the deposition procedure is the number of deposition events, which dictates the A_{ecsa} value and the mass loading of Pt.

The electrocatalytic activity of Pt / Ni foams, unmodified Ni foam, and Pt_{poly} towards the HER, HOR, ORR, and OER in alkaline media can be investigated using LSV profiles and steady-state Tafel polarization plots. In the case of the HER, Pt_{poly} is the most active electrocatalyst, followed by Pt / Ni foams, and unmodified Ni foam. For this reaction, there is a synergistic effect of having Pt supported on Ni foams. In the case of the HER, The j_{HER} values obtained for the Pt deposit on the Pt / Ni foam are higher than that of Pt_{poly}. In the case of the HOR, unmodified Ni foams and Pt / Ni foams are poor electrocatalysts. The Pt / Ni foams generate small anodic j_{HOR}

only at large η values. In the case of the ORR, unmodified Ni foam displays no electrocatalytic activity. Polycrystalline Pt and Pt / Ni foam materials display good electrocatalytic activity; the activity of Pt / Ni foam correlates with the A_{ecsa} of Pt deposited. There is no enhancement in the j_{ORR} for the Pt /Ni foam relative to that of $\mathrm{Pt_{poly}}$. The unmodified Ni foam, Pt / Ni foams and $\mathrm{Pt_{poly}}$ are active electrode materials for the OER. Unmodified Ni foam is a highly active electrode for this reaction. The OER electrocatalytic behaviour of Pt / Ni foams is lower than that of the unmodified Ni foam. Thus, we conclude that Pt / Ni foams can be fabricated reproducibly using an electroless deposition method. These materials can be tailored in terms of the Pt A_{ecsa} and Pt mass loading. The resulting Pt / Ni electrodes are very interesting electrode materials for the HER due to the beneficial electrocatalytic effect of the Ni foam support. These materials are also applicable to the ORR because the electrocatalytic activity of the deposited Pt is preserved, although the Ni foam support is inactive towards this reaction. Pt / Ni foams are not good electrode materials for the HOR. Unmodified Ni foams are excellent electrode materials for the OER, however, the deposition of Pt on Ni foam diminishes the electrocatalytic activity.

6.6 References

(1) G. F. Naterer, M. Fowler, J. Cotton and K. Gabriel, *International Journal of Hydrogen Energy,* **2008**, 33, 6849-6857.

(2) K. Zeng and D. Zhang, *Prog Energ Combust,* **2010**, 36, 307-326.

(3) H. Carmo, D. L. Fritz and J. S. Mergel D., *Int J Hydrogen Energy,* **2013**, 38, 4901-4934.

(4) J. Divisek, *J Electroanal Chem,* **1986**, 214, 615-632.

(5) D. Harrington and B. E. Conway, *J. Electroanal. Chem.,* **1987**, 221, 1-12.

(6) A. Lasia and A. Rami, *J. Electroanal. Chem.,* 1990, 294, **123**.

(7) L. Chen and A. Lasia, *J. Electrochem. Soc.,* **1991**, 138, 3321-3328.

(8) S. A. S. Machado and L. A. Avaca, *Electrochim. Acta,* **1994**, 39, 1385.

(9) N. Krstajic, K. D. Popovic, B. N. Grgur, M. Vojnovic and D. Sepa, *J Electroanal Chem,* **2001**, 512, 16-26.

(10) S. Marini, P. Salvi, P. Nelli, R. Presenti, M. Villa, M. Berrettoni, G. Zangari and Y. Kiros, *Electrochim. Acta,* **2012**, 82, 384-391.

(11) D. E. Hall, *J. Electrochem. Soc.,* **1985**, 132, 42C-48C.

(12) D. l. L. Floner C. and J. -. Leger, *Surface Science,* **1990**, 243, 87-97.

(13) M. H. Miles and Y. H. Huang, *J. Electrochem. Soc.,* **1978**, 125, 1930-1933.

(14) J. de Carvalho, G. Tremiliosi-Filho, L. A. Avaca and E. R. Gonzalez, *Int J Hydrogen Energy,* **1989**, 14, 161-165.

(15) E. R. Gonzalez and M. J. de Giz, *Chem. Ind.*, **2000**, 54, 123-132.

(16) F. Rosalbino, G. Scavino and M. A. Grande, *J. Electroanal. Chem.*, **2013**, 694, 114-121.

(17) M. J. de Giz, G. Tremiliosi-Filho, E. R. Gonzalez, S. Srinivasan and A. J. Appleby, *Int J Hydrogen Energy*, **1995**, 20, 423-427.

(18) R. Simpraga and B. E. Conway, *J. Appl. Electrochem.*, **1995**, 25, 628-641.

(19) N. A. Assuncao, M. J. de Giz, G. Tremiliosi-Filho and E. R. Conzalez, *J. Electrochem. Soc.*, **1997**, 144, 2794-2800.

(20) R. N. Singh, D. Mishra, A. Anindita, A. S. K. Sinha and A. Singh, *Electrochem. Commun.*, **2007**, 9, 1369-1373.

(21) S. Song, V. Maragou and P. Tsiakaras, *J. Fuel Cell Sci. Technol.*, **2007**, 4, 203-209.

(22) D. M. F. Santos, C. A. C. Sequeira, D. Maccio, A. Saccone and J. L. Figueiredo, *Int J Hydrogen Energy,* **2013**, 38, 3137-3145.

(23) J. Friedl and U. Stimming, *Electrochimica Acta*, **2013**, 101, 41-58.

(24) J. Ma, N. A. Choudhury and Y. Sahai, *Renew Sust Energ Rev*, **2010**, 14, 183-199.

(25) E. H. Yu, U. Krewer and K. Scott, *Energies*, **2010**, 3, 1499-1528.

(26) B. Sljukic, D. M. F. Santos and C. A. C. Sequeira, *J Electroanal Chem*, **2013**, 694, 77-83.

(27) J. Banhart, *Prog. Mater. Sci.*, **2001**, 46, 559-632.

(28) S. A. Francis and S. H. Bergens, *J. Power Sources*, **2011**, 196, 7470-7480.

(29) S. Cimino, L. Lisi, G. Mancino, M. Musiani, L. Vázquez-Gómez and E. Verlato, *Int J Hydrogen Energy*, **2012**, .

(30) S. Fiameni, I. Herraiz-Cardona, M. Musiani, V. Pérez-Herranz, L. Vázquez-Gómez and E. Verlato, *Int J Hydrogen Energy*, **2012**, 37, 10507-10516.

(31) E. Verlato, S. Cattarin, N. Comisso, L. Mattarozzi, M. Musiani and L. Vazquez-Gomez, *Electrocatalysis*, 2013, DOI 10.1007/s12678-013-0129-2.

(32) E. Verlato, S. Cattarin, N. Comisso, A. Gambirasi, M. Musiani and L. Vazquez-Gomez, *Electrocatal.*, **2012**, 3**,** 48-58.

(33) B. Yang, G. Yu and D. Shuai, *Chemosphere*, **2007**, 67, 1361-1367.

(34) Y. Cheng, Y. Liu, D. Cao, G. Wang and Y. Gao, *J. Power Sources*, **2011**, 196, 3124-3128.

(35) J. Chen, C. X. Zhao, M. M. Zhi, K. Wang, L. Deng and G. Xu, *Electrochim. Acta*, **2012**, 66, 133-138.

(36) C. Yang, D. Zhang, Y. Zhao, Y. Lu, L. Wang and J. B. Goodenough, *J. Power Sources,* **2011**, 196, 10673-10678.

(37) H. Dai, Y. Liang, P. Wang, X. Yao, T. Rufford, M. Lu and H. Cheng, *Int J Hydrogen Energy,* **2008**, 33, 4405-4412.

(38) V. Paserin, S. Marcuson, J. Shu and D. S. Wilkinson, *Adv. Eng. Mater.,* **2004**, 6, 454-459.

(39) D. Ostgard, L. Kustov, K. Poeppelmeier and W. Sachtler, *Journal of Catalysis,* **1992**, 133, 342-357.

(40)E. Antolini, J. Salgado, A. Dos Santos and E. Gonzalez, *Electrochemical and Solid-State Letters*, **2005**, 8, A226-A230.

(41) A. Esmaeilifar, S. Rowshanzamir, M. H. Eikani and E. Ghazanfari, *Electrochim. Acta,* **2010**, 56, 271-277.

(42) J. Rooke, C. de Matos Passos, M. Chatenet, R. Sescousse, T. Budtova, S. Berthon-Fabry, R. Mosdale and F. Maillard, *J. Electrochem. Soc.,* **2011**, 158, B779-B789.

(43) N. Veizaga, J. Fernandez, M. Bruno, O. Scelza and S. de Miguel, *Int J Hydrogen Energy,* **2012**, .

(44) M. Grden, M. Alsabet and G. Jerkiewicz, *ACS Appl. Mater. Interfaces,* **2012**, 4, 3012-3021.

(45) J. van Drunen, B. Kinkead, M. C. P. Wang, B. D. Gates, E. Sourty and G. Jerkiewicz, *ACS Appl. Mater. Interfaces,* **2013**, 5, 6712-6722.

(46) H. Angerstein-Kozlowska, in *Comprehensive Treatise of Electrochemistry Volume 9*, ed. E. Yeager, Plenum Press, New York, **1984**, p. 15-58.

(47) D. S. Hall, C. Bock and B. R. MacDougall, *J. Electrochem. Soc.*, **2013**, 160, F235-F243.

(48) F. A. Stevie, L. A. Giannuzzi and B. I. Prenitzer, in *Introduction to focused ion beams instrumentation, theory, techniques and practice*, ed. L. A. Giannuzzi and F. A. Stevie, Springer, Ney York, USA, **2005**, p. 1-12.

(49) N. Furuya and M. Shibata, *J Electroanal Chem*, **1999**, 467, 85-91.

(50) T. J. Schmidt, P. N. Ross and N. M. Markovic, *J Electroanal Chem*, **2002**, 524, 252-260.

(51) S. Trasatti and O. A. Petrii, *J Electroanal Chem*, **1992**, 327, 353-376.

(52) D. Chen, Q. Tao, L. W. Liao, S. X. Liu, Y. X. Chen and S. Ye, *Electrocatal.*, **2011**, 2, 207-219.

(53) C. H. Hamann, A. Hamnett and W. Vielstich, *Electrochemistry*, Wiley-VCH, Darmstadt, Germany, **2007**.

(54) B. Kinkead, J. van Drunen, M. Y. T. Paul, K. Dowling, G. Jerkiewicz and B. D. Gates, *Electrocatal.*, **2013**, 4, 179-186.

(55) S. Kim and J. P. Meyers, *Electrochimica Acta*, **2011**, 56, 8387-8393.

(56) L. Xing, G. Jerkiewicz and D. Beauchemin, *Analytica Chimica Acta*, **2013**, http://dx.doi.org/10.1016/j.aca.2013.04.048.

(57) A. A. Topalov, I. Katsounaros, M. Auinger, S. Cerevko, J. C. Meier, S. O. Klemm and K. J. J. Mayrhofer, *Agnew. Chem. Int. Ed.,* **2012**, 51, 1-4.

(58) U. Holzwarth and N. Gibson, *Nat. Nanotechnol.,* **2011**, 6, 534-538.

(59) S. Trasatti, *Electroanal. Chem. Intertacial Electrochem.,* **1972**, 39, 163-184.

(60) K. Park, J. Choi, B. Kwon, S. Lee, Y. Sung, H. Ha, S. Hong, H. Kim and A. Wieckowski, *The Journal of Physical Chemistry B,* **2002**, 106, 1869-1877.

(61) T. Toda, H. Igarashi, H. Uchida and M. Watanabe, *J. Electrochem. Soc.,* **1999**, 146, 3750-3756.

(62) A. Tegou, S. Papadimitriou, S. Armyanov, E. Valova, G. Kokkinidis and S. Sotiropoulos, *J Electroanal Chem,* **2008**, 623, 187-196.

(63) C. A. Martinez-Huitle, S. Ferro and A. De Battisti, *Electrochimica Acta,* 2004, 49, **4027**.

(64) G. Jerkiewicz, *Electrocatalytic Parameters*, lecture notes CHEM 415, Queen's University, **2013**.

(65) R. F. Scarr, *J. Electrochem. Soc.,* **1969**, 116, 1526-1532.

Chapter 7

Conclusions

During the course of this thesis work, Ni and Ni-based foams were studied for applications in electrocatalysis. In the field of electrochemistry, Ni foams are gaining interest as electrode materials due to their advantageous structural properties (high A_s, low material use, chemical and electrochemical stability in alkaline media, and physical robustness). Very little information on the chemical, electrochemical, and micro-structural characteristics of these materials was previously available in the literate. This work presents the first comprehensive structural, chemical, and electrochemical characterization of Ni-based metallic foams using materials and surface science techniques (TEM, SEM, EDS, FIB and XPS) and electrochemical methods (CV). The specific and electrochemically active surface areas (A_s, A_{ecsa}) for Ni foams of various densities were determined using cyclic voltammetry (CV); the A_s values are in the 200 – 600 $cm^2\ g^{-1}$range. Electron microscopy studies of multi-component Ni-based foams (Inconel and FE2 foams) demonstrate that the distribution of the constituent metals is non uniform in these materials. Using electron microscopy and electron tomography, we have shown that Ni-based metallic foams are dual-porosity materials and possess both macro and meso pores.

In the second section, Ni foams are applied as electrocatalysts in an electrolysis study where isopropanol is converted to acetone. The electrochemical oxidation of isopropanol in alkaline media is of direct relevance to alcohol fuel cell technologies. In addition, studies that help to understand the mechanistic details of organic electrochemical reactions have important ramifications for the development of electrochemical functional group inter-conversion methods.

The oxidation of isopropanol on a Ni-foam anode was examined using CV under well-defined experimental conditions that include variation of the isopropanol concentration and the concentration of the KOH supporting electrolyte, the presence of O_2(g), several different temperatures, and several CV scan rates. These studies allowed us to determine that the formation of a β-NiOOH species at the surface of the electrode is necessary for the conversion of isopropanol to acetone; however, the two processes do not proceed simultaneously in all conditions. The role of nickel oxides and hydroxides in the electrochemical oxidation of alcohols is a topic that is often debated in the electrochemical community. We have also shown that the oxidation of isopropanol is unaffected by the presence of oxygen within the electrolyte and interfacial electrode region. A controlled-potential electrolysis study using a Ni foam anode successfully converted isopropanol to acetone at a rate of about 5.6 mM per hour with a consistent j value of 2.6 mA cm^{-2}. From this study, we are able to we conclude that Ni foams are promising electrode materials that can be applied to organic electrochemical processes for simple functional group inter-conversions, such as the conversion of an alcohol to a ketone.

In the third section, we investigated the applicability of Ni foams as support materials for Pt in electrochemical applications. The Pt / Ni foams were prepared via an electroless deposition method and extensively characterized in terms of their surface morphology, their electrochemical stability, the mass loading of Pt, and the A_{ecsa} of Pt. The deposition method developed over the course of this work allowed the amount of deposited Pt to be tailored by controlling the concentration of Pt in the deposition solution and by adjusting the number of deposition events. Correlation of SEM and EDS results demonstrated that the surface of Pt / Ni foams is covered uniformly with small Pt particles that are in the 5 – 30 nm size range. The electrochemical stability of Pt / Ni foams was evaluated through the analysis of four electrochemical parameters (A_{ecsa}, I_{DL}, Q_{anodic}, and $Q_{cathodic}$) as a function of CV cycle number. The data obtained from CV measurements allowed us to suggest that losses in A_{ecsa} over the course of CV cycling may be due to the following concurrently-occurring processes: (i) Pt particle detachment; (ii) electro-dissolution of Pt; and (iii) surface smoothening as a result of electrochemical grain growth. In this study, we prepared Pt / Ni foams using Pt^{2+} and Pt^{4+} originating from two different Pt salts and determined that the oxidation state of Pt in the starting salt does not affect the morphology or distribution of the deposited Pt particles. The resulting Pt / Ni foams display the same electrochemical and electrocatalytic behavior, regardless of the oxidation state of Pt in the compound used for their deposition. The electrocatalytic activity of the Pt / Ni foams, unmodified Ni foam, and Pt_{poly} towards the HER, HOR, ORR, and OER in aqueous alkaline media was investigated using linear sweep voltammetry and steady-state Tafel polarization plots. We determined that the Pt / Ni foam materials are very promising electrodes for the HER due to a beneficial electrocatalytic effect of the Ni foam support. The Pt / Ni foams are also applicable as electrode materials for the ORR because the electrocatalytic activity of the deposited Pt is preserved; however, the Ni foam support is inactive in this case. The Pt / Ni foams are not good electrode materials for the HOR or the OER because the electrocatalytic activity of Pt is reduced when it is supported on the Ni foam. Unmodified Ni foams are excellent electrode materials for the OER

The outlook for Ni-based metallic foams in the field of electrocatalysis is promising. Herein, we present only a few examples which demonstrate how these materials can be effectively implemented as elecatalysts. We believe that Ni foams could be applied to a variety of organic electrochemical reactions including the oxidation and hydrogenation of compounds for alcohol fuels cells technologies, and for the broader field of electro-organic synthesis. An examination of the recent literature reveals an increasing number of papers that are dedicated to modified Ni foam electrocatalyst materials; studies on the topic of Pt, Pd, Rh, Ag, and Sn – modified Ni foams have been published in the last five years. We believe that a number of novel and industrially relevant materials can be produced using this approach. Finally, we believe that the characterization of Ni-based metallic foams presented herein provides key information that will be beneficial to researches who are currently working on developing new applications for these materials.